Vers une approche microscopique unifiée de la description de les structures et des réactions nucléaires

S. T. Hoang

To cite this version:

S. T. Hoang. Vers une approche microscopique unifiée de la description de les structures et des réactions nucléaires. Physique Nucléaire Théorique [nucl-th]. Université Paris Sud - Paris XI, 2009. Français. NNT : . tel-00488850

HAL Id: tel-00488850
https://theses.hal.science/tel-00488850

U.F.R. SCIENTIFIQUE D'ORSAY
INSTITUT DE PHYSIQUE NUCLÉAIRE D'ORSAY

THÈSE DE DOCTORAT

présentée par

HOÀNG Sỹ Thân
pour obtenir le grade de docteur en sciences de l'université Paris XI Orsay

Sujet:

VERS UNE APPROCHE MICROSCOPIQUE UNIFIÉE DE LA DESCRIPTION DE LA STRUCTURE ET DES RÉACTIONS NUCLÉAIRES

Soutenue le 22 Septembre 2009 devant la Commission d'examen

M.	**Eric BAUGE**	Rapporteur
M.	**Tien Khoa DAO**	Directeur de Thèse
M.	**Pierre DESESQUELLES**	Président
Mme.	**Francesca GULMINELLI**	Rapporteur
M.	**Elias KHAN**	Directeur de Thèse
M.	**Van Giai NGUYEN**	Examinateur

To my family.

Résumé

Cette thèse comporte 3 parties.

1. **Matière nucléaire:**
Les propriétés de la matière nucléaire sont examinées à l'aide d'interactions effectives de portée finie, soit dérivées de la théorie de Brueckner (interactions de type M3Y), soit purement phénoménologiques (forces de Gogny). Le but de ce travail est d'établir un lien entre l'interaction nucléon-nucléon nue et les propriétés de la matière nucléaire à travers la matrice G de Brueckner paramétrisée sous la forme M3Y. La discussion est concentrée sur les principaux aspects suivants: la pression dans la matière nucléaire symmétrique et la matière de neutrons, la dépendance en densité de l'énergie de symmétrie, le refroidissement des étoiles à neutrons, le module d'incompressibilité de la matière nucléaire symmétrique et non symmétrique.

2. **Structure des noyaux et de la croûte interne des étoiles à neutrons:**
Nous présentons les approches Hartree-Fock (HF) et HF-BCS en espace de coordonnées dans le cas des interactions de portée finie avec dépendance en densité dans les voies particule-trou et particule-particule. La méthode de résolution est exposée. Nous nous limitons à la symétrie sphérique. Les équations intégro-différentielles self-consistantes sont résolues par itération. Nous utilisons la méthode de Brueckner-Gammel-Weizner qui permet d'éviter d'avoir des pôles dans les potentiels locaux équivalents, contrairement à la méthode de Vautherin-Vénéroni. Nous développons aussi une méthode alternative de résolution utilisant une base de fonctions de Bessel sphériques. Cette dernière méthode est utilisée pour traiter des grands systèmes tels que les cellules de Wigner-Seitz (WS) dans les étoiles à neutrons. Nous avons ainsi

étudié, à l'aide des différentes interactions mentionnées plus haut, les noyaux doublement magiques, les isotopes de l'étain et l'éventualité de structures en bulle dans les noyaux ^{22}O, ^{34}Si, ^{46}Ar et ^{68}Ar. Nous présentons aussi la première étude des cellules de WS dans la croûte interne des étoiles à neutrons faite avec des forces de portée finie. Nous avons ainsi examiné les structures correspondant aux diverses régions de la croûte interne allant des densités les plus faibles jusqu'aux environs de la demi-densité de saturation nucléaire.

3. Réactions nucléaires:

Utilisant de même les interactions effectives dérivées de M3Y nous avons procédé à l'analyse en voies couplées des réactions d'échange de charge (p, n) sur des cibles de ^{48}Ca, ^{90}Zr, ^{120}Sn et ^{208}Pb aboutissant aux états isobariques analogues, pour des protons d'énergies incidentes de 35 MeV et 45 MeV. Les facteurs de forme sont calculés soit microscopiquement par le modèle de convolution, soit à partir du potential optique global nucléon-noyau de la littérature. Nous avons d'abord déterminé la partie dépendante de la densité isovectorielle de l'interaction CDM3Y6 en nous basant sur le potentiel optique microscopique de Jeukenne, Lejeune et Mahaux, puis l'avons utilisée dans le modèle de convolution. Ceci nous a permis de tester la validité de la partie dépendante de la densité isovectorielle de la force CDM3Y6.

Abstract

This thesis contains 3 main parts:

1. Nuclear matter:

The properties of nuclear matter are examined using finite range effective interactions, either derived from the Brueckner theory (M3Y-type interactions) or determined in a purely phenomenological way (Gogny-type interactions). Skyrme-type interactions are also used for comparison. The motivation of the study is to establish a link between the bare NN interaction and nuclear matter properties via the effective Brueckner G-matrix parameterized in the M3Y form. We have concentrated our discussion on several main aspects: the pressure in symmetric nuclear matter and in neutron matter, the density dependence of the symmetry energy S, the neutron star cooling, and the nuclear matter incompressibility for the symmetric and asymmetric nuclear matter.

2. Structure of finite nuclei and of the inner crust of neutron stars:

We present the non-relativistic HF and HF-BCS approaches in coordinate representation using finite-range density-dependent interactions in both the mean field and pairing channels. The method for solving the HF equations in coordinate space is presented. We limit the study to the spherical symmetry case. An iterative scheme is used for solving the integro-differential HF equations. We adopt the method of Brueckner-Gammel-Weizner which is free of poles in the local equivalent potentials, in contrast to the usually used Vautherin-Vénéroni method. Alternatively, we have developed a method using a basis of spherical Bessel functions. The latter method is useful for treating systems containing many nucleons in large boxes like the Wigner-Seitz (WS) cells of the neutron star inner crust. We have thus studied, using the

effective interactions mentioned above, the doubly magic nuclei, the Sn isotopes, and the possible occurrence of bubble structures in the nuclei ^{22}O, ^{34}Si, ^{46}Ar and ^{68}Ar. We also present for the first time a study of Wigner-Seitz cells in the inner crust of neutron stars using finite range interactions. We have thus examined the structures of the different zones of the inner crust, from the lowest densities up to densities close to the vicinity of half saturation density where the spherical assumption breaks down.

3. Nuclear reactions:

Using the same effective interactions derived from the M3Y-type interactions we have performed a coupled channel analysis of (p,n) charge exchange reactions at 35 and 45 MeV incident energies on ^{48}Ca, ^{90}Zr, ^{120}Sn and ^{208}Pb targets leading to isobaric analog states. The form factors are either calculated microscopically by the convolution model, or evaluated from the global optical potential taken from the literature. We have first determined the component of the CDM3Y6 interaction which depends on the isovector density by using the microscopic optical potential of Jeukenne, Lejeune and Mahaux, and then this was used for the folding model. Thus, we have been able to assess the validity of the component of CDM3Y6 which depends on the isovector density.

Acknowledgments

First, I would like to thank my supervisors at IPN-Orsay, Dr. Elias Khan and Prof. Nguyen Van Giai, for their advice and support, and spending their time to guide this work and help me whenever I was in need. Prof. Nguyen Van Giai has given me the opportunity to work in Orsay. I am grateful for his help and support he gave me on this occasion. I express my deepest gratitude to Prof. Dao Tien Khoa, my supervisor at INST Hanoi, who taught and led me to the real research in nuclear physics. I would like to thank the Institute of Physics Hanoi and Université Paris-Sud XI for providing me the opportunity to carry out my Ph.D. thesis in *co-tutelle*. The hospitality of IPN-Orsay is gratefully acknowledged.

I am grateful to Prof. Eric Bauge, Prof. Pierre Desesquelles and Prof. Francesca Gulminelli for accepting to be on my thesis review committee. I would like to thank Prof. Michel Davier (Conseiller aux Thèses), Prof. Yves Charon (Former Directeur de l'Ecole Doctorale) and Prof. Achille Stocchi (Directeur de l'Ecole Doctorale), for their help.

I express my thanks to my colleagues in the Groupe de Physique Théorique at IPN-Orsay, Bachir Moussallam, Peter Schuck, Nicole Vinh Mau, Jérôme Margueron, Marcella Grasso, Michael Urban, Jean Libert..., for their help, the useful discussions and their kind friendship that made the atmosphere in our group so lively and pleasant. Nathalie Escoubeirou sloved for me a number of administrative problems, for which I am very grateful. I also would like to thank my colleagues and friends of the Center for Basic Research and Computation at Hanoi for their friendship and encouragements.

I acknowledge Mario Centelles, Bao-An Li and Herbert Müther for their discussions on the nuclear matter part of my thesis, and Athena Pakou for her helpful communication on the charge exchange (p, n) reactions. I would like also to thank Nicu Sandulescu for his discussions in the calculations of the Wigner-Seitz cells.

Finally, I would like to give my deep gratitude to my grandfather, grandmother, parents, sister, and my niece for their strong support and encouragement at all time. My wife and my beloved daughter (Hoàng Ngọc Minh Khuê) receive special thanks for their patience and love throughout my studies.

This work was partially supported by the Institute for Nuclear Science and Technology Hanoi (INST), the Groupe de Physique Théorique of Institut de Physique Nucléaire (IPN) - Université Paris-Sud XI Orsay, the Asia Link Programme CN/Asia-Link 008 (94791), and the Bourse Eiffel program of the French Ministry of Foreign Affairs in France. Some of the numerical calculations were carried out on the “GRILLE” supercomputers of Institut National de Physique Nucléaire et de Physique des Particules (IN2P3) which is supported by the Centre National de la Recherche Scientifique (CNRS) in France.

List of Publications

This thesis is based on the first four papers.

1. H.S. Than, N.V. Giai, and E. Khan
   Wigner-Seitz cells in neutron star crust with finite range interactions,
   Manuscript, 2009.

2. H.S. Than, D.T. Khoa, and N.V. Giai,
   Neutron star cooling: A challenge to the nuclear mean field ?,
   Submitted to Physical Review **C**, 2009.

3. H.S. Than, D.T. Khoa, N.V. Giai and E. Khan,
   Continuum properties of the Hartree-Fock mean field with finite-range interactions,
   Proceedings of the International Symposium on Physics of Unstable Nuclei (ISPUN07), Hoi An, Vietnam, p. 457, World Scientific, Singapore, 2008.

4. D.T. Khoa, H.S. Than and D.C. Cuong,
   Folding model study of the isobaric analog excitation: Isovector density dependence, Lane potential, and nuclear symmetry energy,
   Physical Review **C 76**, 014603, 2007.

5. D.T. Khoa, H.S. Than and D.C. Cuong,
   Microscopic study of the isobaric analog excitations and its astrophysical implication,
   Proceedings of the 7^{th} National Conference on Nuclear Science and Technology, Da Nang, VietNam, 2007.

6. D.T. Khoa, W. von Oertzen, H.G. Bohlen, H.S. Than,
Probing the Nuclear Equation of State in the quasi-elastic nucleus-nucleus scattering,
Proceedings of the Asia-Pacific Forum on Frontiers of Basic Science, Osaka University Press, p. 25, 2006.

7. H.S. Than, D.T. Khoa,
Study of the nuclear equation of state based on the description of the charge exchange (p, n) reactions,
Proceedings of the 6th National Conference on Nuclear Science and Technology, Da Lat VietNam, p. 81, 2006.

8. E. Becheva, Y. Blumenfeld, E. Khan, D. Beaumel, J. M. Daugas, F. Delaunay, Ch-E. Demonchy, A. Drouart,M. Fallot, A. Gillibert, L. Giot, M. Grasso,N. Keeley, K. W. Kemper, D. T. Khoa, V. Lapoux, V. Lima, A. Musumarra, L. Nalpas, E. C. Pollacco, O. Roig, P. Roussel-Chomaz, J. E. Sauvestre, J. A. Scarpaci, F. Skaza, and H.S. Than,
N=14 Shell Closure in ^{22}O Viewed through a Neutron Sensitive probe,
Physical Review Letters **96**, 012501, 2006.

9. D.T. Khoa and H.S. Than,
Isospin dependence of $^{6}He+p$ optical potential and the symmetry energy,
Physical Review **C 71**, 044601, 2005.

10. D.T. Khoa, H.S. Than, T.H. Nam, M. Grasso and N.V. Giai,
Microscopic calculation of the interaction cross section for stable and unstable nuclei based on a non-relativistic nucleon-nucleon t-matrix,
Physical Review **C 69**, 044605, 2004.

11. D.T. Khoa, H.S. Than and M. Grasso,
Microscopic study of interaction cross sections measured at relativistic energies for stable and unstable nuclei,
Nuclear Physics **A 722**, 92c ,2003.

Contents

Chapter 1

INTRODUCTION

The existence of the atomic nucleus was discovered by Rutherford using the bombarding of a gold-foil with α-particles in 1911 and the atomic nucleus is one of the most complex quantum mechanical many-body systems. The weight of nuclei was explored by Thomson, who found also the existence of isotopes. We know that the neutron was found by Chadwick in 1932 and together with the discovery of proton, these nucleons became the basic constituents of nuclei. It was natural to think that there is a strong interaction between nucleons, that supports an existence of the nucleus. This interaction is known to some degree within the meson exchange picture. However, this picture is only true for the medium- and long-range parts of the interaction while its short-range part is not well known. Furthermore, even if we can understand the free nucleon-nucleon (NN) interaction, there still remain many questions in the determination of the effective NN interaction in medium. Therefore, the effective NN interaction between nucleons has been one of the basic problems and tasks of nuclear physics to understand its principle, and consequently, to describe the structure and properties of atomic nuclei.

The main goal of modern nuclear physics science is associated with the rare isotope beams, which address basic questions of nuclear structure, nuclear astrophysics and fundamental interaction physics. Up to now experimental data are only available for the nuclei relatively close to the stability region. The problem lies in the experimental difficulties of obtaining and measuring the properties of short lived nuclear systems. However, thanks to the technological developments of accelerators, intense beams of short-lived nuclei [Mue01, Tan95] provide a good chance to study the properties of exotic nuclei [Mue93, Tan95, Han95, Cas00], and many interesting phenomena are discovered like neutron/proton halo [Tan85, War95], neutron/proton -skin [Tan88, Chu96, Bro00, Fur02], neutron subshell closures [Sta04, Sch07, Ele07, Thi00, Bec06, Hof08], bubble structure of atomic nuclei [Wil46, Dec03, Ben03, Kha08], the enhancement of fusion cross sections of heavy-ion reactions [Alm95, Yos95], etc... Among many existing rare isotope research laboratories in the world are the CERN ISOLDE facility [CER], TRIUMF [TRI], NSCL at Michigan State University [NSC], ATLAS at the Argonne National Laboratory [ATL], HRIBF at Oak Ridge National Laboratory [HRI], RIKEN [RIK], GSI [GSI] and GANIL [GAN]. Along with these advances, increased computing power and progress in computational techniques have greatly enhanced theoretical progress in addressing the nuclear many-body problem and many new features of nuclei are found and analyzed.

The mean field theories provide us with a good first approximation for bound states of nuclei. The Hartree-Fock (HF) theory, in which we can construct the nuclear mean field in a self-consistent manner, is an effective tool to describe the single-particle levels of nuclei from a microscopic standpoint. One knows that the nuclei close to the limit of nuclear stability present interesting features. The most difficult implications from the point of view of theoretical modeling arise from the strong pairing correlations and the coupling to the continuum. As nuclei move away from the stability line and approach the proton/neutron drip line, the corresponding Fermi surface gets closer to zero energy. A significant number of the high-lying single-particle states are then shifted to the continuum. Several approximations in the mean field theory have been used to address the physics of the pairing correlations (e.g. HF-BCS [Bar57] or HFB [Goo79, Rin80]). The strong pairing correlations near the driplines can no longer be described by a small residual interaction. It becomes, therefore, necessary to treat the mean field and pairing correlation in self-consistent theory. Furthermore, an important physics problem lies in the effective NN interaction. A variety of effective NN interactions have been used in the HF or HF-BCS (HFB) calculations of nuclei. For the zero-range interactions, the Skyrme interaction [Sky56] has become popular, since the zero-range form is easy to handle and the self-consistent HF equations can be conveniently solved in coordinate space. The self-consistent mean field HF calculations with this kind of interaction was first performed in the work of Vautherin and Brink [Vau72]. Unlike the case of the familiar Skyrme-HF potentials which are essentially local (the non-locality being simply described by a position-dependent effective mass [Dov72]), the HF potential generated by a finite-range interaction is fully non-local. The self-consistent HF mean field of finite nuclei using the finite-range effective interaction of Brink and Boeker [Bri67], which is density-independent and consists of a sum of two Gaussians, was calculated by Vautherin and Vénéroni [Vau67] in coordinate representation. In that work, the non-local Fock potential was treated by a method called "*trivially equivalent local potential*" [Vau67]. However, the disadvantage of this method is that this equivalent local potential can have poles at the nodes of the wave functions and this requires a linearization approximation. In a recent study by Hofman and Lenske [Hof98], the non-locality of exchange term is treated by using the density-matrix expansion introduced by Negele and Vautherin [Neg72]. However, despite the success of this method for the stable and unstable nuclei [Hof98], it has not been inspected sufficiently whether the first few terms of the density-matrix expansion can give a good enough description of the nuclei far from the β-stability. In contrast to the coordinate representation method, the basis expansion method can be used to avoid the difficult problems of the non-locality of the exchange potential. The finite-range Gogny interaction [Gog75, Dec80] has been used in such an approach where its parametrization is obtained by fitting the two-body scattering data as well as the ground state properties of double-closed shell nuclei and open shell nuclei using the harmonic-oscillator basis. However, a disadvantage of this method is that the solutions depend on the choice of the basis. Another kind of finite-range effective interaction is the family of M3Y interactions [Ana83]. Using the basis expansion method, new parametrization of the M3Y force has been obtained by Nakada [Nak02, Nak03, Nak08].

In general, the effective NN interactions mentioned above can be divided into two distinct groups. The first group consists of those where the effective NN interaction is directly parametrized as a whole, leaving out any connection with a realistic free NN interaction. In the non-relativistic approaches, the parameters of the effective NN interaction belonging to this group are obtained by fitting the HF mean field results to the experimental data. On the other hand, the effective NN interactions in the relativistic mean field model are generated through the exchange of effective mesons. The parameters of the Lagrangian which represent a system of interacting nucleons are obtained by fitting the bulk properties of a set of spherical nuclei. Alternatively, one first derives the effective NN interaction in the lowest-order of many-body calculation from a realistic free NN interaction which reproduces the free NN scattering data (e.g. a solution of the Bethe-Goldstone equation), and higher-order corrections are then parametrized in terms of a density and momentum dependence [Kho93, Kho96].

While the approach consisting of a direct parametrization of the effective NN interaction in the first group might be less fundamental than those of the second group, they have a certain number of advantages. First, one can get a somewhat better physical insight from the simplicity of the calculations because simple relations connecting different nuclear properties can often be derived. Also it is a useful tool to extrapolate in a rather simple and reliable way to nuclei far from the stability line and to superheavy nuclei. One of these effective interactions belonging to the first group is the Skyrme interaction [Sky56]. The reason why the effective Skyrme interaction is popular is due to its simple expression in term of the $\delta(\boldsymbol{r_1}\text{-}\boldsymbol{r_2})$ interaction, which makes the calculations in the HF mean field much simpler. Since the pioneering work of Vautherin and Brink [Vau72], many different parameterizations of the Skyrme interaction have been realized to better reproduce data in nuclear masses, radii and other physical quantities. Most of the parameter sets of the Skyrme interaction are obtained by fitting the HF results to reproduce the nuclear matter properties, properties of nuclei at the β-line and of nuclei near the proton/neutron drip line. In 1972, Vautherin and Brink produced two sets of parameters SI and SII [Vau72] by fitting the ground state properties (biding energies and radii) to experimental data for two spherical nuclei ^{16}O and ^{208}Pb. In 1975, Beiner et al. generated the SII to SVI parameter sets [Bei75] using more experimental data, such as the binding energies and charge radii of ^{40}Ca, ^{48}Ca, ^{56}Ni, ^{90}Zr, ^{140}Ce and ^{208}Pb. The SkM interaction [Kri80] was obtained by including the experimental data on the monopole energy to the fit in 1980. In 1981, N. V. Giai and Sagawa produced two parameter sets SGI and SGII [Gia81] by including additional constraints on the Landau parameters G_0 and G'_0. These interactions reproduced quite well the values of the incompressibility coefficient K =215 MeV and of G'_0= 0.503 for SGII. More recently, many sets of the Skyrme parameters have been generated, such as SkI1-5 [Rei95], SLy4-7,10 [Cha98], SKX [Bro98] and SkO [Rei99], to reproduce the properties of nuclear matter and nuclei (at the β-line and near the proton/neutron drip line). Although the Skyrme-type effective NN interactions have been introduced by parameterizing the interaction as a whole, it is not fully fundamental. However, the HF mean field calculations using the Skyrme interaction have been very successful in studying the ground state properties of nuclei as well as in the calculations of symmetric NM.

The Gogny force was first introduced in 1975 [Gog75]. It consists of a sum of two Gaussians corresponding to a long range and a short range central forces, a zero-range spin-orbit force and a zero-range density-dependent term. It can reproduce nucleon-nucleon scattering phase shifts up to moderate energies. The first parametrization D1 [Dec80] gave satisfying results for masses, radii and pairing properties of many nuclei. However, the surface energy obtained by this version was too high and this version was not able to reproduce fission barriers. To correct for this deficiency, a new parametrization D1S of the Gogny force was proposed [Ber91]. In spite of the numerous advantages of this new interaction compared to the D1 parametrization, one can observe that the version D1S is still unable to reproduce the neutron matter Equation Of State (EOS) in comparison with the Friedman-Pandharipande's description of EOS of neutron matter [Cha08]. The new versions of the Gogny D1N [Cha08] and D1M [Gor09] remedy to this defect and they can reproduce the neutron matter EOS better than the D1S version while still giving simultaneously good description of the nuclear structure properties and nuclear mass data.

Among different kinds of finite range effective NN interactions, the well-known M3Y interaction was originally constructed by the Michigan State University group [Ana83]. This interaction has been derived by fitting its matrix elements in an oscillator basis (the oscillator parameters were chosen to reproduce the ^{16}O ground state) to those matrix elements of the G-matrix obtained with the Reid [Ber77] and Paris [Ana83] NN potentials. The ranges of the M3Y interactions were chosen to ensure a long-range tail of the one-pion-exchange potential (OPEP) as well as a short-range repulsive part simulating the exchange of heavier mesons [Ber77]. The shorter ranges correspond to boson masses $m = 490$ MeV and 780 MeV and thus mimicking δ, ω and ρ meson exchange interactions. Represented by a sum of the Yukawa functions, the M3Y type interaction will be tractable in various models. We know that the saturation of density and energy is a basic property of nuclei. In developing effective interactions, they are required to reproduce the saturation properties of nuclear matter. However, the non-relativistic G-matrix fails to describe the saturation point at the right density and energy. Therefore, it will not be appropriate to use the G-matrix for HF calculations without any modification. The M3Y interaction was obtained so that the G-matrix at a certain density could be reproduced by a sum of Yukawa functions. The originally density-independent M3Y interaction gives no saturation point within the HF calculation of nuclear matter [Kho93]. By introducing a realistic density dependence the modified effective M3Y interaction can describe the known nuclear matter properties. During the last decade, different density-dependent versions of the M3Y interaction have been used in the HF calculations of symmetric and asymmetric NM [Kho95, Nak02, Nak03, Kho96, Kho07b, Chi09, Bas08, Hof98], in the mean-field studies of nuclear ground states [Nak02, Nak03, Nak08, Hof98], as well as in numerous folding model studies of the nucleon-nucleus and nucleus-nucleus scattering [Kho96, Kho97, Kho05, Chi09, Kho07b].

One of the main goals of using realistic models of NN interactions in microscopic nuclear structure calculations is to obtain reliable prediction for the EOS of nuclear matter. Knowledge about the nuclear symmetry energy extracted from the EOS of nuclear matter is essential in understanding not only many aspects of nuclear physics, such as heavy-ion collisions induced by radioactive nuclei and the structure of exotic nuclei, but also a number of important issues in astrophysics, such as r-process of stellar nucleosynthesis during pre-supernova evolution of massive stars and the cooling of neutron stars [Bet90, Swe94, Sum94, Lat04]. In particular, the knowledge of the EOS is necessary for the determination of the maximum mass M_{max} of neutron stars. The EOS is predominantly determined by the effective NN interaction between elementary constituents of dense matter. Even in the crust of neutron stars, where the density is below the normal nuclear density $\rho_0 = 0.16$ fm^{-3}, the effective NN interactions are responsible for the properties of neutron rich nuclei, crucial for the crust EOS. The knowledge of these interactions is particularly important for the structure of the inner crust of neutron stars, where nuclei are immersed in a neutron gas. However, the calculation of the properties of the neutron star crust starting from an experimentally determined *bare* NN *in vacuum* is not feasible. This is due to the prohibitive complexity of the many-body problem to be solved in the case of heavy nuclei immersed in a neutron gas. To make a calculation feasible, one uses a mean-field approximation with an effective NN interaction, an approach used with great success in terrestrial nuclear physics. The first successful attempt to determine in this approach the structure of the neutron star crust is the classical work of Negele and Vautherin [Neg73]. Following the standard models, the inner crust of neutron star consists of a lattice of Wigner-Seitz cells, each cell containing a neutron-rich nucleus immersed in a sea of dilute gas of neutrons and relativistic electrons uniformly distributed inside the cell [Pet95].

One knows that the most efficient process of the neutron star cooling, the so-called *direct* Urca process in which nucleons undergo direct beta (and inverse-beta) decays [Lat91, Pag04], can take place only if the proton-to-neutron ratio exceeds 1/8 or the proton fraction $x_p \geq 1/9$ in beta equilibrium. The proton fraction x_p can be entirely determined from the NM symmetry energy $S(\rho)$. It is a fundamental question whether the direct Urca process is possible or not. If the x_p value cannot reach the threshold for the direct Urca process, then the neutron star cooling should proceed via the indirect or *modified* Urca process which has a reaction rate of $10^4 \sim 10^5$ times smaller than that of the direct beta decay and implies, therefore, a much longer duration of the cooling process. Although a recent test [Kla06] of the microscopic EOS against the measured neutron star masses and flow data of HI collisions has shown that the direct Urca process is possible when the neutron star mass is above a lower limit of $1.35 \sim 1.5$ solar mass ($M_\odot$), the overall cooling time of a neutron star is still unknown as yet [Lat04] due to the uncertainty about the high-density behavior of $S(\rho)$.

As we know the basic inputs for any microscopic models to calculate the nucleon-nucleus and nucleus-nucleus potentials are the nuclear densities of the target (and projectile) and the effective NN interaction. Among various models of nuclear reactions, the folding model is one of the successful models that has been used for years to calculate the nucleon-nucleus and nucleus-nucleus optical potential [Sin75, Bri77, Rik84, Dor98, Kho02, Kho03, Kho96, Kho95, Kho07b, Chi09] and inelastic form factors [Mac78, Che85, Kho07b, Chi09]. It can be seen from the basic folding formulas that this model generates the first-order term of the microscopic optical potential that is derived from Feshbach's theory of nuclear reactions [Fes92]. The success of this approach in describing the observed nucleon-nucleus elastic scattering data for many targets suggests that the first-order term of the microscopic optical potential is indeed the dominant part of the nucleon optical potential. In the same way, the inelastic (folded) form factor is also the most important input for the analysis of inelastic scattering data within the distorted wave Born approximation (DWBA) or coupled-channel (CC) approaches.

One knows that if we have realistic nuclear densities, available from different nuclear models or directly from the electron-scattering data, it still remains necessary to have a realistic effective NN interaction before the success of the folding model can be reliably assessed. In the folding model, popular choices for the effective NN interaction have frequently been based upon the M3Y interactions. The latest versions of these interactions have been denoted as CDM3Yn interactions [Kho97] which were designed to reproduce the G-matrix elements of the Paris [Ana83] NN potential. The isoscalar density dependence of the CDM3Yn interactions has been parametrized to properly reproduce the saturation properties of symmetric NM [Kho97]. These interactions, especially the latest CDM3Y6 version, have been widely tested in numerous folding model analyses of the elastic, refractive α-nucleus and nucleus-nucleus scattering. There are two main methods to determine the isospin dependence of the nucleon-nucleus OP: (i) study the elastic (p,p) and (n,n) at the same energy and from the same target, and (ii) study the charge exchange (p,n) reactions. Thus, the isovector part of the latest CDM3Y6 interaction has been parametrized to reproduce the Brueckner-Hartree-Fock (BHF) results of the nucleon optical potential (OP) in the nuclear matter limit [Jeu77b]. This version of the CDM3Y6 interaction has been applied to the folding coupled-channel analysis of the charge exchange (p, n) reactions [Kho05, Kho07b] and the inelastic ^{18,20,22}O(p, p') scattering [Chi09]. Furthermore, the nucleon-nucleus OP has been studied over the years and there are several "global" sets of the OP parameters deduced from the extensive optical model analyses of nucleon elastic scattering, like that by Becchetti and Greenlees [Bec69], the CH89 global OP [Var91], and a recent systematics by Koning and Delaroche [Kon03] which covers a wide range of energies (from 1 keV to 200 MeV) and target masses $(24 \leq A \leq 209)$. Although parameterized in the empirical Woods-Saxon form, these global systematics are very valuable in predicting the nucleon-nucleus OP when elastic scattering data are not available or cannot be measured which is the case for the unstable nuclei.

Based on the above arguments, we concentrate on the non-relativistic models to study the properties of nuclear matter within the HF approach using phenomenological interactions, such as the Gogny D1S [Ber91] (D1N [Cha08]) and Skyrme SLy4 [Cha98] interactions, and the two different sets of the density-dependent M3Y interaction named as CDM3Yn [Kho95, Kho07b] and M3Y-Pn [Nak08]. These latest versions of the M3Y-Pn have not been used in the HF study of asymmetric NM and it is, therefore, of interest to probe them in the present HF calculations. In this work we will show which interactions will support for the direct Urca process of the neutron star cooling. For the study of finite nuclei, we have developed the non-relativistic HF and HF-BCS approaches in coordinate representation using finite-range density-dependent interactions in both the mean field and pairing channels. One of the aims of this thesis is to show how the coordinate space HF equations for a non-local self-consistent potential can be actually solved with correct boundary conditions. However, this method where the radial HF equations are solved in coordinate space becomes more difficult in larger boxes or with larger l-values (for example, in calculations of the Wigner-Seitz (WS) cells [Neg73]). Therefore, in this thesis we have also developed a basis expansion method, in which the radial HF equations are solved using a spherical Bessel function basis whenever necessary. We restrict our study to spherical symmetry. The first application is to study the possibility of bubble structures of ^{34}Si, ^{22}O, ^{46}Ar and ^{68}Ar using the finite-range density-dependent interactions in both the mean field and pairing channels. Furthermore, for the first time the properties of the WS cells in the inner crust of neutron stars are studied using finite-range density-dependent interactions in HF and HF-BCS approaches. Among different kinds of finite-range density-dependent interactions, the CDM3Y6 interaction can be used in studying the properties of NM and in calculations of the nucleon-nucleus potentials using the folding model. Therefore, we have studied the charge exchange (p, n) reaction measured with ^{48}Ca, ^{90}Zr, ^{120}Sn and ^{208}Pb targets at the proton energies of 35 and 45 MeV within a two-channel coupling formalism using the folding model.

The structure of this thesis is the following: the introduction of this thesis is presented in **Chapter I**. A brief description of the finite-range density-dependent M3Y interactions is presented in **Chapter 2**. The necessity of using the phenomenological interactions (Gogny D1S (D1N) or Skyrme SLy4) instead of the effective ones obtained by solving the Bethe-Goldstone equation is also explained. We have developed a compact method to construct the complex CDM3Yn interaction, which will be used in the next chapters. In **Chapter 3**, the properties of symmetric and asymmetric nuclear matter are studied using the above interactions within the non-relativistic HF approach. The nuclear pressure P for symmetric nuclear matter and pure neutron matter is calculated and compared with the experimental data extracted from analyzing the collective flow data in relativistic heavy-ion collisions. The density dependence of the nuclear symmetry energy $S(\rho)$, up to 0.8 fm^{-3}, will be discussed. Corresponding results given by the microscopic predictions of Akmal-Pandhanripande-Ravenhall (APR) [Akm98], by the Dirac Brueckner Hartree Fock (DBHF) calculations with the Bonn A interaction [Dal04] and by other versions of the mean-field approach, such as V$_{lowk}$+CT [Dal09], MDI [Li08, Xia09] and Hybrid models [Pie09], are also presented for comparison. The results obtained in the relativistic mean field studies using the G2 [Aru04] and FSUgold [Tod05] parameter sets are shown and compared. In **Chapter 4**, the general formalism of HF and HF-BCS approaches is developed with the finite-range effective interactions. The HF equations are solved both in coordinate space and using a basis expansion method. The description of the techniques used to perform the HF-BCS calculations is presented. The codes thus developed are used to study the properties of doubly magic nuclei and the Sn isotopes using the finite-range effective interactions. The results obtained for bubble nuclei and for the WS cells in the inner crust of neutron stars are discussed. In **Chapter 5**, the folding model is applied to the study of charge exchange (p,n) reactions using the CDM3Y6 interaction. In the end, conclusions and perspectives are drawn in **Chapter 6**.

CHAPTER 2

EFFECTIVE NN INTERACTIONS

In this chapter, we will introduce the phenomenological effective Gogny and Skyrme interactions. The finite-range density-dependent M3Y interactions are also presented in this chapter, such as CDM3Yn and M3Y-Pn interactions. In particular, we will show how to construct a *complex* density-dependent CDM3Yn interaction. All considered interactions in this chapter will be used and discussed in next chapters.

2.1 The free V_{NN} nucleon-nucleon interaction

The free NN potential can be derived in essentially three different ways: *i*) its mathematical structure can be inferred from general symmetry principles; *ii*) the derivation of V_{NN} from free meson-exchange theory; *iii*) the effective filed approach where the NN interaction is derived for chiral perturbation theory up to some given order [Vre04]. We will give a brief review of the two approaches following the textbook by Ring and Schuck [Rin80]. The two-body V_{NN} nuclear potential in coordinate representation depends on the position vectors ($\boldsymbol{r_1}$, $\boldsymbol{r_2}$), momenta ($\boldsymbol{p_1}$, $\boldsymbol{p_2}$), spin ($\boldsymbol{\sigma_1}$, $\boldsymbol{\sigma_2}$), and isospin ($\boldsymbol{\tau_1}$, $\boldsymbol{\tau_2}$) of the two interacting nucleons

$$V_{NN} \equiv V_{NN}(\boldsymbol{r_1}, \boldsymbol{r_2}, \boldsymbol{p_1}, \boldsymbol{p_2}, \boldsymbol{\sigma_1}, \boldsymbol{\sigma_2}, \boldsymbol{\tau_1}, \boldsymbol{\tau_2}). \tag{2.1}$$

The potential V_{NN} must obey several symmetries [Rin80]:

- Permutation invariance. Invariance under an exchange of the coordinates

$$V_{NN}(\boldsymbol{r_1}, \boldsymbol{r_2}, \boldsymbol{p_1}, \boldsymbol{p_2}, \boldsymbol{\sigma_1}, \boldsymbol{\sigma_2}, \boldsymbol{\tau_1}, \boldsymbol{\tau_2}) = V_{NN}(\boldsymbol{r_2}, \boldsymbol{r_1}, \boldsymbol{p_2}, \boldsymbol{p_1}, \boldsymbol{\sigma_2}, \boldsymbol{\sigma_1}, \boldsymbol{\tau_2}, \boldsymbol{\tau_1}). \quad (2.2)$$

- Translational invariance. The potential depends only on the relative coordinate $\boldsymbol{r} = \boldsymbol{r_1} - \boldsymbol{r_2}$.

$$V_{NN} \equiv V_{NN}(\boldsymbol{r}, \boldsymbol{p_1}, \boldsymbol{p_2}, \boldsymbol{\sigma_1}, \boldsymbol{\sigma_2}, \boldsymbol{\tau_1}, \boldsymbol{\tau_2}). \quad (2.3)$$

- Galilean invariance. The potential depends only on the relative momentum $\boldsymbol{p} = \frac{1}{2}(\boldsymbol{p_1} - \boldsymbol{p_2})$

$$V_{NN} \equiv V_{NN}(\boldsymbol{r}, \boldsymbol{p}, \boldsymbol{\sigma_1}, \boldsymbol{\sigma_2}, \boldsymbol{\tau_1}, \boldsymbol{\tau_2}). \quad (2.4)$$

- Isospin invariance. Nuclear forces are independent of the charge of nucleons (invariance under rotation in isospin space). Only isospin scalars are allowed.

$$V_{NN} \approx \boldsymbol{\tau_1}.\boldsymbol{\tau_2}. \quad (2.5)$$

- Parity invariance. Invariance under space reflection.

$$V_{NN}(\boldsymbol{r}, \boldsymbol{p}, \boldsymbol{\sigma_1}, \boldsymbol{\sigma_2}, \boldsymbol{\tau_1}, \boldsymbol{\tau_2} = V_{NN}(-\boldsymbol{r}, -\boldsymbol{p}, \boldsymbol{\sigma_1}, \boldsymbol{\sigma_2}, \boldsymbol{\tau_1}, \boldsymbol{\tau_2}). \quad (2.6)$$

- Time reversal invariance. Physical observables do not depend on the direction of time.

$$V_{NN}(\boldsymbol{r}, \boldsymbol{p}, \boldsymbol{\sigma_1}, \boldsymbol{\sigma_2}, \boldsymbol{\tau_1}, \boldsymbol{\tau_2}) = V_{NN}(\boldsymbol{r}, -\boldsymbol{p}, -\boldsymbol{\sigma_1}, -\boldsymbol{\sigma_2}, \boldsymbol{\tau_1}, \boldsymbol{\tau_2}). \quad (2.7)$$

- Rotational invariance in coordinate space.

The total angular momentum of the NN system must be conserved (invariance under rotation in a combined configuration and spin spaces implies only scalar products).

The only allowed scalars invariant under parity and time reversal transformations are [Rin80]

$$V_{NN} \propto r^2 = |\boldsymbol{r}|^2, \boldsymbol{\sigma_1}.\boldsymbol{\sigma_2}, \boldsymbol{\sigma_i}.\boldsymbol{r}, \boldsymbol{\sigma_i}.(\boldsymbol{r} \times \boldsymbol{p}). \tag{2.8}$$

It is valid to consider in first approximation velocity independent forces (static forces). Such an approximation is valid at low energies. Additionally it can be assumed that the force is central (depending only on the magnitude $r \equiv |\boldsymbol{r}|$ of the vector $\boldsymbol{r}$). The most general potential, which satisfies rotational, parity, isospin and time reversal invariances can be symbolically written as

$$V_{NN} \propto \begin{bmatrix} 1 \\ \boldsymbol{\sigma_1}.\boldsymbol{\sigma_2} \end{bmatrix} \times \begin{bmatrix} 1 \\ \boldsymbol{\tau_1}.\boldsymbol{\tau_2} \end{bmatrix} \times u(r) \tag{2.9}$$

where $u(r)$ denotes arbitrary radial functions. The symbol "×" means that we have to form all possible combinations. More explicitly, we can write the potential V_{NN} as [Rin80]

$$V_{NN} = V_0(r) + V_\tau(r)(\boldsymbol{\tau_1}.\boldsymbol{\tau_2}) + [V_\sigma(r) + V_{\sigma\tau}(r)(\boldsymbol{\tau_1}.\boldsymbol{\tau_2})](\boldsymbol{\sigma_1}.\boldsymbol{\sigma_2}) \tag{2.10}$$

where $V_0(r)$, V_σ, V_τ and $V_{\sigma\tau}$ are arbitrary radial functions that cannot be determined from the invariance principles. Additionally, the requirement that V_{NN} obeys permutation invariance implies that the spin dependence must enter symmetrically as

$$\boldsymbol{S} = \frac{1}{2}(\boldsymbol{\sigma_1} + \boldsymbol{\sigma_2}), \tag{2.11}$$

where $\boldsymbol{S}$ is the total spin. Therefore, the velocity dependent term in the potential V_{NN} has the following form

$$\boldsymbol{L}.\boldsymbol{S} = \frac{1}{2}(\boldsymbol{r} \times \boldsymbol{p})(\boldsymbol{\sigma_1} + \boldsymbol{\sigma_2}). \tag{2.12}$$

Nucleon-nucleon scattering experiments also give a hint of the existence of non central terms. Particularly, the measured quadrupole moment of the deuteron cannot be explained by a central force [Eis75]. An example of non central force is the tensor force ($\sigma.\boldsymbol{r}$) in Eq. (2.8). The only possible combination that does not violate parity and time reversal invariance must be proportional to $(\boldsymbol{r}.\boldsymbol{\sigma_1})(\boldsymbol{r}.\boldsymbol{\sigma_2})$. The tensor force is usually introduced in terms of the following operator [Rin80]

$$S_{12} = \frac{3(\boldsymbol{r}.\boldsymbol{\sigma_1})(\boldsymbol{r}.\boldsymbol{\sigma_2})}{r^2} - \boldsymbol{\sigma_1}.\boldsymbol{\sigma_2}. \tag{2.13}$$

The above considerations leave us with the velocity-dependent non central NN interaction that can be symbolically written as

$$V_{NN} \propto \begin{bmatrix} 1 \\ \boldsymbol{\sigma_1}.\boldsymbol{\sigma_2} \end{bmatrix} \times \begin{bmatrix} 1 \\ \boldsymbol{\tau_1}.\boldsymbol{\tau_2} \\ S_{12} \\ \boldsymbol{L}.\boldsymbol{S} \end{bmatrix} \times u(r), \tag{2.14}$$

or

$$\begin{aligned} V_{NN} &= V_0(r) + V_\tau(r)(\boldsymbol{\tau_1}.\boldsymbol{\tau_2}) + [V_\sigma(r) + V_{\sigma\tau}(r)(\boldsymbol{\tau_1}.\boldsymbol{\tau_2})](\boldsymbol{\sigma_1}.\boldsymbol{\sigma_2}) \\ &+ [V_T(r) + W_T(r)(\boldsymbol{\tau_1}.\boldsymbol{\tau_2})]S_{12} + [V_{LS}(r) + W_{LS}(r)(\boldsymbol{\tau_1}.\boldsymbol{\tau_2})](\boldsymbol{L}.\boldsymbol{S}). \end{aligned} \tag{2.15}$$

The radial functions in Eq. (2.15) cannot be determined from the invariance principles. They can be obtained from a fit to experimental data.

As mentioned above, the NN interaction can be derived from the free meson-exchange theory. In 1935, Yukawa postulated that the NN interaction can be understood by the virtual exchange of pions just as the Coulomb interaction is caused by the exchange of (virtual) photons; the original theory involved a scalar (spin 0) meson and was later generalized to vector mesons (spin 1). At large distances the problem can be described by the relativistic Klein-Gordon equation for pions (spinless particles) and relativistic Dirac equations for nucleons [Bjo65]. One calculates the T-matrix for one-pion exchange; in the static limit, this quantity is identical to the NN interaction. Taking the correct invariance properties of the pion field with respect to spin, isospin and parity into account and regarding the nucleon as a static source of the pion field, one obtains [Wal95] the so-called one-pion exchange potential

(OPEP)

$$\begin{aligned} V_{OPEP}(\boldsymbol{r},\boldsymbol{\sigma_1},\boldsymbol{\sigma_2},\boldsymbol{\tau_1},\boldsymbol{\tau_2}) &= \frac{-g^2}{3\hbar c} m_\pi c^2 (\boldsymbol{\tau_1}.\boldsymbol{\tau_2}) \\ &\times \left(\boldsymbol{\sigma_1}.\boldsymbol{\sigma_2} + S_{12}\left(1+\frac{3}{\mu r}+\frac{3}{(\mu r)^2}\right)\right)\frac{e^{-\mu r}}{r}. \end{aligned} \tag{2.16}$$

where $1/\mu = \hbar/m_\pi c$ is the Compton wavelength of the pion and g stands for the pion-nucleon coupling ($g^2/\hbar c \approx 0.081$).

2.2 Effective NN interaction inside the nuclear medium

The in-medium NN interaction is significantly modified compared to the free NN interaction. The presence of other particles in the nuclear medium allows for non-conservation of the energy and momentum of the NN pairs (energy and momentum can be transferred to other particles). Another new feature compared to the two-body system is that not all of the scattering states are available. Particularly, only scattering states above the Fermi level ($E_n > E_f$) are allowed, as all of the states below the Fermi sea are occupied. To illustrate the features of the NN system inside the medium we analyze first the scattering matrix T for two free nucleons, which is governed by the Lippman-Schwinger equation [Rin80]

$$T^E_{\boldsymbol{k_1}\boldsymbol{k_2},\boldsymbol{k'_1}\boldsymbol{k'_2}} = \bar{v}_{\boldsymbol{k_1}\boldsymbol{k_2},\boldsymbol{k'_1}\boldsymbol{k'_2}} + \frac{1}{2}\sum_{\boldsymbol{p_1},\boldsymbol{p_2}} \bar{v}_{\boldsymbol{k_1}\boldsymbol{k_2},\boldsymbol{p_1}\boldsymbol{p_2}} \frac{1}{E-(\frac{\boldsymbol{p_1}^2}{2m})-(\frac{\boldsymbol{p_2}^2}{2m})+i\nu} T^E_{\boldsymbol{p_1}\boldsymbol{p_2},\boldsymbol{k'_1}\boldsymbol{k'_2}}, \tag{2.17}$$

where $\boldsymbol{k_1}$, $\boldsymbol{k_2}$ and $\boldsymbol{k'_1}$, $\boldsymbol{k'_2}$ are the momenta of the incoming and outgoing particles respectively, and E is the total energy of the NN system. In the summation there are no restrictions for the momenta $\boldsymbol{p_1}$, $\boldsymbol{p_2}$ and we have conserved energy and momenta,

$$\boldsymbol{k_1} + \boldsymbol{k_2} = \boldsymbol{k'_1} + \boldsymbol{k'_2}. \tag{2.18}$$

In the operator form Eq. (2.17) is often written as [Rin80]

$$T = \overline{v} + \overline{v}\frac{1}{E - H_0}T \Rightarrow T = \frac{\overline{v}}{1 - \overline{v}(E - H_0)^{-1}}, \tag{2.19}$$

where $\overline{v}$ represents the free NN interaction, and

$$H_0 = \frac{\boldsymbol{p_1}^2}{2m} + \frac{\boldsymbol{p_2}^2}{2m}. \tag{2.20}$$

In a similar way the NN scattering inside the nuclear medium is governed by the analogous equations (Bethe-Goldstone) for an analog of the T-matrix so-called Brueckner "G-matrix" [Rin80]. We can write the equation for the G-matrix by substituting in the Lippman-Schwinger equation (2.17) plane waves with shell model states $(\boldsymbol{k_1}, \boldsymbol{k_2} \rightarrow m, n)$ including in the summation only states above the Fermi energy $(E_n > E_f)$, and removing the restrictions for the conservation of energy and momentum $\boldsymbol{k_1} + \boldsymbol{k_2} \neq \boldsymbol{k_1'} + \boldsymbol{k_2'}$. The Bethe-Goldstone equation for the Brueckner's G-matrix has the following form [Bet57, Rin80]

$$G^E_{ab,cd} = \overline{v}_{ab,cd} + \frac{1}{2}\sum_{m,n>E_f} \overline{v}_{ab,mn}\frac{1}{E - E_m - E_n + i\nu}G^E_{mn,cd}, \tag{2.21}$$

where ab, cd, mn and E_n, E_m are shell-model indices and energies, respectively. The potential $\overline{v}$ is a free NN potential. We can see that the effective NN interaction can be obtained from the bare NN interaction if only the shell-model energies E_n, E_m are known. Symbolically the G-matrix can be written as

$$G = \overline{v} + \overline{v}\frac{Q_F}{E - H_0}G \Rightarrow G = \frac{\overline{v}}{1 - \overline{v}Q_F(E - H_0)^{-1}}, \tag{2.22}$$

where

$$Q_F = \sum_{(m<n)>E_f} |mn><mn|. \tag{2.23}$$

is a projection operator excluding occupied states (Pauli blocking). Eqs. (2.17) and (2.21) look very similar and one can be mislead that they possess the same properties. The fact that energy and momentum are conserved in a scattering of free nucleons ("on-shell" scattering) while they are not conserved inside the medium ("off-shell" scattering) leads to the completely different behaviors at small distances ($|\boldsymbol{r_1}-\boldsymbol{r_2}| \approx 0, \overline{v} \rightarrow \infty$). The "on-shell" scattering case introduces a singularity in Eq. (2.19), and therefore at small distances the interaction is infinite. By contrast the G-matrix remains finite, because in the denominator of Eq. (2.22) the projector operator Q_F guarantees that there is no zero. At large distances ($|\boldsymbol{r_1}-\boldsymbol{r_2}| \approx \infty, \overline{v} \rightarrow 0$) both interactions have the same asymptotic behavior and go to zero as the potential $\overline{v}$ also goes to zero.

2.3 Phenomenological effective NN interactions

In practice solving the Bethe-Goldstone equation is rather difficult and requires several approximations. Another drawback is the not too good agreement with the experimental data of nuclear structure even if the calculations are feasible [Rin80]. As a remedy we can use the phenomenological forces, with several free parameters that need to be adjusted to reproduce the nuclear experimental data. The most widely used effective interactions are the Skyrme [Sky56, Vau72] and Gogny [Gog75, Bri67, Dec80, Cha08, Gor09] interactions.

2.3.1 Skyrme interactions

The standard form of the Skyrme-type effective NN interactions has the following form [Sky56, Vau72, Cha98]:

$$\begin{aligned}
V_{NN}(|\boldsymbol{r_1}-\boldsymbol{r_2}|) &= t_0(1+x_0P^{\sigma})\delta(\boldsymbol{r_1}-\boldsymbol{r_2}) \\
&+ \frac{1}{2}t_1(1+x_1P^{\sigma}) \times \left[\overleftarrow{k}^2\delta(\boldsymbol{r_1}-\boldsymbol{r_2}) + \delta(\boldsymbol{r_1}-\boldsymbol{r_2})\overrightarrow{k}^2\right] \\
&+ t_2(1+x_2P^{\sigma})\overleftarrow{k}.\delta(\boldsymbol{r_1}-\boldsymbol{r_2})\overrightarrow{k} \\
&+ \frac{1}{6}t_3(1+x_3P^{\sigma})\rho^{\alpha}(\frac{\boldsymbol{r_1}+\boldsymbol{r_2}}{2})\delta(\boldsymbol{r_1}-\boldsymbol{r_2}) \\
&+ iW_0(\boldsymbol{\sigma_1}+\boldsymbol{\sigma_2}).(\overleftarrow{k} \times \delta(\boldsymbol{r_1}-\boldsymbol{r_2})\overrightarrow{k}) \qquad (2.24)
\end{aligned}$$

Table 2.1: Skyrme parameters for SLy4 interaction [Cha98].

t_0 (MeV.fm^3)	t_1 (MeV.fm^5)	t_2 (MeV.fm^5)	t_3 (MeV.fm$^{3(1+\alpha)}$)	x_0	x_1	x_2	x_3
-2488.91	486.82	-546.39	13777.0	0.834	-0.344	-1.0	1.354
α	W_0						
	(MeV.fm^5)						
1/6	123.0						

where t_i, x_i, α and W_0 are the parameters of the Skyrme interactions; $P^\sigma = \frac{1+\vec{\sigma_1}\vec{\sigma_2}}{2}$ is the spin exchange operator; $\boldsymbol{\sigma_i}$ is the Pauli spin operator; $\overleftarrow{k} = i(\overleftarrow{\nabla_1} - \overleftarrow{\nabla_2})/2$ and $\overrightarrow{k} = -i(\overrightarrow{\nabla_1} - \overleftarrow{\nabla_2})/2$ are the momentum operators acting on the right and on the left, respectively. The first term of Eq. (2.24) describes a pure δ force. The next two terms approximate a finite-range force. The fourth term introduces the density dependence, which describes the many-body effects. The last term represents a two body spin-orbit interaction. The properties of nucleons in the nucleus are influenced by the state of other nucleons in the system. The parameters of the Skyrme interaction are obtained by fitting the HF results to the experimental data. In our calculations, we have used the so-called SLy4 interaction [Cha98], which has been adjusted to describe properly the mean field properties of neutron-rich nuclei and infinite neutron matter. The parameters of SLy4 interaction are listed in Table 2.1.

The total binding energy in the Skyrme HF approach is given by the sum of the kinetic energy, the potential Skyrme energy, the Coulomb energy, and the corrections for spurious center-of-mass motion. Due to the local nature of the Skyrme energy functional, it has several technical advantages. The number of integrations required for solving of the Skyrme HF equations is significantly reduced because of the similar structure of direct and exchange terms.

2.3.2 Gogny interactions

Despite the great success of the Skyrme interaction, is has been argued that zero-range forces might not be able to simulate the long range or even the intermediate range parts of the realistic effective interaction. All the Skyrme forces are well known to have unrealistic pairing properties in intruncated pairing space. In particular, this forbids to solve HFB equations in unlimited r-space. In practice, a cut-off in single-spectra is applied and the pairing strength is adjusted accordingly. The Gogny force [Gog75] is a sum of a medium-range and a short-range term with Gaussians form factor and different with spin-isospin exchange admixtures. The divergence of the zero-range pairing force in untruncated space is avoided and this enables one to use Gogny interaction simultaneously in both the mean field and pairing channels. The interaction has been adjusted with the direct and exchange Coulomb terms calculated exactly.

The Gogny interaction is written in the following form [Dec80, Ber91, Gog75],

$$V(\rho,|\boldsymbol{r_1}-\boldsymbol{r_2}|) = V^{(C)}(|\boldsymbol{r_1}-\boldsymbol{r_2}|) + V^{(DD)}(\rho,|\boldsymbol{r_1}-\boldsymbol{r_2}|) + V^{(LS)}(|\boldsymbol{r_1}-\boldsymbol{r_2}|), \quad (2.25)$$

where

$$\begin{aligned}
V^{(C)}(|\boldsymbol{r_1}-\boldsymbol{r_2}|) &= \sum_{\nu=1}^{2}(W_\nu + B_\nu P^\sigma - H_\nu P^\tau - M_\nu P^\sigma P^\tau) f_\nu(|\boldsymbol{r_1}-\boldsymbol{r_2}|) \\
V^{(DD)}(\rho,|\boldsymbol{r_1}-\boldsymbol{r_2}|) &= t_0(1+x_0P^\sigma)\rho^\alpha(\frac{r_1+r_2}{2})\delta(\boldsymbol{r_1}-\boldsymbol{r_2}) \\
V^{(LS)}(|\boldsymbol{r_1}-\boldsymbol{r_2}|) &= iW_0\{\overleftarrow{\nabla}_{12}\delta(\boldsymbol{r_1}-\boldsymbol{r_2}) \times \overrightarrow{\nabla}_{12}\} \cdot (\boldsymbol{\sigma_1}+\boldsymbol{\sigma_2}) \\
V^{(Coul)}(|\boldsymbol{r_1}-\boldsymbol{r_2}|) &= (\frac{1+\tau_{1z}}{2})(\frac{1+\tau_{2z}}{2})\frac{e^2}{|\boldsymbol{r_1}-\boldsymbol{r_2}|}. \qquad (2.26)
\end{aligned}$$

In this expression, the first line represents the central finite-range part of the force. The second line represents the density-dependent term and the third line is the spin-orbit term having a zero range. Finally, the last line describes the Coulomb interaction between protons ($\tau_{iz} = +1$ for protons and $\tau_{iz} = -1$ for neutrons). In the finite range component $V^{(C)}(|\boldsymbol{r_1}-\boldsymbol{r_2}|)$ of the Gogny interaction, the form factor $f_\nu(|\boldsymbol{r_1}-\boldsymbol{r_2}|)$ is of a Gaussian type

$$f_\nu(|\boldsymbol{r_1}-\boldsymbol{r_2}|) = exp(-\frac{|\boldsymbol{r_1}-\boldsymbol{r_2}|^2}{\mu_\nu^2}), \quad (2.27)$$

Table 2.2: The values of the parameters of D1S [Ber91] and D1N [Cha08] interactions.

ν	W_ν (MeV)	B_ν (MeV)	H_ν (MeV)	M_ν (MeV)	μ_ν (fm)	t_0 (MeVfm^4)	x_0	α	W_0 (MeVfm^5)
D1S									
1	-1720.3	1300	-1813.53	1397.6	0.7	1390	1	1/3	130
2	103.639	-163.483	162.812	-223.934	1.2	-	-	-	-
D1N									
1	-2047.61	1700	-2414.93	1519.35	0.8	1609.46	1	1/3	115
2	293.02	-300.78	414.59	-316.84	1.2	-	-	-	-

and W_ν, B_ν, H_ν, M_ν, μ_ν, t_0, x_0, α, and W_0 are the parameters of the Gogny interaction; $P^\sigma = \frac{1+\vec{\sigma_1}\vec{\sigma_2}}{2}$ and $P^\tau = \frac{1+\vec{\tau_1}\vec{\tau_2}}{2}$ are the spin and isospin exchange operators; $\boldsymbol{\sigma_i}$ is the Pauli spin operator; $\overleftarrow{\nabla}_{12} = \overleftarrow{\nabla_1 - \nabla_2}$ and $\overrightarrow{\nabla}_{12} = \overrightarrow{\nabla_1 - \nabla_2}$ are the gradient operators acting on the left and on the right, respectively. In this work, we use the two versions of Gogny D1S [Ber91] and D1N [Cha08] interactions (Table 2.2). The parameters of these two versions were adjusted to the properties of finite nuclei in the HFB approach, and to nuclear matter. One notes that the latest version of the Gogny D1N interaction has been shown [Cha08] to reproduce the neutron matter equation of state better than the older D1S version while still giving simultaneously a good description of the nuclear structure properties and nuclear mass data.

2.4 Density-dependent M3Y interactions

As mentioned above, the effective NN interaction can be either obtained from a sophisticated Brueckner's G-matrix calculation (Eq. (2.21)) or directly parametrized the phenomenological way, like the Skyrme [Sky56, Vau72] or Gogny [Gog75, Bri67, Dec80, Cha08, Gor09] interactions. Among the different kinds of effective interactions, relating to the first case, very popular choice is the M3Y interactions [Ana83]. Our aim is to build and use G-matrix inspired effective interactions for self-consistent mean field calculations, in the spirit of the pioneering work of Negele [Neg70].

In this section, we will introduce two different sets of the density-dependent M3Y interactions, called M3Y-Pn (n =3, 4, 5) and CDM3Yn (n = 3, 4, 6) interactions.

Concerning the first set, the M3Y-Pn interactions have been carefully parametrized by Nakada [Nak02, Nak03, Nak08] in terms of a sum of Yukawa functions added by a zero-range density-dependent term, to consistently reproduce the NM saturation properties an ground state shell structure for double-closed shell nuclei as well as unstable nuclei close to the neutron dripline. In contrast to the first set, the density dependence of the CDM3Yn interactions is included directly into the finite-range Yukawa terms, and the parameters are adjusted [Kho95] to reproduce the saturation properties of symmetric NM. The CDM3Yn interactions have been used in numerous folding model studies of the nucleon-nucleus and nucleus-nucleus scattering [Kho96, Kho97, Kho05, Chi09, Kho07b].

2.4.1 M3Y-Pn type interactions

The starting point of the M3Y-Pn [Nak08] interaction is the M3Y Paris interaction [Ana83]. The Coulomb interaction between protons ais treated as in Eq. (2.26). One knows that the saturation properties are important to describe many nuclei in a wide mass range. Since it is still hard to describe accurately the saturation properties by the bare NN interaction, it will be appropriate to modify realistic effective interaction so as to reproduce the saturation properties. It has been known that density-dependent in the effective interaction is essential in obtaining the saturation. A density-dependent contact force $V^{(DD)}(\rho, r_{12})$ is therefore added to the original M3Y interaction, as in the Skyrme and Gogny interactions. The original density-independent M3Y interaction is denoted as "M3Y-P0" and the modified M3Y interaction is denoted "M3Y-Pn" like in Ref. [Nak02, Nak08]. The range parameters for the Yukawa functions $f_i^{(C)}(r_{12})$ (in Eq. (2.29)) are μ_1^{-1}=0.25, μ_2^{-1}=0.4 and μ_3^{-1}=1.414 fm, which correspond to the Compton wavelengths of mesons with masses of about 790, 490 and 140 MeV, respectively. The latest versions of M3Y-Pn interactions have been parametrized [Nak08] not only to reproduce the saturation properties of symmetric NM, but also to give a good description of ground state shell structure in double-closed shell nuclei. The strength parameters t_i in $V^{(C)}$ and $t^{(SE)}$, $t^{(TE)}$ in $V^{(DD)}$ are fitted to the measured binding energies of double magic nuclei from ^{16}O to ^{208}Pb in HF approximation. All parameters of the versions of M3Y-Pn (n=3,4,5) interactions are listed in Tables 2.3, 2.4 and 2.5. The new parameter sets of the M3Y-P3 and M3Y-P5 [Nak08] interactions are obtained by keeping the similar finite-range tensor term $V^{(TN)}$ like the original M3Y interaction of Ref. [Ana83]. The set M3Y-P4 is obtained by assuming $V^{(TN)} = 0$.

Table 2.3: Parameters of the central term $V^{(C)}(r_{12})$ in the original M3Y Paris [Ana83] and M3Y-Pn (n=3,4,5) [Nak08] interactions.

Inter.	i	$1/\mu_i^{(C)}$ (fm)	$t_i^{(SE)}$ (MeV)	$t_i^{(TE)}$ (MeV)	$t_i^{(SO)}$ (MeV)	$t_i^{(TO)}$ (MeV)
M3Y-P0	1	0.25	11466.0	13967.0	-1418.0	11345.0
	2	0.40	-3556.0	-4594.0	950.0	-1900.0
	3	1.414	-10.463	-10.463	31.389	3.488
M3Y-P3	1	0.25	8027.0	7130.0	-1418.0	11345.0
	2	0.40	-2637.0	-4594.0	950.0	-1900.0
	3	1.414	-10.463	-10.463	31.389	3.488
M3Y-P4	1	0.25	8027.0	5503.0	12000.0	3700.0
	2	0.40	-2637.0	-4183.0	4500.0	-1000.0
	3	1.414	-10.463	-10.463	31.389	3.488
M3Y-P5	1	0.25	8027.0	5576.0	-1418.0	11345.0
	2	0.40	-2650.0	-4170.0	2880.0	-1780.0
	3	1.414	-10.463	-10.463	31.389	3.488

The density-dependent M3Y-Pn interaction can be written in the following form [Nak02, Nak08]:

$$V(\rho, r_{12}) = V^{(C)}(r_{12}) + V^{(DD)}(\rho, r_{12}) + V^{(TN)}(r_{12}) + V^{(LS)}(r_{12}), \tag{2.28}$$

where

$$\begin{aligned}
V^{(C)}(r_{12}) &= \sum_{i=1}^{3}\left(t_i^{(SE)}P_{SE}+t_i^{(TE)}P_{TE}+t_i^{(SO)}P_{SO}+t_i^{(TO)}P_{TO}\right)f_i^{(C)}(r_{12}),\\
V^{(DD)}(\rho,r_{12}) &= \left(t^{(SE)}P_{SE}[\rho(\boldsymbol{r_1})]^{\alpha^{(SE)}}+t^{(TE)}P_{TE}[\rho(\boldsymbol{r_1})]^{\alpha^{(TE)}}\right)\delta(\boldsymbol{r_{12}}),\\
V^{(TN)}(r_{12}) &= \sum_{i=1}^{2}\left(t_i^{(TNE)}P_{TE}+t_i^{(TNO)}P_{TO}\right)f_i^{(TN)}(r_{12})r_{12}^2S_{12},\\
V^{(LS)}(r_{12}) &= \sum_{i=1}^{2}\left(t_i^{(LSE)}P_{TE}+t_i^{(LSO)}P_{TO}\right)f_i^{(LS)}(r_{12})\boldsymbol{L_{12}}.(\boldsymbol{s_1}+\boldsymbol{s_2}), \qquad (2.29)
\end{aligned}$$

and the relative coordinate is denoted by $\boldsymbol{r_{12}}=\boldsymbol{r_1}-\boldsymbol{r_2}$ and $r_{12}=|\boldsymbol{r_{12}}|$. The relative momentum is defined by $\boldsymbol{p_{12}}=(\boldsymbol{p_1}-\boldsymbol{p_2})/2$. $\boldsymbol{L_{12}}$ is the relative orbital angular momentum $\boldsymbol{L_{12}}=\boldsymbol{r_{12}}\times\boldsymbol{p_{12}}$, $\boldsymbol{s_1}$, $\boldsymbol{s_2}$ are the nucleon spin operators, and S_{12} is the tensor operator,

$$S_{12}=4[3(\boldsymbol{s_1}.\hat{r}_{12})(\boldsymbol{s_j}.\hat{r}_{ij})-\boldsymbol{s_1}.\boldsymbol{s_2}], \qquad (2.30)$$

with $\hat{r}_{12}=\boldsymbol{r_{12}}/r_{12}$ and $\rho(\boldsymbol{r})$ denotes the nucleon density.

The Yukawa form factor is

$$f_i(\mathbf{r_{12}})=\frac{exp(-\mu_i\mathbf{r_{12}})}{\mu_i\mathbf{r_{12}}}, \qquad (2.31)$$

which is assumed for all terms except $V^{(DD)}(\rho,r_{12})$ in the M3Y-Pn interactions. The projection operators on the singlet-even (SE), triplet-even (TE), singlet-odd (SO) and triplet-odd (TO) two-particle states are defined as

$$\begin{aligned}
P_{SE}&=\frac{1-P^{\sigma}}{2}\frac{1+P^{\tau}}{2}, P_{TE}=\frac{1+P^{\sigma}}{2}\frac{1-P^{\tau}}{2},\\
P_{SO}&=\frac{1-P^{\sigma}}{2}\frac{1-P^{\tau}}{2}, P_{TO}=\frac{1+P^{\sigma}}{2}\frac{1+P^{\tau}}{2}, \qquad (2.32)
\end{aligned}$$

where $P^{\sigma}(P^{\tau})$ is the spin (isospin) exchange operator.

In handling the spin-isospin degrees of freedom, we can rewrite the central term

Table 2.4: Same notation as in Table 2.3, but for the density-dependent term $V^{(DD)}(\rho, r_{12})$.

Inter.	$\alpha^{(SE)}$	$t^{(SE)}$ (MeV.fm^3)	$\alpha^{(TE)}$	$t^{(TE)}$ (MeV.fm)
M3Y-P0	-	0	-	0
M3Y-P3	1	220.0	1/3	1198.0
M3Y-P4	1	248.0	1/3	1142.0
M3Y-P5	1	126.0	1/3	1147.0

$V^{(C)}(r_{12})$ in Eq. (2.29) like that in Eq. (2.26) of Gogny interaction as

$$V^{(C)}(r_{12}) = \sum_i \left(t_i^{(W)} + t_i^{(B)} P^\sigma - t_i^{(H)} P^\tau - t_i^{(M)} P^\sigma P^\tau \right) f_i^{(C)}(r_{12}). \tag{2.33}$$

where the relations between the coupling constants are

$$\begin{aligned} t_i^{(SE)} &= t_i^{(W)} - t_i^{(B)} - t_i^{(H)} + t_i^{(M)}, \\ t_i^{(TE)} &= t_i^{(W)} + t_i^{(B)} + t_i^{(H)} + t_i^{(M)}, \\ t_i^{(SO)} &= t_i^{(W)} - t_i^{(B)} + t_i^{(H)} - t_i^{(M)}, \\ t_i^{(TO)} &= t_i^{(W)} + t_i^{(B)} - t_i^{(H)} - t_i^{(M)}. \end{aligned} \tag{2.34}$$

2.4.2 CDM3Yn type interactions

In this subsection we introduce the density-dependent CDM3Yn interaction, which is also based on the original M3Y interaction deduced from the G-matrix elements of the Paris NN potential [Ana83].

The starting point in developing the effective CDM3Yn interactions is to reproduce the saturation properties of nuclear matter. Therefore, we just consider the central part of the M3Y interaction [Ana83]. The direct and exchange parts of the

Table 2.5: Same notation as in Table 2.3, but for the spin-orbit $V^{(LS)}(r_{12})$ and tensor $V^{(TN)}(r_{12})$ terms.

Inter.	i	$1/\mu_i^{(LS)}$ (fm)	$t_i^{(LSE)}$ (MeV)	$t_i^{(LSO)}$ (MeV)	$1/\mu_i^{(TN)}$ (fm)	$t_i^{(TNE)}$ (MeV.fm^{-2})	$t_i^{(TNO)}$ (MeV.fm^{-2})
M3Y-P0	1	0.25	-5101.0	-1897.0	0.40	-1096.0	244.0
	2	0.40	-337.0	-632.0	0.70	-30.9	15.6
M3Y-P3	1	0.25	-10712.1	-3983.7	0.40	-1096.0	244.0
	2	0.40	-707.7	-1327.2	0.70	-30.9	15.6
M3Y-P4	1	0.25	-8671.7	-3224.9	0.40	0.0	0.0
	2	0.40	-572.9	-1074.4	0.70	0.0	0.0
M3Y-P5	1	0.25	-11222.2	-4173.4	0.40	-1096.0	244.0
	2	0.40	-741.4	-1390.4	0.70	-30.9	15.6

central (energy- and density dependent) NN forces can be written in terms of spin-isospin dependent components as

$$\begin{aligned} v_{\mathrm{D(EX)}}(E,\rho,s) &= v_{00}^{\mathrm{D(EX)}}(E,\rho,s) + v_{10}^{\mathrm{D(EX)}}(E,\rho,s)(\boldsymbol{\sigma}\boldsymbol{\sigma}') \\ &+ v_{01}^{\mathrm{D(EX)}}(E,\rho,s)(\boldsymbol{\tau}\boldsymbol{\tau}') + v_{11}^{\mathrm{D(EX)}}(E,\rho,s)(\boldsymbol{\sigma}\boldsymbol{\sigma}')(\boldsymbol{\tau}\boldsymbol{\tau}'), \end{aligned} \tag{2.35}$$

where s is the internucleon distance and ρ is the nuclear density around the interacting nucleon pair. The contribution from the spin dependent terms (v_{10} and v_{11}) to the nucleon-nucleus potential is exactly zero for a spin-saturated target like those considered in the present work.

The original density-independent M3Y interactions [Ber77, Ana83, Kho93] do not give a correct description of the saturation properties of symmetric nuclear matter within the HF scheme. The introduction of a density dependence can improve this situation. Thus, several forms of density dependence were introduced [Kho96, Kho97], with parameter values adjusted to produce the observed nuclear matter saturation density and binding energy. While the isoscalar density dependence of the CDM3Yn interaction has been well tested in the folding model analysis [Kho97, Kho95] of the elastic, refractive α-nucleus and nucleus-nucleus scattering, its isovector density dependence can be probed in the study of the charge exchange (p, n) reaction only. Our aim is to develop a compact method to construct the isovector density dependence of the CDM3Yn interaction based on the Brueckner-Hartree-Fock (BHF) description of the nucleon optical potential (OP) in nuclear matter by Jeukenne-Lejeune-Mahaux (JLM) group [Jeu77b]. The isoscalar density dependence of the CDM3Yn interaction has been introduced [Kho97] into the interaction (2.35) as

$$v_{00}^{\rm D(EX)}(E,\rho,s) = g(E)F_{\rm IS}(\rho)v_{00}^{\rm D(EX)}(s), \tag{2.36}$$

$$F_{\rm IS}(\rho) = C_0^V[1+\alpha_0^V\exp(-\beta_0^V\rho)-\gamma_0^V\rho]. \tag{2.37}$$

The parameters of the isoscalar density dependence $F_{\rm IS}(\rho)$ were chosen [Kho97] to reproduce the NM saturation properties in the HF calculation of symmetric NM, which yielded the incompressibility K = 217, 228 and 252 MeV for the versions CDM3Y3, CDM3Y4 and CDM3Y6 respectively [Kho97]. One notes that the original M3Y interaction [Ana83] is energy independent and one needs to introduce an appropriate energy dependence in order to reproduce the empirical energy dependence of the nucleon optical potential, likes the Fig. 2 of Ref. [Kho93]. The intrinsic energy dependence of the optical potential can account roughly for the data at low incident energies only. With the increasing energy, the nucleon OP is somewhat more attractive than the empirical one. This effect had shown in the light of the microscopic JLM results for the nucleon OP [Jeu77a, Jeu77b], where the energy dependence was shown to come from the direct and exchange parts of the Brueckner G-matrix. We have assumed for simplicity that the energy dependent interaction is the original M3Y one multiplied with an energy dependent factor $g(E)$, where E is the incident nucleon energy [Kho97]. The intrinsic energy dependence of the CDM3Yn interaction is $g(E) \approx 1 - 0.0026E$.

We have assumed a similar form for the isovector density dependence of the CDM3Yn interaction

$$v_{01}^{\rm D(EX)}(E,\rho,s) = F_{\rm IV}(E,\rho)v_{01}^{\rm D(EX)}(s). \tag{2.38}$$

Table 2.6: Yukawa strengths of the central components of the original M3Y-Paris interaction (2.39).

ν	$1/\mu_\nu$ (fm)	$Y^{\rm D}_{00}(\nu)$ (MeV)	$Y^{\rm D}_{01}(\nu)$ (MeV)	$Y^{\rm EX}_{00}(\nu)$ (MeV)	$Y^{\rm EX}_{01}(\nu)$ (MeV)
1	0.25	11061.625	313.625	-1524.25	-4118.0
2	0.4	-2537.5	223.5	-518.75	1054.75
3	1.414	0.0	0.0	-7.8474	2.6157

The radial shapes of the isoscalar and isovector interactions were kept unchanged, as derived [Kho96] from the M3Y-Paris interaction [Ana83], in terms of three Yukawas

$$v^{\rm D(EX)}_{00(01)}(s) = \sum_{\nu=1}^{3} Y^{\rm D(EX)}_{00(01)}(\nu)\frac{\exp(-\mu_\nu s)}{\mu_\nu s}. \tag{2.39}$$

The functions ($Y_{00}^{D(EX)}$, $Y_{01}^{D(EX)}$) can be expressed in the (SE,TE,SO,TO) representation (see Table 2.3) as

$$\begin{aligned} Y^D_{00} &= \frac{1}{16}[3t^{(SE)} + 3t^{(TE)} + 1t^{(SO)} + 9t^{(TO)}], \\ Y^D_{01} &= \frac{1}{16}[1t^{(SE)} - 3t^{(TE)} - 1t^{(SO)} + 3t^{(TO)}], \\ Y^{EX}_{00} &= \frac{1}{16}[3t^{(SE)} + 3t^{(TE)} - 1t^{(SO)} - 9t^{(TO)}], \\ Y^{EX}_{01} &= \frac{1}{16}[1t^{(SE)} - 3t^{(TE)} + 1t^{(SO)} - 3t^{(TO)}] \ . \end{aligned} \tag{2.40}$$

Since the nucleon OP in nuclear matter can be defined [Bri77, Huf72] in term of the *antisymmetrized* matrix elements of the effective NN interaction between the incident nucleon and those bound in the Fermi sea, it is given by the same Hartree-Fock potential, but using *plane waves* for the single-nucleon states [Kho93, Fet03]. In the nuclear matter limit the nucleon optical potential can be obtained as [Kho93]

$$U(E,\rho) = \sum_{j\leq k_F}[< kj|v_D(E,\rho,s)|kj > + < kj|v_{EX}(E,\rho,s)|jk >], \tag{2.41}$$

where $k_F = [1.5\pi^2\rho]^{1/3}$ and k is the momentum of the incident nucleon. The nucleon OP (2.41) can be expressed in terms of the isoscalar (U_{IS}) and isovector (U_{IS}) parts as [Kho07b]

$$U(E,\rho) = U_{IS}(E,\rho) \pm U_{IV}(E,\rho). \tag{2.42}$$

where the + sign pertains to incident neutrons and − sign to incident protons.

To construct a *complex* microscopic OP by a folding procedure, it is also desirable to have a realistic *imaginary* part added to the real part (2.36) of the CDM3Yn interaction. We have adjusted the nucleon OP obtained with the CDM3Yn interaction to reproduce the JLM density- and isospin dependent nucleon OP [Jeu77b]. The original JLM interaction was simply deduced from the JLM nucleon OP in nuclear matter using a local density approximation. In this model, the potential is folded with a Gaussian form factor [Jeu77b, Bau98] using a range of 1 fm for the effective interaction, in which the range has been chosen to give a good global fit to the elastic data. However, the form of JLM model already contains strengths of both direct and exchange parts of the G-matrix, the nucleon-nucleus OP for finite nuclei is given by the direct folding integration only. Despite the simplicity, the original JLM interaction has been used quite successfully to study the elastic nucleon-nucleus scattering [Bau98, Kha01] as well as the (p,n) reaction to IAS [Pak01, Bau01]. Since the JLM potential is *complex*, we define the imaginary isoscalar interaction based on the same density dependent functional (2.36) as

$$w_{00}^{\mathrm{D(EX)}}(E,\rho,s) = F_{\mathrm{IS}}^{\mathrm{W}}(E,\rho) v_{00}^{\mathrm{D(EX)}}(s), \tag{2.43}$$

$$F_{\mathrm{IS}}^{W}(E,\rho) = C_0^W[1 + \alpha_0^W \exp(-\beta_0^W\rho) - \gamma_0^W\rho]. \tag{2.44}$$

Then the real $V_{\mathrm{IS}}(E,\rho) \equiv Re[U_{\mathrm{IS}}(E,\rho)]$ and imaginary $W_{\mathrm{IS}}(E,\rho) \equiv Im[U_{\mathrm{IS}}(E,\rho)]$ isoscalar nucleon OP (2.42) in the nuclear matter limit are given by [Kho93, Kho07b]

$$\begin{aligned} V_{\mathrm{IS}}(E,\rho) &= g(E)F_{\mathrm{IS}}(\rho)\{\rho J_{00}^{\mathrm{D}} + \int [\rho_n \hat{j}_1(k_F^n r) + \rho_p \hat{j}_1(k_F^p r)] v_{00}^{\mathrm{EX}}(r) j_0(kr) d^3r\}, \\ W_{\mathrm{IS}}(E,\rho) &= F_{\mathrm{IS}}^{\mathrm{W}}(E,\rho)\{\rho J_{00}^{\mathrm{D}} + \int [\rho_n \hat{j}_1(k_F^n r) + \rho_p \hat{j}_1(k_F^p r)] v_{00}^{\mathrm{EX}}(r) j_0(kr) d^3r\}. \end{aligned} \tag{2.45}$$

where $J_{00}^D = \int v_{00}^{\rm D}(r)d^3r$, $\hat{j}_1(x) = 3j_1(x)/x$ and $j_1(x)$ is the first-order spherical Bessel function; ρ_n and ρ_p are the neutron and proton densities of asymmetric NM with a total density $\rho = \rho_n + \rho_p$ and the corresponding Fermi momenta $k_F^{p(n)} = (3\pi^2\rho_{p(n)})^{1/3}$. The momentum k of the incident nucleon of mass m is determined self-consistently [Kho93] from the nucleon incident energy E and real OP as

$$k = \sqrt{\frac{2m}{\hbar^2}\{E - [V_{\rm IS}(E,\rho) \pm V_{\rm IV}(E,\rho)]\}}. \tag{2.46}$$

Here $V_{\rm IS}(E,\rho)$ and $V_{\rm IV}(E,\rho)$ are the isoscalar and isovector parts of the *real* nucleon OP in Eq. (2.42). Due to the self-consistent definition (2.46) of the momentum k, the imaginary isoscalar nucleon OP (2.45) is obtained by an iterative procedure.

In order to determine the isovector density dependence, we have used two different CDM3Yn functionals to match separately the real and imaginary parts of the isovector CDM3Yn potential to those of the JLM potential

$$F_{\rm IV}^u(E,\rho) = C_1^u(E)[1 + \alpha_1^u(E)\exp(-\beta_1^u(E)\rho) - \gamma_1^u(E)\rho], \tag{2.47}$$

so that the real ($u = V$) and imaginary ($u = W$) parts of the isovector CDM3Yn interaction are determined as

$$v_{01}^{\rm D(EX)}(E,\rho,s) = F_{\rm IV}^{\rm V}(E,\rho)v_{01}^{\rm D(EX)}(s), \tag{2.48}$$

$$w_{01}^{\rm D(EX)}(E,\rho,s) = F_{\rm IV}^{\rm W}(E,\rho)v_{01}^{\rm D(EX)}(s). \tag{2.49}$$

Using Eqs. (2.48) and (2.49) , the real ($V_{\rm IV}(E,\rho) \equiv Re[U_{\rm IV}(E,\rho)]$) and imaginary ($W_{\rm IV}(E,\rho) \equiv Im[U_{\rm IV}(E,\rho)]$) parts of the isovector nucleon OP (2.42) in the NM limit is given explicitly as [Kho07b]

$$\begin{aligned} V_{\rm IV}(E,\rho) &= F_{\rm IV}^{\rm V}(E,\rho)\{(\rho_n - \rho_p)J_{01}^{\rm D} + \int[\rho_n\hat{j}_1(k_F^n r) - \rho_p\hat{j}_1(k_F^p r)]v_{01}^{\rm EX}(r)j_0(kr)d^3r\}, \\ W_{\rm IV}(E,\rho) &= F_{\rm IV}^{\rm W}(E,\rho)\{(\rho_n - \rho_p)J_{01}^{\rm D} + \int[\rho_n\hat{j}_1(k_F^n r) - \rho_p\hat{j}_1(k_F^p r)]v_{01}^{\rm EX}(r)j_0(kr)d^3r\}. \end{aligned} \tag{2.50}$$

Table 2.7: Parameters of the isoscalar (2.37) and isovector (2.47) density dependence of the real parts of the CDM3Yn (n=3,4,6) interaction at energy $E = 0$ MeV.

Interaction	ν	C_ν^V	α_ν^V	β_ν^V (fm^3)	γ_ν^V (fm^3)
CDM3Y3	0	0.2985	3.4528	2.6388	1.5
	1	0.1574	9.7016	16.2704	-11.9946
CDM3Y4	0	0.3052	3.2998	2.3180	2.0
	1	0.1318	11.7739	16.0279	-15.1987
CDM3Y6	0	0.2658	3.8033	1.4099	4.0
	1	0.1824	8.8819	16.4346	-10.8703

where $J_{01}^D = \int v_{01}^{\rm D}(r) d^3r$. After $V_{\rm IV}(E,\rho)$ is determined, the isovector part $W_{\rm IV}(E,\rho)$ of the *imaginary* nucleon OP is obtained with $F_{\rm IV}^{\rm V}(E,\rho)$ replaced by $F_{\rm IV}^{\rm W}(E,\rho)$.

Our approach is to find realistic parameters of the isoscalar (2.44) (isovector (2.47)) density dependence of the CDM3Yn interaction by a χ^2-fitting procedure which gives the isoscalar (isovector) part of the nucleon OP as close as possible to that of the JLM nucleon optical potential $V_{\rm IS(IV)}^{\rm JLM}(E,\rho)$ tabulated in Ref. [Jeu77b]. To keep a good accuracy of this fitting procedure, instead of introducing an energy dependent scaling factor like $g(E)$ in Eq. (2.36), the density dependent parameters in Eqs. (2.44) and (2.47) have been adjusted separately at each energy.

For the HF calculation of nuclear matter, the isovector density dependence (2.47) of the CDM3Yn (n=3,4,6) interaction at energy E approaching zero has also been constructed based on the JLM results [Lej80] for low energies ($0 < E < 10$ MeV). This set of density dependent parameters is used in the present work to calculate the density dependent NM symmetry energy $S(\rho)$ by the HF method developed in Chapter 3. The parameters of the isoscalar (2.37) and isovector (2.47) density dependence of the real parts of the CDM3Yn (n=3,4,6) interaction are shown in Table 2.7, which will be used in HF calculations of symmetric and asymmetric nuclear matter in the next chapter.

In order to study the charge exchange (p,n) reactions measured on ^{48}Ca, ^{90}Zr, ^{120}Sn and ^{208}Pb targets at proton energies of 35 and 45 MeV, we have constructed

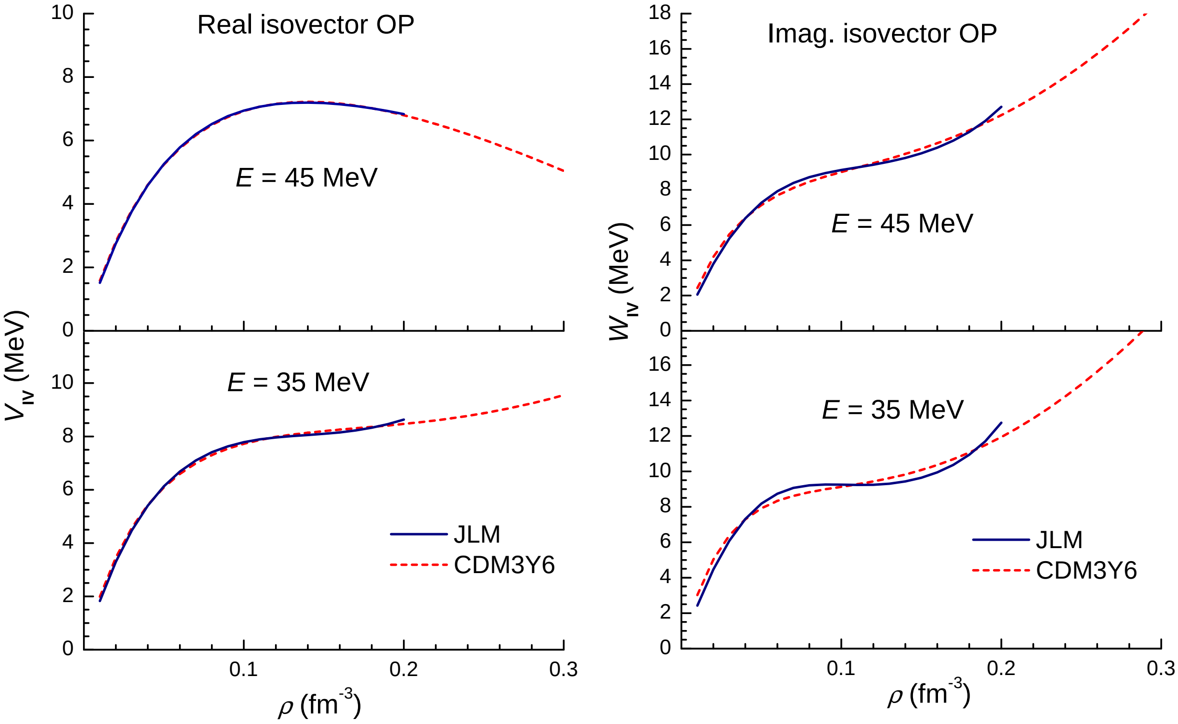

Figure 2.1: Real part $V_{\rm IV}(E,\rho)$ (left side) and imaginary part $W_{\rm IV}(E,\rho)$ (right side) of the isovector nucleon OP given by the isovector density dependence (2.47) of the CDM3Y6 interaction in comparison with the JLM results [Jeu77b] at $E = 35$ and 45 MeV.

the isovector density-dependence of the CDM3Y6 interaction in this work. The real $V_{\rm IV}(E,\rho)$ and imaginary $W_{\rm IV}(E,\rho)$ parts of the isovector nucleon OP at 35 and 45 MeV given by the best-fit density dependent parameters (2.47) are compared with the JLM results [Jeu77b] in Fig. 2.1. In all cases, the isovector nucleon OP given by the best-fit parameters agree closely with the JLM results as shown in Fig. 2.1 for $E = 35$ and 45 MeV. The parameters of the isovector density dependence (2.47) of the CDM3Y6 interaction are shown in Table 2.8.

The isoscalar potential $W_{\rm IS}(E,\rho)$ given by the best-fit parameters and the corresponding JLM potential at $E = 35$ and 45 MeV are shown in Fig. 2.2. We must note that the imaginary OP based on the JLM results for nuclear matter describes

Table 2.8: Parameters of the isovector density dependence (2.47) of the CDM3Y6 interaction.

E (MeV)	u	C_1^u	α_1^u	β_1^u (fm^3)	γ_1^u (fm^3)
35	V	0.1501	6.8259	8.8798	1.2897
	W	0.2607	5.3066	12.4624	2.2291
45	V	0.1141	7.9430	6.4105	-2.7835
	W	0.2689	5.0889	12.9811	3.1865

the absorption due to the Pauli blocking effect which leads to a *finite* mean-free path of nucleons in nuclear medium. As a result, $W_{\rm IS}(E,\rho)$ tends to have a volume shape (deep in the center and shallow at the surface). In general, the imaginary part of the nucleon OP at low and medium energies has been found [Var91, Kon03] to be best represented by a combination of volume and surface terms. The surface absorption is caused mainly by the collective excitations and transfer reactions which occur at the nuclear surface and are not related to the "volume" absorption given by $W_{\rm IS}(E,\rho)$.

In the HF calculation of nuclear matter, the matrix elements of the spin-orbit potential between the HF states vanish. However, in nucleon-nucleus scattering it is an important part of the interaction. The spin-orbit potential arises naturally in the folding model if the effective NN interaction itself has a two-body spin-orbit term [Kho02]

$$v_{LS}(s)\boldsymbol{L}.\boldsymbol{S} \equiv v_{LS}(s)\ \frac{1}{4}[(\boldsymbol{r}_i-\boldsymbol{r}_j)\times(\boldsymbol{p}_i-\boldsymbol{p}_j)].(\boldsymbol{\sigma}_i+\boldsymbol{\sigma}_j) \tag{2.51}$$

For simplicity, we assume that the spin-orbit part of the CDM3Y6 interaction has the same density- and energy dependences as the central part (2.36)

$$v_{LS}(E,\rho,s) = g(E)F^V(\rho)v_{LS}(s). \tag{2.52}$$

The radial strength of the spin-orbit components (with the total isospin T=0 and

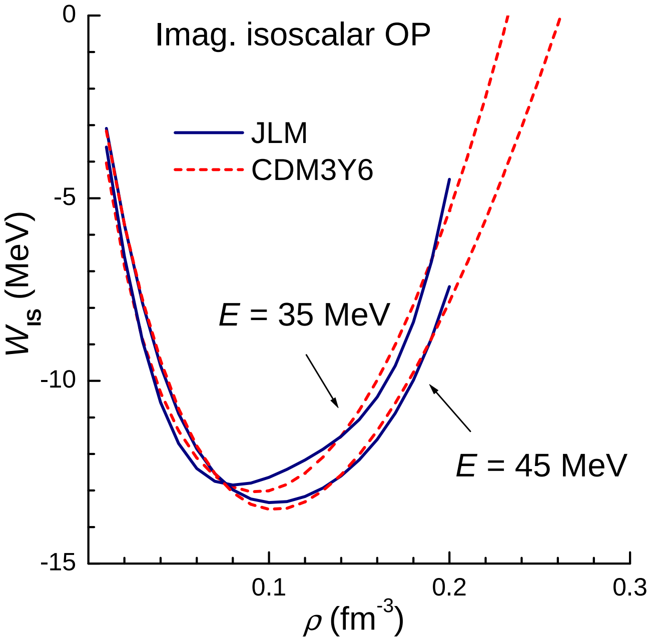

Figure 2.2: Imaginary part $W_{\rm IS}(E,\rho)$ of the isoscalar nucleon OP given by the isoscalar density dependent interaction (2.43) in comparison with the JLM results [Jeu77b] at $E = 35$ and 45 MeV.

T=1) of the M3Y-Paris interaction [Ana83] can also be obtained in terms of Yukawas

$$v_{LS}^{(T)}(s) = \sum_{\nu=1}^{3} Y_{LS}^{(T)}(\nu)\frac{\exp(-\mu_\nu s)}{\mu_\nu s}, \tag{2.53}$$

with the explicit Yukawa strengths tabulated in Table 2.5.

The proton-nucleus optical potential calculated by the folding model has to be supplemented by a corresponding Coulomb potential. It can be obtained from the same folding method to evaluate microscopically the proton-nucleus Coulomb potential, using the (target) charge density matrix

$$V_C(E,\boldsymbol{R}) = \int \frac{e^2}{|\boldsymbol{r}-\boldsymbol{R}|}\left[\rho_{\rm charge}(\boldsymbol{r}) - \rho_{\rm charge}(\boldsymbol{R},\boldsymbol{r})j_0(k(E,R)|\boldsymbol{r}-\boldsymbol{R}|)\right]d^3r. \tag{2.54}$$

The proton finite size is taken into account [Sat79] in the charge distribution $\rho_{\text{charge}}(\boldsymbol{r})$ when calculating the Coulomb potential (2.54). $V_C(E, \boldsymbol{R})$ can then be expanded into a multipole series as for the nuclear potential [Kho02]. In the OM analysis of the elastic proton-nucleus scattering, the Coulomb potential $V_C(\lambda = 0, E, R)$ is usually represented by the Coulomb potential between a point charge and a uniform charge distribution of radius $R_C = r_C A^{1/3}$. This option for the elastic Coulomb potential can be shown to have about the same strength and shape at the surface as the microscopic potential.

In conclusion of this Chapter, we have presented the phenomenological effective (Gogny, Skyrme) interactions and the density-dependent M3Y interactions which are named as CDM3Yn and M3Y-Pn interactions. In particular, the complex isovector density-dependent CDM3Y6 interaction has constructed based on the density dependent JLM nucleon OP [Jeu77b]. All the considered effective interactions will be used in this thesis to study in the three different parts of nuclear physics. All the effective interactions mentioned above will be used in the HF calculations of nuclear matter in Chapter 3. The Gogny [Ber91, Cha08] and M3Y-Pn [Nak08] interactions will be used to study the structure of finite nuclei and neutron stars in Chapter 4. For nuclear reactions part, we will use the complex density-dependent CDM3Y6 interaction which will be presented in Chapter 5.

Chapter 3

NUCLEAR MATTER

In this chapter, we will study the basic properties of asymmetric nuclear matter within the non-relativistic HF scheme using different versions of the density-dependent M3Y interactions. We note that HF calculations of asymmetric nuclear matter have been performed by Basu *et al.* in Ref. [Bas08] using the effective M3Y interaction supplemented with a zero-range density-dependent term. In contrast, our aim is to use exactly the HF approximation to describe homogeneous nuclear matter with the same finite-range density-dependent M3Y interactions which are used in microscopic calculations of the nucleon and heavy-ion optical potentials. Furthermore, we calculate the nuclear pressure P using these M3Y-type interactions and we compare the results with the experimental data in symmetric nuclear matter and neutron matter extracted by Danielewicz, Lacey and Lynch from analyzing the collective flow data in relativistic heavy-ion collisions [Dan02]. For completeness, results calculated with other phenomenological interactions like the Gogny (D1S, D1N) [Ber91, Cha08] and Skyrme (SLy4) [Cha98] forces are also presented.

3.1 Hartree-Fock calculations of Nuclear Matter

Theoretical studies of the equation of state (EOS) of asymmetric nuclear matter were started by Brueckner *et al.* [Bru67] and Siemens [Sie70] in the late 60's. Since then, the subject has much expanded with the introduction of different many-body theories using various two-body and three-body forces or interaction Lagrangians. These theories provide very useful tools for understanding the properties of hot and dense nuclear matter. In this work, we will only consider homogeneous nuclear matter at zero temperature and where neutrons as well as protons are spin-saturated. Thus, the system is characterized by the values of neutron and proton densities, ρ_n and ρ_p, or equivalently by its total density $\rho = \rho_n + \rho_p$ and its neutron-proton asymmetry $\delta = (\rho_n - \rho_p)/(\rho_n + \rho_p)$. One of the important quantities of interest is the symmetry energy $S(\rho)$ of nuclear matter, defined as the energy required per nucleon to change the neutron-proton symmetric nuclear matter into pure neutron matter [Kho96, Zuo99, Kla06, Li08]:

$$S(\rho) \equiv \frac{E}{A}(\rho, \delta = 1) - \frac{E}{A}(\rho, \delta = 0) \ , \tag{3.1}$$

where $\frac{E}{A}(\rho, \delta)$ is the energy per nucleon at density ρ and asymmetry δ. The value of S at saturation density ρ_0 is usually known as the symmetry energy coefficient:

$$E_{\rm sym} = S(\rho_0) \ . \tag{3.2}$$

Various nuclear many-body calculations have predicted $E_{\rm sym}$ to be around 30 MeV [Kho96, Zuo99, Bra85, Pea00]. In our recent study of the isobaric analog state (IAS) excitation in the (p, n) reaction on ^{6}Li [Kho05], ^{48}Ca, ^{90}Zr, ^{120}Sn and ^{208}Pb [Kho07b] targets using the folded Lane potential U_1 for the charge-exchange form factor (see Chapter 5), we have found a value of 31 ± 2 MeV for $E_{\rm sym}$. On the other hand, the density dependence of the symmetry energy $S(\rho)$ is the most important issue about the EOS of neutron-rich matter. In fact, to determine $S(\rho)$ has been a longstanding goal of extensive research using various microscopic and phenomenological models. However, the predicted $S(\rho)$ are still rather divergent, especially at higher densities.

Actually, the symmetry energy depends somewhat on the effective nucleon-nucleon (NN) interaction one considers. There are a large variety of effective in-medium NN interactions used in nuclear structure models and in microscopic calculations of nucleon-nucleus, nucleus-nucleus potentials relevant to the analysis of nucleon-nucleus and heavy-ion scattering problems. These effective interactions are either obtained from a sophisticated G-matrix calculation or phenomenologically parametrized in a form convenient for numerical calculations, such as the Skyrme forces [Vau72]. Among the different kinds of finite-range interactions the so-called Michigan three-range Yukawa (M3Y) interactions [Ana83], which have been obtained by fitting the calculated G-matrix by Yukawa functions are often used in Hartree-Fock (HF) calculations of asymmetric nuclear matter [Kho96, Kho97, Bas08, Nak02, Nak03], mean-field calculations of nuclear structure model [Nak02, Nak03], and in many folding calculations of the optical potential [Kho96, Kho97, Kho05, Chi09, Kho07b].

3.1.1 HF calculations with finite-range interactions

First, we recall the main features of a HF calculation of the nuclear matter binding energy using a finite-range density-dependent interaction. The basic formulae are extracted mainly from Ref. [Kho96]. With the direct (v_D) and exchange (v_{EX}) parts of the interaction determined from the singlet- and triplet-even (V_{SE}, V_{TE}) and odd (V_{SO}, V_{TO}) components of the two-nucleon force [Ber77, Ana83], we can obtain the ground state energy of nuclear matter as

$$\begin{aligned} E = E_{kin} + \frac{1}{2}\sum_{k\sigma\tau}\sum_{k'\sigma'\tau'} [&< \mathbf{k}\sigma\tau, \mathbf{k}'\sigma'\tau'|v_D|\mathbf{k}\sigma\tau, \mathbf{k}'\sigma'\tau' > \\ &+ < \mathbf{k}\sigma\tau, \mathbf{k}'\sigma'\tau'|v_{EX}|\mathbf{k}'\sigma\tau, \mathbf{k}\sigma'\tau' >], \end{aligned} \tag{3.3}$$

where the single-particle (s.p.) wave functions $|\mathbf{k}\sigma\tau>$ are ordinary plane waves:

$$|\mathbf{k}\sigma\tau> = \frac{e^{i\mathbf{k}.\mathbf{r}}}{\sqrt{V}}\chi_\sigma\chi_\tau \tag{3.4}$$

Here, V is the box volume of the uniform nuclear matter; χ_σ and χ_τ are the spin and isospin wave functions.

1. Symmetric nuclear matter:

Symmetric nuclear matter is represented by a uniform (translationally invariant) Fermi gas containing an equal number of neutrons and protons per unit volume. Using the effective interactions of the CDM3Yn family in Eq. (2.35), in which the direct and exchange parts of the (central) NN force can be written in terms of spin-isospin dependent components, the energy per nucleon of symmetric nuclear matter can be obtained as:

$$\frac{E}{A}(\rho) = \frac{3\hbar^2 k_F^2}{10m} + \frac{F_{\rm IS}(\rho)\rho}{2}\left\{ J_0^D + \int [\hat{j}_1(k_F r)]^2 v_{00}^{EX}(r) d^3r \right\} \ , \tag{3.5}$$

where the Fermi momentum k_F is related to the symmetric nuclear matter density ρ by $k_F = (\frac{3}{2}\pi^2\rho)^{1/3}$, m is the bare nucleon mass. $F_{\rm IS}(\rho)$ is the density-dependent strength of the isoscalar part of the CDM3Yn-type interaction (2.37) [Kho97]. J_0^D is the volume integral of the direct part of the interaction as in Eq. (2.45)

The equilibrium density ρ_0 is determined by the saturation condition

$$\frac{\partial}{\partial\rho}(\frac{E}{A}(\rho))\Big|_{\rho\, =\, \rho_0} = 0$$

The nuclear pressure P_0 of symmetric matter is:

$$P_0(\rho) = \rho^2 \frac{\partial}{\partial\rho}(\frac{E}{A}(\rho)), \tag{3.6}$$

This pressure must be equal to zero at the saturation point.

The incompressibility K, or compression modulus of symmetric nuclear matter, which is a measure of the curvature of the EOS at saturation density, is defined as

$$K = 9\rho^2 \frac{\partial^2}{\partial\rho^2}(\frac{E}{A}(\rho))\Big|_{\rho=\rho_0} \ . \tag{3.7}$$

The M3Y-Pn interactions of Nakada [Nak08] have a different form of density dependence. The density dependence is considered as in Eq. (2.29). All parameters of these M3Y-Pn interactions (including the values of $t^{(SE)}$, $\alpha^{(SE)}$, $t^{(TE)}$, and $\alpha^{(TE)}$) were adjusted to the saturation properties of symmetric nuclear matter and the empirical binding energies of doubly magic nuclei from ^{16}O to ^{208}Pb.

The contributions of the density-dependent term $V^{(DD)}(\rho, r_{12})$ of Eq. (2.29) to the energy per particle $\frac{E}{A}(\rho)$, nuclear pressure P_0 and incompressibility K are:

$$\begin{aligned}
\frac{E}{A}^{(DD)}(\rho) &= \frac{3}{8}\left(t^{(SE)}\rho^{\alpha^{(SE)}+1} + t^{(TE)}\rho^{\alpha^{(TE)}+1}\right) \ , \\
P^{(DD)}(\rho) &= \rho^2 \frac{\partial}{\partial\rho}(\frac{E}{A}^{(DD)}(\rho)) \\
&= \frac{3\rho^2}{8}\left[t^{(SE)}(\alpha^{(SE)}+1)\rho^{\alpha^{(SE)}} + t^{(TE)}(\alpha^{(TE)}+1)\rho^{\alpha^{(TE)}}\right] \ , \\
K^{(DD)}(\rho) &= 9\rho^2 \frac{\partial^2}{\partial\rho^2}(\frac{E}{A}^{(DD)}(\rho)) \\
&= \frac{27\rho^2}{8}\left[t^{(SE)}\alpha^{(SE)}(\alpha^{(SE)}+1)\rho^{\alpha^{(SE)}-1} + t^{(TE)}\alpha^{(TE)}(\alpha^{(TE)}+1)\rho^{\alpha^{(TE)}-1}\right] \ .
\end{aligned} \tag{3.8}$$

For comparison, we also calculate symmetric matter and pure neutron matter properties with the Gogny (D1S, D1N) [Ber91, Cha08] interactions. The only technical difference is to replace the Yukawa functions of the M3Y interactions by the Gaussian functions of the Gogny interactions, and the zero-range density-dependence is treated as for the M3Y-Pn interactions of Nakada.

2. Asymmetric nuclear matter:

The EOS for asymmetric nuclear matter is calculated by adding to the isoscalar part the isovector component of the interaction that does not contribute to the EOS of symmetric nuclear matter. In terms of the interaction (2.35) the energy per particle of asymmetric nuclear matter is:

$$\begin{aligned}
\frac{E}{A}(\rho,\delta) = \frac{3\hbar^2[k_F^2(n)\rho_n + k_F^2(p)\rho_p]}{10m} &+ \frac{F_{\rm IS}(\rho)}{2}\left\{\rho J_0^D + \frac{1}{\rho}\int A_0^2(r) v_{00}^{EX}(r) d^3r\right\} \\
&+ \frac{F_{\rm IV}^V(E,\rho)\rho}{2}\left\{\frac{(\rho_n-\rho_p)^2}{\rho} J_1^D + \frac{1}{\rho}\int A_1^2(r) v_{01}^{EX}(r) d^3r\right\} \ ,
\end{aligned} \tag{3.9}$$

where

$$A_0(r) = \rho_n \hat{j}_1(k_F(n)r) + \rho_p \hat{j}_1(k_F(p)r),$$

$$A_1(r) = \rho_n \hat{j}_1(k_F(n)r) - \rho_p \hat{j}_1(k_F(p)r).$$

The symmetry energy coefficient can be derived from Eq. (3.5):

$$a_S = \frac{1}{2}\frac{\partial^2}{\partial\delta^2}(\frac{E}{A}(\rho,\delta))\bigg|_{\delta=0} \tag{3.10}$$

The energy per nucleon of pure neutron matter can be obtained from Eq. (3.9) with δ =1 ($\rho_p = 0$) and the nuclear pressure P_1 of pure neutron matter is calculated as

$$P_1(\rho,\delta=1) = \rho^2\frac{\partial}{\partial\rho}(\frac{E}{A}(\rho,\delta=1)). \tag{3.11}$$

With the M3Y-Pn interactions of Nakada, the contributions of the density-dependent term (Eq. (2.29)) to the energy per particle $\frac{E}{A}(\rho,\delta)$ and nuclear pressure $P(\rho,\delta)$ of asymmetric nuclear matter are:

$$\begin{aligned}
\frac{E^{(DD)}}{A}(\rho,\delta) &= \frac{1}{8}\Big[3(t^{(SE)}\rho^{\alpha^{(SE)}+1} + t^{(TE)}\rho^{\alpha^{(TE)}+1}) \\
&\quad + \delta^2(t^{(SE)}\rho^{\alpha^{(SE)}+1} - 3t^{(TE)}\rho^{\alpha^{(TE)}+1})\Big]\ , \\
P^{(DD)}(\rho,\delta) &= \frac{\rho^2}{8}\Big\{3[t^{(SE)}(\alpha^{(SE)}+1)\rho^{\alpha^{(SE)}} + t^{(TE)}(\alpha^{(TE)}+1)\rho^{\alpha^{(TE)}}] \\
&\quad + \delta^2[t^{(SE)}(\alpha^{(SE)}+1)\rho^{\alpha^{(SE)}} - 3t^{(TE)}(\alpha^{(TE)}+1)\rho^{\alpha^{(TE)}}]\Big\}\ .
\end{aligned} \tag{3.12}$$

The symmetry energy $S(\rho)$ in Eq. (3.1) can be expanded in terms of some bulk parameters around the saturation density ρ_0 as

$$S(\rho) = E_{sym} + Lx + \frac{1}{2}K_{sym}x^2 + ... \tag{3.13}$$

where $x = \frac{(\rho-\rho_0)}{3\rho_0}$ is a parameter that characterizes the deviations of the density from its saturation value and E_{sym} (see Eq. (3.2)), L and K_{sym} are the symmetry energy, the coefficients of slope and curvature at saturation density, respectively. L and K_{sym}

Table 3.1: Energy per particle $E_0 = \frac{E}{A}(\rho, 0)$, incompressibility K of symmetric nuclear matter, the values of volume symmetry energy a_S, symmetry energy E_{sym}, coefficients L and K_{sym} at saturation point calculated with CDM3Yn [Kho97, Kho07b], M3Y-Pn [Nak08], the Skyrme (SLy4) [Cha98] and the Gogny (D1S, D1N) [Ber91, Cha08] interactions. $K_\tau = K_{sym} - 6L$.

Interaction	ρ_0	E_0	K	a_S	E_{sym}	L	K_{sym}	K_τ
	(fm^{-3})	(MeV)	(MeV)	(MeV)	(MeV)	(MeV)	(MeV)	(MeV)
CDM3Y6	0.17	-15.9	252	28.1	29.8	62.5	39.0	-336
CDM3Y4	0.17	-15.9	228	28.1	29.0	62.9	49.8	-328
CDM3Y3	0.17	-15.9	217	28.1	29.0	62.5	46.2	-329
M3Y-P3	0.16	-16.5	245	29.8	31.0	28.3	-213	-383
M3Y-P4	0.16	-16.1	234	28.8	30.0	21.1	-234	-361
M3Y-P5	0.16	-16.1	235	29.7	30.9	27.9	-217	-384
SLy4	0.16	-16.0	230	32.0	32.15	46.0	-120	-396
D1S	0.16	-16.0	203	31.10	31.90	23.7	-248	-390
D1N	0.16	-16.0	221	29.61	30.15	32.4	-182	-376

can be calculated as:

$$\begin{aligned} L &= 3\rho_0 \left. \frac{\partial S(\rho)}{\partial \rho} \right|_{\rho=\rho_0}, \\ K_{sym} &= 9\rho_0^2 \left. \frac{\partial^2 S(\rho)}{\partial \rho^2} \right|_{\rho=\rho_0}. \end{aligned} \tag{3.14}$$

The coefficients L and K_{sym} can be used conveniently to characterize the density dependence of the symmetry energy around the saturation density ρ_0.

3.1.2 HF calculations with zero-range interactions

In this subsection, we summarize the expressions for the equation of state, pressure and symmetry energy obtained with the Skyrme-type interactions (Eq. (2.24)). Numerical results corresponding to the SLy4 interaction will be presented for comparison with the predictions of finite-range interactions. The SLy4 interaction will be used in the next chapter for finite nuclei and the inner crust of neutron stars. The basic formalism of the Skyrme-HF method are found in Ref. [Cha98], thus we only recall the main results of nuclear matter calculated with Skyrme forces.

Within the Skyrme-HF approach the energy per nucleon in symmetric nuclear matter can be expressed as [Cha98]

$$\frac{E}{A}(\rho) = \frac{3\hbar^2}{10m}\left(\frac{3\pi^2}{2}\right)^{2/3} + \frac{3}{8}t_0\rho + \frac{3}{80}\Theta_s\left(\frac{3\pi^2}{2}\right)^{2/3}\rho^{5/3} + \frac{1}{16}t_3\rho^{\sigma+1}, \tag{3.15}$$

where $\Theta_s = 3t_1 + (5+4x_2)t_2$. The nuclear pressure P and incompressibility K of symmetric nuclear matter, defined in Eq. (3.7), can be obtained as

$$\begin{aligned} P(\rho) &= \rho\left\{\frac{\hbar^2}{5m}\left(\frac{3\pi^2}{2}\right)^{2/3}\rho^{2/3} + \frac{3}{8}t_0\rho + \frac{1}{16}\Theta_s\left(\frac{3\pi^2}{2}\right)^{2/3}\rho^{5/3} + \frac{1}{16}t_3(\sigma+1)\rho^{\sigma+1}\right\}, \\ K(\rho) &= -\frac{3\hbar^2}{5m}\left(\frac{3\pi^2}{2}\right)^{2/3}\rho^{2/3} + \frac{3}{8}\Theta_s\left(\frac{3\pi^2}{2}\right)^{2/3}\rho^{5/3} + \frac{9}{16}\sigma(\sigma+1)t_3\rho^{\sigma+1}. \end{aligned} \tag{3.16}$$

For asymmetric nuclear matter, the energy per nucleon is [Cha98]

$$\begin{aligned} \frac{E}{A}(\rho, \delta \text{ or } x_p) &= \frac{3}{5}\frac{\hbar^2}{2m}\left(\frac{3\pi^2}{2}\right)^{2/3}\rho^{2/3}F_{5/3} + \frac{1}{8}t_0\rho[2(x_0+2) - (2x_0+1)F_2] \\ &+\frac{1}{48}t_3\rho^{\sigma+1}[2(x_3+2) - (2x_3+1)F_2] \\ &+\frac{3}{40}\left(\frac{3\pi^2}{2}\right)^{2/3}\rho^{5/3}\left\{[t_1(x_1+2) + t_2(x_2+2)]F_{5/3}\right. \\ &\left.+\frac{1}{2}[t_2(2x_2+1) - t_1(2x_1+1)]F_{8/3}\right\}, \end{aligned} \tag{3.17}$$

With $\delta = \frac{N-Z}{A}$, $x_p = \frac{Z}{A}$ and the following definition of the factors F:

$$F_\alpha(\delta) = \frac{1}{2}[(1+\delta)^\alpha + (1-\delta)^\alpha],$$

$$F_\alpha(x_p) = 2^{\alpha-1}[x_p^\alpha + (1-x_p)^\alpha].$$

From Eq. (3.17) for $\delta = 1$ ($x_p = 0$), we can obtain the the energy per particle $\frac{E}{A}(\rho, \delta = 1 \text{ or } x_p = 0)$ and nuclear pressure $P_1(\rho, \delta = 1 \text{ or } x_p = 0)$ for pure neutron matter.

3.2 Results and discussion

The bulk properties of symmetric nuclear matter calculated with all interactions considered in this work are summarized in Table 3.1. We will now discuss in more details the EOS of symmetric and non-symmetric nuclear matter, the behavior of pressure in symmetric matter and neutron matter, and the density dependence of the symmetry energy.

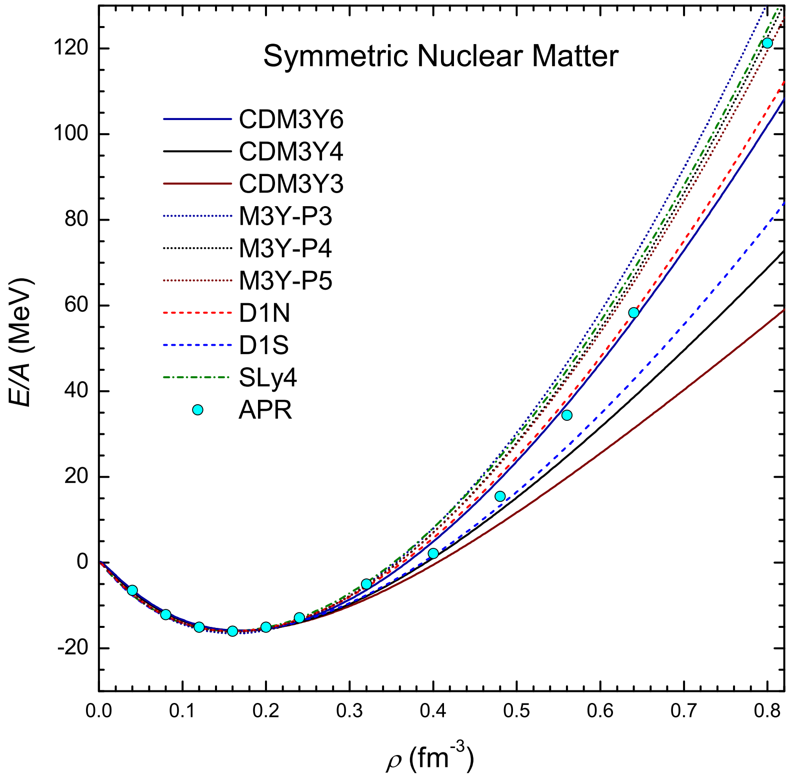

Figure 3.1: EOS of symmetric nuclear matter calculated in HF approximation with the interactions of Table 3.1.

3.2.1 Equation of state

In symmetric nuclear matter the isovector component of the interaction does not contribute to the energy per particle and therefore, the various interactions considered here are expected to give similar EOS up to moderate values of the density. Fig. 3.1 shows the energy per nucleon $\frac{E}{A}(\rho, \delta = 0)$ as a function of ρ (up to 0.8 fm^{-3}) calculated with the interactions of Table 3.1. For comparison the results obtained by Akmal-Pandhanripande-Ravenhall (APR) [Akm98] are also shown. These results correspond to calculations with the Argonne v_{18} interaction plus the relativistic boost interaction δv of the Urbana model IX (UIX). At densities below ρ_0 the differences among the various results are small. At densities above $2\rho_0$ the energies per particle calculated with the M3Y-Pn interactions are the highest whereas those corresponding to CDM3Y3 and CDM3Y4 interactions are the lowest. The results of other interactions and from APR are in between. One can observe that the behavior of the results obtained with CDM3Y6 is similar to that of D1N interaction even though the predicted incompressibilities are different (K=252 MeV and 221 MeV for CDM3Y6 and D1N, respectively).

As mentioned in Chapter 2 , the isoscalar part of the CDM3Yn-type interactions has been well tested in the folding model analyses of refractive α-nucleus and nucleus-nucleus scattering [Kho96, Kho97, Kho07a]. On the other hand, the guidelines leading to the M3Y-Pn interactions are somewhat different. The M3Y-Pn interactions have been carefully parametrized not only to reproduce the saturation properties of symmetric NM like the parameter choice for the CDM3Yn interactions, but also to give good description of ground state properties of the double-closed shell nuclei. Thus, the differences in the isoscalar properties of the various M3Y-type interactions are reflected in the symmetric matter, EOS at high densities.

We turn now to the case of asymmetric matter. The nucleon optical potential calculated with CDM3Yn interactions in nuclear matter was adjusted to reproduce the JLM density- and isospin dependence of the optical potential [Jeu77b] at each energy. Then, the isovector part of the CDM3Y6 interaction was used in the coupled-channel (CC) analysis of the charge-exchange (p, n) reactions exciting the 0^+ isobaric analog states of targets ranging from ^{6}He [Kho05] to ^{208}Pb [Kho07b] and in the ^{18,20,22}O(p, p')

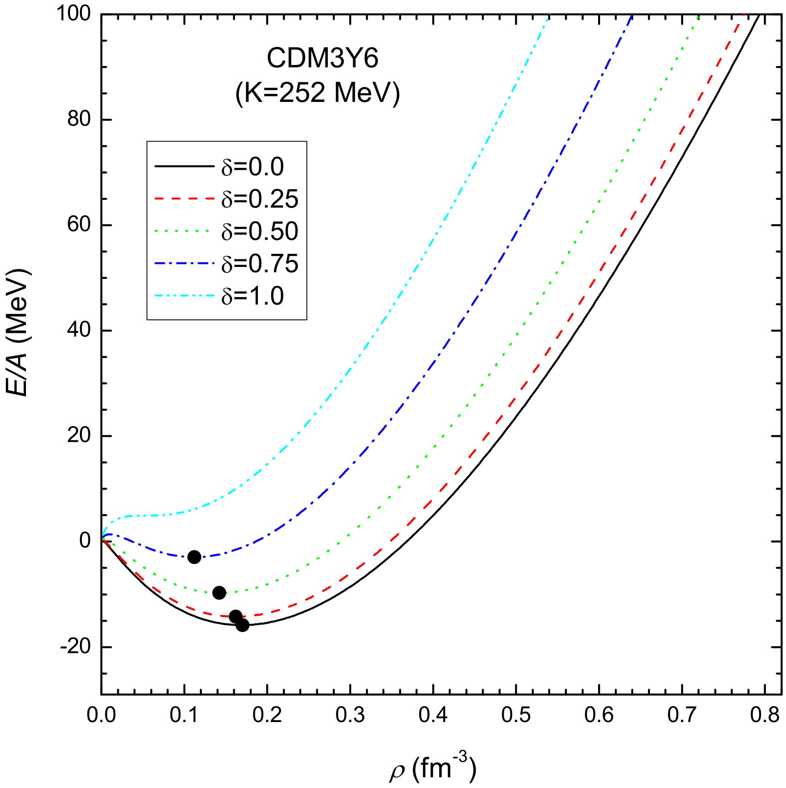

Figure 3.2: EOS of nuclear matter at different values of neutron-proton asymmetry δ, calculated with CDM3Y6 interaction. The black dots indicate the corresponding saturation points.

[Chi09] scattering. It was thus found [Kho07b, Chi09] that a renormalization of the (real) isovector density dependence of the CDM3Y6 interaction by a factor of 1.3 is needed for a good CC description of the (p, n) and (p, p) reactions. Therefore, we have made this readjustment, i.e., the parameter C_1 has been multiplied by 1.3 when calculating asymmetric nuclear matter with the CDM3Yn interaction. The results thus obtained with the CDM3Y6 interaction are shown in Fig. 3.2 for different values of the asymmetry parameter δ. One can observe the familiar trend that the saturation energy becomes less and less negative while the saturation density becomes smaller for increasing values of δ. For $\delta \geq 0.81$ the saturation point disappears.

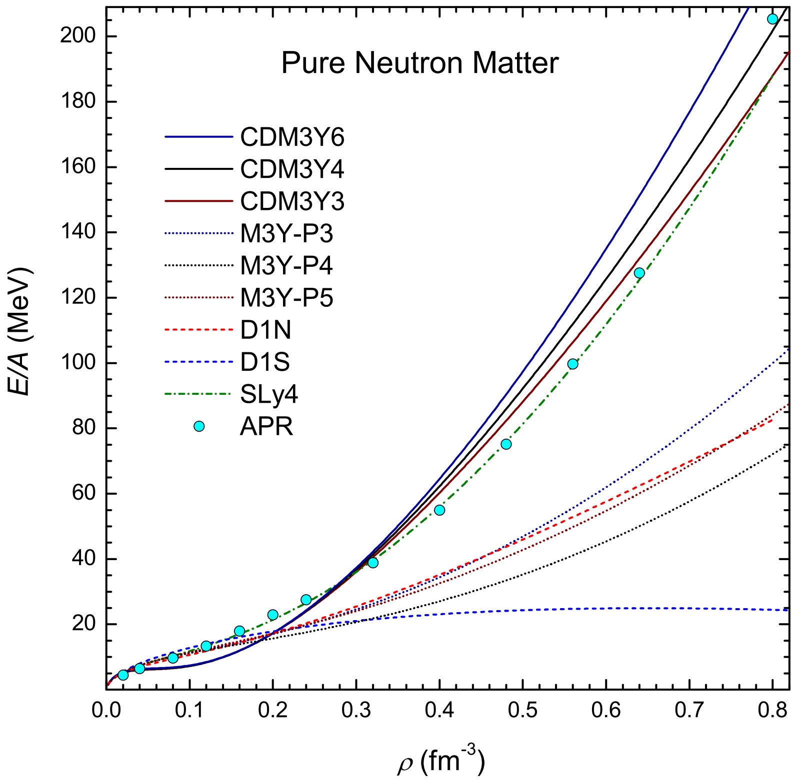

Figure 3.3: The same notation as Fig. 3.1, but for pure neutron matter.

Fig. 3.3 displays the energy per nucleon in the spin-saturated pure neutron matter. The result from the APR calculation in Ref. [Akm98] is also shown as a reference. One observes that the results obtained with CDM3Yn-type interactions are smaller than those obtained with other interactions at densities below 0.2 fm^{-3}, whereas these results are larger at high densities. The behavior of the density-dependent energies per nucleon obtained with CDM3Yn-type and SLy4-Skyrme interactions are similar to those of APR predictions at the high densities. The lowest results at high ρ are obtained with the D1S interaction. It is obvious that such a large difference seen in the HF results for the neutron matter energy is due to the difference in the *isovector* components of the considered interactions. Since the isovector density dependence of the CDM3Yn interactions has been parametrized [Kho07b] to reproduce simultaneously the isospin- and density dependent nucleon optical potential given by the BHF calculation of the JLM group [Jeu77b] and charge exchange (p, n) data for the IAS excitations, the high density behavior of the neutron matter energy given by the CDM3Yn interactions should approximate that given by the BHF calculation of the neutron matter. In this sense, the proximity between the HF results given by the CDM3Yn interactions and APR results of the microscopic many-body calculation [Akm98] is not unexpected. In contrast to the CDM3Yn interactions, the isovector density dependence of the M3Y-Pn, D1S and D1N interactions were carefully fine tuned against the structure data observed for the neutron (and proton-) dripline nuclei and it is also natural to expect that EOS of the neutron matter predicted by these interactions should be quite realistic.

3.2.2 Pressure in symmetric matter and neutron matter

We now discuss the predictions of pressure coming from the various models. The results are summarized in Fig. 3.4 where the calculated values are compared to the data [Dan02] in the case of neutron matter and of symmetric nuclear matter in a range of density values up to $\rho = 0.8$ fm^{-3} ($\sim 5\rho_0$).

In the case of symmetric matter, experimental constraints on the pressure can be extracted from the analysis of the collective flow data in relativistic heavy-ion collisions [Dan02] in the density range of (0.32 - 0.74) fm^{-3}. In the lower panel of Fig. 3.4 the values of pressure P_0 calculated with the different interactions of Table 3.1 are shown. The shaded area represents the region of experimental constraints. All models are consistent with the data at higher densities, but some predictions are at the borderline below $\rho = 0.4$ fm^{-3}.

In the upper panel of Fig. 3.4, the calculated values of pressure in neutron matter are presented together with phenomenological data. Here, the data for neutron matter are the resulting best estimate of the pressure at high densities based on the predictions of the phenomenological momentum-dependent interaction (MDI) model

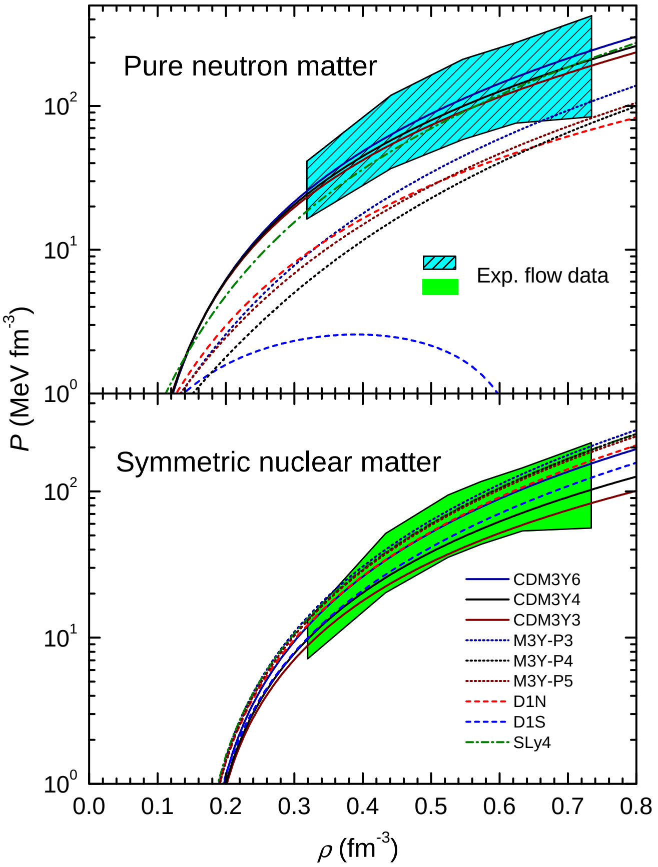

Figure 3.4: Pressure as a function of density for pure neutron matter (upper panel) and symmetric matter (lower panel). The shaded areas show the experimental constraints (from Ref. [Dan02]) in the two cases of neutron matter and symmetric matter.

[Li08, Das03] at the lower and upper bounds of the symmetry energy and the flow-constrained EOS of symmetric nuclear matter. The pressure P_1 of neutron matter is related to the pressure P_0 of symmetric matter and to the symmetry energy by (see Eqs.(3.1,3.7)):

$$P_1(\rho) = P_0(\rho) + \rho^2 \frac{dS(\rho)}{d\rho} \ . \tag{3.18}$$

Thus, once the density dependence of P_0 is established, the difference between P_1 and P_0 gives a direct measure of the density dependence of the symmetry energy $S(\rho)$.

The results of SLy4 and CDM3Yn interactions shown in Fig. 3.4 are in good agreement with the experimental flow data at densities up to $\rho = 0.74$ fm^{-3} ($\sim 4.5\rho_0$).

The other M3Y-Pn interactions predict values of pressure close to the lower limit of the region of the experimental flow data. The two Gogny forces lead to a too low pressure in neutron matter, especially the D1S which fails badly. This confirms again that the D1S interaction is not suited for describing the properties of neutron matter, a result already known from the comparison with calculations using the Argonne bare NN interaction and correlated wave function approach [Fri81, Wir88, Akm98]. Looking at Fig. 1 of Ref. [Cha08] one would conclude that a Gogny-type interaction giving a neutron matter EOS steeper than D1N beyond 0.24 fm^{-3} and closer to the Friedman-Pandharipande's curve [Fri81] would improve the description of the neutron matter pressure.

3.2.3 Nuclear symmetry energy and proton fraction x$_p$

The nuclear symmetry energy $S(\rho)$ can be defined as the energy required per nucleon to change symmetric nuclear matter into pure neutron matter. The determination of the exact form of the density dependence of the nuclear symmetry energy is very important for studying the structure of the neutron rich nuclei, and for astrophysical problems such as the dynamics of supernova explosions [Li01], neutron star formation [Bet90, Swe94], and the cooling of proton-neutron stars [Pet92, Lat91]. There are two possibilities for the cooling of neutron stars: the standard and enhanced cooling scenarios. The dominant neutrino cooling reactions are the general type, known as Urca processes [Pet92, Lat91]. Each reaction produces a neutrino or antineutrino. Therefore, the thermal energy is continuously lost. The most efficient Urca process is the direct Urca process involving nucleons [Lat91]:

$$n \rightarrow p + e^- + \bar{\nu}_e, \qquad p + e^- \rightarrow n + \nu_e. \tag{3.19}$$

This process is only permitted if energy and momentum can be simultaneously conserved. This requires that the ratio of proton to neutron exceeds 1/8, or the proton fraction $x_p \geq 1/9$. If muons and other charged species are ignored, the equilibrium proton fraction x_p $(=\rho_p/\rho)$ is determined by [Lat91]

$$\hbar c(3\pi^2\rho x_p)^{1/3} = 4S_{sym}(\rho)(1-2x_p). \tag{3.20}$$

where the electrons are assumed ultrarelativistic and degenerate. In some case, the proton fraction x_p increases with density, thus the direct Ucra process might still occur above some density threshold. However, if the direct process is not possible, the neutron cooling must occur by other model of neutron star cooling based upon neutrino emission from the interior that is dominated by the modified Urca process [Lat91]

$$n + (n,p) \to p + (n,p) + e^- + \bar{\nu}_e, \qquad p + e^- + (n,p) \to n + (n,p) + \nu_e. \tag{3.21}$$

in which an additional nucleon (n,p) participates in order to conserve momentum.

Fig. 3.5 shows the symmetry energy curves calculated with the interactions listed in Table3.1 together with existing data extracted from charge-exchange reactions [Kho05, Kho07b], neutron-skin [Fur02] and heavy ion fragmentation studies [She07] (upper panel). At $\rho = \rho_0$ the models predict values of $E_{\rm sym} = S(\rho_0)$ around 29 MeV with a dispersion of about ±3 MeV. The empirical value deduced from the CC analysis of the p(^{6}He,^{6}Li*)n reaction is 31 ± 2 MeV [Kho05]. Another method of determining $E_{\rm sym}$ consists in relating this quantity to the neutron skin thickness of ^{208}Pb [Bro00]. Adopting a neutron-skin value of $(0.1-0.2)$ fm then a systematics based on mean-field calculations [Fur02] leads to $E_{\rm sym} \approx$ 27-31 MeV. All interactions of Fig. 3.5 including CDM3Y6 ($E_{\rm sym}$ = 29.77 MeV) are within the present experimental uncertainties of $E_{\rm sym}$.

In the low-density region $\rho \sim$ (0.054 - 0.089) fm^{-3} there exist some empirical values extracted from heavy ion fragmentation data analysis [She07]. They are represented in Fig. 3.5 (inverted triangles from ^{58}Fe + ^{58}Fe and ^{58}Ni + ^{58}Ni pair of reactions, solid circles from ^{58}Fe + ^{58}Ni and ^{58}Ni + ^{58}Ni pair of reactions). The values of $S(\rho)$ calculated with CDM3Yn-type interaction is in good agreement with the data. Those corresponding to M3Y-Pn (n=3,4,5), SLy4, D1S and D1N interactions are larger, whereas these results are similar to those of APR prediction [Akm98]. We should note

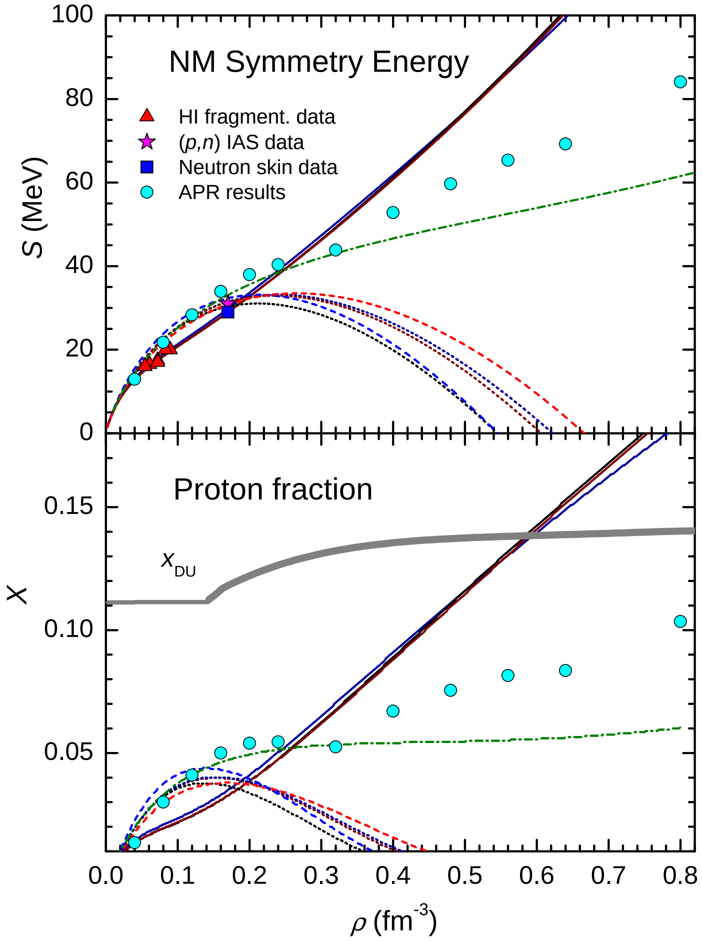

Figure 3.5: Density dependence of the nuclear symmetry energy $S(\rho)$ (upper panel) and the proton fraction x_p (lower panel). The empirical values of nuclear symmetry energies taken from the CC analysis of the charge exchange (p, n) reactions [Kho05, Kho07a], the neutron-skin [Fur02] and heavy ion fragmentation [She07] studies are also shown for comparison. The curve x_{DU} is the threshold for the direct Urca cooling process taken from Ref. [Kla06].

Table 3.2: Same notations as in Table 3.1 but for other mean-field studies: (V_{lowk}+CT) [Dal09], DBHF (Bonn A) [Dal04], MDI [Li08, Xia09], Hybrid [Pie09], G2 [Aru04], and FSUGold [Tod05].

Interaction	ρ_0 (fm^{-3})	E_0 (MeV)	K (MeV)	E_{sym} (MeV)	L (MeV)	K_{sym} (MeV)	K_τ (MeV)
V_{lowk}+CT	0.16	-16.0	258	33.4	86.8	-44.6	-565
DBHF (Bonn A)	0.18	-16.1	230	34.3	70.1	6.88	-414
MDI (x=-1)	0.16	-16.0	211	31.6	107	94.1	-550
MDI (x=1)	0.16	-16.0	211	30.55	16.4	-270	-369
Hybrid	0.15	-16.2	230	37.3	119	111	-603
G2	0.15	-16.1	215	36.4	100.7	-7.5	-612
FSUGold	0.15	-16.3	230	32.6	60.5	-51.3	-414

that the analysis of heavy ion fragmentation data was based on the Antisymmetrized Molecular Dynamic (AMD) simulation [Ono03] at finite temperatures from 5.8 to 7.0 MeV for the ^{58}Fe + ^{58}Fe and ^{58}Ni + ^{58}Ni pairs, and from 5.7 to 6.8 MeV for the ^{58}Fe + ^{58}Ni and ^{58}Ni + ^{58}Ni pairs [She07]. Thus, the comparison with predictions made for cold matter is meaningful only if temperature effects on $S(\rho)$ at low densities can be neglected.

At densities above ρ_0 one sometimes discusses the density dependence of $S(\rho)$ in terms of Asy-stiff and Asy-soft behaviors [She07, Bra05]. The symmetry energy predicted by CDM3Yn-type interaction obviously belongs to the Asy-stiff category and it is even stiffer than the APR prediction.The predictions of SLy4 and M3Y-Pn (n=3,4,5) are moderately Asy-soft. Note that other versions of the Skyrme parametrization can be of the Asy-stiff type [Che05, Li08]. The two Gogny D1S and D1N interactions are definitely Asy-soft.These behaviors are closely related to the pressure curves $P_0(\rho)$ and $P_1(\rho)$ discussed in the previous subsection. Indeed, the relation (3.18) and Fig. 3.4 show for example that, in the region $\rho \sim 0.32$ fm^{-3} the derivative $\frac{dS}{d\rho}$ is strongly positive for CDM3Yn-type interaction, slightly negative for D1N and strongly negative for D1S.

As mentioned above, the equilibrium proton fraction x_p is entirely determined by the nuclear symmetry energy. In the lower panel of Fig. 3.5, the proton fractions x_p calculated with all interactions are plotted with the curve x_{DU} that is the threshold for the direct Urca (DU) cooling process taken from Ref. [Kla06]. The DU-threshold x_{DU} can be estimated from the momentum conservation and charge neutrality condition for p, n and e^- only. We have plotted in the lower panel of Fig. 3.5 the *averaged* DU threshold as a function of the NM density taken from Ref. [Kla06]. At low densities $x^{\rm DU} \approx 1/9$ as found by Lattimer *et al.* [Lat91] in the muon-free approximation. At densities above ρ_0, the charge neutrality is corrected by the muon presence which slightly enhances $x_{\rm DU}$ [Kla06]. As shown in the lower panel of Fig. 3.5, only the proton fractions of the CDM3Yn interactions can reach the DU threshold at moderate densities $\rho \approx 0.6$ fm^{-3}. According to the microscopic APR study [Akm98], such a central density is reachable in a neutron star having mass $M \approx 1.6 M_\odot$ which is well above a lower limit of $1.35 \sim 1.5 M_\odot$ for the DU process established in Ref. [Kla06]. The NM density $\rho \approx 0.6$ fm^{-3} happens also to be within the range of average central densities of the neutron star estimated from a nuclear EOS with $K \approx 240$ MeV [Lat91] which is quite close to K values given by the CDM3Yn interactions (see Table 3.1). As a result, the direct Urca process (3.19) is possible if one chooses the CDM3Yn interactions for in-medium NN interaction in the baryon matter of neutron star. Such a scenario for the DU process is also favored by the HF results for the NM pressure shown in Fig. 3.4 where the CDM3Yn interactions consistently give the best description of empirical data for both the symmetric NM and pure neutron matter. In contrast to the CDM3Yn interactions, the choice of the (Asy-soft) Gogny or M3Y-Pn interactions would definitely exclude the possibility of the DU process because the corresponding proton fractions can never reach the DU threshold as shown in Fig. 3.5. The microscopic APR results obtained with the A18+δv+UIX* version of the Argone NN interaction approach the muon-free threshold $x_{\rm DU} \approx 1/9$ only at $\rho \approx 0.8$ fm^{-3}. Such a central density can exist only if the neutron star mass $M \geq 2 M_\odot$ (see Fig. 11 of Ref. [Akm98]) and the DU process is, therefore, very unlikely in this case as well as in the case of the SLy4 interaction.

In Fig. 3.6, the density-dependence of nuclear symmetry and its proton fraction x_p obtained the low-momentum interaction (V_{lowk} + CT) from Ref. [Dal09], Dirac Brueckner Hartree Fock (DBHF) calculation from Ref. [Dal04], momentum-dependent interaction (MDI) model from Ref. [Li08, Xia09], and Hybrid model [Pie09] are plotted. The bulk properties of symmetric and asymmetric nuclear matter calculated with these models are listed in Table 3.2.

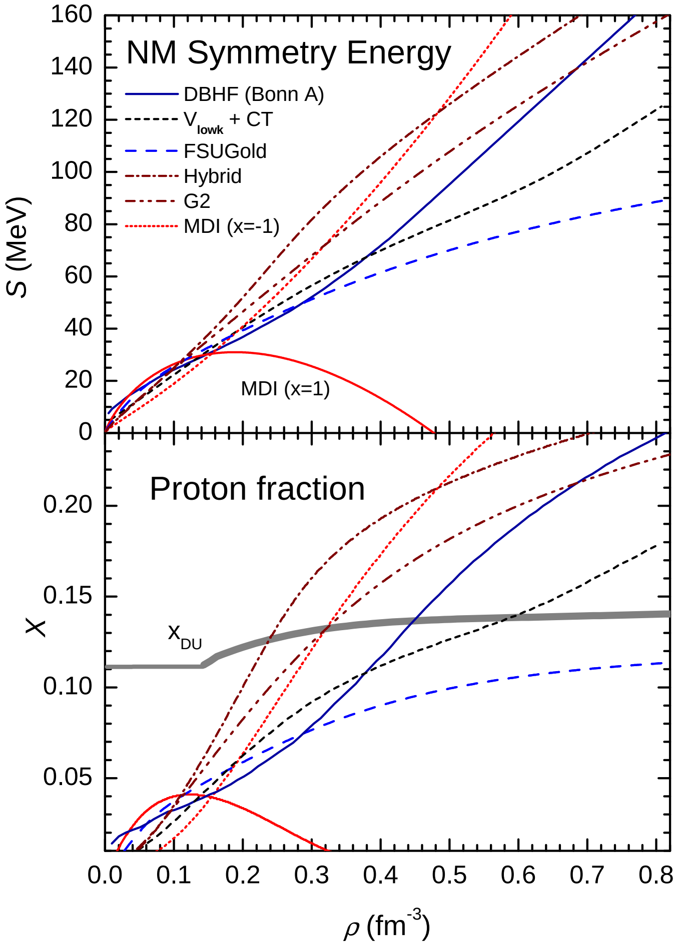

Figure 3.6: Same notation as in Fig. 3.5, but for other interactions [Aru04, Li08, Xia09, Dal04, Pie09, Tod05]. See text for more details.

Since the DU process has also been considered [Pag04, Bal07] in the framework of the EOS given by the fully microscopic many-body calculations of NM using realistic free NN interaction, it is quite complementary to compare the present HF results with those of a recent Dirac-Brueckner Hartree-Fock (DBHF) study [Dal04] using an improved treatment of the Bonn-A interaction. It can be seen from the upper panel of Fig. 3.6 that the NM symmetry energy curve given by this DBHF study is somewhat stiffer than that given by the CDM3Yn interactions. As a result, the proton fraction estimated from the DBHF results is reaching the DU threshold already at NM densities $\rho \approx 0.45$ fm^{-3}. Such a central density is higher than that ($\rho \approx 0.37$ fm^{-3}) given by earlier DBHF results (see Fig. 2 and Table IV of Ref. [Kla06]) and it should lift the corresponding star mass to above the lower limit of $1.35 \sim 1.5 M_\odot$ for the DU process. It is interesting to note that the inclusion of three-body forces into the many-body BHF calculations [Li06] not only essentially improves the description of saturation properties of the symmetric NM but also makes the NM symmetry energy much stiffer at high NM densities (see Fig. 4 of Ref. [Li06]), in the opposite direction from the Asy-soft type interactions. Given highly accurate parametrizations of the bare NN interaction, these microscopic many-body calculations are practically parameter-free and it is natural to assume an Asy-stiff behavior of $S(\rho)$ which allows both the direct and indirect Urca processes to take place during the neutron star cooling. It is highly desirable that results of such a microscopic many-body study can be accurately reproduced at the mean-field level using some effective (in-medium) NN interaction which is also amenable to the nuclear structure and/or reaction calculations. However, such "microscopic" mean-field interactions remain technically complicated to construct and most of the structure and reaction studies still use different kinds of effective NN interactions with parameters adjusted to the optimal (mean-field) description of structure and/or reaction data.

An effective NN interaction can be either fully phenomenological like the Skyrme forces or partially based on a microscopic many-body approach like the CDM3Yn interactions considered above. An alternative approach has been suggested recently by the Tuebingen group [Dal09] which considers only the low-momentum (below a cut-off $\Lambda = 2$ fm^{-1}) part of the bare NN interaction. While this "low k" interaction V_{lowk} still describes well the NN scattering data up to the pion threshold, the short-range correlations originated from high-momentum components of the NN force must be treated phenomenologically at the mean-field level [Boz06]. Namely, the V_{lowk} has been supplemented by an empirical density-dependent contact (CT) interaction adjusted to reproduce the saturation properties of symmetric NM and the empirical symmetry energy E_{sym} within the HF approximation [Dal09]. This V_{lowk}+CT interaction was shown to give also a reasonable description of the g.s. properties of some finite nuclei including ^{208}Pb. The NM symmetry energy and proton fraction predicted by the V_{lowk}+CT interaction are shown in Fig. 3.6 and they are quite close to those predicted by the CDM3Yn interactions shown in Fig. 3.5. Like the CDM3Yn interactions, the V_{lowk}+CT interaction should also belong to the Asy-stiff type and allow both the direct and indirect Urca processes during the neutron star cooling.

Another famous choice of the effective interaction is the Skyrme-type momentum dependent interaction (MDI) which has been first parametrized [Che05] for the transport model simulation of HI collisions. By varying the x parameter of the MDI interaction, the experimental data from NSCL-MSU on the isospin diffusion have been shown to favor the MDI (x=-1) version which gives the NM symmetry energy nearly linear in the NM density (see Fig. 3.6 or Fig. 1 of Ref. [Che05]). One can see in Fig. 3.6 that the NM symmetry energy $S(\rho)$ given by the MDI (x=-1) interaction is somewhat stiffer than that predicted by the DBHF calculation using the Bonn A interaction [Dal04]. The proton fraction given by this (Asy-stiff) MDI (x=-1) interaction is reaching the DU threshold at NM densities $\rho \approx 0.3$ fm^{-3}. Since the star mass corresponding to such a central NM density is probably smaller than the lower limit of $1.35 \sim 1.5 M_{\odot}$ for the DU process [Kla06], it remains questionable if the DU process is possible in this case. The MDI interaction has also been used to describe neutron skin in finite nuclei in the Gogny Hartree Fock model [Xia09], and the MDI interaction with x between 0 and -1 was shown to reproduce reasonably well the empirical neutron skin data for ^{124,132}Sn and ^{208}Pb. However, the situation with the MDI interaction becomes somewhat confused after the new FOPI data on the π^-/π^+ ratio in the central HI collisions at SIS/GSI energies have been shown to clearly favor the MDI (x=1) interaction [Xia09]. In terms of symmetry energy, the MDI (x=1) interaction belongs to the Asy-soft type (see Fig. 3.6) like the Gogny or M3Y-Pn interactions considered above and therefore it excludes the DU process during the neutron star cooling. Given experimental evidences favoring both the Asy-stiff and Asy-soft versions of the MDI interaction, the behavior of the NM symmetry energy at high densities as well as the possibility of the DU process still remain an open question.

The NM symmetry energy has also been the subject of various relativistic mean field (RMF) studies. In the present work, we compare our non-relativistic HF results with those of some recent RMF studies using carefully chosen parameters for the energy-density functional [Aru04, Tod05, Pie09]. The G2 parameter set [Aru04] has been shown to consistently reproduce the g.s. structure of finite nuclei and bulk NM properties. In particular, the RMF calculation using the G2 set reproduces very well the empirical pressure for both the symmetric NM and pure neutron matter [Aru04]. Quite popular is the FSUgold parameter set developed by Piekarewicz *et al.* [Tod05] which has been used to study not only the bulk NM properties and g.s. structure of finite nuclei but also the excitation of the nuclear giant monopole resonance (GMR). While the FSUgold parameters give a good description of the GMR in ^{208}Pb, the observed GMR excitation energies in Sn isotopes could not be reproduced with this parameter set. In order to improve the RMF description of the NM saturation properties as well as monopole strength distribution in Sn isotopes, a *hybrid* model of the RMF parameters has been developed [Pie09] based on a realistic RMF parameter set (the NL3 model). However, the Hybrid parameters turned out to give a worse description of the GMR in ^{208}Pb compared with that given by the FSUgold model and it remains, therefore, difficult to choose between these two parameter sets. The RMF results using these parameters are shown in Fig. 3.6 and one can see that the stiffness of the NM symmetry energy is gradually increased as one goes from FSUgold and G2 to the Hybrid results. It has been found by Steiner [Ste06] that the RMF models typically have a large symmetry energy and a large proton fraction, and the DU process becomes possible at rather low NM densities. This effect can be clearly seen in the Hybrid and G2 results shown in Fig. 3.6 where the corresponding proton fractions reach DU threshold at the NM densities of $\rho \approx 0.24$ and 0.32 fm^{-3}, respectively. We note further that $S(\rho)$ predicted in the Hybrid model is very close to the RMF result by Klähn *et al.* [Kla06] using the NL$\rho\sigma$ parametrization where the proton fraction is reaching the DU threshold at $\rho \approx 0.28$ fm^{-3}. The behavior of the proton fraction predicted by the FSUgold model is somewhat different from those predicted by the Hybrid and G2 models. Namely, it approaches the muon-free threshold $x_{\rm DU} \approx 0.11$ only at $\rho \approx 0.8$ fm^{-3}, like the microscopic APR result. With the predicted maximum neutron star mass of $M \approx 1.72 M_{\odot}$, the FSUgold model has been shown in Ref. [Tod05] to allow partially the DU process in the neutron star cooling. However, if we assume the *averaged* DU threshold taken from Ref. [Kla06] which takes into account the muon presence at high densities, then the DU process is unlikely in this case because the proton fraction predicted by the FSUgold model seems to saturate at $x \sim 0.11$ at $\rho \geq 0.8$ fm^{-3} (see lower panel of Fig. 3.6), like the APR results [Akm98] discussed above. Given a dilemma in the choice between the FSUgold and Hybrid models [Pie09], possibility of the DU process is again an open question.

3.2.4 Nuclear matter incompressibility

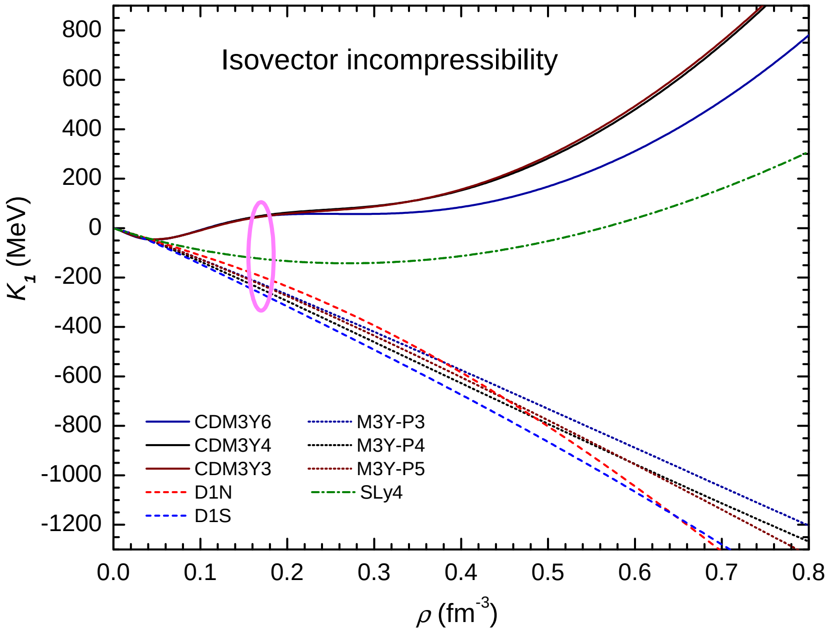

Figure 3.7: Isovector part of the NM incompressibility given by the present HF calculation using the interactions of Table 3.1. Encircled part shows K_1 values near the saturation density ρ_0 of symmetric NM, i.e., the K_{sym} values given in Table 3.1. See text for more details.

Although the experimental evidences are still divergent with respect to the Asy-stiff and Asy-soft type mean-field interactions, it is of interest to further explore the difference between these two groups in terms of the NM incompressibility. The NM incompressibility $K(\rho)$ can be written explicitly in terms of the isoscalar (K_0) and isovector (K_1) parts as

$$K(\rho,\delta) = K_0(\rho) + K_1(\rho)\delta^2 + O(\delta^4) + ... \tag{3.22}$$

$$\text{where } K_0(\rho) = 9\rho^2 \frac{\partial^2}{\partial\rho^2}\left[\frac{E}{A}(\rho,\delta=0)\right];\ K_1(\rho) = 9\rho^2 \frac{\partial^2 S(\rho)}{\partial\rho^2}. \tag{3.23}$$

It is clear from Eq. (3.23) that the behavior of the isovector incompressibility K_1 should correlate closely with that of the NM symmetry energy $S(\rho)$. We have plotted in Fig. 3.7 the density dependence of K_1 given by the numerical differentiation of the HF results for $S(\rho)$ and one can see that the K_1 value given by the (Asy-stiff) CDM3Yn interactions is positive over the density range $\rho \geq \rho_0$ and gradually increases to 200 $\sim$ 400 MeV at ρ approaching 0.6 fm $^{-3}$ (the DU-onset density found with these interactions). On the contrary, the K_1 value given by the (Asy-soft) M3Y-Pn and Gogny interactions is negative over the same density range and decreases linearly to about -1000 MeV at ρ approaching 0.6 fm $^{-3}$. Since $K(\rho)$ is actually related to the first derivative of NM pressure with respect to the density, a strongly *negative* isovector incompressibility $K_1(\rho)$ corresponds to a decrease of the NM pressure $P(\rho)$ as one goes from the symmetric NM to the pure neutron matter and this effect can be seen clearly in Fig. 3.5. Such a decrease of $P(\rho)$ in the pure neutron matter case found with the (Asy-soft) M3Y-Pn and Gogny interactions pulls the calculated $P(\rho)$ out of the empirical area deduced from the collective flow data measured in relativistic HI collisions [Dan02]. Based on this discussion, we conclude that the behavior of the isovector incompressibility $K_1(\rho)$ given by the (Asy-stiff) CDM3Yn interactions is more consistent with the HI flow data compared with the (Asy-soft) M3Y-Pn and Gogny interactions.

In the literature, the discussion on the isovector part of the NM incompressibility is very often made based on the K values estimated at the saturation density ρ_0 of symmetric NM. It should be noted, however, that the saturation density of asymmetric NM decreases rather quickly with the increasing neutron-proton asymmetry δ and pure neutron matter ($\delta = 1$) becomes *unbound* (see Fig. 3.3 and also Fig. 2

of Ref. [Kho96]). As a result, ρ_0 is no more a stable extremum in the NM energy curve and various expansions around it like (3.13) might not be accurate for large neutron-proton asymmetries δ. For example, the second derivative of the approximated expression (3.13) for $S(\rho)$ gives a purely parabolic density dependence of the isovector incompressibility as $K_1(\rho) \approx K_{\rm sym}(\rho/\rho_0)^2$ which can deviate from the exact HF result at high densities (see Fig. 3.7). In any case, the calculated K_1 values near ρ_0 (encircled in Fig. 3.7) converge quite well to the corresponding $K_{\rm sym}$ coefficients of the expansion (3.13), so that $K_1(\rho \to \rho_0) \approx K_{\rm sym}$. In the studies of the HI isospin diffusion [Che05] or isospin dependence of giant monopole resonance [Li07], the asymmetry of the NM incompressibility near ρ_0 was associated with the quantity $K_\tau = K_{\rm sym} - 6L$ which has been confined by these data to $K_\tau \approx -550 \pm 100$ MeV. The empirical K_τ value has been shown by a recent study of the neutron-skin thickness by Centelles *et al.* [Cen09] to be around $K_\tau \approx -500 \pm 100$ MeV. From Table 3.2 one can see that K_τ values obtained from the (Asy-stiff) DBHF, V_{lowk}+CT, Hybrid and MDI (x=-1) results are in good agreement with empirical value. However, the Asy-stiff CDM3Yn interactions give K_τ values of about -330 MeV which are somewhat above the upper limit of empirical data. The Asy-soft MDI (x=1), M3Y-Pn and Gogny interactions give K_τ values of about -400 MeV, right at the empirical upper limit. While no definitive conclusion can be made on the stiffness of NM symmetry energy $S(\rho)$ based on the K_τ values, some preference for the Asy-stiff interactions can be made based on the empirical constraints on the E_{sym} and L parameters established recently in the analysis of the isospin diffusion data and ratios of neutron and proton spectra measured in HI collisions [Tsa09]. One can see in Table 3.1 that only the (Asy-stiff) CDM3Yn and SLy4 interactions are lying within the borders of the (double) constraints deduced from the isospin diffusion data: $L \approx 40 \sim 70$ MeV and $J \approx 30 \sim 34$ MeV (see Fig. 1 of Ref. [Tsa09]). It is complementary to note a similar range for the slope parameter $L \approx 45 \sim 75$ MeV established recently from a systematic study of the correlation between the neutron skin thickness and symmetry energy [War09].

Finally we note that the mean-field calculations discussed in the present work did not take into account the *hyperon* presence in the neutron star. The hyperon population has been estimated to make up about 18% of the neutron star matter and shown to significantly soften the EOS as well as reduce the limiting neutron star mass [Gle91, Gle00]. Another important effect is that the proton fraction is significantly enhanced by the hyperon presence. Namely, the proton fraction of a hyperon star having mass $M \approx 1.5 M_{\odot}$ is about 50% larger than that of a neutron-proton-lepton star of the same mass (see Fig. 5.28 of Ref. [Gle00]). Consequently, if we assume a 50% rise in the proton fractions predicted, e.g., by the microscopic APR calculation or FSUgold model at $\rho \approx 0.6 \sim 0.8$ fm^{-3} (see lower panel of Fig. 3.6), then the DU process is well allowed within these models. Concerning a typical Asy-soft interaction like the Gogny, M3Y-Pn or MDI (x=1), such a 50% increase of the proton fraction will definitely not make the DU process possible.

In conclusion of this Chapter, we have studied the bulk nuclear matter properties predicted by two different sets (CDM3Yn and M3Y-Pn) of the density-dependent M3Y interaction, SLy4 version of the Skyrme as well as D1S and D1N versions of the Gogny interaction in the framework of the self-consistent HF mean field. The HF results for the density dependence of the NM symmetry energy and proton fraction are also compared with those given by the microscopic many-body studies (the DBHF and APR calculations) using the bare NN interaction, and by the RMF studies using different parameter sets. We have concentrated our discussion on several main aspects: the NM binding energy and pressure in the symmetric NM and pure neutron matter, and the density dependence of the NM symmetry energy $S(\rho)$ and the associated proton fraction. For the symmetric NM, the main conclusion is that all the effective NN interactions used here are more or less consistent with the microscopic APR prediction and empirical pressure deduced from the collective flow measurements in relativistic HI collisions. For the pure neutron matter, the HF prediction for the NM binding energy and pressure shows clearly that the considered mean-field interactions are divided into two families which are associated with two different behaviors (Asy-soft and Asy-stiff) of the NM symmetry energy at high densities, where only the Asy-stiff type interactions comply with the empirical data for the NM pressure. These two families were shown to predict two different scenarios for the proton-to-neutron ratio in the beta equilibrium which, in turn, imply two distinct mechanisms for the neutron star cooling (with or without the direct Urca process).

Although an ambiguity in the high-density behavior of the NM symmetry energy still remains due to the experimental evidences from HI studies favoring both the Asy-soft and Asy-stiff versions of the MDI mean-field interaction, recent analysis of the isospin diffusion data and ratios of neutron and proton spectra measured in HI collisions [Tsa09] or systematic study of the correlation between the neutron skin thickness and NM symmetry energy [Cen09, War09] seem to provide evidence favoring the Asy-stiff type interactions. The Asy-stiff behavior is also predicted by many microscopic BHF or DBHF calculations using realistic choices for the bare NN interaction [Li06] and by the latest RMF studies [Aru04, Tod05, Pie09]. It is, therefore, highly probable that the neutron star cooling proceeds indeed via both the direct and modified Urca processes.

CHAPTER 4

FINITE NUCLEI

In this chapter, we present the general formalism of the non-relativistic HF and HF-BCS approaches in coordinate representation using finite-range density-dependent interactions (e.g. Gogny D1S [Ber91], D1N [Cha08], and M3Y-Pn [Nak08]) in both the mean field and pairing channels. We will show how the coordinate space HF equations for a non-local self-consistent potential can be actually solved with correct boundary conditions. In this thesis, we have also presented a basis expansion method, in which the radial HF equations are solved using a spherical Bessel function basis. The description of the techniques used to perform the HF-BCS calculations will be shown. The first application is to study the possibility of bubble structures of ^{34}Si, ^{22}O, ^{46}Ar and ^{68}Ar using the finite-range density-dependent interactions in both the mean field and pairing channels. Furthermore, for the first time the properties of the Wigner-Seitz (WS) cells [Neg73] in the inner crust of neutron stars will be studied using finite-range density-dependent interactions, such as Gogny (D1S & D1N) and M3Y-Pn, in HF and HF-BCS approaches.

4.1 Hartree-Fock Calculations

4.1.1 The Variational Principle and the Hartree-Fock method

The microscopic models are models that describe the structure of the nucleus in terms of degrees of freedom of its microscopic constituents - the nucleons. The basic idea of the Hartree-Fock method is that the mutual interactions among nucleons lead to an average potential felt by each one of the nucleons. The nucleus is a many-body system of fermions so the wave function of the nucleus of any state must be antisymmetric under the interchange of the coordinates of any two nucleons. The mean field theory provides an approximate solution to the nuclear many-body problem, based on a Hamiltonian containing a suitable two-body interaction. In second quantization, this Hamiltonian is given by [Rin80]

$$\hat{H} = \sum_{ij} t_{ij} \hat{c}_i^{\dagger} \hat{c}_j + \frac{1}{4} \sum_{ijkl} \bar{v}_{ijkl} \hat{c}_i^{\dagger} \hat{c}_j^{\dagger} \hat{c}_l \hat{c}_k, \tag{4.1}$$

where t is the kinetic energy operator,

$$\bar{v}_{ijkl} =< i, j|v|k, l > - < i, j|v|l, k > \tag{4.2}$$

represents the antisymmetrized two-body interaction matrix elements, and $\hat{c}_i^{\dagger}, \hat{c}_i$ single-particle creation and annhilation operators in a single-particle state i. All indices in Eq. (4.1) run over a complete set of states. An eigenstate of this Hamiltonian can be expanded as a sum over states which all have the same total number of nucleons, but with the nucleons occupying the available single-particle states in all possible combinations.

The Schrödinger equation can be written as

$$\hat{H}|\Phi_k >= E_k|\Phi_k > \tag{4.3}$$

where $(|\Phi_k >, E_k)$ are the exact eigenstates and eigenenergies of $\hat{H}$. If E_0 denotes the ground state energy, it is a well-known result of quantum mechanics that the expectation value

$$E[\Phi] = \frac{< \Phi|\hat{H}|\Phi >}{< \Phi|\Phi >} \tag{4.4}$$

satisfies the inequality

$$E[\Phi] \geq E_0 \tag{4.5}$$

for any arbitrary state vector $|\Phi >$. The essence of all variational methods is to find a model state vector $|\Phi >$ which gives the lowest possible value of $E[\Phi]$. This is obtained by the variational condition

$$\delta E[\Phi] =< \delta\Phi|\hat{H} - E|\Phi > + < \Phi|\hat{H} - E|\delta\Phi >= 0 \tag{4.6}$$

where E is a Lagrange multiplier which will be interpreted as the energy corresponding to $|\Phi >$. The Hartree-Fock method, or self-consistent mean field method, is a particular case of the general variational method where the trial state vectors belong to the space of the Slater determinants built on a set of single-particle states.

In general, the wave function Φ is a complex function, so the variation can be carried out either with the real part or imaginary part, which is equivalent to carrying out the variation over $|\delta\Phi >$ and $< \delta\Phi|$. Thus, with Eq. (4.6) can be reduced to

$$< \delta\Phi|\hat{H} - E|\Phi >= 0 \tag{4.7}$$

and its complex conjugate equation.

Finally, it must be noted that Eqs. (4.6,4.7) implicitly assume that $\hat{H}$ does not depend on $|\Phi >$. Actually, many effective Hamiltonains do depend on densities and/or currents, i.e., they implicitly depend on $|\Phi >$ itself and therefore, variations of $E[\Phi]$ involе also rearrangement contributions which are not explicited in Eqs. (4.6,4.7), but they are of course treated in our numerical applications.

4.1.2 HF Equations in Coordinate Space

a- Energy functional

Standard HF theory yields the following expression for the total binding energy of the nucleus in its ground state as

$$E^{HF} =< \Phi|\hat{H}|\Phi > \tag{4.8}$$

where the many-body Hamiltonian $\hat{H}$ is written in second quantization by the creation and annhilation operators $\hat{c}_i^\dagger, \hat{c}_i$ in Eq. (4.1). Using the Wick's theorem, we can calculate the energy E^{HF} as a functional of the single-particle density ρ_{ij}

$$\begin{aligned} E^{HF}[\rho] &= \sum_{ij} t_{ij} < \Phi|\hat{c}_i^\dagger \hat{c}_j|\Phi > + \frac{1}{4}\sum_{ijkl} \bar{v}_{i,j,k,l} < \Phi|\hat{c}_i^\dagger \hat{c}_j^\dagger \hat{c}_l \hat{c}_k|\Phi > \\ &= \sum_{ij} t_{ij}\rho_{ij} + \frac{1}{2}\sum_{ijkl} \rho_{ki}\bar{v}_{i,j,k,l}\rho_{lj}, \end{aligned} \tag{4.9}$$

In the Hartree-Fock theory, a single Slater determinant is selected to be the many-body wave function:

$$|\Phi >= \prod_{i=1}^{A} \hat{c}_i^\dagger|0 >, \tag{4.10}$$

where the index i runs over a set of single-particle states with orthonormal wave functions φ_i, $i = 1, ..., A$ which are themselves eigenfunctions of a single-particle Hamiltonian h,

$$h(x)\varphi_i(x) = \epsilon_i\varphi_i(x), x = \{\boldsymbol{r_i}, \sigma_i, q_i\} \tag{4.11}$$

This Hamiltonian will be determined by the variational condition (4.7). Here the single-particle wave functions $\varphi_i(\boldsymbol{r_i}, \sigma_i, q_i)$ are a coordinate space representation of the eigenstates $|i >$ of the single-particle Hamiltonian h, and ϵ_i are the corresponding single-particle energies. The many-body Hartree-Fock Hamiltonian is

$$\hat{H}^{HF} = \sum_{i=1}^{A} \hat{h}(i) \tag{4.12}$$

The variational condition (4.7) together with the ansatz (4.10) with respect to the single-particle wave function φ_i leads to a set of coupled, non-linear equations

$$h_{kl} = t_{kl} + \sum_{i=1}^{A} \bar{v}_{kili} = \epsilon_k \delta_{kl} \tag{4.13}$$

The total Hartree-Fock energy E^{HF} (4.9) calculated with the trial wave function (4.10) is given explicitly as

$$\begin{aligned} E^{HF} \; &= \; -\sum_{i=1}^{A} \frac{\hbar^2}{2m_{q_i}} \int \varphi_i^*(\boldsymbol{r_1}) \Delta \varphi_i(\boldsymbol{r_1}) d\boldsymbol{r_1} \\ &+ \; \frac{1}{2} \sum_{ij}^{A} \int \varphi_i^*(\boldsymbol{r_1}) \varphi_j^*(\boldsymbol{r_2}) V(\boldsymbol{r_1}, \boldsymbol{r_2}) \varphi_i(\boldsymbol{r_1}) \varphi_j(\boldsymbol{r_2}) d\boldsymbol{r_1} d\boldsymbol{r_2} \\ & -\frac{1}{2} \sum_{ij}^{A} \int \varphi_i^*(\boldsymbol{r_1}) \varphi_j^*(\boldsymbol{r_2}) V(\boldsymbol{r_1}, \boldsymbol{r_2}) \varphi_i(\boldsymbol{r_1}) \varphi_j(\boldsymbol{r_2}) d\boldsymbol{r_1} d\boldsymbol{r_2}, \end{aligned} \tag{4.14}$$

where $V(\boldsymbol{r_1}, \boldsymbol{r_2})$ is the two-body interaction between nucleons 1 and 2 (see Eq. (4.2)). Here and in the following , $q_i = +1$ (-1) if nucleon is a neutron (a proton) and m_{q_i} is the corresponding nucleon mass.

We can obtain the Hartree-Fock equations (4.13) for the single-particle wave functions $\varphi_i(\boldsymbol{r})$ in coordinate space as,

$$-\frac{\hbar^2}{2m_{q_i}} \Delta \varphi_i(\boldsymbol{r_1}) + U_H(\boldsymbol{r_1}) \varphi_i(\boldsymbol{r_1}) - \int U_F(\boldsymbol{r_1}, \boldsymbol{r_2}) \varphi_i(\boldsymbol{r_1}) d\boldsymbol{r_2} = \epsilon_i \varphi_i(\boldsymbol{r_1}) \tag{4.15}$$

where $U_H(\boldsymbol{r_1})$ is the local direct potential (*Hartree potential*)

$$U_H(\boldsymbol{r_1}) = \sum_j \int \varphi_j(\boldsymbol{r_2}) V(\boldsymbol{r_1}, \boldsymbol{r_2}) \varphi_j(\boldsymbol{r_2}) d\boldsymbol{r_2} \tag{4.16}$$

and $U_F(\boldsymbol{r_1}, \boldsymbol{r_2})$ is the non-local exchange potential (*Fock potential*),

$$U_F(\boldsymbol{r_1}, \boldsymbol{r_2}) = \sum_j \varphi_j(\boldsymbol{r_2}) V(\boldsymbol{r_1}, \boldsymbol{r_2}) \varphi_j(\boldsymbol{r_1}) \tag{4.17}$$

The Hartree-Fock equations (4.15) are quite similar in form to Schrödinger equations for each of the single-particle states and present a *self-consistent* problem, since the Hartree and Fock potentials depend on the single-particle wave functions of the solution of the single-particle eigenvalue problem. It is usually solved by iteration methods in which one starts from an initial guess for the potentials. Solving the HF equations then yields a new set of wave functions, which is used to build the mean fields for next step. This process is repeated until the convergence is achieved.

b- Hartree-Fock calculations with finite-range interactions

In this section we explain in details the analytical expressions needed for Hartree-Fock calculations with a finite-range interaction, taking the Gogny interaction [Dec80, Ber91] as an illustrative example. Expression for other types of finite-range interactions can be easily deduced from this case. Throughout this work we limit ourselves to spherically symmetric systems because this greatly simplifies the numerical efforts and reduces the numerical integrations only to the radial coordinate while all reductions of spin-angular variables can be carried out analytically.

In order to obtain the Hartree potential $U_H(r_1)$ of Eq. (4.16) and the Fock potential $U_F(r_1, r_2)$ of Eq. (4.17), it is convenient to use the multipolar decomposition of the Gaussian functions $f_\nu(|\vec{r_1} - \vec{r_2}|)$ of Eq. (2.27) as [Bri93]

$$\begin{aligned} f_\nu(|\boldsymbol{r_1} - \boldsymbol{r_2}|) &= 4\pi \sum_{LM} (-)^M i^{-L} j_L\left(2i\frac{r_1 r_2}{\mu_\nu^2}\right) \exp^{-\frac{r_1^2+r_2^2}{\mu_\nu^2}} Y_L^{-M}(\hat{r_1}) Y_L^M(\hat{r_2}) \\ &= 4\pi \sum_{LM} (-)^M v_L^\nu(r_1, r_2) Y_L^{-M}(\hat{r_1}) Y_L^M(\hat{r_2}), \end{aligned} \tag{4.18}$$

where $j_L(ix)$ is the spherical Bessel function of pure imaginary argument [Abr72]. For the M3Y-Pn interaction [Nak08], we use the multipole expansion of Yukawa form factor of Eq. (2.31) as [Bri93]

$$\begin{aligned} f_\nu(|\boldsymbol{r_1}-\boldsymbol{r_2}|) &= 4\pi\sum_{LM}(-)^M j_L(i\mu_\nu r_<)h_L^{(1)}(i\mu_\nu r_>)Y_L^{-M}(\hat{r_1})Y_L^M(\hat{r_2}) \\ &= 4\pi\sum_{LM}(-)^M v_L^\nu(r_1,r_2)Y_L^{-M}(\hat{r_1})Y_L^M(\hat{r_2}). \end{aligned} \tag{4.19}$$

where $h_L^{(1)}(i\mu_\nu r_>)$ is the Hankel function of pure imaginary argument [Abr72] and $r_<$ ($r_>$) is the smaller (the larger) of (r_1,r_2). Using P_σ we rewrite $P_\sigma = \frac{1+\vec{\sigma_1}\vec{\sigma_2}}{2}$, therefore

$$W_\nu+B_\nu P^\sigma-H_\nu P^\tau-M_\nu P^\sigma P^\tau = \left(W_\nu - H_\nu P^\tau + \frac{B_\nu - M_\nu P^\tau}{2}\right)+\frac{1}{2}\left(B_\nu - M_\nu P^\tau\right)\vec{\sigma_1}\vec{\sigma_2} \tag{4.20}$$

and we express the central potential $V^{(C)}(|\boldsymbol{r_1}-\boldsymbol{r_2}|)$ in the form

$$V(|\boldsymbol{r_1}-\boldsymbol{r_2}|) = 4\pi\sum_{SLJ}\sum_{\nu=1}^{2}A_\nu(S)(-1)^{L+S+J+M}v_L^\nu(r_1,r_2)\left(T_{(1)}^{(SL)J}.T_{(2)}^{(SL)J}\right), \tag{4.21}$$

where

$$A_\nu(S=0) = W_\nu - H_\nu P^\tau + \frac{B_\nu - M_\nu P^\tau}{2}; A_\nu(S=1) = \frac{B_\nu - M_\nu P^\tau}{2}. \tag{4.22}$$

Here, we have introduced the tensors $T_{(\mu)}^{(SL)J}$, which are tensorial products of a spherical harmonic Y_L^M with a Pauli spin matrix

$$T^{(SL)J} = \left[\sigma_\eta^S \otimes Y_L^M\right] \tag{4.23}$$

with

$$\begin{aligned} T_M^{(0L)L} &\equiv Y_L^M \qquad (4.24) \\ T_\mu^{(1L)J} &\equiv \sum_{M,\nu}(-1)^{L-1+\mu}\hat{J}\begin{pmatrix} L & 1 & J \\ M & \nu & -\mu \end{pmatrix}\sigma_\nu Y_L^M. \qquad (4.25) \end{aligned}$$

Here, we use the notation $\hat{J} = (2J+1)^{1/2}$.

In the Hartree-Fock approximation the nucleon densities $\rho_q(\boldsymbol{r})$, kinetic energy densities $\tau_q(\boldsymbol{r})$, and spin densities $\boldsymbol{J}_q(\boldsymbol{r})$ are expressed in term of the single-particle wave functions $\varphi_i(\boldsymbol{r},\sigma,q)$,

$$\begin{aligned}
\rho_q(\boldsymbol{r}) &= \sum_{i,\sigma} |\varphi_i(\boldsymbol{r},\sigma,q)|^2, \\
\tau_q(\boldsymbol{r}) &= \sum_{i,\sigma} |\overrightarrow{\nabla}\varphi_i(\boldsymbol{r},\sigma,q)|^2, \\
\boldsymbol{J}_q(\boldsymbol{r}) &= -i\sum_{i,\sigma,\sigma'} \varphi_i^*(\boldsymbol{r},\sigma,q)[\overrightarrow{\nabla}\varphi_i(\boldsymbol{r},\sigma',q)\times <\sigma|\vec{\sigma}|\sigma'>]. \qquad (4.26)
\end{aligned}$$

The sums in Eq. (4.26) run over all occupied single-particle states.

Because of the spherical symmetry assumption, the single- particle wave functions $\varphi_i(\boldsymbol{r},\sigma,q)$ can be factorized into a radial function $u_i(r)$, a spin-angular part $\mathcal{Y}_{ljm}(\hat{r},\sigma)$, and isospin function $\chi_q(\tau)$:

$$\varphi_i(\boldsymbol{r},\sigma,q) = \frac{u_\alpha(r)}{r}\mathcal{Y}_{ljm}(\hat{r},\sigma)\chi_q(\tau) \qquad (4.27)$$

where

$$\mathcal{Y}_{ljm}(\hat{r},\sigma) = \sum_{m_l m_s} < l\frac{1}{2}m_l m_s|jm > Y_{lm_l}(\hat{r})\chi_{m_s}(\sigma)$$

We have introduced the notation $\alpha \equiv \{q,n,l,j\}$ where $q = +1(-1)$ for neutrons (protons), n is the principal quantum number, l is the orbital angular momentum, j is the total angular momentum, and m is the magnetic quantum number.

From the definitions (4.26) for the density $\rho(\boldsymbol{r})$ and the kinetic energy density $\tau(\boldsymbol{r})$ one can see that these functions depend only on the radial coordinate and they can be written as,

$$\begin{aligned}
\rho(r) &= \frac{1}{4\pi r^2}\sum_\alpha (2j_\alpha+1)u_\alpha^2(r) \\
\tau(r) &= \frac{1}{4\pi}\sum_\alpha (2j_\alpha+1)[(\frac{dR_\alpha(r)}{r})^2 + \frac{l_\alpha(l_\alpha+1)}{r^2}R_\alpha^2(r)] \qquad (4.28)
\end{aligned}$$

where $R_\alpha(r) = u_\alpha(r)/r$. The sums in Eq. (4.28) are restricted to neutron and proton orbitals to obtain the neutron and proton densities. The spin density $J(r)$ can be written in the following way

$$J(r) = \frac{1}{4\pi r^3}\sum_{\alpha}(2j_\alpha+1)[j_\alpha(j_\alpha+1) - l_\alpha(l_\alpha+1) - \frac{3}{4}]u_\alpha^2(r) \qquad (4.29)$$

where the vector spin density is $J(\boldsymbol{r}) = \frac{\boldsymbol{r}}{r}J(r)$.

b.1- The direct and exchange potentials

Using the tensor $T_{(\mu)}^{(SL)J}$ in Eq. (4.23) and the single particle wave functions $\varphi_i(\boldsymbol{r}, \sigma, q)$ defined in Eq. (4.27), we can calculate the direct and exchange angular-momentum couple which are needed to build the Hartree-Fock potential in each (l, j) partial wave.

The calculations of the contributions of the central $V^{(C)}(|\boldsymbol{r_1}-\boldsymbol{r_2}|)$ term in Eq. (2.26) to the mean field are presented in Appendix A.1. These contributions are separated into a Hartree (direct) and a Fock (exchange) contribution as

$$U_i^H(r_1) = \sum_j\sum_{\nu=1}^{2}\hat{j_j}^2(W_\nu + \frac{B_\nu}{2} - H_\nu\delta_{q_iq_j} - \frac{M_\nu}{2}\delta_{q_iq_j})\int u_j^2(r_2)v_0^\nu(r_1,r_2)r_2^2dr_2, \quad (4.30)$$

$$\begin{aligned} U_i^F(r_1,r_2) &= \sum_{jL}\sum_{\nu=1}^{2}\hat{j_j}^2 u_j(r_1)u_j(r_2)v_L^\nu(r_1,r_2)\begin{pmatrix} l_i & l_j & L \\ 0 & 0 & 0\end{pmatrix}^2 \\ &\times \left[\hat{l_i}^2\hat{l_j}^2\begin{Bmatrix} l_i & j_i & 1/2 \\ j_j & l_j & L\end{Bmatrix}^2(W_\nu\delta_{q_iq_j} - H_\nu) + B_\nu\delta_{q_iq_j} - M_\nu\right], (4.31)\end{aligned}$$

with $|l_i - l_j| \leq L \leq (l_i + l_j)$.

For the density-dependent term $V^{(DD)}(\rho, |\boldsymbol{r_1} - \boldsymbol{r_2}|)$ of Eq. (2.26), it is very similar to the zero-range density-dependent term of Skyrme interactions [Vau72, Cha97], and therefore, its contribution to the mean field is well-known [Vau72, Cha97, Dec80]:

$$\begin{aligned} U_q^{DD}(r) &= \frac{t_0}{4}\{(2+x_0)(2+\alpha)\rho^{\alpha+1}(r) \\ &- (2x_0+1)[2\rho^\alpha(r)\rho_q(r) + \alpha\rho^{\alpha-1}(r)(\rho_p^2(r)+\rho_n^2(r)]\} \qquad (4.32)\end{aligned}$$

where ρ is the total nucleon density and q stands for protons or neutrons.

b.2- The spin-orbit potential

Concerning the contribution of the two-body spin orbit interaction, it is easily derived since this interaction is of zero range. The result is [Vau72, Cha97, Dec80]:

$$\begin{aligned} V_q^{LS}(r) &= W_0 \left\{ \frac{1}{r}\frac{d}{dr}(\rho(r)+\rho_q(r))\boldsymbol{l}.\boldsymbol{s} - \left[\frac{1}{r}J(r) + J'(r) + \frac{1}{r}J_q(r) + J_q'(r) \right] \right\} \\ &= W_q^{LS0}(r)\boldsymbol{l}.\boldsymbol{s} + W_q^{LS1}(r) \end{aligned} \tag{4.33}$$

where $J(r)$ is the spin density of Eq. (4.29), and $J' = \frac{dJ}{dr}$.

b.3- The Coulomb potential

The Coulomb interaction between protons, e^2/r_{12}, has multi-poles $v_L^C(r_1,r_2) = r_<^L/r_>^{L+1}$ where $r_<$ ($r_>$) is the smaller (the larger) of (r_1,r_2). The direct term of the Coulomb potential is

$$\begin{aligned} V^{DC}(r_1) &= e^2 \sum_{j\in\text{protons}} \hat{j}_j^{\,2} \int u_j^2(r_2) v_0^C(r_1,r_2) r_2^2 dr_2 \\ &= e^2 \int \rho_p(r_2) v_0^C(r_1,r_2) r_2^2 dr_2, \end{aligned} \tag{4.34}$$

while the exchange term of the Coulomb potential is

$$\begin{aligned} V_i^{EC}(r_1,r_2) = e^2 \sum_{jL} \delta_{q_i,-1/2}\delta_{q_i,q_j} \hat{l}_i^{\,2} \hat{l}_j^{\,2} \hat{j}_j^{\,2} u_j(r_1) u_j(r_2) v_L^C(r_1,r_2) \\ \times \begin{pmatrix} l_i & l_j & L \\ 0 & 0 & 0 \end{pmatrix}^2 \begin{Bmatrix} l_i & j_i & 1/2 \\ j_j & l_j & L \end{Bmatrix}^2 \end{aligned} \tag{4.35}$$

b.4- The HF equations

With the help of the results (4.27, 4.30, 4.31, 4.32, 4.33, 4.34, 4.35) it is straightforward to obtain the radial integro-differential HF equations for the radial wave functions $u_i(r_1)$ as

$$\begin{aligned}\frac{\hbar^2}{2m}[-u_i^{''}(r_1) &+ \frac{l_i(l_i+1)}{r_1^2}u_i(r_1)] + [U_i^H(r_1) + U_q^{DD}(r_1) + V^{DC}(r_1) + W_q^{LS1}(r_1)]u_i(r_1) \\ &- \int (U_i^F(r_1,r_2) + V_i^{EC}(r_1,r_2))u_i(r_2)r_2^2dr_2 \\ &+ [j_i(j_i+1) - l_i(l_i+1) - \frac{3}{4}]W_q^{LS0}(r_1)u_i(r_1) = \epsilon_i u_i(r_1) \qquad (4.36)\end{aligned}$$

The iterative Hartree-Fock method consists in the following: for a given effective potential $V(\rho, |\boldsymbol{r_1} - \boldsymbol{r_2}|)$, we start from an initial guess (a Woods-Saxon potential) and solve the HF equations to get the single-particle wave functions and the single-particle energies of the occupied states, then we calculate the potentials $U_i^H(r_1)$, $U_q^{DD}(r_1)$, $V^{DC}(r_1)$, $W_q^{LS1}(r_1)$, $U_i^F(r_1,r_2)$, $V_i^{EC}(r_1,r_2)$, $W_q^{LS0}(r_1)$ for the next iteration and solve the HF equations again. One can proceed in this way until reaching convergence with a required accuracy. In our calculations, the convergence criteria is that all single-particle energies change by less than a fixed amount $\delta\epsilon$ between two iterations.

c- Numerical solutions

c.1-The boundary conditions

The system of differential equations is solved in the redial coordinate space in a spherical box for a given choice of boundary conditions. At origin (r=0) all solutions $\frac{u_i(r)}{r}$ must be regular and therefore, $u_i(r) \overset{r\to 0}{\to} \alpha r^{l_i+1}$. At the wall of the box, we can use two possible boundary conditions: vanishing wave functions (Dirichlet condition) or vanishing derivatives of the wave functions (Neumann condition). The first condition is the natural choice when calculating an isolated nucleus. A combination of the first and the second condition is more appropriate if we calculate nuclear systems inside a Wigner-Seitz cell as we shall explain in subsection 4.4.

c.2-The Numerov algorithm for HF equations

In the context of HF equations with finite-range interactions, Vautherin and Vénéroni [Vau67] have introduced a method called "*trivially equivalent local potential*" where one can transform the HF integro-differential equations (4.36) into a purely differential equation. In fact, a drawback of the method is that this equivalent local potential can have poles at the nodes of the wave functions $u_i(r)$ [Vau67, Gra02] . In Ref. [Vau67] an iterative method was introduced to overcome this problem, based on the linearization of the local equivalent potential around the poles. However, in this work we would like to use another method for solving the HF equations, the so-called Brueckner-Gammel-Weizner (BGW) method [Bru58]. Three functions $D_i(r)$, $G_i(r)$ and $H_i(r)$ are introduced as

$$\begin{aligned} D_i(r_1) &= u_i^2(r_1) + a^2[u_i^{'}(r_1)]^2 \\ G_i(r_1) &= \frac{1}{D_i(r_1)} \int (U_i^F(r_1,r_2) + V_i^{EC}(r_1,r_2))[u_i(r_1)u_i(r_2) + a^2 u_i^{'}(r_1)u_i^{'}(r_2)]dr_2 \\ H_i(r_1) &= \frac{a^2}{D_i(r_1)} \int (U_i^F(r_1,r_2) + V_i^{EC}(r_1,r_2))[u_i(r_2)u_i^{'}(r_1) - u_i(r_1)u_i^{'}(r_2)]dr_2 \ , \end{aligned} \tag{4.37}$$

where a can take an arbitrary value. The case $a = 0$ corresponds to the trivially equivalent local potential method of Vautherin and Vénéroni [Vau67] . With the help of the definitions (4.37) it is straightforward to transform the integro-differential HF equations (4.36)for the radial wave functions $u_i(r)$ into

$$-u_i^{''}(r_1) + \frac{l_i(l_i+1)}{r_1^2}u_i(r_1) + \frac{2m}{\hbar^2}[U_i^{HF}(r_1) - \epsilon_i]u_i(r_1) \quad + \quad \frac{2m}{\hbar^2}H_i(r_1)u_i^{'}(r_1) = 0 \ . \tag{4.38}$$

where

$$\begin{aligned} U_i^{HF}(r_1) &= U_i^H(r_1) + U_q^{DD}(r_1) + V^{DC}(r_1) + W_q^{LS1}(r_1) + G_i(r_1) \\ &+ [j_i(j_i+1) - l_i(l_i+1)] - \frac{3}{4}]W_q^{LS0}(r_1) \end{aligned} \tag{4.39}$$

One can see that Eq. (4.38) becomes formally a differential equation where the potentials depend on the solutions and therefore they must be solved iteratively. At each iteration of the HF scheme we evaluate the potentials of all states by using the wave functions of the previous iteration and we repeat this procedure until convergence. An additional difficulty comes from the fact that the first derivative of the wave function $u_i(r_1)$ appears in Eq. (4.38). This is not a major problem since the wave function $u_i(r)$ and its derivative can be determined together by a Numerov method. More details about the Numerov method are given in Appendix A.2.

4.1.3 HF Equations in Basis Representation

Solving the Hartree-Fock equations in coordinate space has several advantages: the results do not depend on the choice of a basis and its truncation, and the individual wave functions have a correct asymptotic behavior. On the other hand, if we try to solve the HF equations in rather large boxes (for example in the calculations of Wigner-Seitz cells [Neg73] neutron stars, one needs box radii typically beyond 40 or 50 fm in the outer most layers of the inner crust) and with large values of orbital momentum l (l can be larger than 15 or 16 in the calculations of Wigner-Seitz cells), we encounter strong numerical instabilities. The cause of the problem is that the HF wave functions are proportional to r^{l+1} in the region which is near the origin. Calculations requiring a certain number of nodes can fail in this region if the HF potential is not good enough at a given iteration. To avoid this problem, we have also developed a basis expansion method. Using this method, solving the HF equations can be reduced to an eigenvalue problem. The advantage of the basis expansion method is that it produces a high accuracy (measured by the orthogonality of the solutions) with a smaller number of points, while this may be not obtained if we solve the HF equations in coordinate space. Another advantage is that the integro-differential nature of the HF equations no longer represents a problem.

Normally, the harmonic-oscillator basis-set is widely applied in describing the single-particle orbits of nuclei. In this work, we choose instead to use a the spherical Bessel functions basis. In this section, we describe how the HF equations are solved in a spherical Bessel functions basis. This method will be later used for calculating the Wigner-Seitz cells in the inner crust of neutron stars, as we will discuss in the next sections.

a- Hamiltonian matrix

The spherical Bessel function $j(kr)$ satisfies equation,

$$j_l''(kr) + \frac{2}{kr} j_l'(kr) + \left(1 - \frac{l(l+1)}{(kr)^2}\right) j_l(kr) = 0, \tag{4.40}$$

where $k = (\frac{2mE}{\hbar^2})^2$.

The radial part $\frac{u_{nlj}(r)}{r}$ of the single-particle wave function in Eq. (4.27) can be expanded on the normalized spherical Bessel functions as

$$\frac{u_{nlj}(r)}{r} = \sum_{i=1}^{N} C_{nlj,i} \tilde{j}_l(k_i^{(l)} r) \tag{4.41}$$

where N is the dimension of the basis, the normalized spherical Bessel functions $\tilde{j}_l(k_i^{(l)} r)$ are determined by

$$\tilde{j}_l(kr) = \frac{j_l(kr)}{\sqrt{\int (j_l(kr))^2 dr}} \tag{4.42}$$

and they satisfy the orthogonality conditions $< \tilde{j}_l(k_i^{(l)} r) | \tilde{j}_l(k_{i'}^{(l)} r) >= \delta_{ii'}$.

The single-particle wave function $\varphi(\boldsymbol{r}, \sigma, q)$ in Eq. (4.27) can be expanded as

$$\begin{aligned} \varphi_{nljm}(\boldsymbol{r}, \sigma, q) &= \sum_{i=1}^{N} C_{nlj,i} \tilde{j}_l(k_i^{(l)} r) \mathcal{Y}_{ljm}(\hat{r}, \sigma) \chi_q(\tau) \\ &= \sum_{i=1}^{N} C_{nlj,i} \psi_{nljm,i}(\boldsymbol{r}, \sigma, q) \end{aligned} \tag{4.43}$$

Under the l and j conservation, the single-particle Hamiltonian matrix is given by

$$H_{ii'}^{(lj)} =< \psi_{ljm,i} | H | \psi_{ljm,i'} > \tag{4.44}$$

where the single particle Hamiltonian can be written as

$$\begin{aligned} H &= -\frac{\hbar^2}{2m}\nabla^2 + V(\boldsymbol{r}_1, \boldsymbol{r}_2) \\ &= -\frac{\hbar^2}{2m}\left[\frac{1}{r}\left(\frac{d^2}{dr^2}r\right) - \frac{\hat{L}^2}{r^2}\right] + \sum_{LJM} Y_{LJM}(\hat{r}_1)V(r_1, r_2)Y^{\dagger}_{LJM}(\hat{r}_2) \end{aligned} \tag{4.45}$$

b- Hartree-Fock equations in a basis

The HF equations (4.15) in spherical symmetry, i.e., when $\{nljm\}$ are good quantum numbers, become:

$$H|\varphi_{nljm}>=\epsilon_{nljm}|\varphi_{nljm}> \tag{4.46}$$

With the help of expansion (4.43), the HF equations (4.45) take the form of a matrix eigenvalue problem:

$$\sum_{i'=1}^{N} H^{(lj)}_{ii'}C_{nlj,i'} = \epsilon_{nljm}C_{nlj,i} \tag{4.47}$$

where $H^{(lj)}_{ii'}$ is a symmetric $N \times N$ matrix,

$$H^{(lj)}_{ii'} = \frac{\hbar^2}{2m}(k^{(l)}_i)^2\delta_{ii'} + \int\int V^{HF}_{lj}(r_1, r_2)\tilde{j}_l(k^{(l)}_i r_1)\tilde{j}_l(k^{(l)}_{i'} r_2)d\boldsymbol{r_1}d\boldsymbol{r_2}. \tag{4.48}$$

Here, the potentials $V^{HF}_{lj}(r_1, r_2)$ for each state can be obtained from the formulas (4.30), (4.31), (4.32), (4.33), (4.34) and (4.35). The HF equations are now solved by an iterative procedure. We start from an initial Woods-Saxon potential, and then the diagonalization of the symmetric matrix $H^{(lj)}_{ii'}$ will provides a set of single-particle states (ϵ_{nljm} and $C_{nlj,i'}$) which permit us to calculate a new density $\rho(r)$ according to the expressions given in Eqs. (4.28) and (4.41). With the new density $\rho(r)$ we calculate the potential $V^{HF}_{lj}(r_1, r_2)$ and obtain the matrix $H^{(lj)}_{ii'}$, then diagonalize it, etc. The convergence is reached when the differences of the single- particle energies ϵ_{nljm} between two iterations is less than a given accuracy value ε.

4.1.4 Center of mass corrections

The expectation value of the Hamiltonian with respect to the total wave function Φ gives us not only the ground state energy but also the translational energy of the nucleus with respect to the fixed referential system. All the nuclei in this work are spherical nuclei, so the rotation energy is zero. Because the contribution from the motion of the nucleons around the center of mass and the motion of the center of mass in the total wave function Φ are not clearly separated, the exact value of the ground state energy in the center of mass (c.m.) system differs from $<\Phi|H|\Phi>$. Thus, one has to extract the contributions of the c.m. motion to the total binding energy. In this part, we explain the different possible schemes for the c.m. corrections to the binding energy. Although, one can make the c.m. corrections to the binding energy and the rms radii in various ways, the c.m. corrections are more easily treated using a harmonic oscillator approximation. In this section concentrate on the c.m. corrections to the binding energy.

To obtain the total binding energy in the c.m. frame, one must subtract from $<\Phi|H|\Phi>$ the c.m. energy,

$$E^{c.m.} = \frac{1}{2mA} < \boldsymbol{P}^2_{c.m.} > . \tag{4.49}$$

Thus, the correct quantity to be minimized is:

$$E =< \Phi|T + \frac{1}{2}\sum_{ij} V(\boldsymbol{r_i}, \boldsymbol{r_j})|\Phi > - < \Phi|\frac{\boldsymbol{P}^2_{c.m.}}{2mA}|\Phi >, \tag{4.50}$$

where the total linear momentum operator $\boldsymbol{P}$ is given as

$$\boldsymbol{P} = -i\hbar \sum_{i}^{A} \overrightarrow{\nabla}_i. \tag{4.51}$$

We can calculate

$$\begin{aligned}
\boldsymbol{K} - \frac{\boldsymbol{P}^2}{2mA} &= \sum_i^A \frac{\boldsymbol{p}_i^2}{2m} - \frac{(\sum_i^A \boldsymbol{p}_i)^2}{2mA} \\
&= \sum_i^A \frac{\boldsymbol{p}_i^2}{2m} - \frac{1}{2mA}\left[\sum_i^A \boldsymbol{p}_i^2 + \sum_{i\neq j}^A \boldsymbol{p}_i{\cdot}\boldsymbol{p}_j\right] \\
&= \frac{1}{2m}\left(1-\frac{1}{A}\right)\sum_i^A \boldsymbol{p}_i^2 - \frac{1}{2mA}\sum_{i\neq j}^A \boldsymbol{p}_i{\cdot}\boldsymbol{p}_j
\end{aligned} \tag{4.52}$$

The first term in Eq. (4.52) is a one-body term, that is easily handled if one replaces $\frac{1}{m}$ by $\frac{1}{m}(1-\frac{1}{A})$. The second term is a two-body term, which is more difficult to treat if one works in coordinate space because the structure of the integro-differential HF equations is modified. It is usually dropped in most calculations. Here, we simply carry out the self-consistent procedure without this term and we subtract out its contribution after convergence is reached.

This contribution of the two-body term is:

$$\begin{aligned}
E_2^{c.m.} = \frac{\hbar^2}{2mA}\sum_{ij}\delta_{q_iq_j}\hat{l}_i\hat{l}_j\hat{j}_i^2\hat{j}_j^2[1-\delta_{l_il_j}]\begin{Bmatrix} l_i & j_i & \frac{1}{2} \\ j_j & l_j & 1 \end{Bmatrix}^2 \\
\times[\delta_{l_il_j-1}A_{ij}B_{ji} + l_i\delta_{l_jl_i-1}A_{ji}B_{ij}],
\end{aligned} \tag{4.53}$$

where

$$\begin{aligned}
A_{ij} &= \int dr_1 r_1^2 \frac{u_i(r_1)}{r_1}\left(\frac{\partial}{\partial r_1} + \frac{l_j+1}{r_1}\right)\frac{u_j(r_1)}{r_1} \\
B_{ij} &= \int dr_2 r_2^2 \frac{u_i(r_2)}{r_2}\left(\frac{\partial}{\partial r_2} - \frac{l_i}{r_2}\right)\frac{u_j(r_2)}{r_2}.
\end{aligned} \tag{4.54}$$

4.2 Pairing Correlations

4.2.1 BCS equations

The treatment of pairing correlations is very important for the description of the properties of weakly bound nuclei situated close to the drip lines. The HF-BCS (Bardeen-Coopeer-Schrieffer) [Bar57] method and HFB (HF-Bogoliubov) [Rin80, Dec80] method are the commonly adopted approach for treating the pairing correlations. Various effective interactions can be used in the mean field and the pairing channels. In this work the pairing correlations are treated in the BCS approximation with both the zero-range density-dependent and finite range density-dependent forces in the pairing channel.

The formalism of the BCS approximation is based on coupling two nucleons to zero angular momentum through a sum over pairs of states $(k, \bar{k})$, where $\bar{k}$ is the time reversed state of k, and k stands for all quantum numbers which are required to characterize a single particle state:

$$|\bar{k}>=\hat{T}|k>, \tag{4.55}$$

where $\hat{T}$ is the time-reversal operator (see Appendix A.3). This means that the z-components m of the angular momentum j for these states are equal in magnitude and have opposite signs. In the spherical case, the two states are respectively,

$$|k>=|nljm>, |\bar{k}>=|nlj-m>, (m>0) \tag{4.56}$$

The BCS state is given by the product

$$|BCS>=\prod_{k>0}^{\infty}(u_k+v_k a_k^+ a_{\bar{k}}^+)|->, \tag{4.57}$$

where u_k and v_k are variational parameters, $|->$ is the vacuum. In the BCS model, the particles appear in pairs $a_k^+ a_{\bar{k}}^+$. Thus, a single-particle level k is either completely empty, and this occurs with the probability u_k^2, or filled with a pair, in which case the probability is v_k^2. The BCS amplitudes are normalized, one must have

$$|u_k|^2 + |v_k|^2 = 1 \tag{4.58}$$

We can assume that the pairing Hamiltonian $\hat{H}_P$ with pairing interaction of the many-body system can be considered as in Eq. (4.1).The state (4.57) is not an eigenstate of the particle number operator $\hat{N}$. However, one can determine the variational parameters u_k and v_k in such a way that the expectation value of $\hat{N}$ equals the desired number of particles N. This means that, although the BCS ground state does not correspond to a state having a fixed number of particles, it contains on average N particles. This can be achieved by adding a term $-\lambda\hat{N}$ to the pairing Hamiltonian $\hat{H}_P$,

$$\hat{H}' = \hat{H}_P - \lambda\hat{N}, \tag{4.59}$$

where λ is a Lagrange multiplier (sometimes also called the *chemical potential*) which is determined from the requirement

$$< BCS|\hat{N}|BCS >= 2\sum_{k>0} v_k^2 = N. \tag{4.60}$$

Using Eqs. (4.60), one now obtains for the expectation value of $\hat{H}'$ in the BCS ground state

$$< BCS|H'|BCS >= \sum_{k>(<)0} \{(t_{kk} - \lambda)v_k^2 + \frac{1}{2}\sum_{k'>(<)0} \bar{v}_{kk'kk'} v_k^2 v_{k'}^2\} + \sum_{k'k>0} \bar{v}_{k\bar{k}k'\bar{k}'} u_k v_k u_{k'} v_{k'}. \tag{4.61}$$

The variational problem requires

$$\delta < BCS|\hat{H}'|BCS >= 0, \tag{4.62}$$

which yields the system of equations:

$$(\frac{\partial}{\partial v_k} + \frac{\partial u_k}{\partial v_k}\frac{\partial}{\partial u_k}) < BCS|\hat{H}'|BCS >= 0. \tag{4.63}$$

We can write the BCS equations in the form:

$$2\tilde{\epsilon_k} u_k v_k + \Delta_k (v_k^2 - u_k^2) = 0, k > 0. \tag{4.64}$$

Here,

$$\tilde{\epsilon_k} = \frac{1}{2}(t_{kk} + t_{\bar{k}\bar{k}} + \sum_{k'>(<)0} (\bar{v}_{kk'kk'} + \bar{v}_{\bar{k}k'\bar{k}k'}) v_{k'}^2) - \lambda \tag{4.65}$$

and the gap Δ_k is defined as

$$\Delta_k = -\sum_{k'>0} \bar{v}_{k\bar{k}k'\bar{k}'} u_{k'} v_{k'}. \tag{4.66}$$

The only possible solutions v_k^2 and u_k^2 are

$$\begin{aligned} v_k^2 &= \frac{1}{2}\left(1 - \frac{\tilde{\epsilon_k}}{\sqrt{\tilde{\epsilon}_k^2 + \Delta_k^2}}\right) \\ u_k^2 &= \frac{1}{2}\left(1 + \frac{\tilde{\epsilon_k}}{\sqrt{\tilde{\epsilon}_k^2 + \Delta_k^2}}\right). \end{aligned} \tag{4.67}$$

Inserting Eqs. (4.67) into Eq. (4.64), one obtains the so-called *gap equation*

$$\Delta_k = -\frac{1}{2}\sum_{k'>0} \bar{v}_{k\bar{k}k'\bar{k}'} \frac{\Delta_{k'}}{\sqrt{\tilde{\epsilon}_{k'}^2 + \Delta_{k'}^2}}. \tag{4.68}$$

4.2.2 Pairing interactions

The microscopic theory of the pairing interaction has seldom been applied in realistic calculations for finite nuclei [Del95].The pairing interaction obtained from the bare *NN* force with the renormalization procedure (G-matrix) still encounters many problems such as the treatment of the core polarization [Kuc91, Kad87]. Therefore, phenomenological pairing interactions are usually used. There are two open questions in this context: the role of the finite range and the importance of the density dependence. Realistic effective pairing interactions are believed to have a finite range. In fact, the remarkable success of zero range forces (like Skyrme forces) suggests that the effect of finite-range can be mocked up by an explicit velocity dependence. The importance of the density dependence of the pairing interaction can be considered in the theories of superfluidity in neutron stars. As shown in Ref. [Pet95], it is impossible to deduce the magnitude of the pairing gaps in neutron stars with sufficient accuracy. The calculation of the $^1S_0$ pairing gaps in pure neutron matter, or symmetric nuclear matter based on bare NN interaction depends strongly on the forces that are used. In general, the singlet-S pairing is very small at the saturation point.

In this work, we use both the zero-range density dependent and finite-range interactions as pairing interaction. For the finite-range interaction, the effective Gogny D1S interaction [Ber91] or M3Y-P4 interaction [Nak08] (in Eq. 2.26) are used to calculate the pairing field. However, by a specific choice of the exchange contribution, the pairing component of these interactions are density independent. We note that the pairing component of the D1S interaction is repulsive at short distances and attractive at long ranges. In Appendix A.5.1, we show the details of the calculations of pairing matrix element using the finite range interactions.

For the zero-range force in the pairing channel, we utilize the form

$$V(\boldsymbol{r}_1 - \boldsymbol{r}_2) = V_0 F(\boldsymbol{r}) \delta(\boldsymbol{r}_1 - \boldsymbol{r}_2) \tag{4.69}$$

where V_0 is the pairing strength. The pairing parametrization of Eq. 4.69 encompass two types of pairing forces: a pure delta interaction ($F = 1$) that gives rise to volume pairing and a density-dependent delta force that can give rise to surface pairing. In this study, we use the following phenomenological ansatz [Rei99] for the factor F

$$F(\boldsymbol{r}) = 1 - \eta \left(\frac{\rho(\boldsymbol{r})}{\rho_0} \right)^{\alpha} \tag{4.70}$$

where $\rho(\boldsymbol{r})$ is the nuclear density, η and α are parameters that can be adjusted, and ρ_0 is the saturation density (we use $\rho_0 = 0.16$ fm^{-3} in this work).

We can rewrite Eq. (4.70) in the case of the zero-range density-dependent force as

$$V(\boldsymbol{r}_1 - \boldsymbol{r}_2) = V_{eff}(\rho(r))\delta(\boldsymbol{r}_1 - \boldsymbol{r}_2). \tag{4.71}$$

Then the pairing field $\Delta(r)$ can be expressed in term of the pairing density $\kappa(r)$ as

$$\Delta(r) = V_{eff}(\rho(r))\kappa(r) \tag{4.72}$$

where the pairing density $\kappa(r)$ in the BCS model is

$$\kappa(r) = \frac{1}{4\pi}\sum_i u_i v_i |\varphi_(r)|^2. \tag{4.73}$$

Here the factors u_i and v_i correspond to Eq. (4.67).

The pairing matrix elements for both the zero-range density- dependent and finite range density-dependent forces are presented in Appendix A.5. The pairing contribution to the nuclear binding energy in HF-BCS approach is then

$$E^p = -\sum_i \frac{1}{2}\hat{j}_k^2 u_i v_i \Delta_i \tag{4.74}$$

and an important related quantity is the average pairing gap for protons and neutrons which is defined as

$$\overline{\Delta} = \frac{\sum_i \hat{j}_i^2 v_i^2 \Delta_i}{N_{p(n)}} \tag{4.75}$$

where $N_{p(n)}$ is the number of protons or neutrons which is considered.

4.3 Applications to finite nuclear systems

4.3.1 Numerical methods

We start with a description of the techniques used to perform the HF-BCS calculations that we have developed in section 4.2.

As mentioned above, the mesh method where the radial HF equations are solved in coordinate space becomes more difficult in larger boxes or with larger l-values (for example, in calculations of the Wigner-Seitz cells[Neg73]). Therefore, in this work the radial HF equations will be solved either in coordinate space or using a spherical Bessel function basis whenever necessary. The corresponding HF-BCS Fortran codes for two methods are constructed. The flow chart of the code solving radial HF equations in coordinate space is presented in Fig. 4.1. There are two main blocks in the Fortran code: the first one corresponds to the HF calculations and the second is the HF-BCS calculation process itself after reading the initial parameters from the first block such as the HF single-particle energies.

In Fig. 4.1, the starting point in the first block is an initial Woods-Saxon potential. The iterative calculation explained next is done for all proton and neutron occupied orbital. The first wave functions are calculated by solving the HF equations with this potential. Using these wave functions the densities are calculated via Eqs. (4.28, 4.29), from which all potentials are constructed using Eqs. (4.30,4.31,4.32,4.33, 4.34,4.35). The HF equations are solved using the BGW method explained in subsection c.2 of section 4.1.2 and a fourth order Runge-Kutta method given in Appendix A.2 with the chosen boundary conditions (Dirichlet or von Neumann conditions). The obtained wave functions are used to construct the new densities. This procedure is repeated until convergence is reached. The wave functions and the single-particle energies of the first block will be inputs for the second block. The Fermi levels are determined for protons and neutrons. The pairing active space, or BCS pairing window, is chosen for all nuclei to be ± 6 MeV around the Fermi level. After the pairing interaction is chosen, its matrix elements are calculated (Appendix A.5). Then, the gap equations are solved using the routine "C05PBF" of the NAG library [NAG70]. This routine finds a solution of a system of nonlinear equations by a modification of the Powell hybrid method. The occupation probabilities and the gap energies $\triangle_k$ are obtained for each state. Taking these occupation factors v^2 into account, the new densities and potentials are calculated. Afterwards, the HF equations are solved again. One can proceed in this cycle of the second block until reaching the convergence with a chosen accuracy on single-particle energies.

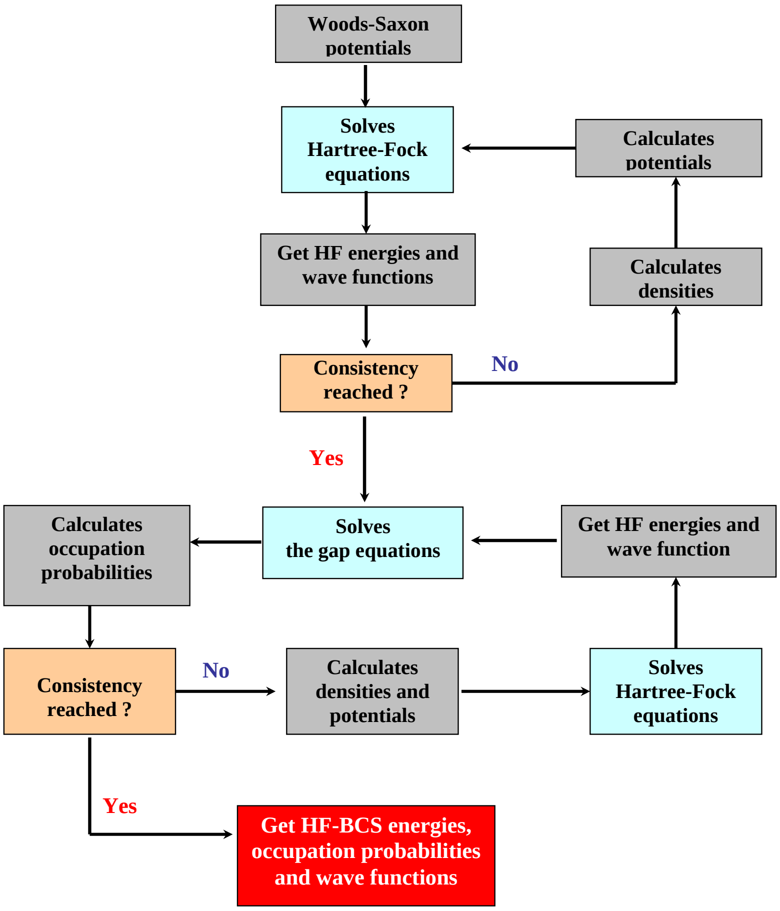

Figure 4.1: Flow chart of the code performing the HF-BCS calculations in coordinate space. There are two main blocks: the first one for the HF calculations and the second one for HF-BCS calculations. The process is iterative until convergence is reached.

The flow chart of the method performing the HF-BCS calculations using a spherical Bessel function basis is presented in Fig. 4.2. There are also two main blocks as in the case of coordinate space. In this method, the basis is built based on the normalized spherical Bessel functions $\tilde{j}_l(k_i^{(l)} r)$ of Eq. 4.42 with two possible boundary conditions. The symmetric matrix $H_{ii'}^{(lj)}$ (4.48) is constructed using the basis $\tilde{j}_l(k_i^{(l)} r)$ and an initial Woods-Saxon potential. This symmetric matrix is then diagonalized using the routine "F02FAF" of the NAG library [NAG70]. The eigenvalues (corresponding to the single-particle energies) and eigenvectors are obtained from this

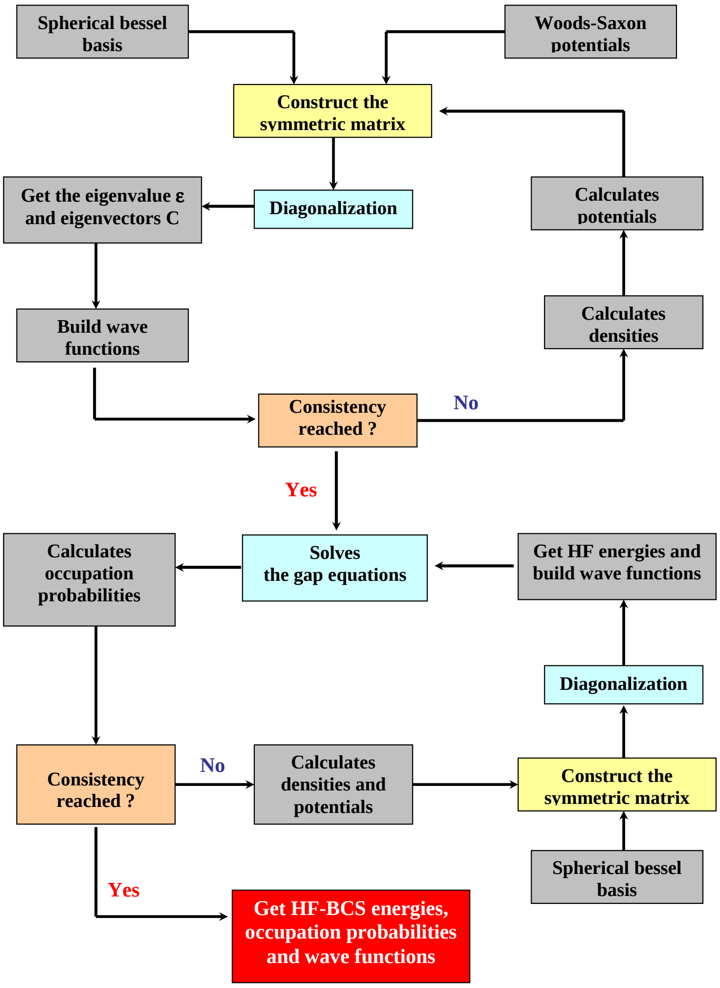

Figure 4.2: The same diagram as in Fig. 4.1, but using a spherical Bessel function basis.

process. The wave functions are constructed from these eigenvectors and the spherical Bessel function basis. A similar process is carried out as in coordinate space case. The difference is only in constructing the symmetric matrix $H_{ii'}^{(lj)}$ and then performing the diagonalization. For the two methods, after a suitable convergence is achieved, the single-particle energies, occupation probabilities, Fermi levels and gap energies are stored in the output files.

In discussing the results, we will call Method 1 and Method 2 the procedure of the solving the HF equations in coordinate space or in the spherical Bessel function basis, respectively.

Table 4.1: Total binding energy and rms matter radius of ^{208}Pb calculated with the different values of the basis dimension N using the D1S interaction.

N	8	10	12	15	18	20
E^{tot} (MeV)	-1629.39	-1640.29	-1641.48	-1642.04	-1642.38	-1642.50
r_m (fm)	5.547	5.516	5.514	5.512	5.511	5.510

4.3.2 Doubly magic nuclei

We now present the results obtained with the finite spherical nuclei by solving the HF equations in coordinate space (Method 1) or using the spherical bessel basis (Method 2), with the finite range density dependent interactions, such as D1S [Ber91] or M3Y-P4 [Nak08]. We should note that the center of mass corrections (Eq. 4.49) have been taken into account in our calculations. The effect of the one-body term is included in the kinetic term before iteration. The contribution of the two-body term is subtracted from the convergent wave functions. The exchange term (Eq. 4.35) from the Coulomb force is treated into account also.

In the HF-BCS approach, the total binding energy is calculated in the following form

$$E^{tot} = E^{HF} + E^{R} + E_2^{c.m.} + E^{p} \tag{4.76}$$

where $E^{HF} = \frac{1}{2}\sum_i (t_i + \epsilon_i)$; t_i and ϵ_i denote the single-particle kinetic energies and single-particle energies, respectively. E^R is the rearrangement energy coming from the density dependence of the interaction. $E_2^{c.m.}$ is the two-body center of mass correction of Eq. (4.53), and E^p is the pairing energy given in Eq. (4.74). Of course, the pairing contribution vanishes in the case of doubly magic nuclei.

The charge density can be obtained from the calculated proton distribution, after correction into account the finite size of the proton. Following Ref. [Vau72], the charge distribution $\rho_c(\boldsymbol{r})$ can be calculated as

$$\rho_c(\boldsymbol{r}) = \int f_p(\boldsymbol{r} - \boldsymbol{s})\rho_p(\boldsymbol{s})d\boldsymbol{s} \tag{4.77}$$

Table 4.2: Total energies E^{tot}, rearrangement energies E^{R} and the contribution of the two-body term coming from C.M. corrections $E_2^{c.m.}$ of some doubly magic nuclei. M1 and M2 correspond to Method 1 and Method 2, respectively (see text for more details). Experimental data are taken from Ref. [Aud95]. All energies are in MeV.

		D1S (M1)	D1S (M2)	D1N (M1)	M3Y-P4 (M1)	Exp.
^{16}O	E^{tot}	-129.78	-129.77	-128.19	-125.28	-127.62
	E^{R}	-59.81	-59.90	-70.91	-57.73	
	$E_2^{c.m.}$	-4.80	-4.81	-4.81	-4.80	
^{40}Ca	E^{tot}	-346.23	-346.20	-344.03	-344.23	-342.05
	E^{R}	-178.53	-178.60	-216.62	-170.38	
	$E_2^{c.m.}$	-6.59	-6.60	-6.65	-6.52	
^{48}Ca	E^{tot}	-416.82	-416.80	-413.51	-411.51	-415.99
	E^{R}	-226.37	-226.57	-263.24	-222.42	
	$E_2^{c.m.}$	-9.56	-9.57	-9.56	-9.55	
^{90}Zr	E^{tot}	-787.31	-787.28	-782.40	-773.51	-783.90
	E^{R}	-458.28	-458.46	-533.28	-445.12	
	$E_2^{c.m.}$	-9.83	-9.84	-9.83	-9.76	
^{132}Sn	E^{tot}	-1105.30	-1105.26	-1106.45	-1095.40	-1102.90
	E^{R}	-676.10	-676.36	-787.85	-663.669	
	$E_2^{c.m.}$	-11.61	-11.61	-11.67	-11.51	
^{208}Pb	E^{tot}	-1642.55	-1642.50	-1642.27	-1632.10	-1636.44
	E^{R}	-1091.17	-1091.37	-1267.26	-1066.54	
	$E_2^{c.m.}$	-11.03	-11.03	-11.05	-10.93	

where the proton distribution is folded with the Gaussian form factor

$$f_p(\boldsymbol{r}) = \frac{1}{(r_0\sqrt{\pi})^3}\exp(-r^2/r_0^2), \quad r_0^2 = 0.65fm^2 \tag{4.78}$$

We first discuss briefly the accuracy of the HF calculations using the spherical Bessel basis method. In the definition (4.41) we have to choose the number N of basis states. The calculations of ^{208}Pb have been performed with the different N values (from 8 to 20). The total energies and root mean square (rms) are shown in Table 4.1. One observes that the increase of binding energy is about 1.19 MeV when N increases from 10 to 12 and about 0.12 MeV for N from 18 to 20. Furthermore, it was checked on other nuclei that energies and radii do not change significantly when increasing the dimension of the basis N from 18 to 20. Therefore, the value $N = 20$ will be used in our further calculations.

In Table 4.2, we show the total energies E^{tot} , the rearrangement energy E^R and the contribution of the two-body term coming from C.M. corrections $E_2^{c.m.}$ of doubly magic nuclei using different finite-range interactions. The new set D1N Gogny interaction [Cha08] is also used in our calculations. The calculations are performed with the two methods as mentioned above. One can observe that, the difference of the results obtained with the two methods is very small as illustrated by the second and the third columns of Table 4.2. The differences are only 0.01 MeV in ^{16}O and 0.05 MeV in ^{208}Pb for the total energy. The results obtained with D1N interaction are similar with those of D1S. The difference is less than 0.07%. The M3Y-P4 interaction reproduces the total energies moderately well. The maximum difference is $\sim$ 10.4 MeV ($\sim$ 1.3%) for ^{90}Zr in comparison with the experimental data. From Eq. (4.76) we see that the E^{HF} term is the most important contribution to the total energy, since it already includes the large cancellation between kinetic and potential energies. The rearrangement energy E^R is the next most important. It continues to increase up through the heavy nucleus ^{208}Pb. In particular, its contribution to the total energy is from $\sim$46% in ^{16}O to $\sim$66% in ^{208}Pb with D1S and M3Y-P4 interactions , and from $\sim$55% to $\sim$77% with the D1N interaction. Therefore, the contribution of the rearrangement term is crucial for a good fit to the binding energy. The contributions

Table 4.3: Same as Table 4.2, but for neutron, proton, charge and mass root mean square radii $r =< r^2 >^{1/2}$. Experimental charge radii are taken from Ref. [Ott89]. All radii are in fm.

		D1S	D1S	D1N	M3Y-P4	Exp.
		(M1)	(M2)	(M1)	(M1)	
^{16}O	r_n	2.638	2.636	2.622	2.632	
	r_p	2.660	2.659	2.644	2.654	
	r_{ch}	2.777	2.777	2.761	2.771	2.73
	r_m	2.649	2.647	2.633	2.643	
^{40}Ca	r_n	3.357	3.357	3.341	3.362	
	r_p	3.402	3.402	3.385	3.407	
	r_{ch}	3.494	3.493	3.477	3.499	3.49
	r_m	3.380	3.379	3.362	3.385	
^{48}Ca	r_n	3.577	3.576	3.576	3.557	
	r_p	3.433	3.432	3.424	3.429	
	r_{ch}	3.524	3.523	3.516	3.520	3.48
	r_m	3.518	3.517	3.513	3.504	
^{90}Zr	r_n	4.262	4.261	4.257	4.255	
	r_p	4.203	4.202	4.196	4.205	
	r_{ch}	4.278	4.277	4.271	4.279	4.27
	r_m	4.236	4.235	4.230	4.233	
^{132}Sn	r_n	4.835	4.835	4.825	4.824	
	r_p	4.643	4.643	4.622	4.653	
	r_{ch}	4.771	4.771	4.690	4.720	
	r_m	4.764	4.764	4.749	4.760	
^{208}Pb	r_n	5.564	5.563	5.561	5.554	
	r_p	5.428	5.428	5.418	5.437	
	r_{ch}	5.486	5.486	5.476	5.495	5.50
	r_m	5.511	5.511	5.505	5.508	

of the two-body C.M. correction are presented in Table 4.2. In the lighter nuclei, such as ^{16}O, the correction contributes about 3.7% to the total energy, and in the heavy nuclei it contributes about 0.6% to the total energy. The root mean square radii of the proton, neutron, charge and matter distributions are displayed in Table 4.3. The charge distribution is obtained from the proton density following the Eq. (4.77). Experimental values of charge radii are shown for comparison. All results obtained with these considered interactions are in good agreement with the experimental data.

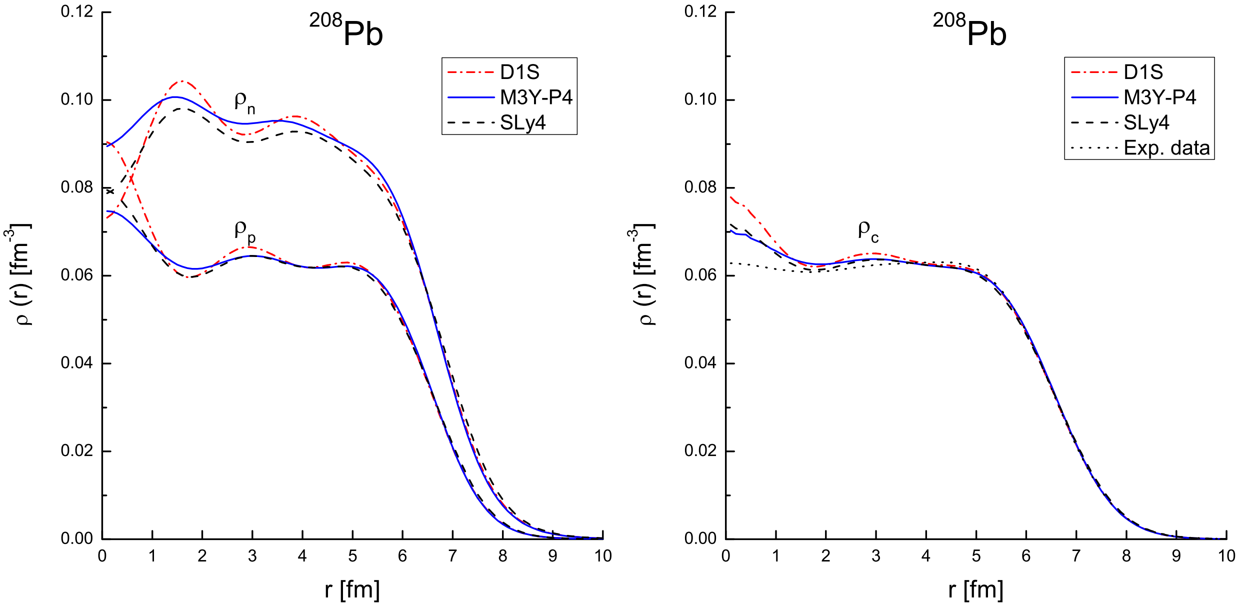

Figure 4.3: The neutron, proton (left panel) and charge (right panel) densities of ^{208}Pb obtained with D1S [Ber91], M3Y-P4 [Nak08], and SLy4 [Cha98, Ben05] interactions. The experimental data of charge density are extracted from electron scattering experiment [Vri87].

We now comment, in particular, on the results concerning ^{208}Pb. On the left panel of Fig. 4.3, the neutron, proton densities distributions are shown. On the right panel, the calculated charge density is plotted together with the experimental charge density extracted from electron scattering experiment [Vri87] for comparison. In this case, the SLy4-Skyrme interaction is also used for comparison. The numerical calculation with SLy4 interaction is taken from Ref. [Ben05]. The SLy4 interaction will be also used in subsection 4.3.5 for Wigner-Seitz cells calculations. On the left panel of Fig. 4.3, the oscillations of the predicted neutron and proton densities obtained with D1S interaction are larger than those from M3Y-P4 and SLy4 interactions, and there is a bump in the center of the nucleus for the calculated ρ_p. This bump is due to the $3s_{1/2}$ proton state which contributes at least 50% of the central density. The charge distributions are also displayed on the right panel of Fig. 4.3. In Ref. [Bla77] it was shown by Gogny et al. that the effects of RPA-type correlations can reduce somewhat this $3s_{1/2}$ bump.

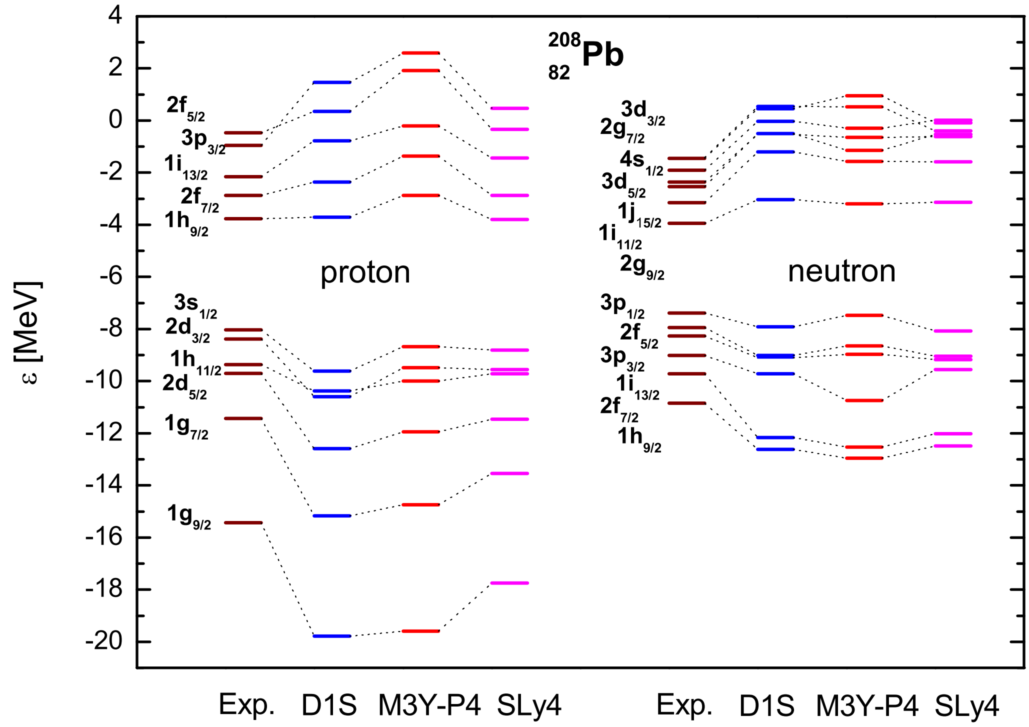

Figure 4.4: Proton and neutron single-particle energies in ^{208}Pb near the Fermi level calculated with D1S [Ber91], M3Y-P4 [Nak08], and SLy4 [Cha98] interactions. Experimental data are taken from Ref. [NNDC].

The single-particle energies of protons and neutrons in ^{208}Pb around the Fermi are shown in Fig. 4.4. The experimental single-particle energies of these states are obtained from the states of the neighboring nuclei: ^{207,209}Pb, ^{207}Tl and ^{209}Bi [NNDC]. Except for a ($2d_{3/2}$,$1h_{11/2}$) inversion with the D1S interaction, the order of the other proton levels is found to be correct. In HF calculations the values of the shell gap between ($1h_{9/2}$,$3s_{1/2}$) in protons and ($2g_{9/2}$,$3p_{1/2}$) in neutrons are larger than the experimental ones. In particular, the proton shell gap is 5.90, 5.80 and 5.01 MeV with D1S, M3Y-P4 and SLy4 interactions, respectively, whereas the experimental value is 4.26 MeV. For neutrons, the experimental shell gap is 3.44 MeV, while the corresponding values with D1S, M3Y-P4 and SLy4 interactions are 4.88, 4.29 and 4.93 MeV. One can conclude that the results obtained with all considered effective interactions are in good agreement with the experimental values, both for protons and neutrons, as viewed in Fig. 4.4.

4.3.3 Sn isotopes

Using the HF-BCS approach we ave performed a comparison study of Sn isotopes using the two finite-range interactions D1S and M3Y-P4. The Sn isotopes are of particular interest for nuclear structure and astrophysical issues, because of the closure of the $Z = 50$ proton shell. Here again, we have checked that our Methods 1 and 2 give very similar results.

Fig. 4.5 displays, on the left panel, the energy per nucleon of $^{110-140}$Sn nuclei using D1S and M3Y-P4 interactions in both mean field and pairing channels. The results obtained with HFB calculations with D1S interaction in Ref. [Hil06] are plotted for comparison. The experimental data taken from Ref. [Aud95] are also displayed. One observes that the difference between the results of D1S + HF-BCS (this work) and D1S + HFB [Hil06] calculations are very small, about 0.3%. we should note that D1S + HFB calculations are performed in Refs. [Ber91, Hil06] using harmonic oscillator basis. In fact the results obtained with D1S + HF-BCS calculations are in good agreement with the experimental values in $N < 78$ and $N = 84$. The results obtained with M3Y-P4 interaction are lying above the curve of the experimental values. The difference is about 1.7% in the region of $N < 80$ and 0.9% for $N \geq 80$. We recall that

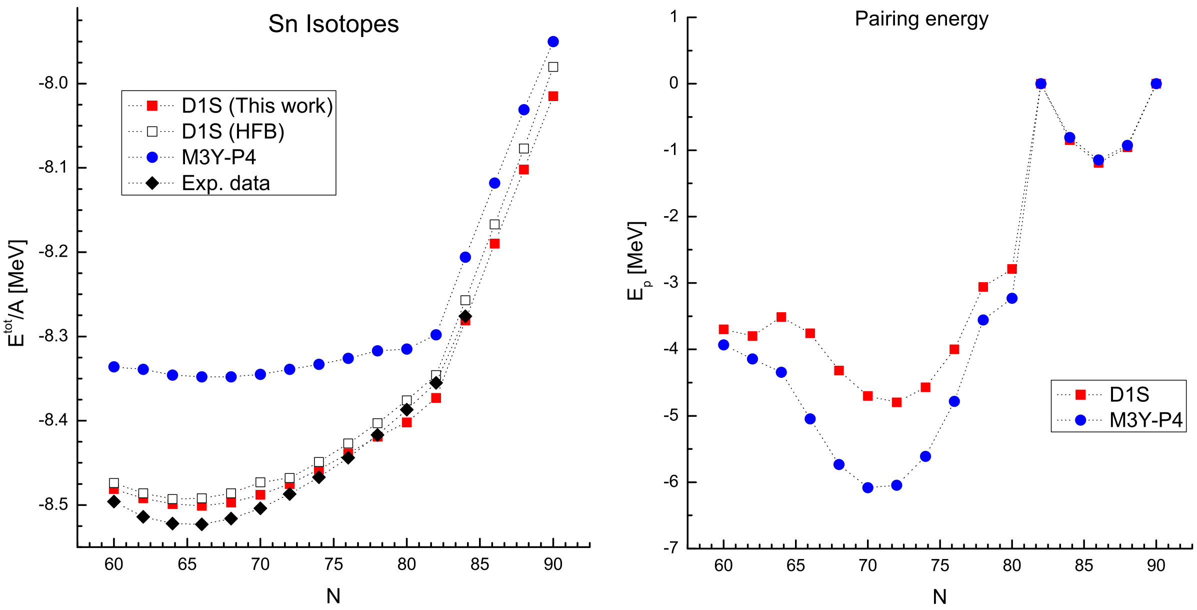

Figure 4.5: On the left panel, energy per nucleon of tin isotopes obtained with D1S and M3Y-P4 interactions in HF-BCS approach, in comparison with the results of D1S-HFB calculation of Ref. [Hil06] and the experimental data [Aud95]. On the right panel, the pairing energy calculated with D1S and M3Y-P4 interactions in HF-BCS approach. Dotted lines are drawn to guide the eye.

the M3Y-P4 interaction does not contain the tensor term [Nak08]. The other versions of M3Y-type interaction (such as M3Y-P3 and -P5) have the realistic tensor part. The contribution of the tensor part can give a good agreement with the experimental data of the different energy between two proton states, such as $\varepsilon_p(1g_{7/2}) - \varepsilon_p(2d_{5/2})$ or $\varepsilon_p(1h_{11/2}) - \varepsilon_p(2d_{5/2})$ (see Fig. 14 in Ref. [Nak08]).

On the right panel of Fig. 4.5, the contribution of the pairing effects to the total energy are presented. The maximum difference of pairing energies obtained with D1S and M3Y-P4 interactions is at $N = 70$, corresponding to ^{120}Sn. The reason of this difference is an inversion between $2d_{3/2}$ and $1h_{11/2}$ neutron orbitals. In HF calculations, the $1h_{11/2}$ neutron orbital is predicted to move significantly above the $2d_{3/2}$ state, and then the $2d_{3/2}$ neutron orbital is fully filled with the D1S interaction. The shell gap of $(2d_{3/2}, 1h_{11/2})$ states is 0.79 MeV in this case. In contrast, the $2d_{3/2}$

neutron orbital is located above the $1h_{11/2}$ state with M3Y-P4 interaction, leading to 4 neutrons occupying the $1h_{11/2}$ orbital in ^{120}Sn. The corresponding shell gap is 0.704 MeV. The difference of the two pairing energies will decrease when N increases. Since the last $1h_{11/2}$ ($2d_{3/2}$) neutron orbital is fully filled at $N = 82$ with D1S (M3Y-P4) interaction, the two sets of pairing energies reach to the value zero, related to the doubly magic nucleus ^{132}Sn. One can conclude that the M3Y-P4 interaction gives stronger pairing than D1S in the region $60 \leq N \leq 80$. In the highly neutron-rich region ($N \geq 82$), the difference in pairing channel between M3Y-P4 and D1S interactions is not quite significant. The neutron shell closure is predicted at $N = 90$ with these interactions.

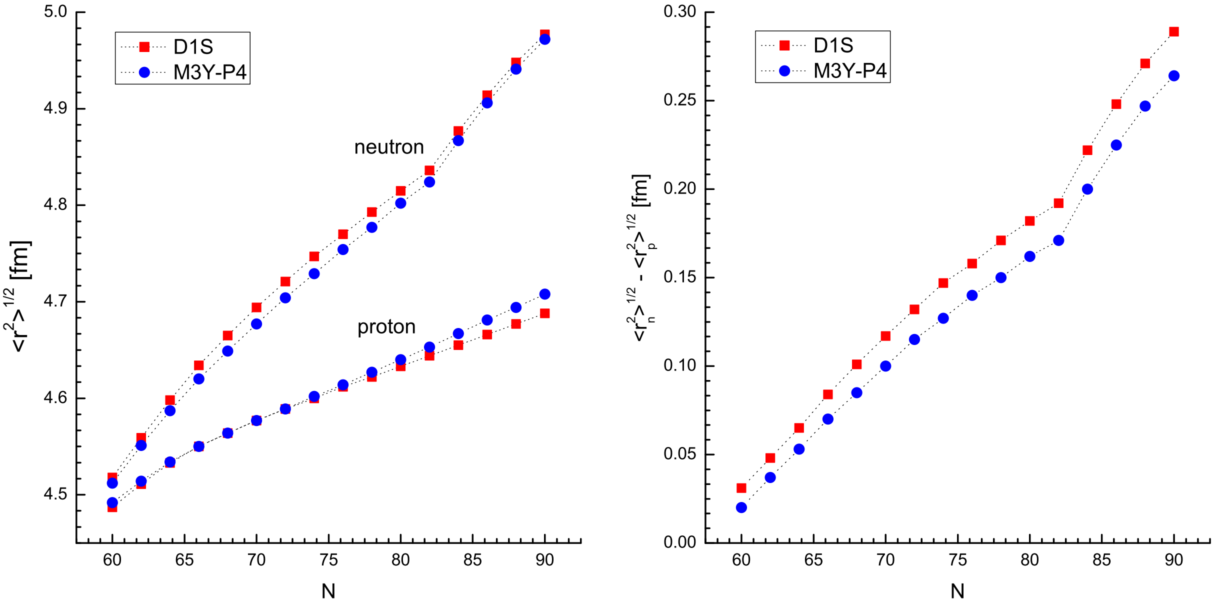

Figure 4.6: Root mean square radii of tin isotopes (on the left panel) and the difference of the root mean square radii of neutrons and protons (on the right panel) obtained with D1S and M3Y-P4 interactions in HF-BCS approach. Dotted lines are drawn to guide the eye.

The root mean square radii of the $^{110-140}$Sn nuclei obtained with HF-BCS calculations with D1S and M3Y-P4 interactions are shown in Fig. 4.6. The difference of the rms radii of neutron and proton are displayed for comparison. The neutron skin thickness is observed on the right panel of Fig. 4.6. An appreciable layer of neutron matter is found about 0.29 fm beyond the proton distribution in $N = 90$, which is a factor of 1.2 larger than the neutron skin in ^{208}Pb. The same phenomenon is predicted also by the M3Y-P4 interaction except for a somewhat smaller neutron excess radius. The increase of the rms neutron radius is directly related to the shell structure in the heavy tin isotopes. The $1h_{11/2}$ and $2d_{3/2}$ neutron orbital are fully filled with D1S and M3Y-P4 interactions at $N = 82$, respectively. The pairing effects do not contribute in this nucleus.

4.3.4 Bubble nuclei

The study of the possible *bubble* structure of atomic nuclei was started by Wilson in 1946 [Wil46], when he studied the low-lying excitations of a thin spherical shell. The bubble nuclei are characterized by a depletion of their central density. The possibility of bubble nuclei was investigated by Bethe and Siemens in the 60s [Sie67], and by Campi and Sprung using a microscopic framework in the 70s [Cam73]. The bubble nuclei were also studied with the liquid drop model [Swi83] and Thomas-Fermi approaches [Boh76]. More recently, bubbles nuclei were discussed in super-heavy and hyper-heavy nuclei [Dec03, Ben03].

We know that only the s state can contribute to the density at $r = 0$, so that the depopulation of this state leads to a depletion of the central density. The other single-particle states, which have non-zero angular momenta, are suppressed in the center of the nucleus and do not give appreciable contributions to the central density. In some nuclei, the s state can be inverted with the neighbouring states. These nuclei can be considered as bubble candidates if their highest s state is depopulated. Indeed, the nuclei can be bubble candidates for protons or neutrons if there is an inversion between ($2s_{1/2}$,$1d_{3/2}$) states or ($3s_{1/2}$, $1h_{11/2}$) states. In the case of proton bubbles, the Ar and Hg isotopes can be considered, and ^{34}Si can be a possible proton bubble candidate with $Z = 14$. In the case of neutron bubbles, the above inversions correspond to the $N = 18$ and $N = 80$ isotones. In Ref. [Cav82], the contribution of the $3s$ state has been measured using electron scattering from ^{206}Pb and ^{205}Tl. However, because of the $1s_{1/2}$ and $2s_{1/2}$ orbitals that are already occupied and contribute to the central density, the depletion in the interior of these nuclei is small. In general, the depletion fraction in the bubble nuclei can be defined as [Gra09]

$$F \equiv \frac{\rho_{max} - \rho_c}{\rho_{max}} \tag{4.79}$$

where ρ_{max} and ρ_c are the maximum value and the central value of the density. Thus, in the case of ^{205}Tl, the value of the depletion fraction is only F $\sim$ 11% [Cav82]. Recently, possible proton bubbles due to the depletion of the $2s_{1/2}$ state have been discussed in ^{34}Si [Gra09], ^{46}Ar [Kha08, Tod04] and in neutron-rich ^{68}Ar [Kha08], and a neutron bubble in ^{22}O [Gra09]. In the case of ^{46}Ar, an inversion between s and d states was predicted using the relativistic mean field approach [Tod04] and non-relativistic Skyrme model [Kha08] with the SkI5 interaction. However, pairing effects could preclude the bubble effect due to the partial occupancy of the $2s_{1/2}$ state. For the case of neutron-rich ^{68}Ar, the $2s_{1/2}$ state of proton is also predicted to move above the $1d_{3/2}$ state [Kha08] if one uses the SkI5 interaction. The pairing effects cannot prevent the bubble structure in this case. But we should note that no-bubble structure of ^{46}Ar and ^{68}Ar can be obtained if the SLy4 interaction used. In Ref. [Gra09], the bubble structures of ^{34}Si and ^{22}O are discussed in the shell-model calculations, in non-relativistic HF and HFB approaches, in relativistic mean field (RMF) and relativistic Hartree-Bogoliubov (RHB) calculations.

It should be noted that the deformation can play against a bubble occurrence. However, the HFB models using Skyrme and Gogny interactions predict a spherical shape for ^{34}Si [Gra09, Hil06] and a soft nucleus for ^{46}Ar (see in Ref. [Kha08] and references therein). Indeed ^{46}Ar is predicted either spherical or with a small deformation parameter in the ground state. More neutron-rich Argon are also predicted spherical in Refs. [Kha08, Hil06]. In the following we will consider the spherical case for ^{34}Si, ^{22}O, ^{46}Ar and ^{68}Ar nuclei in order to study the bubble structures using the finite-range density-dependent interactions (Gogny [Ber91, Cha08] or M3Y-P4 [Nak08] interactions) in non-relativistic HF and HF-BCS approaches. In our HF-BCS approach, the same finite-range density dependent interaction (either D1S (D1N) or M3Y-P4) is used in both mean field and pairing channels.

a-Neutron bubble in ^{22}O

The nucleus ^{22}O can be a good candidate for a neutron bubble nucleus because of the $2s_{1/2}$ neutron state. As shown in Refs. [Sta04, Sch07, Ele07, Thi00, Bec06, Hof08], the neutron subshell closure happens at N =14 and 16 in Oxygen isotopes, corresponding to ^{22}O and ^{24}O nuclei. Since the $2s_{1/2}$ state is located between $1d_{5/2}$ and $1d_{3/2}$ states, then the ^{22}O and ^{24}O nuclei are considered as doubly magic nuclei.

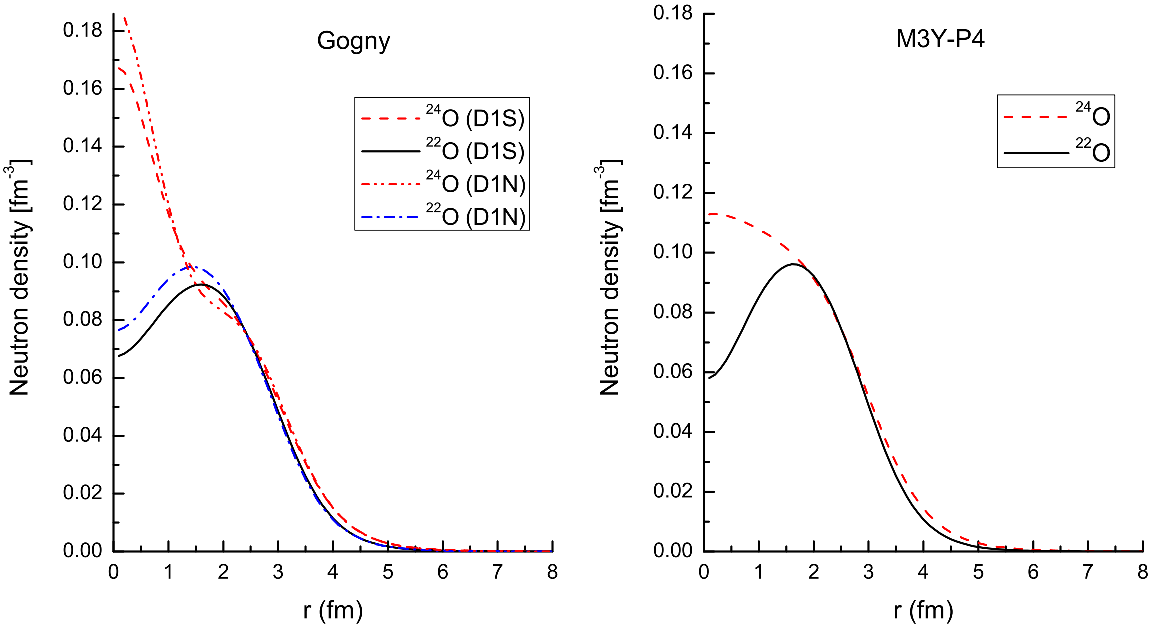

Figure 4.7: Neutron densities of ^{22}O (solid curve) and ^{24}O (dashed curve) obtained with Gogny D1S [Ber91], D1N [Cha08] and M3Y-P4 [Nak08] interactions in HF approach.

In Fig. 4.7, the neutron densities of ^{22}O (solid curve) and ^{24}O (dashed curve), obtained with Gogny D1S [Ber91], D1N [Cha08] and M3Y-P4 [Nak08] interactions in HF approach, are plotted. One can see that with the D1S and D1N interactions, the $2s_{1/2}$ neutron orbital is occupied in ^{24}O, and it makes the central neutron density in

^{24}O to be strongly enhanced, even stronger than the results obtained with SLy4-HF approach (see Fig. 3 in Ref. [Gra09]). The calculated value of the depletion fraction ^{22}O is F = 27% and 22% with D1S and D1N interactions , in very good agreement with the value obtained from shell-model calculations, and RMF and RHB approaches (see Table IV of Ref. [Gra09]). With the M3Y-P4 interaction, the central depletion fraction F ^{22}O is 40%, much stronger than with the D1S and D1N interactions. We know that the pairing correlations can have some effect on the density profiles. We therefore repeat the calculations in HF-BCS approach. We found that the values of the shell gap between $1d_{5/2}$ and $2s_{1/2}$ is 3.6 (3.0) MeV in ^{22}O, and between $2s_{1/2}$ and $1d_{3/2}$ it becomes 4.5 (4.6) MeV in ^{24}O with the D1S (D1N) interaction. On the other hand we obtained a shell gap between $1d_{5/2}$ and $2s_{1/2}$ of 4.9 MeV in ^{22}O, and 4.5 MeV between $2s_{1/2}$ and $1d_{3/2}$ in ^{24}O with the M3Y-P4 interaction. Therefore, the pairing effects are found to collapse in ^{22}O and ^{24}O when the D1S (D1N) and M3Y-P4 interactions are used. These results confirm again the neutron shell closure at N =14 and 16 in Oxygen isotopes and one can conclude that the ^{22}O nucleus is a good candidate for a neutron bubble nucleus. One notes that the neutron bubble structure in ^{22}O can disappear in SLy4-HFB calculations [Gra09]. In this case, the pairing effects modify the occupancy of the $2s_{1/2}$ state, thus reducing the predicted neutron bubble structure in ^{22}O. The shell-model calculations [Gra09] predict a 17% occupancy factor of the $2s_{1/2}$ neutron state, thus showing that pairing correlations can give some effect on this nucleus. However, the experimental values for the occupancy factor of this state are not yet available.

b-Proton bubbles in ^{34}Si, ^{46}Ar and ^{68}Ar

Proton bubble in ^{34}Si:

As shown in Ref. [Sor08], the proton sub-shells are closed at $Z = 14$ and $Z = 16$, and the $2s_{1/2}$ proton orbital state is located between $1d_{5/2}$ and $1d_{3/2}$ states. Therefore, the $2s_{1/2}$ proton orbital may be unoccupied in ^{34}Si nucleus ($Z = 14$, $N = 20$), whereas it is fully filled in ^{36}S nucleus ($Z = 16$, $N = 20$). Thus, the ^{34}Si nucleus might be a good candidate for a proton bubble nucleus. Here, we analyze the structure of the proton density in ^{34}Si and ^{36}S.

The proton densities of ^{34}Si and ^{36}S obtained with the Gogny D1S, D1N and M3Y-P4 interactions in HF approach are plotted in Fig. 4.8. The central depletion fractions F of the proton density in ^{34}Si are 55%, 60% and 37% with D1S, D1N and M3Y-P4 interactions, respectively. The values of the depletion factor F with D1S and D1N interaction are larger than that obtained with SLy4 interaction [Gra09]. The result obtained with M3Y-P4 interaction is in good agreement in comparison with all the predicted values in Table IV of Ref. [Gra09]. One observes from Fig. 4.8 that the proton density of ^{34}Si is significantly depleted in the interior of the nucleus, and when the $2s_{1/2}$ proton orbital is filled in ^{36}S the proton bubble disappears immediately.

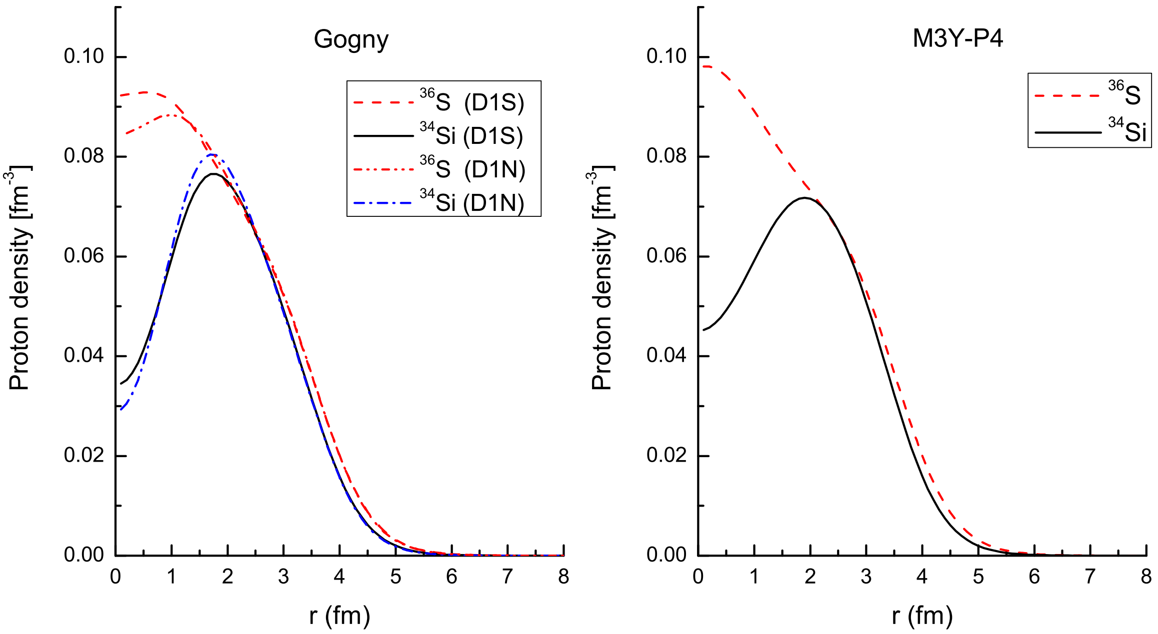

Figure 4.8: Proton densities of ^{34}Si (solid curve) and ^{36}S (dashed curve) obtained with Gogny D1S [Ber91], D1N [Cha08] and M3Y-P4 [Nak08] interactions in HF approach.

As mentioned above, the pairing effects may hinder the bubble structure of the nucleus. The occupancy of the $2s_{1/2}$ state may be modified due to the pairing effects and the depletion in the center of the nucleus may decrease. Therefore, we need to consider the ^{34}Si nucleus in HF-BCS approach. Because of the large gaps between the $1d_{5/2}$ and $2s_{1/2}$ states (5.5 & 5.1 MeV with D1S & D1N interactions and 6.0 MeV with M3Y-P4 interaction), we find a pairing collapse in ^{34}Si if the D1S (D1N) or M3Y-P4 interactions are used in the pairing channel. One notes that, because of the magiciy of $N = 20$ in ^{34}Si the pairing correlations do not make any effect on the neutron density. Together with the results obtained in Ref. [Gra09], where the proton bubble structure of ^{34}Si is studied in a shell model approach as well as in non-relativistic approaches (HF and HFB) and relativistic approaches (RMF and RHB), our predictions with finite-range interactions, lead to the conclusion that ^{34}Si nucleus is an excellent candidate for a proton bubble structure. It would be interesting to have experimental confirmation from future elastic scattering experiments medium energy electron beam or by direct reactions as suggested in Ref. [Kha08].

Proton bubbles in ^{46}Ar and ^{68}Ar:

For the case of ^{46}Ar, the calculations using RMF predict a strong depletion in the central proton density, the depletion factor F being around 63% (see Fig. 1 in Ref. [Tod04]). Recently, a proton bubble is also found with the SkI5 interaction in non-relativistic HFB calculations, with a depletion fraction F around 48% in the HF approach (see Fig. 1 in [Kha08]). However, the bubble effect decreases with the pairing effects. In this subsection, we will analyze the proton bubble in ^{46}Ar (and in ^{68}Ar also) using the finite range interactions in the HF-BCS approach.

The proton densities calculated in ^{46}Ar and ^{68}Ar using Gogny D1S(D1N) and M3Y-P4 interactions in HF calculations are shown in Fig. 4.9. One observes that there is no bubble effect in the proton density in ^{46}Ar with the D1S (D1N) interaction (left side of Fig. 4.9). In this case, the $2s_{1/2}$ proton state is fully filled. However, a depletion in the central proton density is obtained in ^{68}Ar with the D1S and D1N interactions. The effect of the inversion between s and d states in neutron-rich nuclei has been analyzed in Ref. [Gra07], in which the increase of the gap between the inverted $s_{1/2}$ and $d_{3/2}$ states is found in neutron-rich nuclei. Therefore, this effect supports the possibility of a proton bubble in the neutron-rich ^{68}Ar nucleus. As a result, the central depletion fraction F is 50% and 60% in ^{68}Ar with the D1S and D1N interactions, respectively. In contrast, the bubble effects on the proton density are obtained both in ^{46}Ar and ^{68}Ar with the M3Y-P4 interaction (right side of Fig.

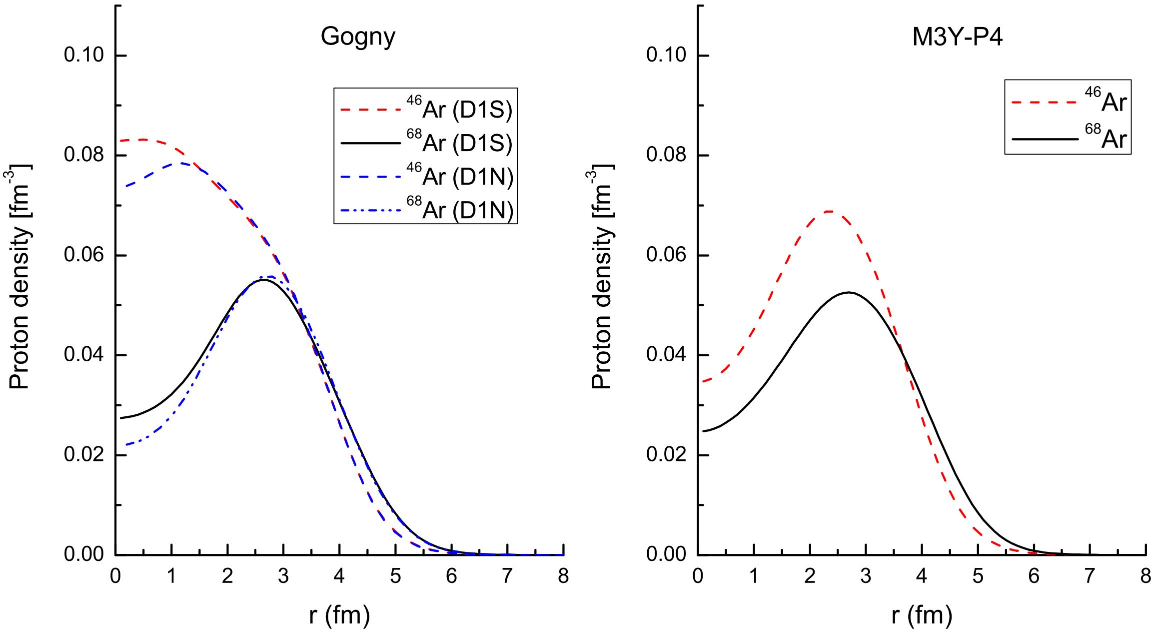

Figure 4.9: Proton densities of ^{46}Ar (dashed curve) and ^{68}Ar (solid curve) obtained with Gogny D1S [Ber91], D1N [Cha08] and M3Y-P4 [Nak08] interactions in HF approach.

4.9). A strong depletion in the central proton densities is predicted and the depletion factors F are 50% and 53% in ^{46}Ar and ^{68}Ar, respectively. These numbers are in good agreement with the non-relativistic predictions of F $\sim$ 48% in ^{46}Ar and $\sim$ 60% in ^{68}Ar with SkI5 interaction [Kha08].

As discussed in Ref. [Kha08], the pairing correlations can reduce the bubble effect on proton densities in ^{46}Ar and ^{68}Ar. In particular, a Skyrme-HFB calculation was performed on ^{46,68}Ar using a zero-range density-dependent pairing interaction, leading to a small depletion in the center of the proton densities. In contrast, we use in this work a finite range interaction in the pairing channel. The HF-BCS proton densities of ^{46}Ar and ^{68}Ar are plotted in Fig. 4.10. With the D1S interaction, because of the pairing effect the $2s_{1/2}$ proton state is depopulated in ^{46}Ar and the occupancy of this state is only 74%. We thus see that the central value of the HF proton density (Fig. 4.9) is much higher than that of HF-BCS proton density in ^{46}Ar (Fig. 4.10). In the

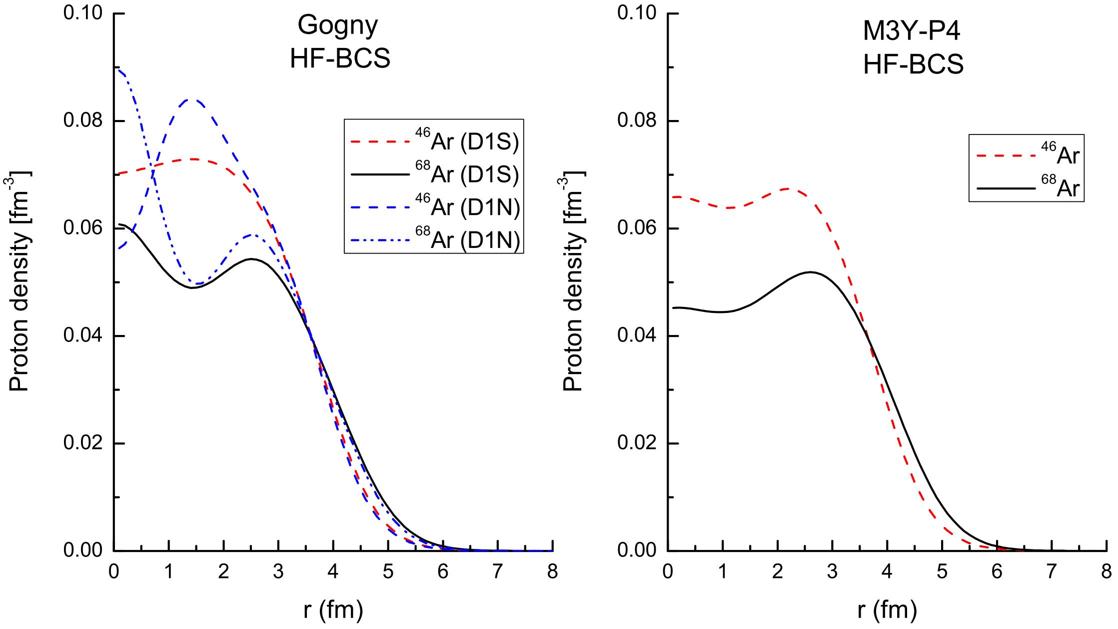

Figure 4.10: Proton densities of ^{46}Ar (dashed curve) and ^{68}Ar (solid curve) obtained with Gogny D1S [Ber91], D1N [Cha08] and M3Y-P4 [Nak08] interactions in HF-BCS approach.

case of D1N interaction, because of the depopulation of the $2s_{1/2}$ proton state, there is a hole in the center proton density of ^{46}Ar. In ^{68}Ar, the pairing effects modify the occupancy of the $2s_{1/2}$ proton state which is found to be 52% (60%) with D1S (D1N) interaction. The central hole in proton density in ^{68}Ar is completely washed out with D1S (D1N) interaction. With the M3Y-P4 interaction, the $2s_{1/2}$ proton state occupations are predicted to be 51% in ^{46}Ar and 37% in ^{68}Ar. The corresponding proton densities are displayed on the right side of the Fig. 4.10. One observes that a depletion is still predicted in the central proton density in ^{68}Ar.

These above results indicate that a proton bubble in ^{46}Ar is not certain. The no-bubble structure of the proton density can be obtained with the D1S and M3Y-P4 interaction in HF-BCS approach (see Fig. 4.10). In Ref. [Kha08] it is also shown that the bubble effect disappears with SLy4 interaction or SkI5 interaction in HFB approach. The pairing interaction can modify the occupancy of the $2s_{1/2}$ and $1d_{3/2}$

states. Thus, experiments to measure these occupation probabilities are needed. In the case of ^{68}Ar, the depletion in the center of the nucleus vanishes due to the pairing effect in HF-BCS calculations with the D1S and D1N interactions. However, the pairing effect cannot prevent a proton bubble with M3Y-P4 interaction. As discussed in Ref. [Gra07], the possibility of an inversion between the $2s_{1/2}$ and $1d_{3/2}$ proton states will increase when going to the neutron-rich nuclei in Calcium isotopes. This effect leaves a possibility for a proton bubble in very neutron-rich Argon isotopes such as ^{68}Ar.

4.4 Inner crust of neutron stars

As mentioned in section 4.1.3, the method 1 where the HF equations are solved in coordinate space is difficult to apply to the Wigner-Seitz (WS) cells of the inner crust of neutron stars because large cell radii and high values of orbital momenta l are required. Therefore, the method 2 was developed with a basis expansion method to circumvent these difficulties. In this work, a spherical Bessel function basis is chosen.

In recent years, the properties of the inner crust of neutrons stars have been investigated using various frameworks, especially focusing on the microscopic structure and the superfluid properties. The microscopic calculations of the inner crust matter are usually studied in the WS approximation [Neg73, Pet95]. Following the standard approaches, the inner crust consists of a lattice of WS cells, each cell containing a neutron-rich nucleus immersed in a sea of dilute gas of neutrons and relativistic electrons uniformly distributed inside the cell [Pet95].The first microscopic calculations of the properties of the inner crust matter were done by Negele and Vautherin in the 70s [Neg73]. The calculations were performed assuming a set of non-interacting cells described in the HF approach with 11 representative cells. These cells are distributed in different zones of the inner crust with densities covering a range from 1.743^{-3} ρ_0 to $0.5\rho_0$, $\rho_0 = 0.16$ fm^{-3} being the nuclear matter saturation density. The optimal number (N,Z) of neutrons and protons in cell is obtained by searching for the lowest binding energy and β-stability of the cell. One notes that the pairing correlations and spin-orbit interaction were neglected in those early calculations. Recently, the

Table 4.4: The Wigner-Seitz cells considered in this work. ρ, N, Z and R_{WS} are the baryonic densities, the number of neutrons, the number of protons and the WS cell radii, respectively. All values of WS cells are taken in Ref. [Neg73].

N_{zone}	$\rho[fm^{-3}]$	N	Z	$R_{WS}[fm]$
10	2.79×10^{-4}	140	40	53.6
9	4.00×10^{-4}	160	40	49.2
8	6.00×10^{-4}	210	40	46.3
7	8.79×10^{-4}	280	40	44.3
6	1.59×10^{-3}	460	40	42.2
5	3.73×10^{-3}	900	50	39.3
4	5.77×10^{-3}	1050	50	35.7
3	8.91×10^{-3}	1300	50	33.1
2	2.04×10^{-2}	1750	50	27.6
1	4.75×10^{-2}	1460	40	19.6
0	7.89×10^{-2}	950	32	14.4

superfluid properties and their influence on the specific heat were investigated in the self-consistent HFB approach [San04a, San04b]. The collective excitations and the cooling time of the inner crust of neutron stars were also studied in the framework of a spherical HFB + quasiparticle random phase approximation [Kha05, Gra08] and of HFB approach at finite temperature [Mon07]. All the above calculations were done with the SLy4 Skyrme interaction in the mean field channel and a density-dependent delta force for the pairing interaction. Later, the properties of the WS cells have been studied in the work of Baldo *et al.* [Bal05a, Bal05b, Bal06] using an energy functional method with the pairing correlation of protons and neutrons.

In this present section, the structure of the WS cells in the inner crust of neutron stars will be analyzed in the framework of fully self-consistent HF-BCS calculations where the same finite-range density-dependent interactions are used to construct the mean field and the pairing field. The HF-BCS calculations are done with the D1S-Gogny and M3Y-P4 interactions, imposing Dirichlet-Neumann boundary conditions at the edge of the cell [Neg73]. This boundary conditions for the single-particle wave functions are taken as follows: *i* - the even parity wave functions vanish at the edge $r = R_{WS}$ and *ii* - the first derivatives of the odd-parity wave functions vanish at $r = R_{WS}$. The purpose of these chosen boundary conditions is to make a constant density at large distance inside the cell, thus simulating a uniform neutron gas [Neg73]. Of course, these chosen boundary conditions are arbitrary, because the two conditions *i* and *ii* can be used for any values of l, in principle. Thus, another kind of boundary conditions can be chosen in the following way: the condition *i* is valid for odd l whereas the condition *ii* for even l. As shown in Ref. [Bal06], the two kinds of boundary conditions can be used in the calculations of the neutron star inner crust. The difference of the binding energies per a nucleon for each cell will increase with the increasing density (see Table 1 of Ref. [Bal06]). However, the values of these uncertainties are smaller than the variations of the equilibrium configuration connected with the pairing effects [Bal05a, Bal06]. Therefore, in our study the boundary conditions are kept the same as in Ref. [Neg73].

It should be noted that the Bloch boundary conditions can be used for the boundary condition at the edge of the WS cell as presented in Refs. [Cha07, Cha09, Has08]. However, in this present study we will not consider these boundary conditions. The aim of this work is to show the behaviour of density distribution of protons and neutrons in each WS cells obtained with a finite range interaction within a self-consistent HF-BCS calculation, where the HF equations are solved with the Dirichlet-Neumann mixed boundary conditions.

As mentioned above, we have performed the HF-BCS calculations for a set of 11 representative WS cells determined in Ref. [Neg73]. The considered density range is from neutron drip density $\rho_{min} = 1.743 \times 10^{-3}\ \rho_0$ to about $\rho_{max} = 0.5\rho_0$. In this density range, the nuclear clusters are considered spherical [Dou00, Kha05]. Above the density ρ_{max} the energy per baryon approaches the value of the uniform neutron system and the cells in the inner crust might deviate from the spherical shape [Mag04]. Following Ref. [Neg73] we denote the WS cells like a nucleus with Z protons and N neutrons. The eleven zones of the representative cells of the inner crust with mean densities and corresponding proton number Z and neutron number N in each cell are listed in Table 4.4. The decreasing zone number N_{zone} are from 10 to 0, corresponding to the increasing density from the minimum density $\rho_{min} = 2.79 \times 10^{-4}$ fm^{-3} to the maximum density $\rho_{max} = 7.89 \times 10^{-2}$ fm^{-3}. The WS cells are denoted like a nucleus as ^{180}Zr, ^{200}Zr, ^{250}Zr, ^{320}Zr, ^{500}Zr, ^{950}Sn, ^{1100}Sn, ^{1800}Sn, ^{1350}Sn, ^{1500}Zr, and ^{982}Ge, as determined in Ref. [Neg73]. The WS cell radii R_{WS} are calculated by the following relation

$$< \rho > = \frac{A}{\frac{4\pi}{3} R_{WS}^3} \tag{4.80}$$

where ρ and A are the density and mass number of the considered cell, respectively. The values of the radii R_{WS} are also shown in the last column in Table 4.4.

In finite nuclei, for a given number of protons there is always a maximum number of bound neutrons. This neutron stability limit defines the neutron drip line. Since the neutron-rich nuclei are quickly beta decaying, then the neutron drip line is usually drastically limited in the laboratory. This is not the case for the neutron-rich systems immersed in the inner crust of neutron stars. In the case of WS cells, the beta decay is blocked by the presence of the degenerate electron gas uniformly distributed inside the cell. Therefore, in this case the nuclei inside the inner crust of neutron stars can bind more neutrons than the nuclei in the vacuum.

First, we will discuss the case of the WS cells calculated in the HF approach. Fig. 4.11 displays the HF proton and neutron density profiles of ^{180}Zr, ^{200}Zr, ^{250}Zr, ^{320}Zr and ^{500}Zr systems obtained with D1S, M3Y-P4 and SLy4 interactions. One notes that the numerical HF calculations with SLy4 are the same as in Ref. [Kha05]. We observe that the HF calculations with the finite-range D1S and M3Y-P4 interactions give very similar results. However, the results obtained with SLy4 interaction are different. We will analyze the case of cell ^{180}Zr. As discussed in the section of bubble nuclei, the depopulation of the s state can leads to a depletion of the central density. In the case of this cell, the $5s_{1/2}$ neutron state is fully filled with SLy4 interaction and empty with D1S and M3Y-P4 interactions. Thus, the neutron densities in the center of the cell obtained with D1S and M3Y-P4 interactions are smaller by a factor of 2.3 than that obtained with SLy4 interaction. However, the neutron gas density obtained with D1S and M3Y-P4 interactions is more than 1.8 times greater than that of SLy4 interaction. It has been checked, if one integrates the neutron density up to $r = 10$ fm, where approximatively the neutron density profile is becoming constant, one finds

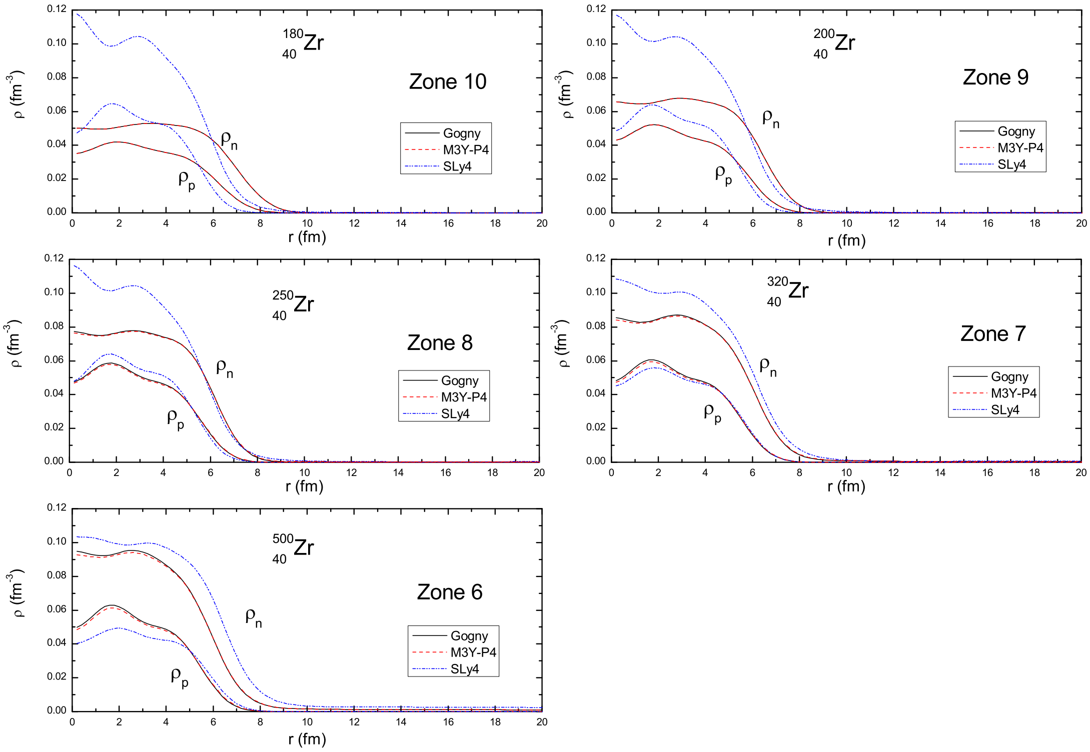

Figure 4.11: The HF proton and neutron densities obtained with the Dirichlet-Neuman boundary condition using D1S [Ber91], M3Y-P4 [Nak08] and SLy4 [Cha98] interactions, corresponding to zone 10 to zone 6.

about 80 neutrons and 90 neutrons with D1S (or M3Y-P4) and SLy4 interactions, respectively. Thus, it appears that large surface regions are observed in the case of D1S and M3Y-P4 interactions, and the neutron gas density of the cell ^{180}Zr is much higher. Similar situations happen in two other cells ^{200}Zr and ^{250}Zr. In the case of cells ^{320}Zr and ^{500}Zr, where the $5s_{1/2}$ neutron state is fully filled, one observes that the nuclear cluster region becomes larger with the SLy4 interaction, while its neutron gas density is smaller by a factor of 2 than those obtained with D1S and M3Y interactions. For these cells above, one concludes that the neutron density in the center of the cell becomes smaller with D1S and M3Y-P4 interactions. However, the situation is

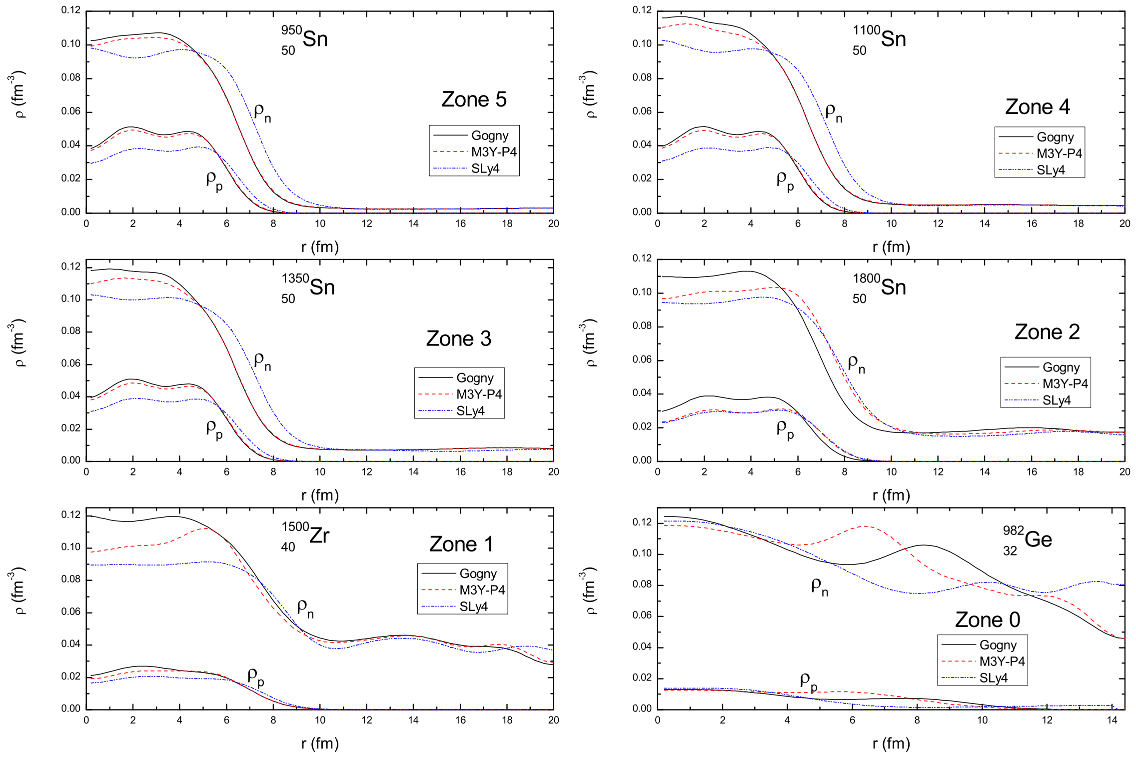

Figure 4.12: Same as Fig. 4.11, but for other zones (from zone 5 to zone 0).

opposite at higher densities, such as in the cells ^{950}Sn, ^{1100}Sn, ^{1800}Sn, ^{1350}Sn and ^{1500}Zr. These changes can be seen in Fig. 4.12, where the neutron densities of the nuclear clusters obtained with SLy4 interaction are always smaller than those obtained with D1S or M3Y-P4 interactions. One can also see that the surface thickness of the nuclear cluster with SLy4 interaction becomes larger by about 10% in the cells ^{950}Sn, ^{1100}Sn, ^{1800}Sn and ^{1350}Sn. In the cell ^{1500}Zr, the nuclear cluster surface is similar with the three interactions. Since the neutron density in the center of this cell obtained with SLy4 interaction is smaller than that obtained with D1S or M3Y-P4 interactions, then its outer neutron gas density is a little higher. For the highest density corresponding to the cell ^{982}Ge, there is still some trace of a central cluster and of an outer neutron gas in the case of SLy4 whereas this separation fades away with D1S and M3Y-P4 interactions.

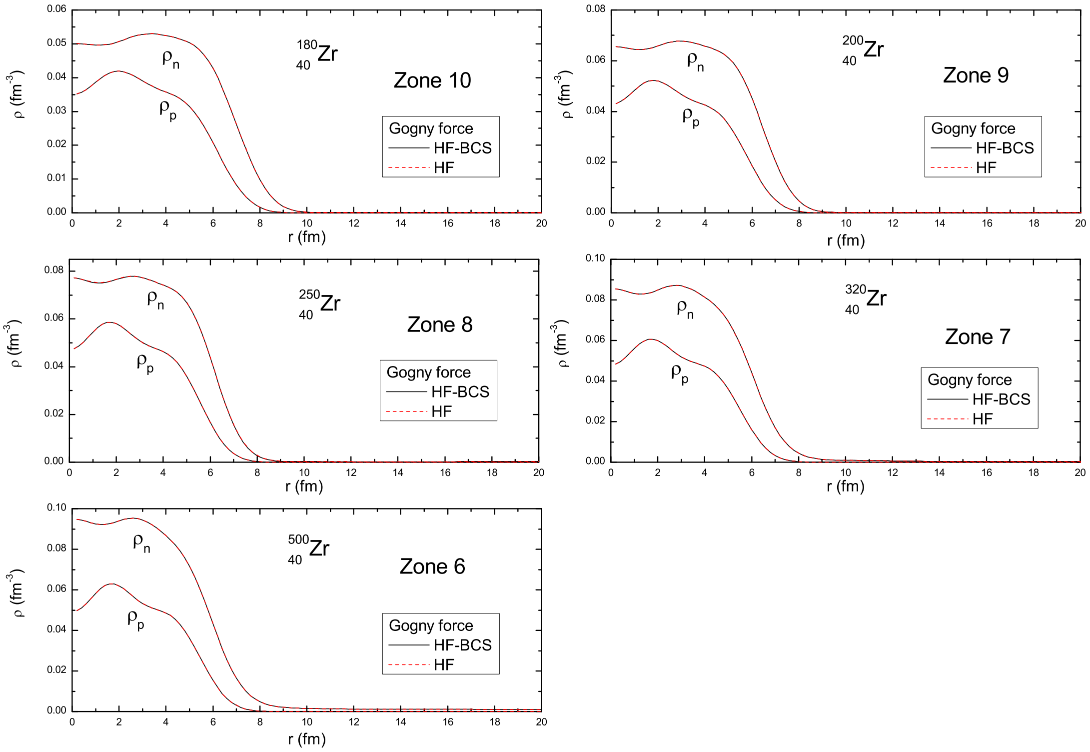

Figure 4.13: The proton and neutron densities obtained with the D1S [Ber91] interaction in HF and HF-BCS approaches. The calculations are done from zone 10 to zone 6.

As mentioned above, the first microscopic calculations of the WS cells in the inner crust matter were done in Ref. [Neg73]. The pairing effects were not taken into account in these calculations because it was assumed that the contribution of the pairing correlations is small in comparison with the total binding energy of the considered system. However, calculations using an energy functional involving the neutron and proton correlations introduced by Baldo *et al.* [Bal05b] show that the interval of the density ρ of the equilibrium configuration (Z, R_{WS}) can be changed significantly due to the pairing effects. We therefore repeat the calculations of all WS

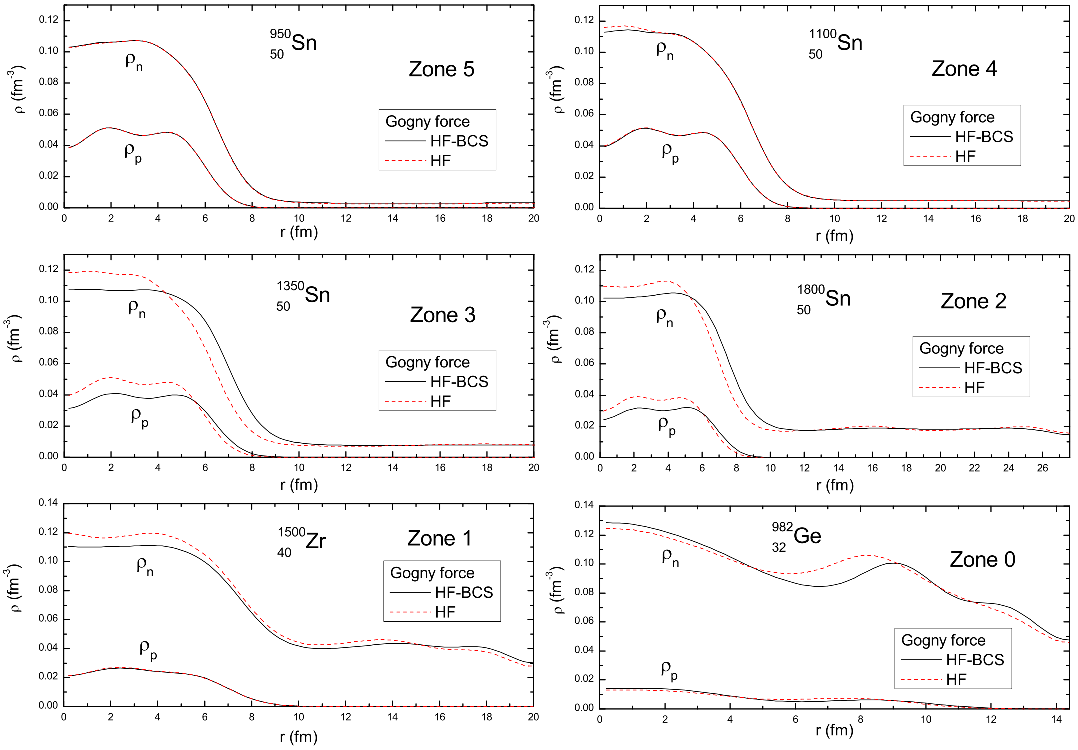

Figure 4.14: Same as Fig. 4.13, but for other zones (from zone 5 to zone 0).

cells in HF-BCS approach. The D1S and M3Y-P4 interactions are used to construct the mean field and the pairing field. For comparison we have also considered a hybrid case where a density-dependent delta force is chosen for the pairing interaction and the D1S interaction is used in the mean field channel. Up to now, the magnitude of pairing correlations in neutron matter is still a subject of debate. We know that the D1S Gogny interaction commonly used in the calculations of finite nuclei gives for pairing gap of infinite neutron matter a maximum value of about 2.4 MeV at a Fermi momentum $k_F \approx 0.8$ fm^{-1} [Gar99]. The maximum value of pairing gap in infinite matter using the M3Y-P4 interaction is about 3.2 MeV at the similar Fermi momentum [Nak08]. On the other hand, the microscopic calculations shown in Ref.

[Wam93, Sch03] predict for the maximum a gap value of about 1 MeV. One observes that there are three different scenarios for pairing correlations in neutron matter. In our study, we use the density dependent delta force for the pairing interaction to simulate the third scenario, in which the parameters of the pairing interaction are chosen so as to obtain in neutron matter approximatively the same pairing gap of about 1 MeV as given in Refs. [San04a, San04b, Wam93]. We use the parameters of Eqs. (4.69, 4.70): V_0=-330 MeV fm^{-3}, η=0.7, and α=0.45 as given in Ref. [San04a]. Thus, for each WS cell we perform three HF-BCS calculations with three pairing forces. The BCS pairing window is chosen to be ± 6 MeV around the Fermi level.

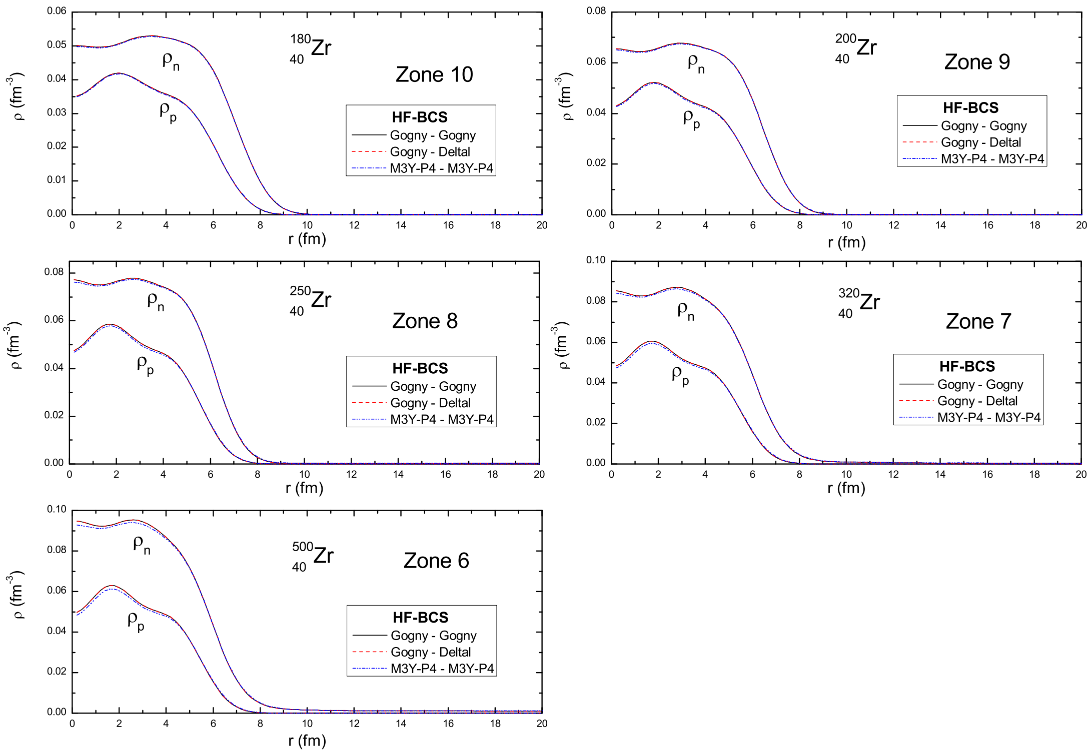

Figure 4.15: The HF-BCS proton and neutron densities obtained in three cases. The notation "Gogny-Gogny" means the D1S Gogny interaction is used in the mean field and pairing channels, and similar notations for other cases. The calculations are done from zone 10 to zone 6.

In Figs. 4.13, 4.14 are shown the proton and neutron densities obtained in HF and HF-BCS approaches for 11 WS cells, in which the D1S Gogny [Ber91] interaction is used in both the mean field and pairing channels. One can see that the behaviour of the proton and neutron densities obtained in the two approaches are similar for ^{180}Zr, ^{200}Zr, ^{250}Zr, ^{320}Zr, ^{500}Zr, ^{950}Sn, and ^{1100}Sn cells corresponding to the range of density $\rho \sim 2.79 \times 10^{-4}$ fm^{-3} $\rightarrow$ 5.77×10^{-3} fm^{-3}. One concludes that the pairing effects are very small on these cells. For the high density region $\rho \sim 8.91 \times 10^{-3}$ fm^{-3} $\rightarrow$ 4.75×10^{-2} fm^{-3}, corresponding to cells ^{1350}Sn, ^{1800}Sn and ^{1500}Zr, we can see the difference between the density profiles obtained in the two above approaches due to the pairing effects. This is because the occupancy of the $8s_{1/2}$ state is modified in HF-BCS calculations. Thus, the difference between HF neutron densities and BCS neutron densities is around 10.5% for the three cells above. Indeed, the occupancies of the $8s_{1/2}$ neutron orbital are 0.91, 0.98 and 0.95 for cells ^{1350}Sn, ^{1800}Sn and ^{1500}Zr in HF-BCS, respectively, while this state is fully filled in HF calculation of these cells. In spite of the cell ^{1500}Zr, the BCS neutron density of the cells ^{1350}Sn, ^{1800}Sn have an extended "surface" before they reach the constant values corresponding to the neutron gas. The neutron gas densities of these cells are similar in both HF and HF-BCS approaches. For the highest-density cell ^{982}Ge, $\rho = 7.89 \times 10^{-2}$ fm^{-3}, the behaviour of neutron density is a little changed due to the pairing effects. However, although the D1S interaction is used in the pairing channel, it cannot produce a constant density around the outer edge of this cell. It seems that the cell ^{982}Ge most probably belongs to the deformed pasta phase.

As discussed above, the density of neutron matter is changing significantly from the center of the cell, where the nuclear cluster is located, to its edge filled by the uniform neutron gas. One knows that the pairing gap of the neutron matter depends strongly on the density. However, the maximum value of the gap and its detailed density dependence are still subjects of debate. Since it is not yet established what are the pairing properties of neutron matter, we perform again the HF-BCS calculations for all WS cells of the inner crust matter using the D1S, M3Y and delta interactions in the pairing channel. The results of proton and neutron density distributions obtained with three interactions in the pairing channel are shown in Figs. 4.15, 4.16. For

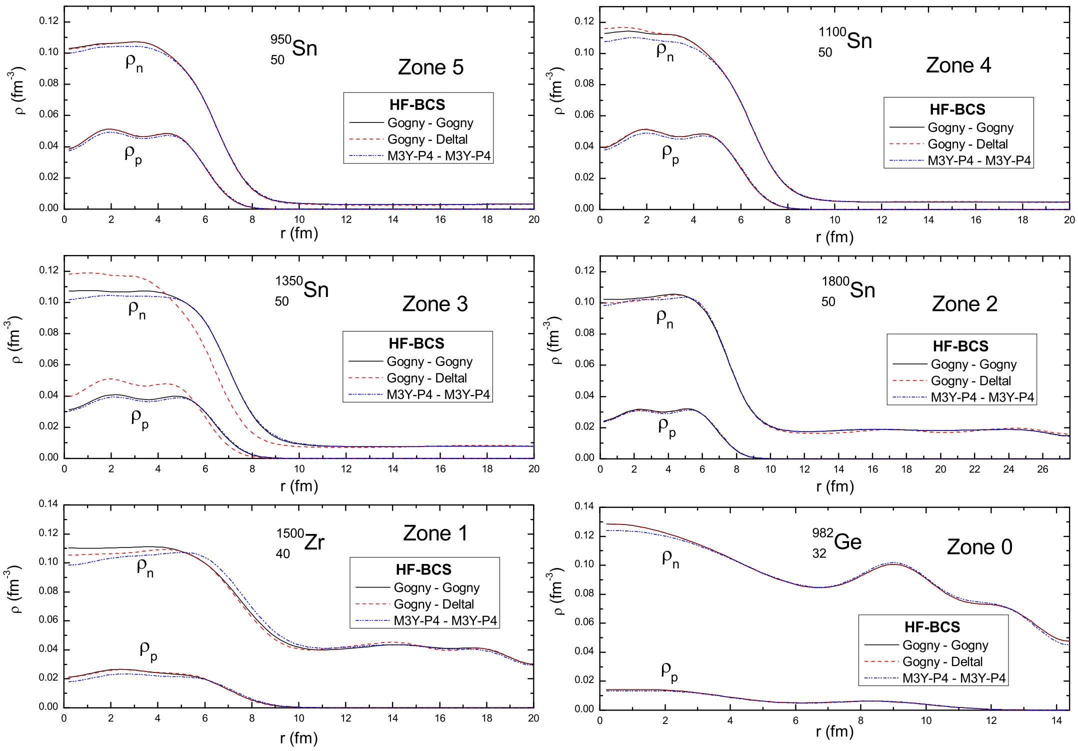

Figure 4.16: Same as Fig. 4.15, but for other zones (from zone 5 to zone 0).

the HF-BCS calculations using the delta interaction in the pairing channel, the D1S interaction will be used in the mean field channel. One observes from the Figs. 4.15, 4.16 that the main features of the WS cells can be obtained with three kinds of pairing interactions. At the low density region (from zone 10 to zone 5), the behaviour of the proton and neutron density distributions are very similar. In these cases the pairing effect is very small and cannot modify the shape of the proton and neutron densities. At the high density region, except for the cell ^{1350}Sn where the pairing effect is strong on the neutron density, the results of proton and neutron densities are similar for other cells such as cells ^{1100}Sn, ^{1500}Zr, ^{1800}Sn and ^{982}Ge. In the case of cell ^{1350}Sn, the neutron density distribution of nuclear cluster inside the cell using delta interaction

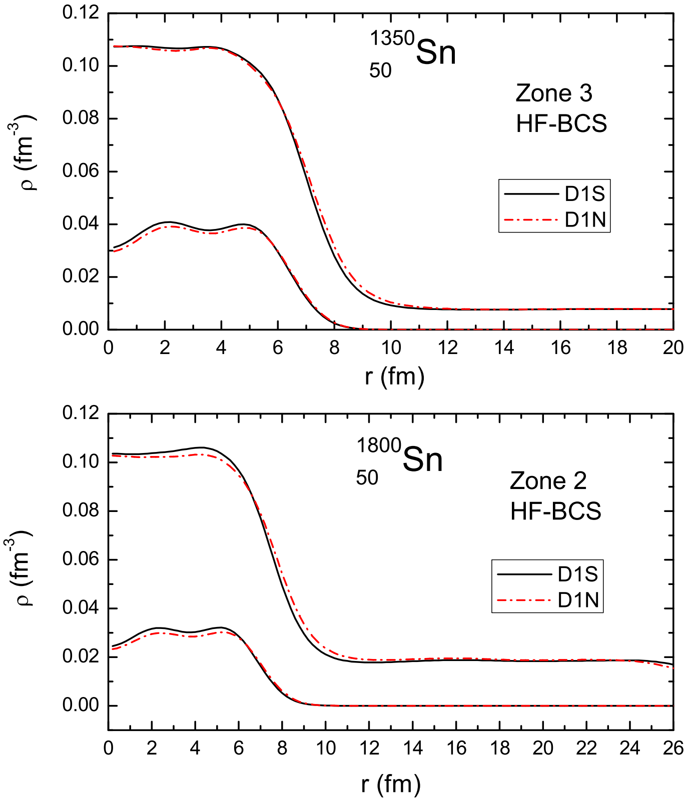

Figure 4.17: The proton and neutron densities for zone 2 and 3 obtained with the D1S [Ber91] and D1N [Cha08] interactions in HF-BCS approach.

in the pairing channel is higher than that obtained with D1S or M3Y-P4 interactions used in the pairing channel, because of the occupancy of the $8s_{1/2}$ neutron orbital obtained with the delta-pairing interaction is larger than those obtained with D1S and M3Y-P4 pairing interactions. In all the cells we observe that the density distribution of the nuclear cluster obtained with the case of M3Y-P4 interaction is a little smaller than those obtained with the case of D1S interaction. This effect may come from the difference of the range and the value of pairing gap in infinite matter with two kinds of effective interactions. Fig. 4.17 displays the proton and neutron densities for zone 2 and 3 obtained with the D1S [Ber91] and D1N [Cha08] interactions in HF-BCS approach. One can see that the results are very similar.

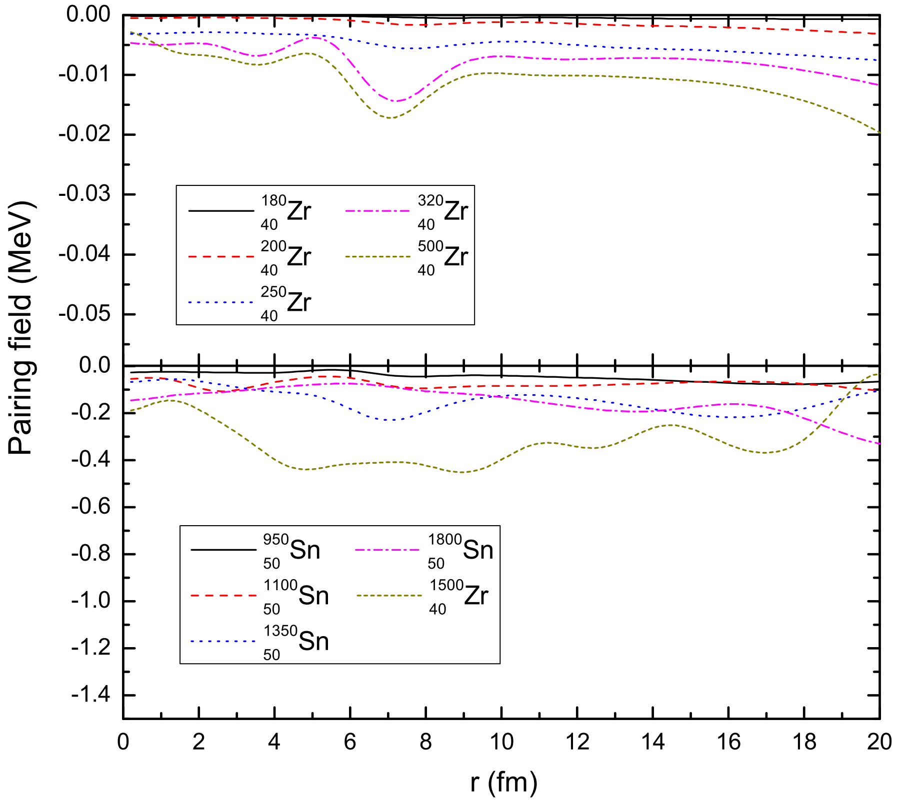

Figure 4.18: The neutron pairing fields given by the delta -pairing interaction using the Eq. (4.72) for the WS cells (from zone 10 to zone 1).

Next, we discuss the neutron pairing fields given by a delta -pairing interaction using the Eq. (4.72). The results calculated for the WS cells (from zone 10 to zone 1) are shown in Fig. 4.18, except for zone 0 (corresponds to the cell ^{982}Ge) which belongs to the deformed pasta phase. In the upper panel of Fig. 4.18, we can see that the pairing field is becoming very small almost everywhere in the cell. However, one can observe that in passing from the low density region of the neutron gas towards the high density region of the cluster, the pairing field is increasing in the intermediate density region of the cluster surface in the cells ^{320}Zr and ^{500}Zr. This is a manifestation of the bell shape dependence of the pairing gap on density. For the cells corresponding to high baryonic densities shown in lower panel of Fig. 4.18 the slope of the pairing field is changing very slowly when it is crossing the region between the nuclear cluster and the uniform neutron gas. Using the same density-dependent delta force in the pairing channel, the pairing fields of the cells ^{950}Sn, ^{1500}Zr and ^{1800}Sn given by the HF-BCS calculation using the Gogny D1S interaction in the mean field are about three times smaller (in absolute value) than that obtained by the HFB calculation using the SLy4 interaction in the mean field (see Figs. 5 and 6 in Ref. [San04a]). We see that the pairing correlations are reduced strongly for all the cells in the present work.

One can conclude that the behaviour of the pairing field in the inner crust matter is rather complex. On the other hand the magnitude of the pairing field inside the inner crust depends strongly on the scenario used for the pairing properties of infinite neutron matter as shown in Refs. [San04a, San04b].

In conclusion of this section, we have studied the properties of the WS cells in the inner crust matter of neutron star using the finite-range density dependent interactions in HF and HF-BCS approaches, for the first time. The calculations are performed with 11 representative WS cells with imposing Dirichlet-Neumann boundary conditions at the edge of the cell. The main features of the WS cell can be observed in our calculations. In the HF-BCS calculations, one finds that the pairing effect is very small in the low density region $\rho \sim 2.79 \times 10^{-4}$ fm^{-3} $\rightarrow 5.77 \times 10^{-3}$ fm^{-3}. In the high density, the pairing effect can make an extended "surface" for neutron density distribution in the cell before they reach the constant density around the outer edge of the cell. However, one cannot obtain the constant neutron gas densities in the cell ^{982}Ge with a finite-range density-dependent interaction. This cell corresponds to the highest-density $\rho = 7.89 \times 10^{-2}$ fm^{-3}, and it seems not to belong to the spherical case as assumed in our study.

CHAPTER 5

NUCLEAR REACTIONS

In this chapter we study the charge exchange (p,n) reactions measured with ^{48}Ca, ^{90}Zr, ^{120}Sn and ^{208}Pb targets at the proton energies of 35 and 45 MeV within a two-channel coupling formalism using the folding model. In this work, the density-dependent CDM3Y6 interaction was used in the folding calculation of the nucleon optical potential and (p,n) form factor. Our results are published in the paper D.T. Khoa *et al.* Physical Review **C 76**, 014603 (2007) [Kho07b]. The basic formalism of the folding model and charge exchange (p,n) reactions can be found in Refs. [Kho02, Kho05, Kho07b, Tha05, Sat83], thus we only recall the main features of a consistent folding model analysis of the charge exchange (p,n) reactions. The other interactions, such as the M3Y-Pn [Nak08], Gogny [Ber91, Cha08] and Skyrme (SLy4) [Cha98], can be applied to analyze the charge exchange (p,n) reactions. Work in this direction is in progress.

5.1 The charge exchange (p,n) reactions

The charge exchange (p,n) reaction is well known as an effective tool to excite the isobaric analog of the target ground state. Such an isobaric analog state (IAS) has essentially the same structure as that of the target ground state (except for the replacement of a neutron by a proton) and which differs in energy by the Coulomb energy of the added proton. The two states are just two members of the isospin multiplet which have the same isobaric spin T and differ only in the orientation of the isospin T in isobaric-spin space. The similarity of the initial and final states makes the (p,n) reaction very much like an elastic scattering (quasielastic) in which the isospin of the projectile is “flipped”. Indeed, the isospin dependent part of the proton-nucleus optical model potential (OMP) was studied by Satchler *et al.* [Sat64] in their study of the (p,n) reaction within the distorted wave Born approximation (DWBA). In general, assuming isospin symmetry in nuclei $[H, \mathbf{T}^2] = [H, T_z] = 0$, the nucleon-nucleus OMP can be written in terms of the isospin operators [Lan62] as

$$U(R) = U_0(R) + 4U_1(R)\frac{\boldsymbol{t}_a.\boldsymbol{T}_A}{A}, \tag{5.1}$$

where $\boldsymbol{t}_a$ is the isospin of the incident nucleon and $\boldsymbol{T}_A$ is that of the target nucleus, and A is the mass of the nucleus. The second term of Eq. (5.1), known as the Lane potential, contributes to both the elastic (p,p) , (n,n) scattering and (p,n) charge exchange reaction [Sat83]. While the contribution of the Lane potential U_1 to the elastic (p,p) and (n,n) cross section is small and amounts only to a few percent for a neutron-rich target [Kho02, Kho03], it determines entirely the (Fermi-type) $\Delta J^\pi = 0^+$ transition strength of the (p,n) reaction exciting the IAS. Therefore, the (p,n) reaction can be used as a reliable probe of the isospin dependence of the proton-nucleus OMP. In addition, the probes of the Lane potential complementary to the charge exchange (p,n) reactions can be given by high energy ion collisions, sensitive observables being given for instance by differential high transverse momentum proton/neutron spectrum, π^+/π^- ratio and proton neutron flow [Li08].

Another very interesting microscopic aspect of the Lane potential is that it provides a direct link between the isospin dependence of the in-medium NN interaction and the charge exchange (p,n) reaction, so that accurately measured (p,n) cross section can serve as a good probe of the isospin dependence of the NN interaction [Doe75] if the wave functions of the involved nuclear states are known. In our recent study of the IAS excitation in the $p(^6\text{He},^6\text{Li}^*)n$ reaction using the folded Lane potential U_1 for the charge exchange form factor [Kho05], we have shown how the NM symmetry energy can be linked to the charge exchange (p,n) transition strength and, hence, be probed in the folding model analysis of the (p,n) reaction. To extend the folding model study of the (p,n) reaction to heavier targets to validate the conclusion made in Ref. [Kho05] for the NM symmetry energy, we have studied in the present work the quasi-elastic (p,n) scattering measured by the MSU group for ^{48}Ca, ^{90}Zr, ^{120}Sn, and ^{208}Pb targets at the incident proton energies of 35 and 45 MeV [Doe75]. By using the Lane potential U_1 to construct the charge exchange (p,n) form factor based on the isospin coupling, one can probe the isospin dependence of existing global nucleon-nucleus OMP, such as that by Becchetti and Greenlees [Bec69], the CH89 global OMP [Var91], and by Koning and Delaroche [Kon03]. In the present work, the description of the considered (p,n) reactions by the three global nucleon optical potentials [Bec69, Var91, Kon03] has been given, with a detailed comparison between the results given by the CH89 potential [Var91] and those of the folding model analysis. While these three global nucleon optical potentials have been widely used in predicting the nucleon-nucleus OMP in numerous direct reaction analyses within the DWBA or coupled-channel (CC) formalism, their isospin dependence has been rarely used to study the charge exchange (p,n) transition between the IAS's. The (phenomenological) Lane potential U_1 has been studied in detail so far at some particular energies only, like the systematics for U_1 deduced from IAS data of the (p,n) reaction measured at 22.8 [Car75] and 35 MeV [Jon00]. Therefore, it is necessary to have a reliable microscopic prediction for U_1 by the folding model, to reduce the uncertainty associated with the isospin dependence of the nucleon-nucleus OMP.

5.2 Lane potential and isospin coupling

5.2.1 Basic formulae

We give here a brief introduction to the coupled-channel formalism for the charge exchange (p,n) reaction to isobaric analog states, and more details can be found in Ref. [Sat83]. Let us restrict our considerations to a given isospin multiplet with fixed values of isospin $\boldsymbol{t_a}$ for the projectile and $\boldsymbol{T_A}$ for the target. The isospin projections are $N_z = (N-Z)/2$ and $\tilde{N}_z = N_z - 1$ for the target nucleus A and *isobaric analog* *nucleus* $\tilde{A}$, respectively. We further denote, in the isospin representation, a state formed by adding a proton to A as $|pA>$ and adding a neutron to $\tilde{A}$ as $|n\tilde{A}>$. In what follows we will use N_i to denote the value of N_{iz} for nucleus i.

The wave function for the pair $|pA>$ can be expressed as a superposition of states with definite total isospin T in the following form [Sat83]

$$\begin{aligned} |pA> &= \Psi_{\frac{1}{2},-\frac{1}{2}}(x_a)\Psi_{T_A N_A}(x_A) = \sum_T < \frac{1}{2} - \frac{1}{2} T_A N_A | TN > \Psi_{T(T_A \frac{1}{2})N}(x_\alpha) \\ &= \frac{1}{\sqrt{2T_A+1}} |T_A + \frac{1}{2}, N_A - \frac{1}{2}\rangle + \sqrt{\frac{2T_A}{2T_A+1}} |T_A - \frac{1}{2}, N_A - \frac{1}{2}\rangle \\ &= \frac{1}{\sqrt{2T_A+1}} [|T_>, N_<\rangle + \sqrt{2T_A} |T_<, N_<\rangle], \end{aligned} \qquad (5.2)$$

where we have suppressed the other quantum numbers of the incident proton and target nucleus for simplicity. $\Psi_{T(T_A\frac{1}{2})N}(x_\alpha)$ is a superposition of the states of different N_A and $N_a(= -\frac{1}{2})$ (but with fixed $N = N_A + N_a$) which are members of the isospin multiplets with given T_A and $t_a(= \frac{1}{2})$, respectively. T is the total isospin, $\boldsymbol{T} = \boldsymbol{T}_A + \boldsymbol{t}_a$, and we use the notation

$$X_> = X_A + \frac{1}{2}, X_< = X_A - \frac{1}{2}.$$

In a similar way, we can obtain the wave function for the pair $|n\tilde{A}>$ as

$$\begin{aligned} |n\tilde{A}\rangle &= \Psi_{\frac{1}{2},\frac{1}{2}}(x_a)\Psi_{T_{\tilde{A}} N_{\tilde{A}}}(x_{\tilde{A}}) \\ &= \sum_T < \frac{1}{2}\frac{1}{2} T_{\tilde{A}} N_{\tilde{A}} | TN > \Psi_{T(T_{\tilde{A}} \frac{1}{2})N}(x_\alpha) \\ &= \sqrt{\frac{2T_A}{2T_A+1}} |T_A + \frac{1}{2}, N_A - \frac{1}{2}\rangle - \sqrt{\frac{1}{2T_A+1}} |T_A - \frac{1}{2}, N_A - \frac{1}{2}\rangle \\ &= \frac{1}{\sqrt{2T_A+1}} [\sqrt{2T_A} |T_>, N_<\rangle - |T_<, N_<\rangle] \end{aligned} \qquad (5.3)$$

In a coupled representation [Sat83] the isoscalar operator $\boldsymbol{t}_a.\boldsymbol{T}_A$ is diagonal in the total isospin T and its projection N:

$$< T'N'|\boldsymbol{t}_a.\boldsymbol{T}_A|TN >= \frac{1}{2}\delta_{TT'}\delta_{NN'}[T(T+1) - t_a(t_a+1) - T_A(T_A+1)]. \tag{5.4}$$

Using Eq. 5.4 we have (with $t_a = \frac{1}{2}$)

$$\begin{aligned} < pA|\boldsymbol{t}_a.\boldsymbol{T}_A|pA > &= \frac{1}{2(2T_A+1)}[\langle N_<, T_>|\boldsymbol{t}_a.\boldsymbol{T}_A|T_>, N_<\rangle + \\ &\qquad +2T_A\langle N_<, T_<|\boldsymbol{t}_a.\boldsymbol{T}_A|T_<, N_<\rangle] \\ &= -\frac{T_A}{2}, \end{aligned} \tag{5.5}$$

$$\begin{aligned} < n\tilde{A}|\boldsymbol{t}_a\boldsymbol{T}_A|n\tilde{A} > &= \frac{1}{2(2T_A+1)}[2T_A\langle N_<, T_>|\boldsymbol{t}_a.\boldsymbol{T}_A|T_>, N_<\rangle - \\ &\qquad -\langle N_<, T_<|\boldsymbol{t}_a.\boldsymbol{T}_A|T_<, N_<\rangle] \\ &= \frac{1}{2}(T_A - 1), \end{aligned} \tag{5.6}$$

$$\begin{aligned} < n\tilde{A}|\boldsymbol{t}_a\boldsymbol{T}_A|pA > &= \frac{\sqrt{2T_A}}{2T_A+1}[\langle T_>, N_<|\boldsymbol{t}_a\boldsymbol{T}_A|T_>, N_<\rangle - \\ &\qquad -\langle T_<, N_<|\boldsymbol{t}_a\boldsymbol{T}_A|T_<, N_<\rangle] \\ &= \sqrt{\frac{T_A}{2}}. \end{aligned} \tag{5.7}$$

The transition matrix elements of the isovector part of the nucleon-nucleus optical model potential (5.1) can then be obtained for the elastic nucleon-nucleus scattering as

$$\begin{aligned} < pA|4U_1(R)\frac{\boldsymbol{t}_a.\boldsymbol{T}_A}{A}|pA >= -\frac{2}{A}T_AU_1(R), \\ < n\tilde{A}|4U_1(R)\frac{\boldsymbol{t}_a.\boldsymbol{T}_A}{A}|n\tilde{A} >= \frac{2}{A}(T_A-1)U_1(R), \end{aligned} \tag{5.8}$$

In the similar way, the transition matrix element or (p,n) form factor (FF) for the

$(\Delta T = 1)$ charge exchange $A_{\text{g.s.}}(p,n)\tilde{A}_{\text{IAS}}$ reaction is obtained as

$$< n\tilde{A}|4U_1(R)\frac{\boldsymbol{t}_a.\boldsymbol{T}_A}{A}|pA > \equiv F_{pn}(R) = \frac{2}{A}\sqrt{2T_A}U_1(R). \tag{5.9}$$

The OMP in the entrance $(p + A)$ and outgoing $(n + \tilde{A})$ channels are determined explicitly through the isoscalar (U_0) and isovector (U_1) parts of the nucleon optical potential (5.1) as

$$\begin{aligned} U_p(R) &= < pA|U_0(R) + 4U_1(R)\frac{\boldsymbol{t}_a.\boldsymbol{T}_A}{A}|pA > \\ &= U_0(R) - \frac{2}{A}T_A U_1(R), \qquad (5.10) \\ U_n(R) &= < n\tilde{A}|U_0(R) + 4U_1(R)\frac{\boldsymbol{t}_a.\boldsymbol{T}_A}{A}|n\tilde{A} > \\ &= U_0(R) + \frac{2}{A}(T_A - 1)U_1(R). \qquad (5.11) \end{aligned}$$

In the two-channel approximation, the total wave function may be written as [Sat83]

$$\Psi = |pA > \chi_{pA}(\boldsymbol{R}) + |n\tilde{A} > \chi_{n\tilde{A}}(\boldsymbol{R}), \tag{5.12}$$

where the wave functions $\chi(\boldsymbol{R})$ describe the relative motion of the scattering system. Then, the elastic (p,p) scattering and charge exchange $A_{\text{g.s.}}(p,n)\tilde{A}_{\text{IAS}}$ cross sections can be obtained from the solutions of the following coupled-channel equations [Sat83]

$$[K_p + U_p(R) - E_p]\,\chi_{pA}(\boldsymbol{R}) = -F_{pn}(R)\chi_{n\tilde{A}}(\boldsymbol{R}), \tag{5.13}$$

$$[K_n + U_n(R) - E_n]\,\chi_{n\tilde{A}}(\boldsymbol{R}) = -F_{pn}(R)\chi_{pA}(\boldsymbol{R}). \tag{5.14}$$

Here $K_{p(n)}$ and $E_{p(n)}$ are the kinetic-energy operators and center-of-mass energies of the $(p + A)$ and $(n + \tilde{A})$ partitions. One notes that $E_n = E_p - \Delta_C$, where Δ_C is the additional internal Coulomb energy of the analogue nucleus and it is also minus the Q value of the (p,n) reaction. The OMP U_p and U_n can be obtained from Eqs. (5.10) and (5.11). In the CC calculation, one must add to U_p and U_n the corresponding spin-orbital potential while the Coulomb potential of the $(p + A)$ system is added to U_p. Since the energies of isobar analog states are separated approximately by the Coulomb displacement energy, the (p,n) transition between them has a nonzero Q value. To account for this effect, the isoscalar U_0 and isovector U_1 potentials used to construct $F_{pn}(R)$ and $U_n(R)$ are evaluated at effective incident energies of $E + Q/2$, as suggested by Satchler in Ref. [Sat64]. In this work, the Q values of the (p,n) reactions taken from Ref. [Doe75] are -7.175, -12.03, -13.41 and -18.82 MeV for ^{48}Ca, ^{90}Zr, ^{120}Sn and ^{208}Pb targets, respectively. Since the existing global OMP parameters [Bec69, Var91, Kon03] can be used to construct the isoscalar (U_0) and isovector (U_1) components of the proton-nucleus OMP, we also use those parameters in the description of the $A_{\text{g.s.}}(p,n)\tilde{A}_{\text{IAS}}$ reaction between the isobaric analog states for comparison.

5.2.2 Folding model

One knows that among various models of nuclear reactions, the folding model is one of the successful models that has been used for years to calculate the nucleon-nucleus and nucleus-nucleus optical potentials [Rik84, Dor98, Kho02, Kho03, Kho96, Kho07b, Chi09] and inelastic form factors [Mac78, Che85, Kho02, Kho07b, Chi09]. Therefore, in this present work we use the folding model to construct the isoscalar (U_0) and isovector (U_1) parts of the nucleon OP. Following the single-folding model in Refs. [Kho02, Kho03], the central nucleon-nucleus potential V is evaluated as a Hartree-Fock-type potential

$$V = \sum_{j\in A}[< ij|v_{\text{D}}|ij > + < ij|v_{\text{EX}}|ji >], \tag{5.15}$$

where v_{D} and v_{EX} are the direct and exchange parts of the effective NN interaction between the incident nucleon i and nucleon j bound in the target A (see Eq. (2.35)). The antisymmetrization of the nucleon-nucleus system is done by taking into account the knock-on exchange effects.

Using the explicit proton (ρ_p) and neutron (ρ_n) densities in the folding input, we can write the real nucleon-nucleus potential (5.15) in terms of the real isoscalar

($V_{\rm IS}$=Re$U_{\rm IS}$) and real isovector ($V_{\rm IV}$ = Re$U_{\rm IV}$) parts like Eq. (2.42)

$$V(E,\boldsymbol{R}) = V_{\rm IS}(E,\boldsymbol{R}) \pm V_{\rm IV}(E,\boldsymbol{R}), \tag{5.16}$$

Here the (+) sign pertains to incident neutron and (-) sign to incident proton. Each term in Eq. (5.16) consists of the corresponding direct and exchange potentials [Kho02]

$$\begin{aligned} V_{\rm IS}(E,\boldsymbol{R}) = \int \{ [\rho_n(\boldsymbol{r}) + \rho_p(\boldsymbol{r})] v_{00}^{\rm D}(E,\rho,s) \\ +[\rho_n(\boldsymbol{R},\boldsymbol{r}) + \rho_p(\boldsymbol{R},\boldsymbol{r})] v_{00}^{\rm EX}(E,\rho,s) j_0(k(E,R)s)\} d^3r, \end{aligned} \tag{5.17}$$

$$\begin{aligned} V_{\rm IV}(E,\boldsymbol{R}) = \int \{ [\rho_n(\boldsymbol{r}) - \rho_p(\boldsymbol{r})] v_{01}^{\rm D}(E,\rho,s) \\ +[\rho_n(\boldsymbol{R},\boldsymbol{r}) - \rho_p(\boldsymbol{R},\boldsymbol{r})] v_{01}^{\rm EX}(E,\rho,s) j_0(k(E,R)s)\} d^3r, \end{aligned} \tag{5.18}$$

where $\rho(\boldsymbol{r},\boldsymbol{r}')$ is the one-body density matrix of the target nucleus with $\rho(\boldsymbol{r}) \equiv \rho(\boldsymbol{r},\boldsymbol{r})$, and the local momentum of relative motion $k(E,R)$ is determined from

$$k^2(E,R) = \frac{2\mu}{\hbar^2}[E_{\rm c.m.} - V(R) - V_{\rm C}(R)]. \tag{5.19}$$

Here, μ is the nucleon reduced mass, $V(R)$ and $V_{\rm C}(R)$ are, respectively, the real central nuclear and Coulomb potentials in the entrance channel ($V_{\rm C} \equiv 0$ for the neutron-nucleus system). More details of the folding calculation of $V_{\rm IS}$ and $V_{\rm IV}$ can be found in Ref. [Kho02].

In this work, the isovector density dependence of the complex CDM3Y6 interaction will be used as the input of the folding calculation. This version of the effective interaction has been constructed in Chapter 2. The imaginary part $W_{\rm IS(IV)} = Im(U_{\rm IS(IV)})$ of the OMP which accounts for the absorption into other channels is given by the same folding procedure (5.17)-(5.18) but using the imaginary parts of the CDM3Y6 interaction constructed separately at each energy.

Given the isovector folded potential (5.18) determined entirely by the neutron-proton difference in the nuclear densities, it is necessary to have the nuclear densities determined as accurately as possible for a good prediction of the Lane potential. In the present work we have used for the considered targets the microscopic ground-state densities given by the HFB approach using the SLy4 interaction [Gra01]. We have calculated the neutron and proton densities of all considered targets using the D1S Gogny interaction which is presented in Chapter 4. Because the considered targets are doubly shell-closure nuclei, we find that the calculated neutron and proton densities are very close with those obtained using SLy4 interaction in Ref. [Gra01]. Therefore the results of the CC analysis of the charge exchange (p, n) reactions to the isobaric analog states of the ground states of ^{48}Ca, ^{90}Zr, ^{120}Sn and ^{208}Pb targets do not change, and we keep our discussions in this Chapter as presented in our paper [Kho07b]. The nucleon-nucleus OMP has been calculated using the CDM3Y6 interaction with the Fortran code DFPD4 written by Khoa [Kho]. All the results of the optical model (OM) analysis of elastic nucleon-nucleus scattering and CC calculation of the $A_{\text{g.s.}}(p,n)\tilde{A}_{\text{IAS}}$ reactions have been obtained with the CC code ECIS97 written by Raynal [Ray72], such as the elastic differential cross sections $(d\sigma/d\Omega)$, analyzing powers (A_y), spin rotation (P_y), reaction cross sections (σ_R), and total cross sections (σ_T for incident neutron only).

5.3 Results and discussions

5.3.1 Predictions by the phenomenological models

The existing nucleon-nucleus global OMP's [Var91, Kon03, Bec69] have been carefully determined based on large experimental databases of both the elastic nucleon-nucleus scattering and analyzing power angular distributions, and it is natural to use them to construct U_p and U_n for our study. Since the elastic neutron scattering on a target being in its *excited* IAS cannot be measured (most of IAS's are either a short-lived bound state or an unbound resonance), we have determined U_n from the isoscalar U_0 and isovector U_1 parts of the proton-nucleus OMP evaluated at the effective incident energy $E = E_{\mathrm{lab}} + Q/2$, as suggested in Ref. [Sat64], using these global proton-nucleus OMP's. Fig. 5.1 displays the OM description of the elastic proton scattering from ^{48}Ca, ^{90}Zr, ^{120}Sn, and ^{208}Pb targets at incident proton energy of 40 MeV given by the three global proton-nucleus OMP's together with the measured data taken from Refs. [Gru72, Fri67]. Except for some underestimation of the calculated elastic

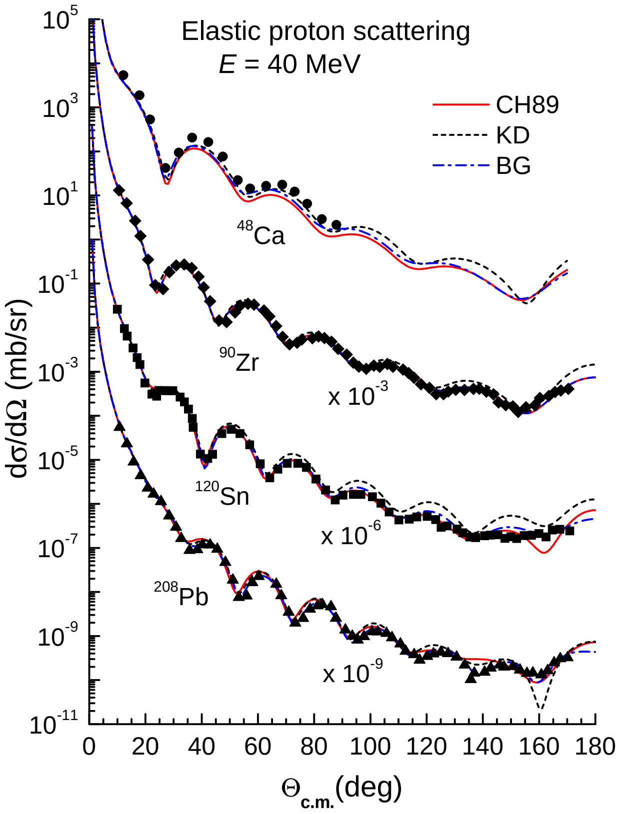

Figure 5.1: OM description of the elastic proton scattering from ^{48}Ca, ^{90}Zr, ^{120}Sn, and ^{208}Pb targets at 40 MeV obtained with the global OMP by Bechetti and Greenlees (BG) [Bec69], by Varner *et al.* (CH89) [Var91], and by Koning and Delaroche (KD) [Kon03]. The data were taken from Refs. [Gru72, Fri67].

cross section in $p+^{48}$Ca case, all results given by the OM description of elastic proton scattering are in good agreement with the experimental data. It should be noted that the isovector strength of the nucleon-nucleus OMP is only about 2-3% of the total OMP and its contribution to the elastic scattering cross section is small. It is, thus, not easy for us to probe the isospin dependence of the OMP directly in the OM analysis of elastic scattering. Therefore, we can only probe the isospin dependence of

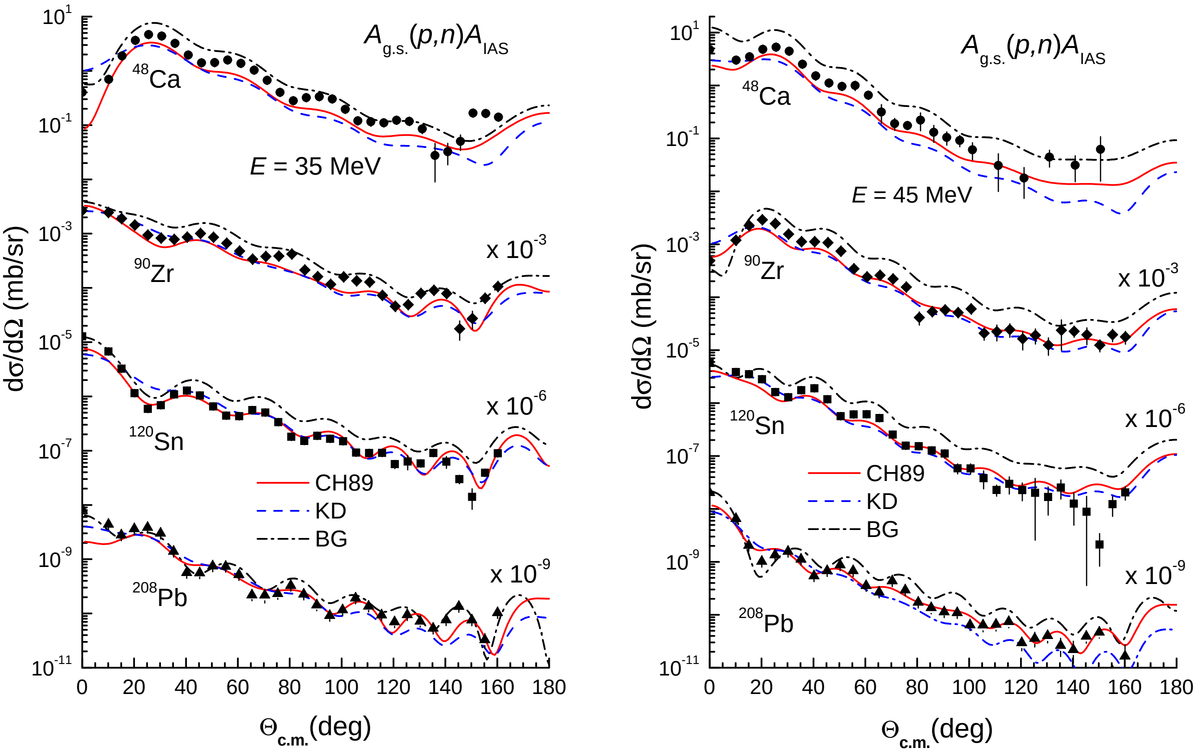

Figure 5.2: CC description of the charge exchange $A_{\text{g.s.}}(p,n)\tilde{A}_{\text{IAS}}$ reaction measured with ^{48}Ca, ^{90}Zr, ^{120}Sn, and ^{208}Pb targets at 35 and 45 MeV obtained with U_1 deduced from the global OMP by Bechetti and Greenlees (BG) [Bec69], by Varner *et al.* (CH89) [Var91], and by Koning and Delaroche (KD) [Kon03]. The data were taken from Ref. [Doe75].

the nucleon-nucleus OMP via the charge exchange $A_{\text{g.s.}}(p,n)\tilde{A}_{\text{IAS}}$ reaction in a "Lane consistent" approach. In such a quasi-elastic scattering, the charge exchange form factor (5.9) used in the CC equations (5.13)-(5.14) is determined entirely by the Lane potential U_1. As a result, any variation of the U_1 strength and shape can sizably affect the calculated (p,n) cross section.

In Fig. 5.2, the CC description of the charge exchange $A_{\text{g.s.}}(p,n)\tilde{A}_{\text{IAS}}$ reaction measured on ^{48}Ca, ^{90}Zr, ^{120}Sn, and ^{208}Pb targets at 35 and 45 MeV obtained with U_1

deduced from the three global OMP's [Bec69, Var91, Kon03] are shown in comparison with the experimental data taken from Ref. [Doe75]. It should be noted that the isospin dependence of the nucleon global OMP has been determined from systematic OM studies of the elastic scattering of proton and neutron from the same target (at about the same energy), without any link to the $A_{\rm g.s.}(p,n)\tilde{A}_{\rm IAS}$ reaction. From the three global OMP's, U_1 determined from the systematics by Bechetti and Greenlees (BG) [Bec69] is energy independent, and we found it too strong for the strength of the charge exchange form factor (5.9), especially, at energy of 45 MeV. Such a deficiency of the BG parameters for U_1 was also found in the extensive OM analysis of elastic nucleon-nucleus scattering [Var91, Kon03]. The isovector parts of both the global optical potentials by Varner *et al.* (CH89) [Var91], and by Koning and Delaroche (KD) [Kon03] were found to be energy dependent and weaker than that given by the BG systematics. Although the KD global OMP is more recent and covers a much wider range of energies and target masses, from the CC results shown in Fig. 5.2 one can see that the description of $A_{\rm g.s.}(p,n)\tilde{A}_{\rm IAS}$ reaction by the KD global OMP is slightly worse than those of the CH89 global OMP. A plausible reason is that the CH89 systematics was developed [Var91] with less constraints, based only on the elastic scattering data for $A \approx 40 - 209$ and energies of 16 to 65 MeV (for proton) and 10 to 26 MeV (for neutron). Although this range of energies and target masses is narrower than that covered by the KD global systematics [Kon03], it includes the proton-nucleus systems considered in the present work. In general, the Lane form factor (5.9) determined from the CH89 global OMP gives a reasonable description of the $A_{\rm g.s.}(p,n)\tilde{A}_{\rm IAS}$ cross sections measured for ^{120}Sn and ^{208}Pb targets, and slightly underestimates the data for ^{48}Ca and ^{90}Zr targets. As will be shown below, such a suppression of the calculated $A_{\rm g.s.}(p,n)\tilde{A}_{\rm IAS}$ cross sections for the two lighter targets is due mainly to an enhanced absorption given by the CH89 global OMP.

5.3.2 Folding model analysis

First, we will check the OM description of elastic nucleon-nucleus scattering at the nearby energies using the complex microscopic OMP as

$$U(R) = N_{\rm V}[V_{\rm IS}(R) \pm V_{\rm IV}(R)] + iN_{\rm W}[W_{\rm IS}(R) \pm W_{\rm IV}(R)], \tag{5.20}$$

where the (+) sign pertains to incident neutron and (-) sign to incident proton. The isoscalar ($V_{\rm IS}(R)$ and $W_{\rm IS}(R)$) and isovector ($V_{\rm IV}(R)$ and $W_{\rm IV}(R)$) parts of the nucleon-nucleus OMP can be calculated explicitly using the complex density-dependent CDM3Y6 interaction by the single-folding approach (5.17)-(5.18). The complex OMP U is further complemented by the spin-orbital potential (and proton-nucleus OMP added also by the Coulomb potential) taken from the CH89 model [Var91]. The strengths $N_{\rm V(W)}$ of the complex folded OMP are adjusted to the best OM fit to the elastic scattering data. In the present folding approach, the factor N_V for the real folded OMP is an approximate way to make small adjustments that may be needed to take into account the higher order contributions to the real microscopic OMP, it is the “dynamic polarization potential” in the Feshbach's formalism [Fes92]. It is obvious that the value of N_V should be close to unity for this procedure to be reasonable.

The OM results obtained for the elastic proton scattering at 40 MeV on ^{48}Ca, ^{90}Zr, ^{120}Sn and ^{208}Pb targets are shown in Fig. 5.3 (on the left panel). A good description of the measured elastic proton scattering data [Gru72, Fri67] can be reached after the complex folded potential is renormalized by $N_{\rm V} \approx 0.90-0.94$ and $N_{\rm W} \approx 0.6-0.8$. On the right panel of Fig. 5.3 the OM results obtained for the elastic neutron scattering are shown, where the best-fit $N_{\rm V} \approx 0.9$ and $N_{\rm W} \approx 0.6-0.7$. For comparison, we have also tried a hybrid choice for the complex OMP, in which the real part obtained by the folding model and imaginary part given by a Woods-Saxon (WS) potential based

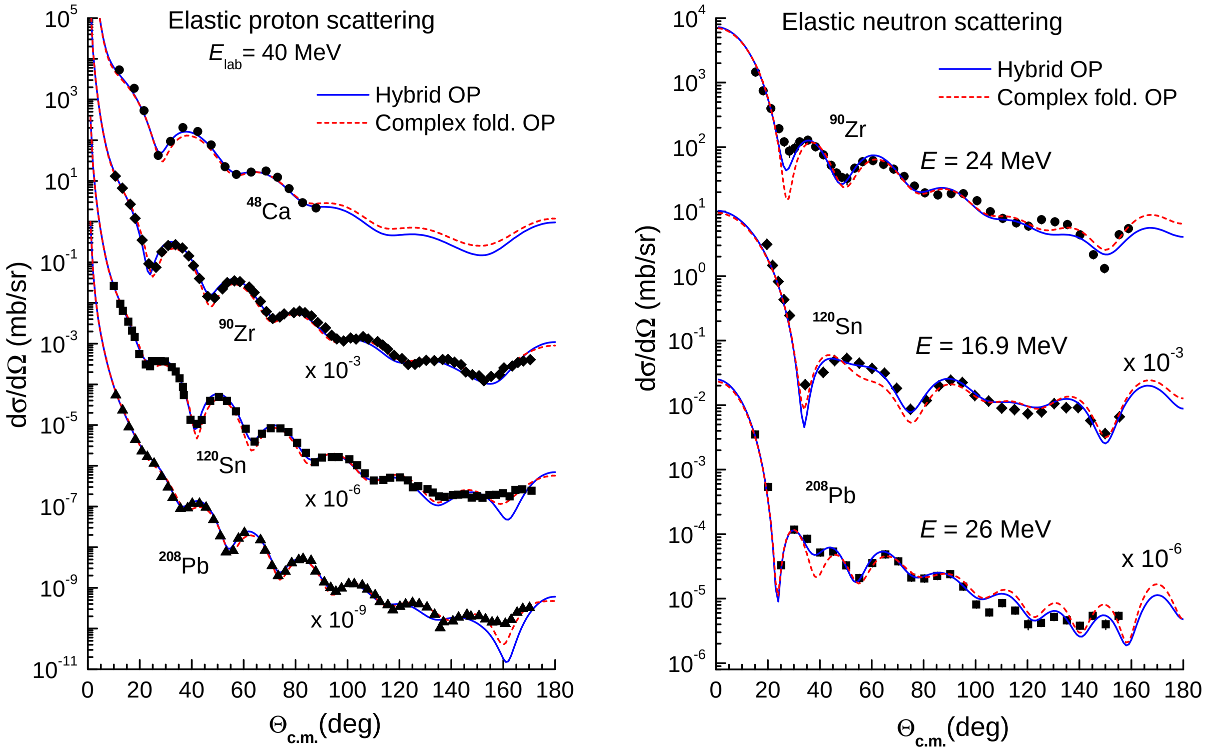

Figure 5.3: OM description of the elastic proton scattering from ^{48}Ca, ^{90}Zr, ^{120}Sn, and ^{208}Pb targets at 40 MeV (on the left panel) and from ^{90}Zr, ^{120}Sn, and ^{208}Pb targets at energies of 17 to 24 MeV (on the right panel) obtained with the complex folded OMP (5.20) and hybrid OMP (5.21). The data were taken from Refs. [Gru72, Fri67, Wan90, Gus89, Rap78].

on the CH89 global systematics [Var91]

$$\begin{aligned} U(R) &= N_V[V_{\rm IS}(R) \pm V_{\rm IV}(R)] - i[W_v f(R) - 4a_w W_s \frac{df(R)}{dR}], \\ \text{where } f(R) &= \frac{1}{1+\exp[(R-R_w)/a_w]}. \end{aligned} \tag{5.21}$$

The normalization factor $N_{\rm V}$, the strengths of the volume ($W_{\rm v}$) and surface ($W_{\rm s}$) terms of the absorptive WS potential are adjusted in each case to fit the elastic scattering data and reproduce the total reaction cross section $\sigma_{\rm R}$ measured for the considered proton-nucleus systems at 35 and 45 MeV [Car96]. The results of the elastic proton

Table 5.1: Renormalization coefficients $N_{\rm V(W)}$ of the complex folded proton-nucleus OMP (5.20) used in the entrance channel. The calculated proton total reaction cross section $\sigma_{\rm R}$ is compared with the data $\sigma_{\rm R}^{\rm exp}$ taken from Ref. [Car96]. $N_{\rm R(I)}$ are the renormalization coefficients of the folded FF (5.22) deduced from the CC fit to the (p,n) data using the OMP (5.20).

Target A	E (MeV)	$N_{\rm V}$	$N_{\rm W}$	$\sigma_{\rm R}$ (mb)	$\sigma_R^{\rm exp}$ (mb)	$N_{\rm R}$	$N_{\rm I}$
^{48}Ca	35	0.933	0.600	969	971 ± 32	1.356	0.970
	45	0.902	0.630	893	908 ± 34	1.738	1.054
^{90}Zr	35	0.893	0.731	1341	1316 ± 65 [a]	2.133	0.978
	45	0.893	0.731	1296	1214 ± 59 [b]	2.193	1.043
^{120}Sn	35	0.937	0.828	1605	1668 ± 59	2.372	0.981
	45	0.937	0.731	1588	1545 ± 38	2.529	0.985
^{208}Pb	35	0.916	0.747	1877	1974 ± 38	2.896	1.018
	45	0.916	0.747	1963	1979 ± 41	2.606	0.985

[a] Total p+^{90}Zr reaction cross section measured at $E = 40$ MeV; [b] at $E = 49.5$ MeV.

and neutron scattering given by this hybrid choice are shown in Fig. 5.3 (named hybrid OMP). One observes that the OM fit given by the hybrid OMP is slightly improved, especially, at forward scattering angles. Although the difference in the OM description of elastic nucleon scattering by the two choices of OMP is marginal as seen in Fig. 5.3, their effect on the calculated (p,n) cross section is surprisingly much more significant.

The complex charge exchange form factor (FF) for the (p,n) transition channel is determined from the real and imaginary parts of the folded isovector potential (5.18) as

$$F_{pn}(R) = \frac{2}{A}\sqrt{2T_A}U_1(R) = \sqrt{\frac{2}{T_A}}[N_{\rm R}V_{\rm IV}(R) + iN_{\rm I}W_{\rm IV}(R)]. \tag{5.22}$$

we calculate the charge exchange FF $F_{pn}(R)$ after the OMP for the entrance proton-nucleus channel is determined based on the OM analysis of the proton elastic scattering at the nearby energies. The OMP parameters are kept unchanged as fixed from the OM calculation described above. The normalization factors $N_{\mathrm{R(I)}}$ are adjusted for the best fit of the calculated (p,n) cross section to the experimental data. Using this method, the folding model analysis of the (p,n) reaction can serve as a good probe of the isospin dependence of the effective NN interaction. In this work, the complex OMP for the outgoing $(n+\tilde{A})$ channel has been determined from the complex proton OMP evaluated at the effective incident energy $E = E_{\mathrm{lab}} + Q/2$. For consistency, the complex folded OMP in the outgoing $(n+\tilde{A})$ channel is renormalized by the same factors $N_{\mathrm{V(W)}}$ as those used in entrance proton-nucleus channel. The WS imaginary part of the hybrid OMP (5.21) in the outgoing $(n+\tilde{A})$ channel is determined from the CH89 global OMP using the same isospin coupling (5.11). The results of the CC calculation of the (p,n) reaction are given in Tables 5.1 and 5.2 for the complex folded and hybrid OMP, respectively.

We discuss now the CC results for the (p,n) reaction measured with ^{48}Ca target. The OM descriptions of the elastic $p+^{48}$Ca scattering data at 35 MeV [Gru72] given by the complex folded OMP (5.20), hybrid OMP (5.21) and CH89 global OMP [Var91] are shown in lower part of Fig. 5.4. Similarly to the results at 40 MeV shown in Fig. 5.3, both complex folded and hybrid OMP give a reasonable description of the measurement after their strengths were adjusted by the OM fit to the elastic data, with the complex folded OMP slightly underestimating data at the forward angles. The CC descriptions of the $^{48}\mathrm{Ca}_{\mathrm{g.s.}}(p,n)^{48}\mathrm{Sc}_{\mathrm{IAS}}$ data at 35 MeV obtained by the unrenormalized folded form factor (5.22) and that deduced from the isovector term of the CH89 potential using Eq. (5.9) are shown in upper part of Fig. 5.4. One can see that the unrenormalized folded FF gives a good agreement with the measured (p,n) cross section at large angles while it underestimates the data points at the forward angles. From the two choices of the OMP, the complex folded OMP (5.20) gives a worse fit to the (p,n) data at forward angles. Since the angular distribution at forward angles is more affected by the surface part of the OMP and given the same real folded OMP used in both calculations, the difference caused by the two OMP's should be due to different surface absorptions described by the two OMP's. The CC description by the CH89 form factor improves significantly when the best-fit hybrid OMP (5.21) is used (see Fig. 5.5). Therefore, the unsatisfactory description of the

Table 5.2: Parameters of the hybrid OMP (5.21) used in the entrance and exit channels. Parameters given in boldface were kept unchanged as determined from the CH89 systematics [Var91]. The calculated proton total reaction cross section $\sigma_{\rm R}$ is compared with the data $\sigma_{\rm R}^{\rm exp}$ taken from Ref. [Car96]. $N_{\rm R(I)}$ are the renormalization coefficients of the folded FF (5.22) deduced from the CC fit to the (p,n) data using the OMP (5.21).

Target A	E (MeV)	Channel	$N_{\rm V}$	W_v (MeV)	W_s (MeV)	R_w (fm)	a_w (fm)	$\sigma_{\rm R}$ (mb)	$\sigma_R^{\rm exp}$ (mb)	$N_{\rm R}$	$N_{\rm I}$
^{48}Ca	35	$(p+A)$	0.925	1.495	5.432	**4.414**	**0.69**	981	971 ± 32	1.265	0.960
		$(n+\tilde{A})$	0.925	1.495	**4.503**	**4.414**	**0.69**	-	-	-	-
	45	$(p+A)$	0.900	1.096	5.358	**4.414**	**0.69**	893	908 ± 34	1.279	0.970
		$(n+\tilde{A})$	0.900	1.096	**3.985**	**4.414**	**0.69**	-	-	-	-
^{90}Zr	35	$(p+A)$	0.913	1.479	6.060	**5.540**	**0.69**	1330	1316 ± 65 [a]	1.202	0.969
		$(n+\tilde{A})$	0.913	**1.891**	**5.267**	**5.540**	**0.69**	-	-	-	-
	45	$(p+A)$	0.913	2.434	5.314	**5.540**	**0.69**	1296	1214 ± 59 [b]	1.298	1.081
		$(n+\tilde{A})$	0.913	**2.918**	**4.721**	**5.540**	**0.69**	-	-	-	-
^{120}Sn	35	$(p+A)$	0.937	**2.305**	**7.792**	**6.140**	**0.69**	1637	1668 ± 59	1.203	0.950
		$(n+\tilde{A})$	0.937	**1.686**	**4.687**	**6.140**	**0.69**	-	-	-	-
	45	$(p+A)$	0.937	2.027	6.529	**6.140**	**0.69**	1570	1545 ± 38	1.225	0.958
		$(n+\tilde{A})$	0.937	**2.653**	**4.218**	**6.140**	**0.69**	-	-	-	-
^{208}Pb	35	$(p+A)$	0.901	2.419	**8.729**	**7.460**	**0.69**	1964	1974 ± 38	1.201	0.955
		$(n+\tilde{A})$	0.901	**1.127**	**4.386**	**7.460**	**0.69**	-	-	-	-
	45	$(p+A)$	0.901	**2.827**	6.334	**7.460**	**0.69**	1998	1979 ± 41	1.150	0.930
		$(n+\tilde{A})$	0.901	**1.871**	**4.000**	**7.460**	**0.69**	-	-	-	-

[a] Total $p+^{90}$Zr reaction cross section measured at $E = 40$ MeV; [b] at $E = 49.5$ MeV.

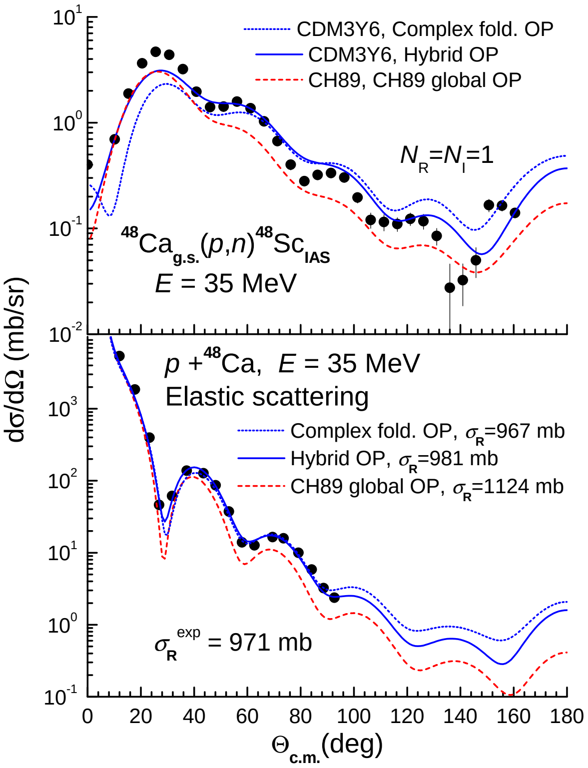

Figure 5.4: Upper part: CC description of the $^{48}\mathrm{Ca}_{\mathrm{g.s.}}(p,n)^{48}\mathrm{Sc}_{\mathrm{IAS}}$ reaction at 35 MeV [Doe75] given by the (unrenormalized) folded (p,n) form factor (5.22) and that deduced from Eq. (5.9) using the CH89 parameters [Var91]. Lower part: OM description of the elastic $p+^{48}\mathrm{Ca}$ scattering at 35 MeV [Gru72] given by the complex folded OMP (5.20), hybrid OMP (5.21) and CH89 global OMP [Var91].

(p,n) data by the CH89 form factor shown in upper part of Fig. 5.4 is caused by a too absorptive imaginary CH89 potential (which gives $\sigma_{\mathrm{R}} \approx 1124$ mb compared to the measurement $\sigma_{\mathrm{R}}^{\mathrm{exp}} \approx 971 \pm 32$ mb [Car96]). We have adjusted the complex strength of the folded FF to the best χ^2-fit of the experimental (p,n) data. We found that N_{R} are around 1.3, while N_{I} remains close to unity (see lower part of Fig. 5.5 and Tables 5.1 and 5.2). The effect by the imaginary OMP becomes more substantial in the CC analysis of the (p,n) data at 45 MeV (upper part of Fig. 5.5). While the results obtained with the hybrid OMP (5.21) are on about the same best-fit $N_{\mathrm{R(I)}}$ coefficients of the folded FF as those found at 35 MeV, the complex folded OMP

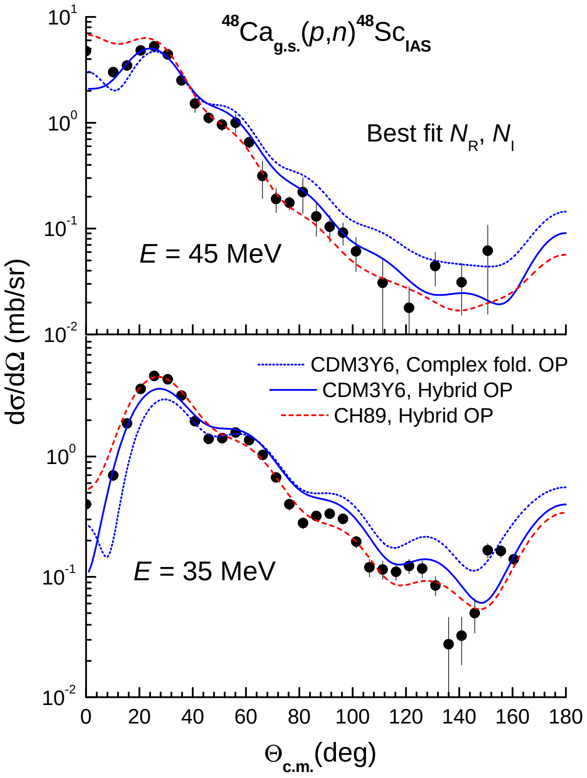

Figure 5.5: CC description of the $^{48}\mathrm{Ca}_{\mathrm{g.s.}}(p,n)^{48}\mathrm{Sc}_{\mathrm{IAS}}$ reaction [Doe75] at 35 MeV (lower part) and 45 MeV (upper part) given by the renormalized folded (p,n) form factor (5.22) and that deduced from Eq. (5.9) with the CH89 global OMP [Var91], using two choices (5.20)-(5.21) of the OMP.

(5.20) gives a much larger N_{R} of around 1.7 and a worse description of the (p,n) data at large angles. The CC calculations using the hybrid OMP (5.21) give a good overall description of the $^{48}\mathrm{Ca}_{\mathrm{g.s.}}(p,n)^{48}\mathrm{Sc}_{\mathrm{IAS}}$ data at 35 and 45 MeV with the folded FF renormalized by $N_{\mathrm{R}} \approx 1.3$ and $N_{\mathrm{I}} \approx 1$. These calculations also give the total (p,n) cross section $\sigma_{pn} \approx 10.7$ and 9.0 mb for the $^{48}\mathrm{Ca}_{\mathrm{g.s.}}(p,n)^{48}\mathrm{Sc}_{\mathrm{IAS}}$ reaction at 35 and 45 MeV, respectively, which agree well with the measured values [Doe75], $\sigma_{pn}^{\mathrm{exp}} \approx 10.2 \pm 1.1$ and 8.4 ± 1.0 mb at 35 and 45 MeV, respectively.

The results of the $^{90}\mathrm{Zr}_{\mathrm{g.s.}}(p,n)^{90}\mathrm{Nb}_{\mathrm{IAS}}$ reaction are plotted with the experimental data in Fig. 5.6. One observes that the peak of the (p,n) cross section is weaker and only around half of that measured for $^{48}\mathrm{Ca}_{\mathrm{g.s.}}(p,n)^{48}\mathrm{Sc}_{\mathrm{IAS}}$ reaction. A weaker charge

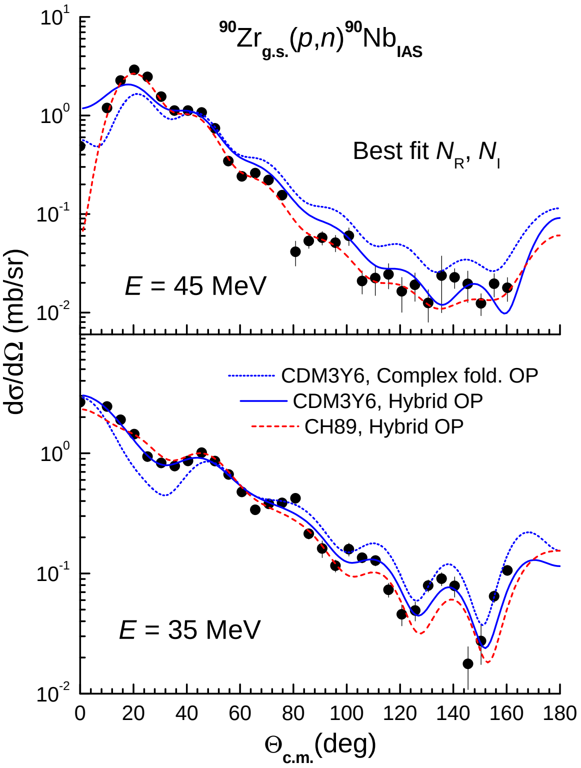

Figure 5.6: The same as Fig. 5.5 but for the $^{90}Zr_{g.s.}(p,n)^{90}Nb_{IAS}$ reaction [Doe75].

exchange strength also leads to a total (p,n) cross section of about 50% smaller than that obtained for ^{48}Ca target (see Table I in Ref. [Doe75]). In terms of the isospin-flip transition (5.9), the charge exchange (p,n) strength is directly proportional to the neutron-proton asymmetry parameter $\delta = (N-Z)/A$ and strength of the Lane potential U_1. Indeed, the isovector folded potential $V_{IV}(R)$ for the $p+^{48}$Ca system is about 30-40% larger than that obtained for the $p+^{90}$Zr system in the surface region and the asymmetry parameter $\delta \approx 0.17$ and 0.11 for ^{48}Ca and ^{90}Zr, respectively. A weaker charge exchange strength observed in the $^{90}Zr_{g.s.}(p,n)^{90}Nb_{IAS}$ reaction is, therefore, well anticipated. Like the $p+^{48}$Ca system, the use of the complex folded OMP (5.20) in the CC calculation with the folded FF gives a poor description of the (p,n) data, especially at forward angles (see Fig. 5.6), even after its real strength is renormalized by $N_R > 2$ as determined from the χ^2 fit to the data. The same folded FF gives a much better fit to the (p,n) data when the hybrid OMP (5.21) is used and its complex strengths need to be renormalized by just $N_R \approx 1.2 - 1.3$ and $N_I \approx 1$ which are close to those obtained for the $p+^{48}$Ca system (see Table 5.2). The CH89 form factor for the $p+^{90}$Zr system slightly underestimates the data. However, the CC description of the (p,n) data by the CH89 form factor is much better when the hybrid OMP (5.21) is used. The CC calculation using the hybrid OMP and renormalized folded FF gives the total (p,n) cross section $\sigma_{pn} = 4.8$ and 4.1 mb for the $^{90}\mathrm{Zr}_{\mathrm{g.s.}}(p,n)^{90}\mathrm{Nb}_{\mathrm{IAS}}$ reaction at 35 and 45 MeV, respectively, which agree nicely with the data ($\sigma_{pn}^{\mathrm{exp}} \approx 4.8 \pm 0.5$ and 4.4 ± 0.5 mb at 35 MeV and 45 MeV, respectively) [Doe75].

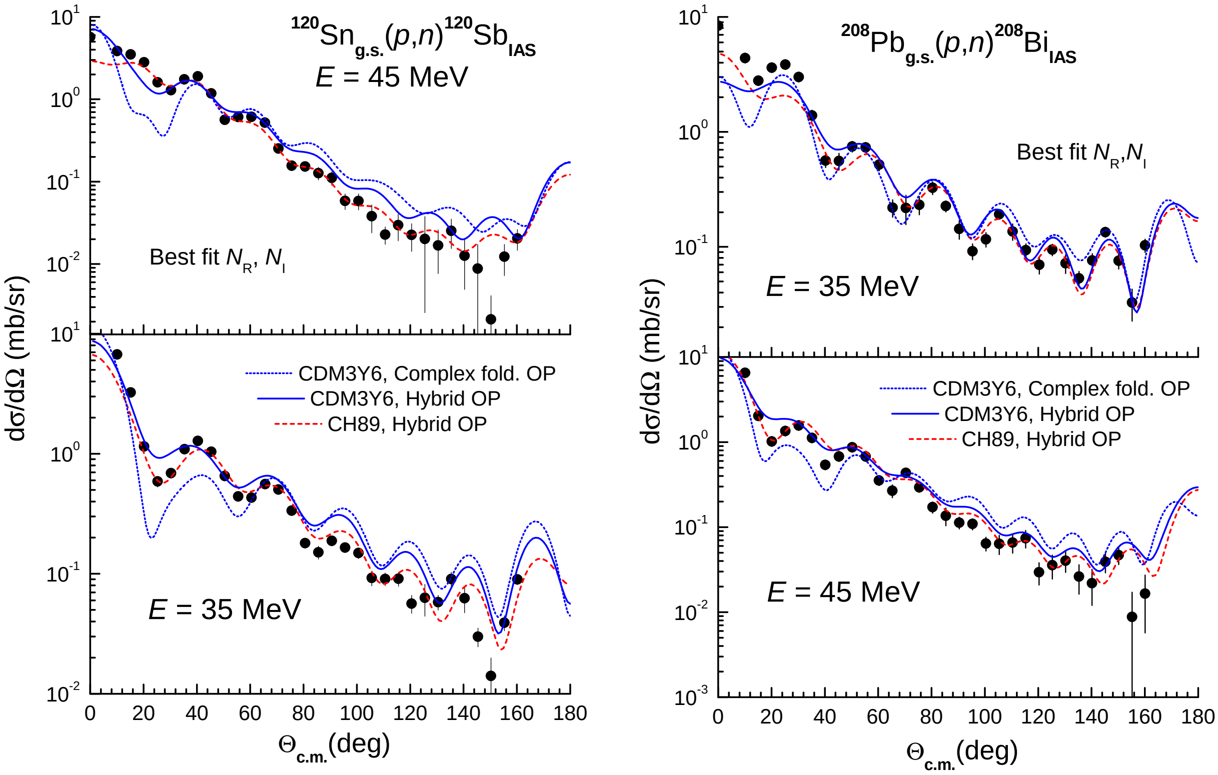

Figure 5.7: The same as Fig. 5.5 but for the $^{120}\mathrm{Sn}_{\mathrm{g.s.}}(p,n)^{120}\mathrm{Sb}_{\mathrm{IAS}}$ and $^{208}\mathrm{Pb}_{\mathrm{g.s.}}(p,n)^{208}\mathrm{Bi}_{\mathrm{IAS}}$ reactions [Doe75].

The CC results for the $^{120}\mathrm{Sn}_{\mathrm{g.s.}}(p,n)^{120}\mathrm{Sb}_{\mathrm{IAS}}$ and $^{208}\mathrm{Pb}_{\mathrm{g.s.}}(p,n)^{208}\mathrm{Bi}_{\mathrm{IAS}}$ reactions are presented in Fig. 5.7. Like the results obtained above for ^{48}Ca and ^{90}Zr targets, the use of the complex folded OMP (5.20) with a volume-shape imaginary part leads to a wrong shape of the calculated (p, n) cross section at forward angles. The CC description of the (p, n) data by both the folded FF and CH89 form factors is very satisfactory when the hybrid OMP's (which describe well the proton elastic scattering at 40 MeV and measured total reaction cross section) are used for the entrance and exit channels. A stronger proton-nucleus Coulomb potential seems to push the main peak of the (p, n) cross section to the forward angles, but the measured data points in the observable angular range still allow us to make an accurate conclusion on the complex strength of the folded (p, n) form factor (5.22). For the two heavy targets, the best CC fit by the folded FF is reached when its real and imaginary strengths are scaled by $N_{\rm R} \approx 1.2$ and $N_{\rm I} \approx 1$ which are reasonably close to those obtained for ^{48}Ca and ^{90}Zr targets.

We have used the CC description of the charge exchange $A_{\rm g.s.}(p, n)\tilde{A}_{\rm IAS}$ reaction measured on ^{48}Ca, ^{90}Zr, ^{120}Sn, and ^{208}Pb targets at 35 and 45 MeV obtained with the folded (p, n) form factor (5.22) using an averaged "*global*" set of $N_R = 1.26 \pm 0.10$ and $N_I = 0.97 \pm 0.06$ extracted from the Table 5.2. The results are plotted in Fig. 5.8. In this case, the hybrid OMP's, which gives a good description of the proton elastic scattering and measured total reaction cross section, are used for the entrance and exit channels. One can see that the renormalized folded FF obtained with this single set of parameters N_R and N_I gives a good agreement with the experimental (p, n) data. We note that our results of the charge exchange (p, n) reaction have been obtained using the "static" g.s. densities of the targets taken from the HFB approach using the SLy4 interaction [Gra01]. In reality, the g.s. densities should also include higher-order terms given, e.g., by the dynamical random phase approximation (RPA) correlations. Such an approach for the HF g.s. densities have been used in the folding model analysis of the same (p, n) data using the JLM interaction [Bau01], and the RPA correlations were shown to have non-negligible effects on the calculated (p, n) cross sections. It may also be necessary to take into account the effect of the variation of the density from the initial nucleus to the final one, on the transition potential [Che85]. One also notes that the same (p, n) reactions have been studied using the original version of the effective JLM interaction by Pakou *et al.* [Pak01]

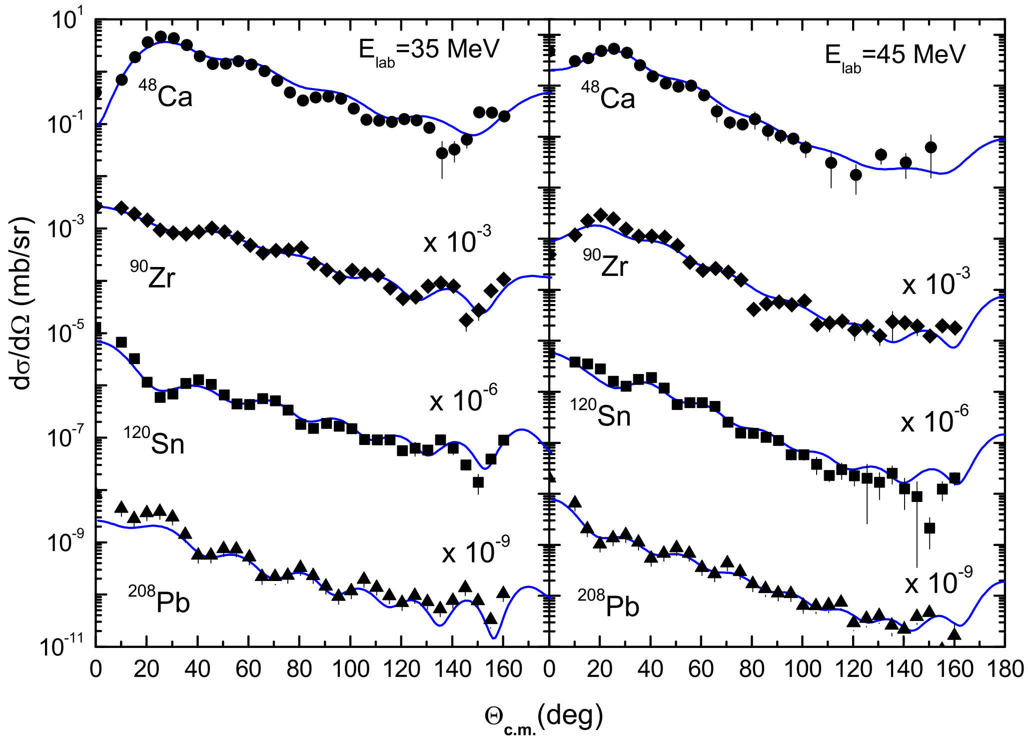

Figure 5.8: CC description of the charge exchange $A_{\rm g.s.}(p,n)\tilde{A}_{\rm IAS}$ reaction measured on ^{48}Ca, ^{90}Zr, ^{120}Sn, and ^{208}Pb targets at 35 and 45 MeV given by the folded (p,n) form factor (5.22) using an averaged "*global*" set of $N_R = 1.26 \pm 0.10$ and $N_I = 0.97 \pm 0.06$ deduced from the Table 5.2.

and Bauge *et al.* [Bau01]. The JLM model analysis of the proton, neutron elastic scattering and (p,n) charge exchange reaction in Ref. [Pak01] has also shown that the isovector part of the JLM interaction is too weak and a very strong renormalization $N_{\rm R} = N_{\rm I} \approx 2 - 2.5$ is needed. From our results obtained with the complex folded OMP (5.20), it is very likely that such large renormalization of the folded FF has been driven by the "volume" absorption of the JLM complex OMP used in Ref. [Pak01]. In a more elaborate treatment of the charge exchange transition within the JLM model, Bauge *et al.* [Bau01] have made the isospin coupling factor in Eq. (5.9) density dependent, i.e., $\sqrt{2T_z/A} = \sqrt{[\rho_n(r) - \rho_p(r)]/\rho(r)}$, and included it into the (direct) folding integral. The JLM nucleon OMP obtained in such a density-dependent isospin coupling assumption has been thoroughly tested in the OM analysis of the proton, neutron elastic scattering and (p, n) reaction over a wide range of energies and target masses, and one can deduce from the results shown in Fig. 1 of Ref. [Bau01] the best-fit renormalization coefficients of the (p, n) folded form factor $N_{\rm R} \approx 1.5 - 1.6$ and $N_{\rm I} \approx 1.3 - 1.4$, in the energy range of $30 - 40$ MeV, which are closer to our results. Despite differences in the best-fit renormalization coefficients of the folded FF obtained in the present work and in the JLM folding-model analyses [Pak01, Bau01], all the results show consistently that the isovector strength of the JLM interaction is much too weak. Since the isovector term of the JLM nucleon OMP has been obtained as the first-order expansion of the mass operator of symmetric nuclear matter perturbed by a neutron excess [Jeu77a], a weakness of the resulting JLM nucleon OMP in asymmetric NM could be expected.

In conclusion of this Chapter, we have studied the charge exchange (p, n) reactions measured with ^{48}Ca, ^{90}Zr, ^{120}Sn and ^{208}Pb targets at the proton incident energies of 35 and 45 MeV [Doe75] within a two-channel coupling formalism using the (p, n) form factors either calculated microscopically in the folding model [Kho02] or determined from the empirical WS parameters of the nucleon global OMP's [Bec69, Var91, Kon03]. The complex isovector density-dependent of the CDM3Y6 interaction, which has been constructed based on the density dependent JLM nucleon OMP [Jeu77b] in chapter 2, was used in the present work. The results obtained with realistic (semi-microscopic) nucleon OMP's for the entrance and exit channels show that the real isovector density dependence of the CDM3Y6 interaction needs to be enhanced by about $20 - 30\%$ to give a good description of the (p, n) reaction. Therefore, one finds that a renormalization of the isovector density dependence of the CDM3Y6 interaction by a factor of 1.3 is needed and used further in HF calculation of asymmetric nuclear matter in Chapter 3. This version of the isovector density-dependent CDM3Y6 interaction has been used in the coupled-channel folding analysis of the ^{18,20,22}O(p, p') scattering in recent work [Chi09] to extract the neutron transition matrix elements M_n as well as the isoscalar and isovector deformation lengths of 2_1^+ states in the Oxygen isotopes. The enhancement of the isovector deformation has been confirmed again in Ref. [Chi09] for open-shell ^{18,20}O nuclei which show a strong core polarization by the valence neutrons.

CHAPTER 6

CONCLUSION

In this thesis, three different parts of nuclear physics have been studied using the effective interactions:

- **Nuclear matter**: the properties of nuclear matter are examined using phenomenological interactions, such as the Gogny ([Ber91], [Cha08]) and Skyrme [Cha98] interactions, and the density-dependent M3Y interactions CDM3Yn [Kho95, Kho07b] and M3Y-Pn [Nak08] within the HF approach.

- **Structure of finite nuclei and neutron stars**: we have calculated the properties of finite nuclei and the Wigner-Seitz cells [Neg73] in the inner crust matter of neutron stars using the finite-range density-dependent interactions, such as the Gogny [Ber91, Cha08] and M3Y-Pn [Nak08] forces, in HF and HF-BCS approaches. The corresponding HF and HF-BCS codes are developed and used in the present calculations.

- **Nuclear reactions**: we have studied the charge-exchange (p, n) reactions using the folding model. In this part, the finite-range density-dependent CDM3Y6 interaction [Kho95, Kho07b] has been used in HF calculations of the nucleon-nucleus optical potentials.

In the first part of this thesis, we have studied the nuclear matter properties using finite-range density-dependent interactions in the framework of the self-consistent

HF mean field. The motivation of the study is to establish a link between the bare NN interaction and nuclear matter properties via the effective Brueckner G-matrix parameterized in the M3Y form [Ana83]. Various readjustments have then to be made to correct for the defects of the G-matrix concerning the saturation properties. It has been known that density dependence in the effective interaction is essential in obtaining the saturation. We have considered two different types of M3Y interactions, the M3Y-Pn ($n = 3, 4, 5$) interactions where the density dependence is assumed to be of zero range, and the CDM3Yn ($n = 3, 4, 6$) interactions with a finite-range density dependence. For the sake of comparison, we have also used the SLy4 interaction as a representative of the Skyrme family, and the D1S and D1N Gogny interactions.

We have concentrated our discussion on several main aspects, the pressure in symmetric nuclear matter and in neutron matter, the density dependence of the symmetry energy $S(\rho)$, the neutron star cooling, and the nuclear matter incompressibility. For the symmetric NM, the main conclusion on NM pressure is that all interactions used here are consistent with the empirical bounds on pressure set by collective flow measurements in relativistic heavy ion collisions, up to $\rho \sim 0.74$ fm^{-3} ($\sim 4.5\rho_0$). On the other hand, the predicted pressure curves show a wide dispersion among the different interactions considered. For the neutron matter, the results obtained with the CDM3Yn and SLy4 interactions agree nicely with the experimental flow data, while those obtained with M3Y-Pn and Gogny (D1S, D1N) interactions are significantly below the data, especially the Gogny D1S which fails badly. This result confirms again that the D1S interaction is not suitable for the study of asymmetric NM. The NM pressure in neutron matter has also been calculated using the latest version of the Gogny force D1M [Gor09], and one observes that this result is better than those of Gogny D1N force and closes to the lower limit of the region of the experimental flow data.

For the NM symmetry energy $S(\rho)$, while the behaviors of the results obtained with the CDM3Yn and SLy4 interactions could be assigned to be of the Asy-stiff type (with symmetry energy steadily increasing with density), the results obtained with the Gogny (D1S, D1N, D1M) and M3Y-Pn interactions belong to the Asy-soft type(with the symmetry energy reaching a maximum and then decreasing to negative values).

One knows that the direct Urca process [Pet92, Lat91] of the neutron star cooling can take place only if the equilibrium proton fraction $x_p \geq 1/9$ (this factor is entirely determined by the nuclear symmetry energy). The values of proton fraction x_p given by the CDM3Yn interactions in the present work show that the direct Urca threshold [Kla06] can be reached at densities around $\rho \approx 0.6$ fm^{-3}. Thus, the direct Urca process is possible if the baryonic matter of neutron stars is described by the CDM3Yn interactions. In contrast, the Gogny (D1S, D1N, D1M) and M3Y-Pn interactions would lead to the indirect or *modified* Urca process, which has a reaction rate of $10^4 \sim 10^5$ times smaller than that of the direct beta decay and the duration of the cooling process should be much longer, because the corresponding proton fractions can never reach the direct Urca threshold. The values of proton fractions obtained with SLy4 interaction can only approach the muon-free threshold $\mathrm{x}_{DU} \approx 1/9$ at $\rho > 0.8$ fm^{-3}. However, a central density can exist only if the neutron star mass $M \geq 2M_{\odot}$ and the direct Urca process is, therefore, impossible in this case.

In the second part of this thesis, related to the finite systems and neutron stars, we have presented the non-relativistic HF and HF-BCS approaches in coordinate representation using finite-range density-dependent interactions in both the mean field and pairing channels. A new method for solving the HF equations in coordinate space with finite range interactions is presented. An iterative scheme is used for solving the integro-differential HF equations via this method. This may be useful because we can avoid the problem of the poles of the trivially equivalent local potential of the Vautherin's method [Vau67]. The basis expansion method is also developed, in which the radial HF equations are solved using a spherical Bessel function basis. We have restricted our study to spherical symmetry. The corresponding HF-BCS Fortran codes with the two methods are made and used to study the properties of doubly magic nuclei, the Sn isotopes and the possibility of bubble structures in ^{22}O, ^{34}Si, ^{46}Ar and ^{68}Ar nuclei using the finite-range density-dependent interactions. The results obtained with the ^{22}O nucleus using the D1S, D1N and M3Y-P4 interactions within the non-relativistic HF and HF-BCS approaches show that the ^{22}O nucleus is a good candidate for a neutron bubble nucleus and confirm again the neutron shell closure at $N = 14$ and 16 in Oxygen isotopes. The central depletion fractions F are

27%, 22% and 40% with D1S, D1N and M3Y-P4 interactions, respectively. However, the neutron bubble structure in ^{22}O disappears in SLy4-HFB calculations [Gra09]. Therefore, a significant model dependence has been found in this case. In contrast, for ^{34}Si the central depletion fractions F of the proton density are 55%, 60% and 37% with D1S, D1N and M3Y-P4 interactions, respectively. Together with the results obtained in Ref. [Gra09], our predictions with finite-range interactions indicate that the ^{34}Si nucleus is an excellent candidate for a proton bubble structure. It would be interesting to have experimental confirmations from future elastic scattering experiments using medium energy electron beam or by direct reactions as suggested in Ref. [Kha08]. For ^{46}Ar nucleus, the results show that a proton bubble is not certain for this nucleus, because the pairing correlations (using D1S and M3Y-P4 interactions) reduce the bubble effect on the proton density. However, a hole occurs with D1N interaction in the center of the HF-BCS proton density. In the case of ^{68}Ar, the depletion in the center of the nucleus vanishes due to the pairing effect with the D1S and D1N interactions. However, the pairing effect cannot prevent a proton bubble with M3Y-P4 interaction. One knows that the possibility of an inversion between the $2s_{1/2}$ and $1d_{3/2}$ proton states can increase when going to the neutron-rich nuclei in Argon isotopes. Therefore, some isotopes more neutron-rich than ^{46}Ar should exhibit a bubble, such as ^{68}Ar.

For the first time we have studied the properties of the WS cells in the inner crust matter of neutron star using the finite-range density dependent interactions in HF and HF-BCS approaches. The calculations are performed with 11 representative WS cells by imposing Dirichlet-Neumann boundary conditions [Neg73] at the edge of the cell and using the finite-range density-dependent D1S and M3Y-P4 interactions in both mean field and pairing channels. Since it is not yet completely established what are the pairing properties of neutron matter, we have also used the density-dependent delta force for the pairing interaction. The parameters of this force have been fixed to reproduce the pairing properties of infinite neutron matter given by microscopic calculations which take into account polarization effects [San04a, Wam93]. For the HF-BCS calculations using the delta force in the pairing channel, the D1S interaction has been used in the mean field channel. With four different pairing interactions (D1S, D1N, M3Y-Pn and delta forces) the main features of the WS cell can be observed in our calculations. It is found that the behaviour of the proton and neutron density distributions are very similar with the three kinds of pairing interactions in the low density region $\rho \sim 2.79 \times 10^{-4}$ fm^{-3} → 5.77×10^{-3} fm^{-3}. One can conclude that the pairing effect is very small in this region. In the high density region, the pairing effect can make an extended "surface" for the neutron density distribution in the cell before they reach a constant density around the outer edge of the cell. However, one cannot obtain the constant neutron gas densities in the cell ^{982}Ge with a finite-range density-dependent interaction. This cell corresponds to the highest-density $\rho = 7.89 \times 10^{-2}$ fm^{-3}, and it seems not to belong to the spherical case as assumed in our study. In all the cells we observe that the density distribution of the nuclear cluster obtained with the case of M3Y-P4 interaction is a little smaller than those obtained with the case of D1S and D1N interactions. This effect may come from the difference of the ranges and the values of pairing gaps in infinite matter given by the two kinds of effective interactions.

The last part of this thesis deals with the nuclear reactions. A consistent coupled-channel analysis of the charge exchange (p,n) reactions to the isobaric analog states of the ground states of ^{48}Ca, ^{90}Zr, ^{120}Sn and ^{208}Pb targets at the proton incident energies of 35 and 45 MeV has been done using the (p,n) form factors either calculated microscopically in the folding model [Kho02, Kho07b] or determined from the existing nucleon global OMP's [Bec69, Var91, Kon03]. Although the isospin dependence of the CH89 global OMP [Var91] has been established based only on the OM studies of the elastic proton and neutron scatterings, it can be used to determine the charge exchange form factor for the (p,n) transition to IAS. This CH89 form factor was shown to account quite well for the (p,n) data if the parameters of the proton OMP are fine tuned to reproduce the measured elastic proton scattering and total reaction cross sections σ_{R}. The complex isovector density dependence of the CDM3Y6 interaction which is carefully parameterized based on the density dependent JLM nucleon OMP [Jeu77b] has been used in the folding model analysis of the (p,n) reaction. Our results show that the isovector strength of the JLM interaction is quite weak to account for the observed (p,n) transitions. The coupled-channel results obtained with realistic (semi-microscopic) nucleon OMP's for the entrance and exit channels have shown that the real isovector density dependence needs to be enhanced by about $20 - 30\%$ to give a good description of the (p, n) reaction. Therefore, the real isovector density dependence of the CDM3Y6 interaction has also been constructed based on the JLM nucleon OMP at energy approaching zero and scaled by a factor 1.3 for further use in the HF calculations of asymmetric nuclear matter which are already discussed in the previous part.

From the ensemble of results obtained in this thesis one can see that the M3Y-Pn (or Gogny) interactions have been carefully parametrized [Nak08] not only to reproduce the saturation properties of symmetric NM like the parameter choice for the CDM3Yn interactions [Kho95], but also to give a good description of the ground state (g.s.) shell structure of magic nuclei. However, we have found by performing spherical HF calculations that the CDM3Yn interactions give a worse description of the g.s. properties of light- and medium mass nuclei with neutron excess compared with the Gogny or M3Y-Pn interactions. Furthermore, the M3Y-Pn interactions have not been much used in folding model analyses of nucleon-nucleus and nucleus-nucleus scattering. Therefore, we plan to improve the G-matrix based interactions in two directions. First, we will readjust the parameters of the CDM3Yn to consistently reproduce the NM saturation properties and g.s. bulk properties of double-closed shell nuclei as well as unstable nuclei. Second, we will apply the M3Y-Pn interactions into the folding model to calculate the nucleon-nucleus and nucleus-nucleus optical model potentials. This would allow one to study both nuclear structure and reaction problems self-consistently with the same starting effective interaction which is itself based on a G-matrix approach. Work in these directions is in progress.

APPENDIX A

A.1 The contributions of the finite range central interaction

The single-particle wave functions $\varphi_i(\vec{r}, \sigma, q)$ of Eq. (4.27) are

$$\varphi_i(\vec{r}, \sigma, q) = \frac{u_\alpha(r)}{r} \mathcal{Y}_{ljm}(\hat{r}, \sigma) \chi_q(\tau), \tag{A.1}$$

where

$$\mathcal{Y}_{ljm}(\hat{r}, \sigma) = \sum_{m_l m_s} < l \frac{1}{2} m_l m_s | jm > Y_{l m_l}(\hat{r}) \chi_{m_s}(\sigma).$$

We use the notation:

$$|i >\equiv \mathcal{Y}_{ljm}(\hat{r}, \sigma) \chi_q(\tau).$$

Using Wigner-Eckart's theorem, we calculate the matrix element of the direct term

$$\begin{aligned}\left\langle ij|V^{(C)}(|\boldsymbol{r_1}-\boldsymbol{r_2}|)|ij\right\rangle &= 4\pi\sum_{\mu SLMJ}\sum_{\nu=1}^{2}A_\nu(S)(-1)^{L+S+J+M}v_L^\nu(r_1,r_2)\times\\ &\times \left\langle l_ij_i|T^{(SL)J}|l_ij_i\right\rangle\left\langle l_jj_j|T^{(SL)J}|l_jj_j\right\rangle\\ &= 4\pi\sum_{\mu SLMJ}\sum_{\nu=1}^{2}A_\nu(S)(-1)^{L+S+J}v_L^\nu(r_1,r_2)\times\\ &\times (-)^{j_i+j_j-m_i-m_j+M}\begin{pmatrix} j_i & J & j_i\\ -m_i & \mu & m_i\end{pmatrix}\begin{pmatrix} j_j & J & j_j\\ -m_j & \mu & m_j\end{pmatrix}\times\\ &\times \left\langle l_ij_i\|T^{(SL)J}\|l_ij_i\right\rangle\left\langle l_jj_j\|T^{(SL)J}\|l_jj_j\right\rangle\\ &= \sum_{SLMJ}\sum_{\nu=1}^{2}A_\nu(S)(-1)^{L+S+J+M}v_L^\nu(r_1,r_2)\widehat{j_i}^2\widehat{j_j}^2\delta_{LJ}\delta_{M0}\delta_{S0}\delta_{L0}\delta_{\mu0}\\ &= \sum_{\nu=1}^{2}\left(W_\nu+\frac{B_\nu}{2}-H_\nu\delta_{q_iq_j}-\frac{M_\nu}{2}\delta_{q_iq_j}\right)v_0^\nu(r_1,r_2)\widehat{j_i}^2\widehat{j_j}^2, \quad \text{(A.2)}\end{aligned}$$

where $\hat{j}=(2j+1)^{1/2}$ and the reduced matrix element is

$$\left\langle l_ij_i\|T^{(SL)J}\|l_jj_j\right\rangle=(-)^{l_i}\frac{\sqrt{2}}{\sqrt{4\pi}}\hat{S}\hat{L}\hat{J}\hat{l}_i\hat{l}_j\hat{j}_i\hat{j}_j\begin{pmatrix} l_i & l_j & L\\ 0 & 0 & 0\end{pmatrix}\begin{Bmatrix} j_i & j_j & J\\ l_i & l_j & L\\ \frac{1}{2} & \frac{1}{2} & S\end{Bmatrix} \qquad \text{(A.3)}$$

we can obtain the direct potential (Hartree potential) $U_i^H(r_1)$ which is presented in Eq. (4.30).

The matrix element of the exchange term is

$$\begin{aligned}
\langle ij|V^{(C)}(|\boldsymbol{r_1}-\boldsymbol{r_2}|)|ji\rangle &= 4\pi\sum_{SLJ\mu}\sum_{\nu=1}^{2}A_\nu(S)(-1)^{L+S+J}v_L^\nu(r_1,r_2) \\
\times(-1)^{j_i+j_j-m_i-m_j+M}&\begin{pmatrix} j_i & J & j_j \\ -m_i & \mu & m_j\end{pmatrix}\begin{pmatrix} j_j & J & j_i \\ -m_j & -\mu & m_i\end{pmatrix} \\
&\times\langle l_ij_i\|T^{(SL)J}\|l_jj_j\rangle\langle l_jj_j\|T^{(SL)J}\|l_ij_i\rangle \\
&= 4\pi\sum_{SLJ\mu}\sum_{\nu=1}^{2}A_\nu(S)(-1)^{L+S+J}v_L^\nu(r_1,r_2) \\
\times(-1)^{j_i+j_j-m_i-m_j+M}&\begin{pmatrix} j_i & j_j & J \\ m_i & -m_j & -\mu\end{pmatrix}\begin{pmatrix} j_i & j_j & J \\ m_i & -m_j & -\mu\end{pmatrix}\times \\
&\times(-1)^{j_i-j_j+L+S+J}|\langle l_ij_i\|T^{(SL)J}\|l_jj_j\rangle|^2 \\
&= 4\pi\sum_{ijSLJ}\sum_{\nu=1}^{2}A_\nu(S)\hat{J}^{-2}v_L^\nu(r_1,r_2)|\langle l_ij_i\|T^{(SL)J}\|l_jj_j\rangle|^2, \qquad \text{(A.4)}
\end{aligned}$$

where we use the relation

$$\langle l_jj_j\|T^{(SL)J}\|l_ij_i\rangle = (-1)^{j_i-j_j+L+S+J}\langle l_ij_i\|T^{(SL)J}\|l_jj_j\rangle$$

and

$$A_\nu(S=0) = W_\nu\delta_{q_iq_j} - H_\nu + \frac{B_\nu\delta_{q_iq_j}-M_\nu}{2};\, A_\nu(S=1) = \frac{B_\nu\delta_{q_iq_j}-M_\nu}{2}. \qquad \text{(A.5)}$$

From the Eq. (A.3) we have

$$\begin{aligned}
|<l_ij_i||T^{(0L)L}||l_jj_j>|^2 &= \frac{1}{4\pi}\hat{l}_i^2\hat{l}_j^2\hat{j}_i^2\hat{j}_j^2\hat{L}^2\begin{pmatrix} l_i & l_j & L \\ 0 & 0 & 0\end{pmatrix}^2\begin{Bmatrix} l_i & j_i & 1/2 \\ j_j & l_j & L\end{Bmatrix}^2 \\
\sum_{S,J}|<l_ij_i||T^{(SL)J}||l_jj_j>|^2 &= \frac{2}{4\pi}\hat{j}_i^2\hat{j}_j^2\hat{J}^2\begin{pmatrix} l_i & l_j & L \\ 0 & 0 & 0\end{pmatrix}^2 \qquad \text{(A.6)}
\end{aligned}$$

Then we can obtain the exchange potential (Fock potential) $U_i^F(r_1,r_2)$ which is presented in Eq. (4.31).

A.2 Numerov method for solving the HF equations

The Numerov method can be used for a precise integration of second-order differential equations. Here, we give some details pertaining to its application to the HF equations (4.38). The radial coordinate r is represented by a mesh of points with a constant spacing h: $r_n = nh$, with $n \in \{0, 1, 2, ..., N\}$. For any quantity $F(r)$ approximated on the mesh we use the notation $F_n \equiv F(r_n)$. Let $y(r)$ be the solution of the differential equation,

$$ay'' + by' + cy = 0 \tag{A.7}$$

If we set $y' = s$, the above second order differential equation becomes two coupled differential equations of the first order:

$$\begin{cases} y' = s \\ s' = F(y, s, r) \end{cases} \tag{A.8}$$

The Numerov algorithm is based on the fourth-order Runge-Kutta formula with a step h,

$$\begin{aligned}
k1 &= h \times F(y_n, s_n, r_n) \\
l1 &= h \times s_n \\
k2 &= h \times F(y_n + \frac{1}{2}l1, s_n + \frac{1}{2}k1, r_n + \frac{h}{2}) \\
l2 &= h \times (s_n + \frac{1}{2}k1) \\
k3 &= h \times F(y_n + \frac{1}{2}l2, s_n + \frac{1}{2}k2, r_n + \frac{h}{2}) \\
l3 &= h \times (s_n + \frac{1}{2}k2) \\
k4 &= h \times F(y_n + \frac{1}{2}l3, s_n + \frac{1}{2}k3, r_n + \frac{h}{2}) \\
l4 &= h \times (s_n + \frac{1}{2}k3)
\end{aligned}$$

$$\begin{aligned} s_{n+1} &= s_n + \frac{k1}{6} + \frac{k2}{3} + \frac{k3}{3} + \frac{k4}{6} + O(h^5) \\ y_{n+1} &= y_n + \frac{l1}{6} + \frac{l2}{3} + \frac{l3}{3} + \frac{l4}{6} + O(h^5) \end{aligned} \tag{A.9}$$

where $O(h^5)$ means that the error in this relation is of the order h^5.

The eigen-energies are found by integrating two linearly dependent solutions, $y^{(1+)}(r)$ and $s^{(1+)}(r)$ (first derivative of the wave function $y^{(1+)}(r)$), from the origin to a given point r_m, called the matching point. These two solutions are selected by imposing that the wave function vanishes near the origin as

$$y^{(1+)} \sim r^{l+1}, s^{(1+)} \sim (l+1)r^l, \text{for } r \to 0, \tag{A.10}$$

whereby we have

$$y_0^{(1+)} = 0 \tag{A.11}$$

and

$$y_1^{(1+)} = Ah^{l+1}, s_1^{(1+)} = A(l+1)h^l. \tag{A.12}$$

Next, another two linearly dependent solutions, $y^{(1-)}(r)$ and $s^{(1-)}(r)$, are found by backward integration from the wall of the box $R_{box} \equiv r_N$ to r_m; again imposing that the wave function vanishes near r_N for the Dirichlet boundary conditions

$$y_N^{(1-)} = 0, s_N^{(1-)} = B, \tag{A.13}$$

or the first derivatives of the wave function vanishes near r_N for the Neumann boundary conditions.

$$y_N^{(1-)} = B, s_N^{(1-)} = 0. \tag{A.14}$$

The eigenenergies are found by requiring that the solutions $y_m^{(1+)}$ and $y_m^{(1-)}$ have the same values, and the first derivatives are continuous at $r = r_m$. This matching condition reads as,

$$\begin{vmatrix} y_m^{(1+)} & y_m^{(1-)} \\ s_m^{(1+)} & s_m^{(1-)} \end{vmatrix} = 0. \tag{A.15}$$

The eigen-energies and the HF wave function are found when the matching condition reach to the zero of the determinant of the 2×2 matrix and the number of nodes in that state is correct. This means that one starts from 2 trial values of eigen-energy, $\epsilon_>$ and $\epsilon_<$, which give opposite signs for the determinant (A.15), then one knows that the exact value ϵ is between $\epsilon_>$ and $\epsilon_<$, and by bi-partition one makes the intervel $[\epsilon_>, \epsilon_<]$ smaller and smaller.

A.3 Time-reversed states

Let us represent by A a state given by the following quantum numbers

$$A = (a, m_a) = (n_a l_a j_a, m_a) \tag{A.16}$$

We consider here only ground state phenomena, and therefore, we use only time-even variational independent-quasiparticle wave functions. The time-reversal operator can be represented as a product of the Pauli matrix $\hat{\sigma}_y$ and the complex conjugation operator:

$$\hat{T} = -i\hat{\sigma}_y \hat{K} \tag{A.17}$$

Where $\hat{\sigma}_y = \begin{pmatrix} 0 & -i \\ i & 0 \end{pmatrix}$

We rewrite the single-particle wave function $\varphi(\boldsymbol{r}, \sigma, q)$ of Eq. (A.1) in the following form:

$$\begin{aligned} \varphi_A &= R_{l_a j_a}(r) \mathcal{Y}_{l_a j_a m_a} \\ &= R_{l_a j_a}(r) (-1)^{l_a - \frac{1}{2} + m_a} \hat{j}_a \begin{pmatrix} l_a & \frac{1}{2} & j_a \\ \mu_a & s_a & -m_a \end{pmatrix} Y_{l_a \mu_a} \chi_{\frac{1}{2}}(s_a) \end{aligned} \tag{A.18}$$

We have

$$\begin{aligned} \hat{T}\varphi_A &= \varphi_{\bar{A}} \\ &= R_{l_a j_a}(r)(-i)(-1)^{l_a - \frac{1}{2} + m_a} \hat{j}_a \begin{pmatrix} l_a & \frac{1}{2} & j_a \\ \mu_a & s_a & -m_a \end{pmatrix} Y_{l_a \mu_a} (-1)^{\mu_A} Y_{l_a - \mu_a} [\hat{\sigma}_y \chi_{\frac{1}{2}}(s_a)]. \end{aligned} \tag{A.19}$$

Using

$$\begin{pmatrix} 0 & -i \\ i & 0 \end{pmatrix} \begin{pmatrix} 1 \\ 0 \end{pmatrix} = \begin{pmatrix} 0 \\ i \end{pmatrix} = (-1)^{\frac{1}{2}-s_a} i \begin{pmatrix} 0 \\ 1 \end{pmatrix} \text{ for } s_a = +\frac{1}{2}$$

and

$$\begin{pmatrix} 0 & -i \\ i & 0 \end{pmatrix} \begin{pmatrix} 0 \\ 1 \end{pmatrix} = \begin{pmatrix} -i \\ 0 \end{pmatrix} = (-1)^{\frac{1}{2}-s_a} i \begin{pmatrix} 1 \\ 0 \end{pmatrix} \text{ for } s_a = -\frac{1}{2}$$

One obtains, $[\hat{\sigma}_y \chi_{\frac{1}{2}}(s_a)] = (-1)^{\frac{1}{2}-s_a} i \chi_{\frac{1}{2}}(-s_a)$

The time-reversed state is:

$$\varphi_{\bar{A}} = (-1)^{l_a+j_a-m_a} \varphi_{a,-m_a} \tag{A.20}$$

A.4 Gap equation with angular momentum coupling

We can rewrite Eq. (4.66) in the following form (see Eq. (6.50) of Ref. [Rin80]):

$$\Delta_A = -\frac{1}{2} \sum_{bm_b} < A\bar{A}|V_p|B\bar{B} - \bar{B}B > u_B v_B \tag{A.21}$$

where V_p is the pairing interaction.

Using the definition (A.20) of the time-reversed states and the fact that $\Delta_A = \Delta_a$ is independent of m_a, have

$$\begin{aligned}
\Delta_a &= -\frac{1}{2}\hat{j_a}^{-2} \sum_{bm_am_b} < A\bar{A}|V_p|B\bar{B} - \bar{B}B > u_b v_b \\
&= -\frac{1}{2}\hat{j_a}^{-2} \sum_{bm_am_b} u_b v_b (-1)^{l_a+j_a-m_a} (-1)^{l_b+j_b-m_b} \left[\sum_{JM} \hat{J}^2 \begin{pmatrix} j_a & j_a & J \\ m_a & -m_a & -M \end{pmatrix} \right. \\
&\times \begin{pmatrix} j_b & j_b & J \\ m_b & -m_b & -M \end{pmatrix} G_J(aabb) \\
&- \left. \sum_{JM} \hat{J}^2 \begin{pmatrix} j_a & j_a & J \\ m_a & -m_a & -M \end{pmatrix} \begin{pmatrix} j_b & j_b & J \\ -m_b & m_b & -M \end{pmatrix} G_J(aabb) \right]
\end{aligned} \tag{A.22}$$

where $G_J(aabb)$ is the pairing matrix element.

Using the relation

$$(-1)^{j_a-m_a}=\hat{j}_a\begin{pmatrix} j_a & j_a & 0\\ m_a & -m_a & 0\end{pmatrix}$$

we obtain

$$\begin{aligned}\sum_{m_a}(-1)^{j_a-m_a}\begin{pmatrix} j_a & j_a & J\\ m_a & -m_a & -M\end{pmatrix} &= \hat{j}_a\begin{pmatrix} j_a & j_a & 0\\ m_a & -m_a & 0\end{pmatrix}\begin{pmatrix} j_a & j_a & J\\ m_a & -m_a & -M\end{pmatrix}\\ &= \hat{j}_a\delta_{J0}\delta_{M0}. \qquad (A.23)\end{aligned}$$

The other terms are similarly calculated. The gap equation with angular momentum coupling becomes:

$$\Delta_a=-\sum_b(-1)^{l_a+l_b}\hat{j}_a^{\,-1}\hat{j}_bG_0(aabb)u_bv_b. \qquad (A.24)$$

Then, the gap equation (4.68) can be rewritten in the following form:

$$\Delta_a=-\frac{1}{2}\sum_b(-1)^{l_a+l_b}\hat{j}_a^{\,-1}\hat{j}_bG_0(aabb).\frac{\Delta_b}{\sqrt{(\varepsilon_b-\lambda)^2+\Delta_b^2}} \qquad (A.25)$$

Here

$$G_0(aabb)=<aa|V_p|bb>_{00} \qquad (A.26)$$

is the $J=0$ coupled matrix element. We will show how to calculate this coupled matrix element using delta interactions or the finite range interactions in the next sections.

A.5 Pairing matrix element

The coupled matrix element of the pairing interaction $V_p(1,2)$ is:

$$<ac|V_p(1,2)|bd>_{JM}=\sum_{\mathrm{all}m}<j_aj_cm_am_c|JM><j_bj_dm_bm_d|JM><AC|V_p(1,2)|BD> \qquad (A.27)$$

Here, $< AC|V_p(1,2)|BD >$ is the uncoupled matrix element.

A.5.1 Particle-particle matrix elements with a finite-range interaction

We first take for $V_p(1,2)$ a Gogny interaction which contains a sum of two gaussians, a zero-range density-dependent part and a zero-range spin-orbit part. Within the parametrisation D1S (D1N) that we adopt in this work the zero-range density-dependent part does not contribute. Since the contribution of the spin-orbit part is quite small, we neglect it in this work.

We use the central part $V^{(C)}(1,2)$ of Eq. (2.26) to calculate matrix elements between neutrons or between protons. Thus, the operator P^τ can be replace by 1. For the operator P^σ, we write $P_\sigma = \frac{1+\boldsymbol{\sigma_1}.\boldsymbol{\sigma_2}}{2}$, and obtain:

$$V_p(1,2) = \sum_{\nu=1}^{2}(A_\nu(0) + A_\nu(1)\boldsymbol{\sigma_1}\boldsymbol{\sigma_2})V_\nu(1,2), \tag{A.28}$$

where

$$A_\nu(0) = W_\nu - H_\nu + \frac{B_\nu - M_\nu}{2}, A_\nu(1) = \frac{B_\nu - M_\nu}{2}.$$

We use the multipole decomposition (4.18) for Gaussian functions and the tensor $T^{(SL)K}_{(\mu)}$ of Eq. (4.23) to calculate the uncoupled matrix element as

$$\begin{aligned} < AC|V_p(1,2)|BD > &= \sum_{\nu LSKM}(-1)^{L+S+K+M}A_\nu(S) \\ &\times \int d\boldsymbol{r_1}d\boldsymbol{r_2}v^\nu_L(r_1,r_2)R_a(r_1)R_b(r_1)R_c(r_2)R_d(r_2) \\ &\times < \mathcal{Y}_A|T^{(SL)K}_{(1)}|\mathcal{Y}_B >< \mathcal{Y}_C|T^{(SL)K}_{(2)}|\mathcal{Y}_D > \end{aligned} \tag{A.29}$$

Using the Wigner-Eckart theorem, we have

$$
\begin{aligned}
< \mathcal{Y}_A|T^{(SL)K}_{(1)}|\mathcal{Y}_B >< \mathcal{Y}_C|T^{(SL)K}_{(2)}|\mathcal{Y}_D > &= (-1)^{j_a+j_c-m_a-m_b+q}\begin{pmatrix} j_a & K & j_b \\ -m_a & q & m_b \end{pmatrix} \\
&\times \begin{pmatrix} j_c & K & j_d \\ -m_b & -q & m_d \end{pmatrix} < \mathcal{Y}_a\|T^{(SL)K}_{(1)}\|\mathcal{Y}_b >< \mathcal{Y}_c\|T^{(SL)K}_{(2)}\|\mathcal{Y}_d >
\end{aligned} \tag{A.30}
$$

where the reduced matrix element $< \mathcal{Y}_a\|T^{(SL)K}\|\mathcal{Y}_b >$ is given by Eq. (A.3).

We now can rewrite the coupled matrix element in Eq. A.27 as,

$$
\begin{aligned}
< ac|V_p(1,2)|bd >_{JM} &= \sum_{\nu LSK}(-1)^{\mathcal{P}}A_\nu(S)\int d\boldsymbol{r_1}d\boldsymbol{r_2}v^\nu_L(r_1,r_2) \\
&\times R_a(r_1)R_b(r_1)R_c(r_2)R_d(r_2) \\
&\times \begin{pmatrix} j_a & j_c & J \\ m_a & m_c & -M \end{pmatrix}\begin{pmatrix} j_b & j_d & J \\ m_b & m_d & -M \end{pmatrix} \\
&\times \begin{pmatrix} j_a & K & j_b \\ -m_a & q & m_b \end{pmatrix}\begin{pmatrix} j_c & K & j_d \\ -m_c & -q & m_d \end{pmatrix} \\
&\times \hat{J}^2 < \mathcal{Y}_a\|T^{(SL)K}_{(1)}\|\mathcal{Y}_b >< \mathcal{Y}_c\|T^{(SL)K}_{(2)}\|\mathcal{Y}_d >
\end{aligned} \tag{A.31}
$$

with the total phase $\mathcal{P} = (-1)^{(L+S+K+q)+(j_a-j_c+M)+(j_b-j_d+M)+(j_a-m_a+j_c-m_c)}$. Then, we can re-express all the above 3j symbols and the phase $(-1)^{\mathcal{P}}$ in the following form [Bri93]:

$$
\begin{aligned}
&(-1)^{\mathcal{P}}\begin{pmatrix} j_a & j_c & J \\ m_a & m_c & -M \end{pmatrix}\begin{pmatrix} j_b & j_d & J \\ m_b & m_d & -M \end{pmatrix}\begin{pmatrix} j_a & K & j_b \\ -m_a & q & m_b \end{pmatrix} \\
&\times \begin{pmatrix} j_c & K & j_d \\ -m_c & -q & m_d \end{pmatrix} = (-1)^{L+S+K+J+j_c+j_b}\hat{J}^{-2}\begin{Bmatrix} j_d & j_b & J \\ j_a & j_c & K \end{Bmatrix}
\end{aligned} \tag{A.32}
$$

Thus, the coupled matrix element in Eq. (A.31) can be obtained as

$$\begin{aligned} < ac|V_p(1,2)|bd >_{JM} = & \int r_1^2 dr_1 r_2^2 dr_2 \sum_{\nu LSK} (-1)^{\mathcal{P}} A_\nu(S) v_L^\nu(r_1,r_2) \\ & \times R_a(r_1) R_b(r_1) R_c(r_2) R_d(r_2) \\ \times & \begin{Bmatrix} j_d & j_b & J \\ j_a & j_c & K \end{Bmatrix} < \mathcal{Y}_a \| T_{(1)}^{(SL)K} \| \mathcal{Y}_b >< \mathcal{Y}_c \| T_{(2)}^{(SL)K} \| \mathcal{Y}_d > \end{aligned} \tag{A.33}$$

Here the total phase is $\mathcal{P} = L + S + K + J + j_b + j_c$. This coupled matrix element can be further simplified for the pairing matrix elements $< aa|V_p(1,2)|bb >_{00}$ as,

$$\begin{aligned} < aa|V_p(1,2)|bb >_{00} &= \hat{j}_a^{-1} \hat{j}_b^{-1} \int r_1^2 dr_1 r_2^2 dr_2 \sum_{\nu LSK} A_\nu(S) v_L^\nu(r_1,r_2) \\ &\times R_a(r_1) R_b(r_1) R_c(r_2) R_d(r_2) \\ &\times (-1)^{L+S} | < \mathcal{Y}_a \| T^{(SL)K} \| \mathcal{Y}_b > |^2 \end{aligned} \tag{A.34}$$

A.5.2 Particle-particle matrix elements with a delta interaction

The density-dependent delta interaction will be taken in the following form:

$$V_p(1,2) = V_0 \left(1 - \eta \left(\frac{\rho(r_{12})}{\rho_0} \right)^\alpha \right) \delta(\boldsymbol{r_1} - \boldsymbol{r_2}) \tag{A.35}$$

The delta function is expanded on the basis of spherical harmonics:

$$\delta(\boldsymbol{r_1} - \boldsymbol{r_2}) = \frac{\delta(r_1 - r_2)}{r_1 r_2} \sum_{L\mu} (-1)^\mu Y_L^\mu(1) Y_L^{-\mu}(2) \tag{A.36}$$

The calculation of the coupled matrix element follows a similar to that of subsection B.3.1. The result is much simpler. The pairing matrix element is:

$$< aa|V_p(1,2)|bb >_{00} = \frac{1}{2} (-1)^{l_a + l_b} \frac{\hat{j}_a \hat{j}_b}{4\pi} I_{aabb} \tag{A.37}$$

where

$$I_{aabb} = V_0 \int \left(1 - \eta \left(\frac{\rho(r)}{\rho_0}\right)^{\alpha}\right) R_a^2(r) R_b^2(r) d\boldsymbol{r}. \tag{A.38}$$

List of Figures

List of Tables

BIBLIOGRAPHY

[Abr72] M. Abramowitz and I.A. Stegun, Handbook of Mathematical Functions, (Dover Publ., New York, 1972).

[Akm98] A. Akmal, V.R. Pandharipande, D.G. Ravenhall, Phys. Rev. **C 58**, 1804 (1998).

[Alm95] T. Alm, Gopke, W. Bauer, F. Daffin, and M. Schmidt, Nucl. Phys. **A587**, 815 (1995).

[Ana83] N. Anantaraman, H. Toki and G.F. Bertsch, Nucl. Phys. **A398** (1983) 269.

[Aru04] P. Arumugam, B.K. Sharma, P.K. Sahu, S.K. Patra, Tapas Sil, M. Centelles, and X. Viñas, Phys. Lett. **B 601**, 51 (2004).

[ATL] http://www.phys.anl.gov/atlas/.

[Aud95] G. Audi and A.H. Wapstra, Nucl. Phys. **A595**, 409 (1995).

[Bal05a] M. Baldo, U. Lombardo, E.E. Saperstein, and S.V. Tolokonnikov, Phys. At. Nucl. **68**, 1812 (2005).

[Bal05b] M. Baldo, E.E. Saperstein, and S.V. Tolokonnikov, Nucl. Phys. **A750**, 409 (2005).

[Bal06] M. Baldo, E.E. Saperstein, and S.V. Tolokonnikov, Nucl. Phys. **A775**, 235 (2006).

[Bal07] M. Baldo and C. Maieron, J. Phys. **G 34**, R243 (2007).

[Bar57] J. Bardeen, L.N. Cooper and J.R. Schrieffer, Phys. Rev. **108**, 1175 (1957).

[Bas08] D.N. Basu, P. Roy Chowdlhury, C. Samanta, Nucl. Phys. **A811**, 140 (2008).

[Bau98] E. Bauge, J.P. Delaroche, and M. Girod, Phys. Rev. **C 58**, 1118 (1998).

[Bau01] E. Bauge, J.P. Delaroche, and M. Girod, Phys. Rev. **C 63**, 024607 (2001).

[Bec69] F.D. Bechetti and G.W. Greenlees, Phys. Rev. **182**, 1190 (1969).

[Bec06] E. Becheva et al., Phys. Rev. Lett. **96**, 012501 (2006).

[Bei75] M. Beiner, H. Flocard, N.V. Giai and P. Quentin, Nucl. Phys. **A238**, 29 (1975).

[Ben03] M. Bender, K. Rutz, P.G. Reinhard, J.A. Maruhn, W. Greiner, Phys. Rev. **C 60**, 55 (2003).

[Ben05] K. Bennaceur, J, Dobaczewski, Comp. Phys. Commu. **168**, 96 (2005).

[Ber77] G. Bertsch, J. Borysowicz, H. McManus, and W.G. Love, Nucl. Phys. **A284**, 399 (1977).

[Ber91] J.F. Berger, M. Girod, and D. Gogny, Comput. Phys. Commun. **63**, 365 (1991).

[Bet57] H.A. Bethe and J. Goldstone, Proc. Roy. Soc. **A238**, 157 (1957).

[Bet90] H.A. Bethe, Rev. Mod. Phys. **62**, 801 (1990).

[Bjo65] J.D. Bjorken, S.D. Drell, *Relativistic quantum fields*, McGraw-Hill, New York, 1965.

[Bla77] J.P. Blaizot and D. Gogny, Nucl. Phys. **A284**, 429 (1977).

[Boh76] O. Bohigas, X. Campi, H. Krivine, J. Treiner, Phys. Lett. **B 64**, 381 (1976).

[Boz06] P. Bozek, D.J. Dean, and H. Müther, Phys. Rev. **C 74**, 014303 (2006).

[Bra05] V. Baran, M. Colonna, V. Greco and M. Di Toro, Phys. Rep. **410**, 335 (2005).

[Bra85] M. Brack, C. Guet, and H.B. Håkansson, Phys. Rep. **123**, 276 (1985).

[Bri67] D.M. Brink and E. Boeker, Nucl. Phys. **91**, 1 (1967).

[Bri77] F.A. Brieva and J.R. Rook, Nucl. Phys. **A291**, 299 (1977); Nucl. Phys. **A291**, 317 (1977).

[Bri93] D.M. Brink and G.R. Satchler, Angular Momentum, (Oxford, 1993).

[Bro98] B.A. Brown, Phys. Rev. **C 58**, 220 (1998).

[Bro00] B.A. Brown, Phys. Rev. Lett. **85**, 5296 (2000).

[Bru58] K. A. Brueckner, J. L. Gammel, H. Weitzner, Phys. Rev. **110**, 431 (1958).

[Bru67] K.A. Brueckner, S.A. Coon and J. Dabrowski, Phys. Rev. **168**, 1184 (1967).

[Cam73] X. Campi, D.W.L. Sprung, Phys. Lett. **B 46**, 291 (1973).

[Car75] J.D. Carlson, C.D. Zafiratos, and D.A. Lind, Nucl. Phys. **A249**, 29 (1975).

[Car96] R.F. Carlson, At. Data and Nucl. Data Tables **63**, 93 (1996).

[Cas00] R.F. Casten and B.M. Sherrill, Prog, Part, Nucl. Phys. **45**, 171 (2000).

[Cav82] J.M. Cavedon, et al., Phys. Rev. Lett. **49**, 978 (1982).

[Cen09] M. Centelles, X. Roca-Maza, X. Vinas, and M. Warda, Phys. Rev. Lett. **102**, 122502 (2009).

[CER] http://isolde.web.cern.ch/isolde.

[Cha97] E. Chabanat, P. Bonche, P. Haensel, J. Meyer, R. Schaeffer, Nucl. Phys. **A627**, 710 (1997).

[Cha98] E. Chabanat, P. Bonche, P. Haensel, J. Meyer, R. Schaeffer, Nucl. Phys. **A635**, 231 (1998).

[Cha08] F. Chappert, M. Girod, S. Hilaire, Phys. Lett. **B 668**, 420 (2008).

[Cha07] N. Chamel,S. Naimi, E. Khan, and J. Margueron, Phys. Rev. **C 75**, 055806 (2007).

[Cha09] N. Chamel, J. Margueron, and E. Khan, Phys. Rev. **C 79**, 012801(R) (2009).

[Che85] T. Cheon, K. Takayanagi and K. Yazaki, Nucl. Phys. **A437** (1985) 301; Nucl. Phys. **A445** (1985) 227.

[Che05] L.W. Chen, C.M. Ko, B.A. Li, Phys. Rev. Lett. **94**, 032701 (2005).
L.W. Chen, C.M. Ko, B.A. Li, Phys. Rev. **C 72**, 064309 (2005).

[Chi09] N.D. Chien and D.T. Khoa, Phys. Rev. **C 79**, 034314 (2009).

[Chu96] L. Chulkov, G. Kraus, O. Bochkare, P. Egelhof, H. Geissel, M. Golovkov, H. Irnich, and Z. Janas, Nucl. Phys. **A603**, 219 (1996).

[Dal04] E.N.E. van Dalen, C. Fuchs, and A. Faessler, Nucl. Phys. **A744**, 227 (2004). E.N.E. van Dalen, C. Fuchs, and A. Faessler, Eur. Phys. J. **A 31**, 29 (2007).

[Dal09] E.N.E. van Dalen, P. G*ö*gelein, and H. M*ü*ther, arXiv:0904.1471v1 (2009).

[Dan02] P. Danielewicz, R. Lacey and W.G. Lynch, Science **298**, 1592 (2002).

[Das03] C.B. Das, S. Das Gupta, C. Gale, and B.A. Li, Phys. Rev. **C 67**, 034511 (2003).

[Dec80] J. Dechargé and D. Gogny, Phys. Rev. **C 21**, 1568 (1980).

[Dec03] J. Dechargé, J.-F. Berger, M. Girod, K. Dietrich, Nucl. Phys. **A176**, 55 (2003).

[Del95] D.S. Delion, M. Baldo, and U. Lombardo, Nucl. Phys. **A593**, 151 (1995).

[Doe75] R.R. Doering, D.M. Patterson, and A. Galonsky, Phys. Rev. **C 12**, 378 (1975).

[Dor98] P.J. Dortmans, K. Amos, S. Karataglidis and J. Raynal, Phys. Rev. **C 58**, 2249 (1998); K. Amos, P.J. Dortmans, S. Karataglidis, H.V. von Geramb and J. Raynal, Adv. in Nucl. Phys. **25**, 275 (2001).

[Dou00] F. Douchin, P. Haensel, Phys. Lett., bf B 485, 107 (2000).

[Dov72] C.B. Dover and N. Van Giai, Nucl. Phys. **A190**, 373 (1972).

[Eis75] J.M. Eisenberg and W. Greiner, *Nuclear Theory*, North Holland, Amsterdam, New York, 1975.

[Ele07] Z. Elekes et al., Phys. Rev. Lett. **98**, 102502 (2007).

[Fes92] H. Feshbach, *Theoretical Nuclear Physics*, Vol. II (Wiley, NY, 1992).

[Fet03] A.L. Fetter and J.D. Walecka, *Quantum Theory of Many-Particle Systems* (Dover Publications Inc., 2003).

[Fri67] M.P. Fricke, E.E. Gross, B.J. Morton, and A. Zucker, Phys. Rev. **156**, 1207 (1967).

[Fri81] B. Friedman, V.R. Pandharipande, Nucl. Phys. **A361**, 502 (1981).

[Fur02] R.J. Furnstahl, Nucl. Phys. **A706**, 85 (2002).

[GAN] http://www.ganil.fr/.

[Gar99] E. Garrido, P. Sarriguren, E. Moya de Guerra and P. Schuck, Phys. Rev. **C60**, 054323 (1999).

[Gau06] L. Gaudefroy et al., Phys. Rev. Lett. **97**, 092501 (2006).
L. Gaudefroy et al., Phys. Rev. Lett. **99**, 099202 (2007).

[Gia81] N.V. Giai and H. Sagawa, Phys. Lett. **B 106**, 379 (1981).

[Gle91] N.K. Glendenning and S.A. Moszkowski, Phys. Rev. Lett. **67**, 2414 (1991).

[Gle00] N.K. Glendenning, *Compact Stars: Nuclear Physics, Particle Physics and General Relativity* (Springer: Springer-Verlag New York, Inc. 2000).

[Gog75] D. Gogny, Proceeding of the International Conference on Nuclear Selfconsistent Fields, Trieste, 1975. G. Ripka and M. Porneuf, Eds. North Holland, Amsterdam, 1975.

[Goo79] A.L. Goodman, Adv. Nucl. Phys. **11**, 263 (1979).

[Gor09] S. Goriely, S. Hilaire, M. Girod, and S. Péru, Phys. Rev. Lett. **102**, 242501 (2009).

[Gra01] M. Grasso, N. Sandulescu, N. Van Giai, and R.J. Liotta, Phys. Rev. **C 64**, 064321 (2001).

[Gra02] M. Grasso, N. Van Giai, N. Sandulescu, Phys. Lett. **B 535**, 103 (2002).

[Gra07] M. Grasso, Z.Y. Ma, E. Khan, J. Margueron, N.V. Giai, Phys. Rev. **C 76**, 044319 (2007).

[Gra08] M. Grasso, E. Khan, J. Margueron, N. Van Giai, Nucl. Phys. **A807**, 1 (2008).

[Gra09] M. Grasso, *et al.*, Phys. Rev. **C 79**, 034318 (2009).

[Gru72] C.R. Gruhn, T.Y.T. Kuo, C.J. Maggiore, and B.M. Preedom, Phys. Rev. **C 6**, 944 (1972).

[GSI] http://www-aix.gsi.de/.

[Gus89] P.P. Guss, R.C. Byrd, C.R. Howell, R.S. Pedroni, G. Tungate, and R.L. Walter, Phys. Rev. **C 39**, 405 (1989).

[Han95] P.G. Hansen, A.S. Jensen and B. Jonson, Ann. Rev. Nucl. Part. Sci. **45**, 591 (1995).

[Has08] K. Hasnaoui, PhD Thesis, Caen University, 2008,*http://tel.archives-ouvertes.fr/tel-00337606/fr*.

[Hil06] S. Hilaire, M. Girod, http://www-phynu.cea.fr/ science_en_ligne/ carte_potentiels_microscopiques/carte_potentiel_nucleaire.htm (2006).

[Hof98] F. Hofman and H. Lenske, Phys. Rev. **C 57**, 2281 (1998).

[Hof08] C.R. Hoffman *et al.*, Phys. Rev. Lett. **100**, 152502 (2008).

[HRI] http://www.phy.ornl.gov/hribf/.

[Huf72] J. Hüfner and C. Mahaux, Ann. Phys. **73**, 525 (1972).

[Jeu77a] J.P. Jeukenne, A. Lejeune, and C. Mahaux, Phys. Rev. **C 15**, 10 (1977).

[Jeu77b] J. P. Jeukenne, A. Lejeune and C. Mahaux, Phys. Rev. **C 16**, 80 (1977).

[Jon00] G.C. Jon *et al.*, Phys. Rev. **C 62**, 044609 (2000).

[Kad87] S.G. Kadenski, P.A. Lukyanovich, Yu. I. Remesov, and V.I. Furman, Sov. J. Nucl. Phys. **45**, 585 (1987).

[Kha01] E. Khan *et al.*, Nucl. Phys. **A 694**, 103 (2001).

[Kha05] E. Khan, N. Sandulescu, and N.V. Giai, Phys. Rev. **C 71**, 042801(R) (2005).

[Kha08] E. Khan, M. Grasso, J. Margueron, N.V. Giai, Nucl. Phys. **A 800**, 37 (2008).

[Kho] D.T. Khoa, the Fortran code DFPD4, unpublished.

[Kho93] D.T. Khoa and W. von Oertzen, Phys. Lett. **B 304**, 8 (1993).

[Kho95] D.T. Khoa and W. von Oertzen, Phys. Lett. **B 342**, 6 (1995).

[Kho96] D.T. Khoa, W. von Oertzen, and A.A. Ogloblin, Nucl. Phys. **A602**, 98 (1996).

[Kho97] D. T. Khoa, G.R. Satchler and W. von Oertzen, Phys. Rev. **C 56** (1997) 954.

[Kho02] D.T. Khoa, E. Khan, G. Colò, and N. Van Giai, Nucl. Phys. **A706**, 61 (2002).

[Kho03] D.T. Khoa, Phys. Rev. **C 68**, 011601(R) (2003).

[Kho05] D.T. Khoa and H.S. Than, Phys. Rev. **C 71**, 044601 (2005).

[Kho07a] D.T. Khoa, W. von Oertzen, H.G. Bohlen, and S. Ohkubo, J. Phys. **G 34**, R111 (2007).

[Kho07b] Dao T. Khoa, Hoang Sy Than, Do Cong Cuong, Phys. Rev. **C 76**, 014603 (2007).

[Kla06] T. Klähn *et al.*, Phys. Rev. **C 74**, 035802 (2006).

[Kon03] A.J. Koning and J.P. Delaroche, Nucl. Phys. **A713**, 231 (2003).

[Kri80] H. Krivine, J. Treiner and O. Bohigas, Nucl. Phys. **A336**, 155 (1980).

[Kuc91] H. Kucharek and P. Ring, Z. Phys. **A339**, 23 (1991).

[Lan62] A.M. Lane, Phys. Rev. Lett. **8**, 171 (1962).

[Lat91] J.M. Lattimer, C.J. Pethick, M. Prakash, P. Haensel, Phys. Rev. Lett. **66**, 2701 (1991) .

[Lat04] J.M. Lattimer and M. Prakash, Science **304**, 536 (2004).

[Lej80] A. Lejeune, Phys. Rev. **C 21**, 1107 (1980).

[Li01] *Isospin Physics in Heavy Ion Collisions at Intermediate Energies,* , Edited by Bao-An Li and W. Schroder (Nova Science, New York, 2001).

[Li06] Z.H. Li, U. Lombardo, H.J. Schulze, W. Zuo, L.W. Chen, and H.R. Ma, Phys. Rev. **C 74**, 047304 (2006).

[Li07] T. Li *et al.*, Phys. Rev. Lett. **99**, 162503 (2007).

[Li08] Bao-An Li, Lie-Wen Chen and Che Ming Ko, Phys. Rep. **464**, 113 (2008).

[Mac78] R.S. Mackintosh, Nucl. Phys. **A307**, 365 (1978); B.Z. Georgiev and R.S. Mackintosh, Nucl. Phys. **A307**, 377 (1978).

[Mag04] P. Magierski, Int. J. Mod. Phys. **E 13**, 371 (2004).

[Mon07] C. Monrozeau, J. Margueron, and N. Sandulescu, Phys. Rev. **C 75**, 065807 (2007).

[Mue93] A.C. Mueller and B.M. Sherrill, Ann. Rev. Nucl. Part. Sci. **43**, 529 (1993).

[Mue01] A.C. Mueller, Prog. Part. Nuclc. Phys. **46**, 359 (2001).

[NAG70] http://www.nag.co.uk/numeric/.

[Nak02] H. Nakada, M. Sato, Nucl. Phys. **A699**, 511 (2002).

[Nak03] H. Nakada, Phys. Rev. **C 68**, 014316 (2003).

[Nak08] H. Nakada, Phys. Rev. **C 78**, 054301 (2008).

[Neg70] J.W. Negele, Phys. Rev. **C 1**, 1260 (1970).

[Neg72] J.W. Negele and D. Vautherin, Phys. Rev. **C 5**, 1472 (1972).

[Neg73] J.W. Negele, D. Vautherin, Nucl. Phys. **A207**, 298 (1973).

[NNDC] Database of the National Nuclear Data Center, Brookhaven, http://www.nndc.bnl.gov/.

[NSC] http://www.nscl.msu.edu/.

[Ono03] A. Ono, P. Danielewicz, W.A. Friedman, W.G. Lynch, and M.B. Tsang, Phys. Rev. **C 68**, 051601(R) (2003).

[Ott89] E.W. Otten, in Treatise on Heavy-Ion Science, vol. 8. Nuclei far from Stability, ed. D.A. Bromley (Plenum, New York, 1989).

[Pag04] D. Page, J.M. Lattimer, M. Prakash, and A.W. Steiner, Astro. Phys. J. Suppl. Series **155**, 623 (2004).

[Pak01] A. Pakou, N. Alamanos, P. Roussel-Chomaz, F. Auger, D. Rosengrant, and A. de Vismes, Nucl. Phys. **A691**, 661 (2001).

[Pea00] J.M. Pearson and R.C. Nayak, Nucl. Phys. **A668**, 163 (2000).

[Pet92] C.J. Pethick, Rev. Mod. Phys. **64**, 1133 (1992).

[Pet95] C.J. Pethick and D.G. Ravenhall, Annu. Rev. Nucl. Part. Sci. **45** (1995).

[Pie09] J. Piekarewicz and M. Centelles, Phys. Rev. **C 79**, 054311 (2009).

[Rap78] J. Rapaport, T.S. Cheema, D.E. Bainum, R.W. Finlay, and J. D. Carlson, Nucl. Phys. **A296**, 95 (1978).

[Ray72] J. Raynal, Computing as a Language of Physics (IAEA, Vienna, 1972) p.75; J. Raynal, coupled-channel code ECIS97 (unpublished).

[Rei95] P.G. Reinhard and H. Flocard, Nucl. Phys. **A584**, 467 (1995).

[Rei99] P.G. Reinhard, D.J. Dean, W. Nazarewicz, J. Dobaczewski, J.A. Maruhn and M.R. Strayer, Phys. Rev. **C 60**, 014316 (1999).

[RIA] http://www.orau.org/ria/.

[RIK] http://www.riken.go.jp/engn/.

[Rik84] L. Rikus, K. Nakano and H.V. von Geramb, Nucl. Phys. **A414** (1984) 413.

[Rin80] P. Ring and P. Schuck, *The nuclear many-body problem*, Springer-Verlag, New York (1980).

[San00] N. Sandulescu, N. Van Giai, R.J. Liotta, Phys. Rev. **C 61**, 061301(R) (2000).

[San04a] N. Sandulescu, N.V. Giai, and R.J. Liotta, Phys, Rev. **C 69**, 045802 (2004).

[San04b] N. Sandulescu, Phys. Rev. **C 70**, 025801 (2004).

[Sat64] G.R. Satchler, R.M. Drisko, and R.H. Bassel, Phys. Rev. **136**, B637 (1964).

[Sat79] G.R. Satchler and W.G. Love, Phys. Rep. **55**, 183 (1979).

[Sat83] G.R. Satchler, *Direct Nuclear Reactions* (Clarendon Press, Oxford, 1983).

[Sch03] A. Schwenk, B. Friman, and G.E. Brown, Nulc. Phys. **A713**, 191 (2003).

[Sch07] A. Schiller *et al.*, Phys. Rev. Lett. **99**, 112501 (2007).

[She03] C. Shen, U. Lombardo, P. Schuck, W. Zuo, and N. Sandulescu, Phys. Rev. **C 67**, 061302R (2003).

[She07] D.V. Shetty, S.J. Yennello, G.A. Souliotis, Nucl. Inst. and Meth. in Phys. Res. **B 261**, 990 (2007).

[Sie67] P. Siemens. H.A. Bethe, Phys. Rev. Lett. **18**, 704 (1967).

[Sie70] P.J. Siemens, Nucl. Phys. **A141**, 225 (1970).

[Sin75] B. Sinha, Phys. Rep. **20**, 1 (1975).

[Sky56] T.H.R. Skyrme, Phil. Mag. **1**, 1043 (1956); T.H.R. Skyrme, Nucl. Phys. **9**, 615 (1959).

[Sor08] O. Sorlin and M.G. Porquet, Prog. Part. Nucl. Phys. **61**, 602 (2008).

[Sta04] M. Stanoiu *et al.*, Phys. Rev. **C 69**, 034312 (2004).

[Ste06] A.W. Steiner, Phys. Rev. **C 74**, 045808 (2006).

[Sum94] K. Summiyoshi and H. Toki, Astro. Phys. J. **422**, 700 (1994).

[Swe94] F.D. Swesty, J.M. Lattimer, and E.S. Myra, Astrophys. J. **425**, 195 (1994).

[Swi83] W.J. Swiatecki, Phys. Scr. **28**, 349 (1983).

[Tan85] I. Tanihata *et al.*, Phys. Rev. Lett., **55** (1985).

[Tan88] I. Tanihata *et al.*, Phys. Lett. **B 206**, 592 (1988).

[Tan95] I. Tanihata, Prog. Part. Nucl. Phys. **35**, 505 (1995).

[Tha05] H.S. Than, Master Thesis, *unpublished* (2005).

[Thi00] P.G. Thirolf *et al.*, Phys. Lett. **B 485**, 16 (2000).

[Tod04] B.G. Todd-Rudel, J. Piekarewicz, P.D. Cottle, Phys. Rev. **C 69**, 021301R (2004).

[Tod05] B. G. Todd-Rutel and J. Piekarewicz, Phys. Rev. Lett. **95**, 122501 (2005).

[TRI] http://www.triumf.ca/.

[Tsa09] M.B. Tsang, Y. Zhang, P. Danielewicz, M. Famiano, Z. Li, W.G. Lynch, and A.W. Steiner, Phys. Rev. Lett. **102**, 122701 (2009).

[Var91] R.L. Varner, W.J. Thompson, T.L. McAbee, E.J. Ludwig, and T.B. Clegg, Phys. Rep. **201**, 57 (1991).

[Vau67] D.G. Vautherin, M. Vénéroni, Phys. Lett. **B 25**, 175 (1967).
D.G. Vautherin, PhD Thesis (1969).

[Vau72] D.G. Vautherin, D.M. Brink, Phys. Rev. **C 5**, 626 (1972).

[Vre04] D. Vretenar, W. Weise, Lect. Notes Phys. **641**,65 (2004).

[Vri87] H. De Vries, C.W. De Jager and C. De Vries, At. Data Nucl. Data Tables **36**, 495 (1987).

[Wal95] J.D. Walecka, *Theoretical nuclear and subnuclear physics*, Oxford University Press, New York, 1995.

[Wam93] J. Wambach, T.L. Anisworth, and D. Pines, Nucl. Phys. **A555**, 128 (1993).

[Wan90] Y. Wang and J. Rapaport, Nucl. Phys. **A517**, 301 (1990).

[War95] R.E. Warner, J. H. Kelley, P. Zecher, F.D. Becchetti, J.A. Brown, C.L. Carpenter, A. Galonsky, J. Kruse, A. Muthukrishnan, A. Nadasen, R.M. Ronningen, P. Schwandt, B.M. Sherrill, J. Wang and J.S. Winfield, Phys. Rev. **C 52**, 1166 (1995).

[War09] M. Warda, X. Vinas, X. Roca-Maza, and M. Centelles, Phys. Rev. **C 80**, 024316 (2009); M. Centelles, private communication (unpublished).

[Wil46] H.A. Wilson, Phys. Rev. **69**, 538 (1946).

[Wir88] R.B. Wiringa, V. Fiks, Phys. Rev. **C 38**, 1010 (1988).

[Xia09] Zhigang Xiao, Bao-An Li, Lie-Wen Chen, Gao-Chan Yong and Ming Zhang, Phys. Rev. Lett. **102**, 062502 (2009).

[Yos95] A. Yoshida, N. Aoi, T. Fukuda, M. Hirai, M. Ishihara, H. Kobinata, Y. Mizoi, L. Mueller, Y. Nagashima, J. Nakano, T. Nomura, Y.H. Pu, F. Scarlassal, C. Signorini, and Y. Watanabe, Nucl. Phys. **A588**, 109c (1995).

[Zuo05] W. Zuo, L.G. Cao, B.A. Li, U. Lombardo, and C.W. Shen, Phys. Rev. **C 72**, 014005 (2005).

[Zuo99] W. Zuo, I. Bombaci, and U. Lombardo, Phys. Rev. **C 60**, 024605 (1999).